Spring 5-13-2019

Fluid Transport in Porous Media for Engineering Applications

Eric M. Benner
University of New Mexico

Eric M. Benner

Candidate

Chemical and Biological Engineering

Department

This dissertation is approved, and it is acceptable in quality and form for publication:

Approved by the Dissertation Committee:

Dr. Dimiter N. Petsev, Chair

Dr. Daniel Appelö, Member

Dr. Plamen Atanassov, Member

Dr. Frank van Swol, Member

Fluid Transport in Porous Media for Engineering Applications

by

Eric Michael Benner

B.S., Chem. Eng., New Mexico Institute of
Mining and Technology, 2011

DISSERTATION

Submitted in Partial Fulfillment of the
Requirements for the Degree of

Doctor of Philosophy
Engineering

The University of New Mexico

Albuquerque, New Mexico

May, 2017

Dedication

For Rachel

and the elder Dr. Benner

We stand on great shoulders

Acknowledgments

Foremost appreciation goes to my advisor, Professor Dimiter N. Petsev, for his oversight and direction in all aspects of my dissertation. Mitko's kind leadership, keen insights, and flexible nature has made graduate school a joy. Thanks to my committee members, Professors Frank van Swol, Plamen Atanassov, and Daniel Appelö, for their advice and feedback. This work is built on the learning and critique of many more professors and teachers and the support of the hardworking staff in the Chemical and Biological Engineering Department, the School of Engineering, and the Center for Micro-Engineered Materials.

All my fellow members of the Petsev research group have been invaluable to this journey; especially, Dr. Mark Fleharty and Raviteja Vangara who were confidants through innumerable moments of difficulty. I thank the undergraduate students who have assisted in computational and experimental work presented in this dissertation: Steven E. Benner, Madelaine S. Chavez, and Daniel M. Gilliam. Also, to my friends from the nuclear engineering and mathematics departments: you have kept alive my enthusiasm for applying theory and computation to engineering!

My parents, Dr. Robert and Jannette Benner, have both excellently exemplified the pursuit of education and loving family: without you I would never have sought after or accomplished so much. My second parents, Jim and Pauline Clements, have supported us these six years in uncountable ways: thank you. Finally, to my wife Rachel: you have so long poured out your life for my learning and research, and now we may rest.

Fluid Transport in Porous Media for Engineering Applications

by

Eric Michael Benner

B.S., Chem. Eng., New Mexico Institute of
Mining and Technology, 2011

Ph.D., Engineering, University of New Mexico, 2017

Abstract

This doctoral dissertation presents three topics in modeling fluid transport through porous media used in engineering applications. The results provide insights into the design of fuel cell components, catalyst and drug delivery particles, and aluminum-based materials. Analytical and computational methods are utilized for the modeling of the systems of interest. Theoretical analysis of capillary-driven transport in porous media show that both geometric and evaporation effects significantly change the time dependent behavior of liquid imbibition and give a steady state flux into the medium. The evaporation–capillary number is significant in determining the time-dependent behavior of capillary flows in porous media. The analytical solutions for the front position for 1D and 2D capillary flows and under normal evaporation agree with experimental results.

The lattice Boltzmann method (LBM) is used for versatile and flexible modeling of pore-scale phenomena in porous media. The LBM is used to show the the effects

of various physical phenomena, such as multiphase, electrochemical, and dissolution, on pitting corrosion of aluminum surfaces in corrosive environments. In particular, each of these phenomena may spontaneously manifest phenomenological asymmetries that influence the growth of the corroding pit. Fluid motion in bimodal porous particles shows heterogeneous flow behavior in the medium. A brief discussion is given on implementations of parallel lattice Boltzmann schemes for future increase in simulation model capabilities. Each of these topic areas may be extended by further combining models of important physical phenomena.

In the appendices, additional prospective results are overviewed. The font shape of capillary wicking from a finite line source into a 2D domain agrees qualitatively with empirical observations. A discussion of the background and application of the LBM to stress corrosion cracking in aluminum is given, where we show that thin cracks will retain liquids better than wide cracks. Using a finite element model, we show that flow through discrete mono-porous particles increases with increasing velocity and permeability for low characteristic velocity; this scaling law shows that flow rate is proportional to the Reynolds number times the square root of the Darcy number.

Contents

Contents

3   Evaporation Influences on Wicking in Thin Porous Strips   **37**

Contents

Contents

Contents

Chapter Supplementary Materials   **214**

Contents

Contents

Contents

List of Figures

Chapter 1

Introduction

1.1 Transport in Porous Media

The study of porous media transcends science, engineering, and mathematics. Porous media are investigated for practical and theoretical reasons in physics, hydrology, mechanical, civil and chemical engineering, physiology, and medicine.[2,3] It is a broad and complex field ranging from supercomputer simulations of fuel cell catalysis at the pore-scale to small continuum porous domains described by the Darcy equation.[4,5] Experiments on porous media flow range over time scales from seconds in microchannels to decades in underground water movement.[6,7] Mathematical analytical techniques of porous flows vary from algebraic expressions, to full fluid models with Navier–Stokes, and even to fractal and group theoretic approaches.[8]

Numerous critical factors need to be considered before attempting to predict the transport in any given porous medium. Porous media generally have multiphase, multi-species, non-isothermal, and non-laminar flows undergoing various chemical and physical changes. Additionally, the media are often anisotropic and expand and contract in a variety of fields, *e.g.* electric, gravitational. Illustrative examples of the

variety of porous media and related phenomena are shown in figure 1.1. Evidently, one must reduce the complexity of the system to be studied; some assumptions are often very easily applied while others are only made as a first-level approximation. These assumptions lead to the determination of a model types appropriate to the fluid being studied; models are often computational or analytical and in some cases may be a simplified experiment. First, the fluid particles may be tracked individually, statistically, or as a collective mass, corresponding to the Liouville, Boltzmann, and Navier–Stokes equations, respectively.[9] These provide what are known as nanoscale, mesoscale, and macroscale descriptions of the fluids and define the transition from discrete to continuum models.[10–12] The system becomes significantly more complex when multiple phases are involved, as is the case in petroleum reservoirs which at the simplest approximation often contain two liquid phases, one gas phase, and one solid phase. Furthermore, within each phase it is very common in a variety of systems for several chemical species to have an important role as is the case in chemically reacting flows and diffusiophoretic mixtures. Additional difficulties which can arise in the study of porous media include turbulent fluids for large pore media with high flow rates, non-Newtonian flows as described by the theory of rheology, and phase transformations such as freezing and evaporation.[13]

The solids in the porous media also admits descriptions from discrete fine scale regimes up to models that utilize only effective parameters over a continuum domain. To fully understand many complex porous media, a model at the scale of the individual pores is required. These discrete pore models are usually more difficult to construct generalized solutions to continuum models. In some cases, the problem of interest may only require modeling of single pores or a small bundle of pores in a simple geometry; in other cases large networks of highly tortuous pores of various sizes need to be considered.[8] A continuum model of a porous medium has certain parameters described empirically or theoretically determined expressions, where different parameter values lead to different behaiors. The most common model is the

(a) Bottle cork.[14]

(b) Fractured rock.[15]

(c) Freezing brick wall.[16]

(d) Fuel cell powered clock.[17]

(e) Silica nanoparticle.[18]

(f) Corroded aluminum part.[19]
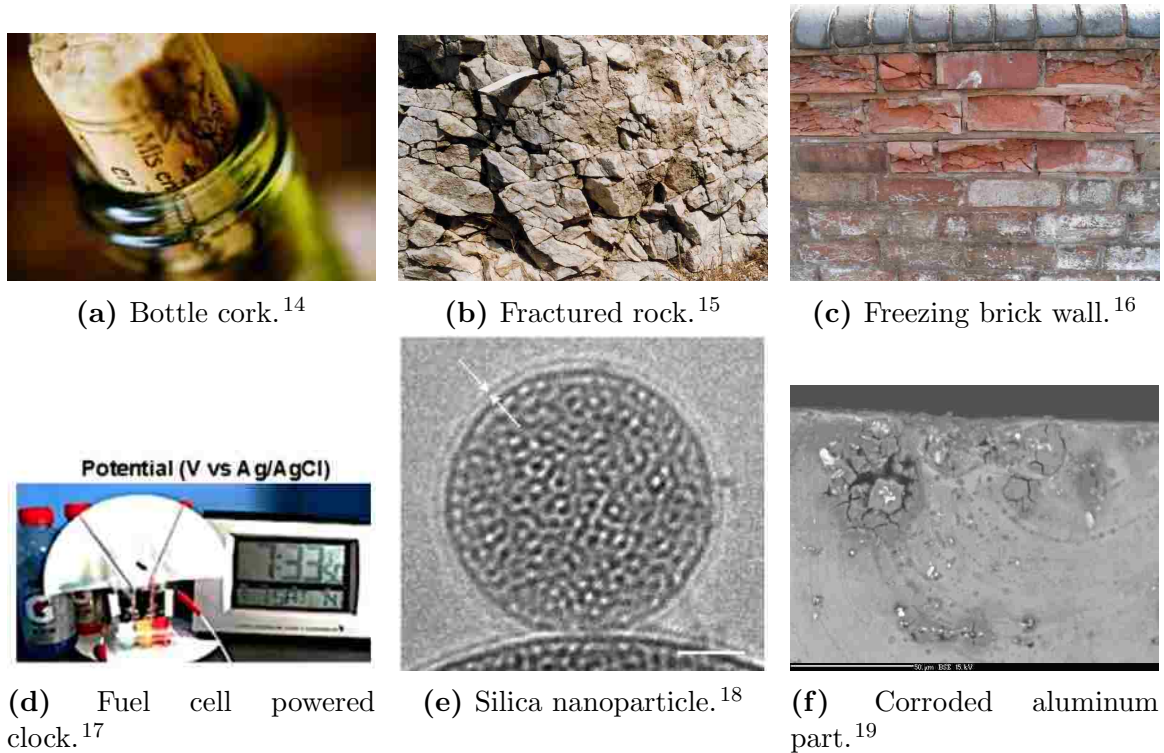
Figure 1.1. Examples of porous media.

Darcy law where the velocity of fluid moving through a medium is directly related to the pressure across the medium. The Darcy equation assumes a continuum approximation of both the medium and the fluid; it was first found experimentally but may be derived by averaging over the Navier–Stokes equations.[5] Incorporating additional terms to the Darcy equation increases the accuracy and validity of its solution to a wider range of media. An example is the Darcy–Brinkman–Forchheimer equation which further accounts for inertia and multiple porosities.[4,20] Other continuum approximations of pores are used for various physical properties beyond fluid transport such as heat transfer and acoustics.

This work primarily focuses on some of the more common models of porous media and additional physical effects. The central viewpoint of the dissertation is continuum fluids flowing in discrete pores, however this perspective branches into different, but

related, descriptions as suitable to the problem. We consider both statistical and continuum models of the fluids, and describe solid domains spanning the scales of single pore, many-pore, and continuum porous media. Gravitational forces, pressure-driven flow, multiphase flows, and mass fluxes are used in multiple topics, while multi-species processes, chemical reactions, and electrochemical transport methods are lightly touched on. Significant extensions to the models employed would include heat transfer, fractal solids, and self-consistent electrokinetic phenomena. We do not consider turbulent or non-newtonian flows, swelling solid media, or solidification in any detail.

1.2 Objectives

In this dissertation, we discuss three topic areas which involve modeling fluid transport in porous media used for engineering applications: capillary wetting in macroscopic fibrous media, single-pore-scale processes in pitting corrosion, and multi-pore scale transport on the microscale. The goal is to apply fluid mechanics techniques to design of materials and devices and to better understand fluid transport phenomena in porous media. Thus, the work in this dissertation has important applications materials and fluid systems engineering.

First we consider the dynamic influence of geometry and evaporation on liquid absorbing into a porous medium by capillary forces. This has applications in designing porous media which are used to drive fluids in small devices; an example system is illustrated in Figure 1.1d where a clock is powered by a glucose reaction.[17,21] The work on capillary imbibition is primarily theoretical with some qualitative and quantitative experimental validation. The designs require quantitative means of knowing the position of the wetted front of the liquid domain, the total rate of fluid entering the domain, and the local flow-speed at given points in the domain.[22] Each of these

variables are dependent on the shape of the domain, particularly the dimensionality of the expansion, and on other physical phenomena impacting the flow such as evaporation and gravity.[23,24] The higher-dimensional or expanding shape of the porous domain increases the flow rate through the inlet.

Secondly, we model species transport in a single pit on a corroding aluminum surface. This project intends to give insights into the electrochemical corrosion process for mitigating damage to aircraft components.[25] Figure 1.1f shows an example of aluminum corrosion which caused mechanical failure. The process is a single-pore scale multiphysics problem which involves oxidation-reduction reactions and acid-base chemistry as well as transport by electrokinetics, diffusion, and dissolution. Ideally, we wish to determine key transport mechanisms of corrosion which can be mitigated using chemical means and thereby protect the aluminum.

Finally, the third topic is on the single-phase flow of fluids through a porous medium of two interconnected, distinct pore sizes. These bimodal porous, or simply biporous, media are not well studied—particularly to understand the pore level effects on the fluid motion—and may be useful in catalysis because the smaller pores increase the surface area per volume of the particle.[1,26] Thus the particles present a means to improve surface reaction rates in catalysts.[27] Computational methods give the flexibility in analyzing how the relative pore sizes and interconnectivity of the pores relates to the overall permeability of the medium. Knowing the transport properties of biporous materials can also be used to improve the delivery rate of anti-cancer compounds in drug delivery as illustrated in Fig. 1.1e.[18]

1.3 Methods

1.3.1 Analytical

In general, appropriate continuum equations are a set of partial differential equations. For some systems, such as in capillary wicking, assumptions are usually made to reduce the complexity of the mathematical system such that the partial or ordinary differential equations are analytically solvable.[28,29] These assumptions include using known problem geometries which are well described by simple coordinate systems.[30,31] In some cases the semi-analytical solutions are derived in the form of non-analytical integrals; then numerical methods are employed to evaluate these expressions.[32,33]

1.3.2 Computational

In fundamental chemical engineering research, several common methods in computational fluid dynamics are applicable to various types of porous simulations, particularly for models of individual or small groups of pores. The finite element method (FEM) is generally flexible in formulating the domains and discretized physical equations.[34,35] FEM is useful for both flows in discrete porous media and directly for continuum equations because it is based on variational methods for differential equations.[36] Two other methods, finite differences (FDM) and finite volumes (FVM), are also widely used partly because they are often simpler to implement.[37,38]

The lattice Boltzmann method (LBM) is a more recent development which has matured over the last twenty years to become significant in the modeling of porous media.[13] Numerous other methods are used for modeling fluids transport such as boundary element method, smooth particle hydrodynamics, dissipative particle dynamics, classical density functional theory, and even molecular dynamics.[39–43] The

lattice Boltzmann method is principally utilized in this dissertation because it handles amorphous solids very easily and is relatively simple to program for multiple physical effects. In an appendix, we also conduct a finite element simulations to analyze flow through pores of a single size through isolated particles.

1.3.3   Experimental

This dissertation is largely focused on theoretical and computational models, although results that are empirically testable are desired for validation of the results. Ultimately, experiment determines when the predictions of models are correctly applied in a given system. Experimental work on the effects of surface evaporation on liquid imbibition has been conducted but needs to be extended to account for front and side boundary evaporation for the proposed theory to be tested comprehensively.* Numerous studies of pitting corrosion in aluminum have been carried out,[44–46] however we are focused on computational investigation of the process to uncover phenomena on a nano to micro scale which may be difficult to observe empirically. Finally, microscale measurements of the permeability in biporous media would be challenging to profile physically and are beyond the reasonable scope of this dissertation.[1]

1.4   Overview

Below we overview the content of this dissertation; the relationships between the chapter topics are illustrated in Fig. 1.2.

The following five chapters discuss continuum models of the capillary wetting behavior of dry porous media. In Ch. 2, two-dimensional and three-dimensional expanding capillary flows are discussed, and the dynamics are compared with the

---

* See Apx. G for details.
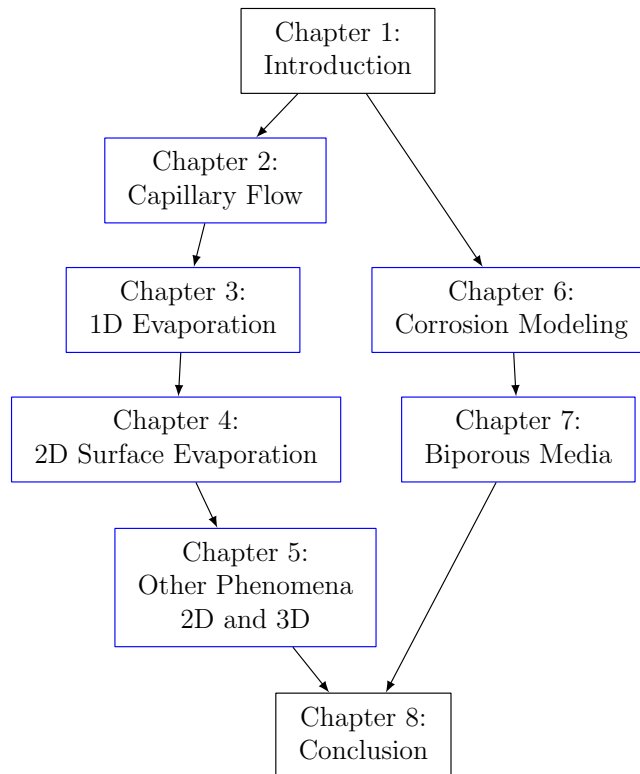
Figure 1.2. Layout of the dissertation.

known one-dimensional Lucas–Washburn solution for wetting Darcy flows. The effects of the three modes of evaporation—normal surface, side, and front evaporation—as well as restraint by gravity, in thin porous media are introduced and discussed in Ch. 3. These two chapters are based on as Refs.[23] and[24], respectively. Normal surface evaporation, which is predominant in thin media, is investigated in Ch. 4 for 2D expanding flows. The other phenomena which affect capillary flow, as first discussed in Ch. 3 for the 1D-like domain, are briefly investigated for 2D and 3D domains in Ch. 5. For the first time in published literature, we observe the evaporation–capillary number which determines the time-dependent behavior of capillary porous media and is central to the analyses given in Chs. 3 through 5.

Chapters 6 and 7 develop computational pore-scale multi-physics models of trans-

port in porous media using the lattice Boltzmann method. Several models of key processes in pitting corrosion are modeled using the LBM in Ch. 6. Ch. 7 discusses flow in biporous media and parallelization of the LBM. Finally, the conclusions are summarized in Ch. 8.

Appendices provide common background material, supplemental chapter details, and further preliminary work.

Chapter 2

Porous Media Capillary Driven Flow into Expanding Geometries

2.1 Introduction

Capillary driven liquid flows in porous media are ubiquitous phenomena that occur both in nature and in various practical applications.[8,21,47–52] The dynamics of such flows was first analyzed about a century ago[53–55] for the simple case of one dimensional transport in porous materials (capillaries) of uniform cross-section. The advancement of the liquid is driven by the capillary pressure due to the curvature of the liquid-gas interface in each individual pore. Hence the liquid should wet the pore walls with a contact angle that is less than 90°. As the liquid penetrates further into the porous material of constant cross section, the total hydrodynamic resistance increases and the bulk flow rate decreases proportionally to $t^{1/2}$ (where t is time). This result is often referred to as the Lucas–Washburn (LW) relationship.[54,55] Strictly the LW model was derived for the flow in a single straight capillary. For a porous media the LW relationship has an average macroscopic meaning, similar to the Darcy equation

[8,56] with pressure drop determined by capillarity and a permeability coefficient that is a complex function of the porosity. The LW model is based on the assumption that the flow is governed by the liquid motion, and the displacement of the gas phase at the front does not significantly slow the flow due to its much lower dynamic viscosity. The model assumes a single-phase system with a moving front, and is valid in the limit of small gas pressure and low density. This has been both experimentally and theoretically shown to be reasonable for a great number of systems involving liquids moving in porous media.[8,50,57–63] In the case of two immiscible liquids displacing each other, the flow needs to be treated as a two-phase and will depend on both viscosities.[8] The focus of the present paper is on liquid phase capillary flow in porous materials without entrapment of air anywhere in the wetted region.

Liquid penetration in porous media that is expanding or contracting in the direction of the flow behaves differently than for a constant cross-section porous media. Estimations of the bulk flows in 2D and 3D expanding porous media were offered[57–59] suggesting that the time dependence of the flow deviates from the LW one-dimensional (1D) case. The cases of 2D radial flow where the front is represented by a gradually expanding circle was analyzed in detail by Hyväluoma *et al.*[61] The authors compared the capillary driven flow Darcy type model to a lattice Boltzmann simulation and obtained excellent agreement, thus validating the analytical approach. The detailed analysis of the 3D case corresponding to an expanding spherical surface was performed by Xiao *et al.*[60] There the capillary driven transport model was tested against carefully performed experiments and again both were found to be in agreement. To maintain circular or spherical symmetries the flows must start from a point or an already circular (for 2D) or spherical (3D) boundary. Hyväluoma *et al.*[61] used the model to describe the penetration of liquid in two dimensions (2D) from a droplet with circular circumference sitting on porous paper. They showed that the liquid velocity decreases with time following a different and more complicated dependence. Xiao *et al.*[60] used the spherical expansion model to fit experimental data on capil-

lary penetration of water in packed glass beads. All these results are very important because they imply that the shape of the porous material leads to qualitative differences in the resulting flow patterns. This means that applications using capillary driven transport in porous media can be optimized by simply shaping the materials accordingly.[50]
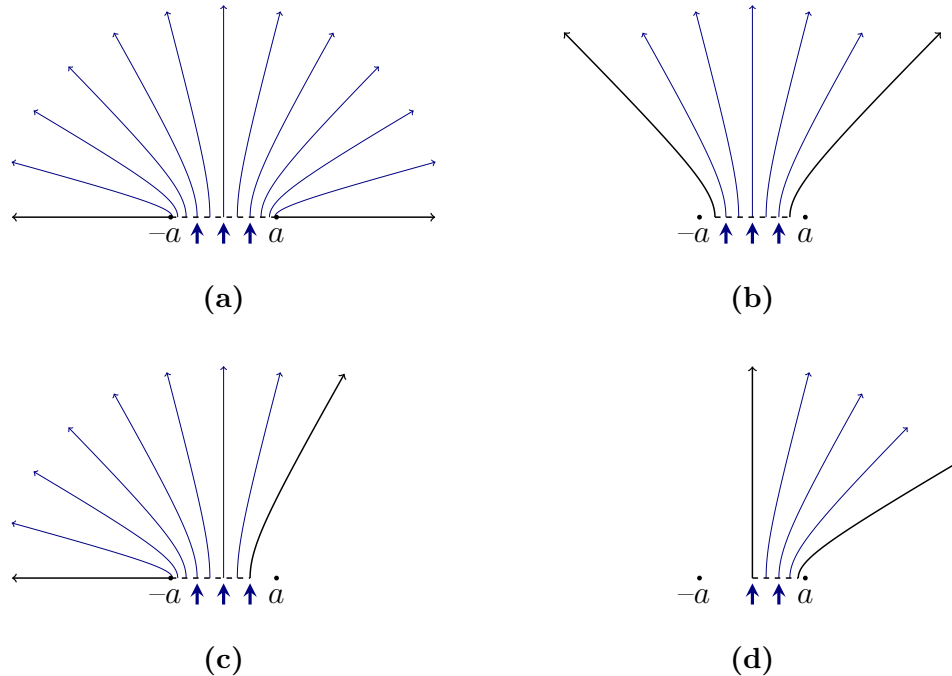
Figure 2.1. Examples for flows in various types of expanding porous media in 2D [see Eqs. (2.3.1) and Figure 2.2]. Case (a) corresponds to $0 \leq \psi \leq \pi$. Case (b) corresponds to where $\psi_1 \leq \psi \leq \pi - \psi_1$ is an arbitrary angle. Case (c) corresponds to $\psi_1 \leq \psi \leq \pi$. Case (d) corresponds to $\psi_1 \leq \psi \leq \pi/2$. Rotating cases (a) and (b) around the y-axis gives a 3D flow in expanding media [see Eqs. (2.4.1) and Figure 2.3] with $0 \leq \theta \leq \pi/2$ and $0 \leq \theta \leq \theta_1$ respectively, where θ_1 is an arbitrary angle.

Here we present analytical results for the flow in porous media that exhibit sudden expansion (see Figure 2.1). The flow in these cases is not necessarily radial as in the Refs.[60,61] because the entrance to the expanding porous space has finite dimension and is usually flat instead of circular. Our results include a linear velocity field at each point (on a scale greater than the typical average pore size) in the domain of interest.

The detailed knowledge of the local fluid velocity is very important for applications like designing paper based diagnostic devices with different shapes,[48,50] delivering solutions to power fuel cells[21] or to better understanding how moisture penetrates construction materials.[57,58] We derive the position of the wetted front as well as the bulk flow rate in the porous material as functions of the elapsed time. The 2D solution is applicable to a wide variety of shapes. The 3D case can be treated analytically only if the domain has axial symmetry. We will limit our analysis to porous domains with zero flow across the side boundaries and will ignore inertial effects. Inertia and hydrodynamic nonlinearity are important in the initial moment of liquid penetration into the porous media and depends on the driving capillary pressure.[64] The latter is a function of the pore (capillary) radius and the wetting contact angle. As the pores may vary in size, the capillary pressure used in our model is an average over the pore size distribution, which has to be sufficiently narrow to prevent capillary fingering from occurring. It was shown by Lavi *et al.*[64] that for radii of the order of 50 µm inertia is usually important. If the wetting contact angle is 0° then inertial terms might be significant down to 10 µm pore radii.[64] Below these pore sizes, viscosity is dominant and inertia does not play a role. The solution is restricted to the assumption that gravitational effects are negligible. For systems that are approximately 2D, this is usually reasonable even for large systems as the dimensions are commonly orthogonal to the gravitational field. However in 3D this means that the solution degrades as the capillary pressure times the surface area approaches the weight of the fluid because this greatly distorts the front of the advancing fluid by gravitational percolation.[59] Finally, our analysis does not include possible evaporation of 2D surfaces or of the side boundaries for both 2D and 3D systems.*

   In the next section, we present a general overview of the capillary driven flow in porous materials. Section 2.3 presents the derivation of results for the flow velocity

---

* Permeable evaporative side boundaries and surface evaporation are discussed in Chs. 3 and 4; the former is published as Ref.[24].

in 2D expanding porous media, Section 2.4 presents the solution for the capillary driven flow in an expanding 3D porous material, Section 2.5 discusses and compares the results for each of the respective geometries, and Section 2.6 summarizes the conclusions.

2.2 Governing Equations for the Flow in Porous Media

The flow of incompressible liquid in porous media is given by the mass balance

$$\boldsymbol{\nabla} \cdot \mathbf{v} = 0, \tag{2.2.1}$$

where $\mathbf{v}$ is the linear liquid velocity on a scale that is larger than the individual pore size. For mass flux a sink or source term, Q, (*e.g.*, evaporation, condensation, etc.) may be added to the right hand side of (2.2.1); this term is presently ignored.* The liquid flow in porous media is irrotational;[65] therefore the velocity can be expressed by means of the velocity potential, φ,

$$\mathbf{v} = \boldsymbol{\nabla}\varphi = -\frac{k}{\mu}\boldsymbol{\nabla}P, \qquad \varphi = -\frac{k}{\mu}P. \tag{2.2.2}$$

The right hand side of Eq. (2.2.2) is the Darcy law[56,65] with k being the permeability of the medium, μ is the dynamic shear viscosity of the liquid, and P is the pressure that drives the flow. In the case of capillary driven flow the pressure is equal to[66]

$$P_{\mathrm{c}} = \gamma \cos(\alpha) \left(\frac{1}{R_1} + \frac{1}{R_2} \right), \tag{2.2.3}$$

where γ is the interfacial tension at the gas-liquid interface, α is the contact angle that characterizes the wetting of the solid. R_1 and R_2 are the two principal radii of

---

* We detail the theoretical basis of this evaporation model in §3.2 and explore it further in §4.2. See the derivation of Eq. (3.2.2).

curvature of the pore. Equations (2.2.1) and (2.2.2) can be combined to give

$$\nabla^2 \varphi = 0. \tag{2.2.4}$$

Eq. (2.2.4) will be used to obtain expressions for the liquid flow in all cases analyzed below.

2.3 Exact Solution for Two–Dimensional Expansion

Different examples illustrating capillary liquid transport in expanding 2D porous media are sketched in Figure 2.1. Figures 2.1a and 2.1b show symmetric regions with different extent of expansion. Figures 2.1c and 2.1d represent two asymmetric cases. The liquid enters the expanding region through an entrance with finite width. Because of the finite size of the entrance, the shape of the expanding liquid front is elliptical rather than circular as in the case discussed by Hyväluoma *et al.*[61] The entrance is saturated with liquid and the pressure there equals the ambient. The front of the moving wetted region is where the liquid meets the gas phase in the pores and the pressure there is equal to the ambient minus the capillary pressure [see Eq. (2.2.3)]. Hence, we look for a solution in the domain that starts at entrance and propagates a wetted front. The problem is best defined in elliptic coordinates[31] (see Figure 2.2)

$$x = a\cosh(\eta)\cos(\psi), \tag{2.3.1a}$$

$$y = a\sinh(\eta)\sin(\psi). \tag{2.3.1b}$$

The general form of Eq. (2.2.4) then becomes

$$\frac{1}{a^2\left(\cosh^2(\eta) - \cos^2(\psi)\right)}\left(\frac{\partial^2\varphi}{\partial\eta^2} + \frac{\partial^2\varphi}{\partial\psi^2}\right) = 0 \tag{2.3.2}$$
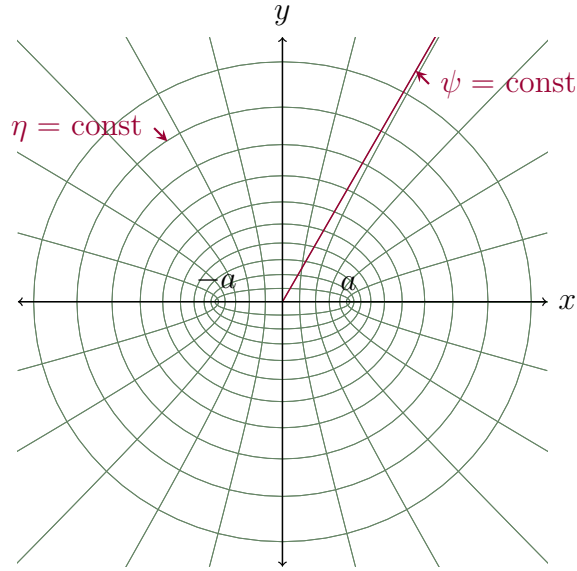
Figure 2.2. Elliptic coordinates, used to describe the flow in an expanding 2D porous domain. The points $-a$ and a are the foci of the ellipses.

If there is no liquid flow across the edges of the domain that are defined by and (see Figure 2.1), there will be no variation of φ with respect to the angular variable ψ. Hence the term $\partial^2\varphi/\partial\psi^2$ can be omitted from Eq. (2.3.2) and the equation simplifies to

$$\frac{\mathrm{d}^2\varphi}{\mathrm{d}\eta^2} = 0. \tag{2.3.3}$$

The solution of this equation describes concentric elliptic lines that correspond to the flow potential φ at a given η. The boundary conditions are

$$\varphi|_{\eta=0} = \varphi_0 = -\frac{k}{\mu}P_\mathrm{c}, \tag{2.3.4a}$$

$$\varphi|_{\eta=\eta_f} = 0, \tag{2.3.4b}$$

where $\eta = 0$ at the entrance and $\eta = \eta_f$ at the front. The solution of Eq. (2.3.3) is then

$$\varphi = -\frac{k}{\mu}P_\mathrm{c}\left(1 - \frac{\eta}{\eta_f}\right). \tag{2.3.5}$$

Hence the velocity of the moving liquid is

$$
v = \nabla\varphi = \frac{1}{a\left(\cosh^2(\eta) - \cos^2(\psi)\right)^{1/2}}\frac{\partial\varphi}{\partial\eta}
$$
$$
= \frac{1}{a\left(\cosh^2(\eta) - \cos^2(\psi)\right)^{1/2}}\left(\frac{kP_c}{\mu}\frac{1}{\eta_f}\right). \tag{2.3.6}
$$

Following the approach outlined by Washburn,[55] we derive an equation for the velocity of the moving front

$$
v_f = a\left(\cosh^2(\eta_f) - \cos^2(\psi)\right)^{1/2}\frac{d\eta_f}{dt}
$$
$$
= \frac{1}{a\left(\cosh^2(\eta_f) - \cos^2(\psi)\right)^{1/2}}\left[\frac{\partial\varphi}{\partial\eta}\Big|_{\eta=\eta_f}\right]
$$
$$
= \left(\frac{kP_c}{a\mu}\right)\frac{1}{\left(\cosh^2(\eta_f) - \cos^2(\psi)\right)^{1/2}}\frac{1}{\eta_f}. \tag{2.3.7}
$$

It is convenient to use a dimensionless velocity that has the form $\tilde{v}_f = (\mu a/kP_c)\,v_f$.

The time dependence of the position of the liquid front $\eta_f(t)$ can be derived by integrating Eq. (2.3.7)

$$
\frac{kP_c}{\mu}\int_0^{\eta_f(\tilde{t})}\frac{\left(\cosh^2(\eta_f) - \cos^2(\psi)\right)}{[\partial\varphi/\partial\eta|_{\eta=\eta_{f'}}]}\,d\eta_f{}' = \tilde{t}, \tag{2.3.8}
$$

were $\tilde{t} = (kP_c/\mu a^2)\,t$. After integrating Eq. (2.3.8) we find the following relationship for the time dependent position of the liquid front

$$
\eta_f\sinh(2\eta_f) - \frac{1}{2}\cosh(2\eta_f) - \cos(2\psi)\eta_f{}^2 + \frac{1}{2} = 4\tilde{t}. \tag{2.3.9}
$$

Differentiating with respect to time and multiplying, Eq. (2.3.9), by the factor $a\left(\cosh^2(\eta) - \cos^2(\psi)\right)$ gives the time-dependent velocity of the front [see the left hand side of Eq. (2.3.7)]. Alternatively $\eta_f(\tilde{t})$ can be introduced in the last line of Eq. (2.3.7) to obtain the time dependence of the linear velocity $\tilde{v}_f(\tilde{t})$.

Another quantity of interest is the volumetric flux of liquid U. It is equal to the integral over the liquid velocity across the area of the front, or [see Eq. (2.3.7)]

$$
\begin{aligned}
U(\tilde{t}) &= \iint_A \mathbf{v} \cdot \mathbf{n}\, dA \\
&= a \int_{\psi_1}^{\psi_2} v_f(\tilde{t}) \left(\cosh^2\left(\eta_f(\tilde{t}) \right) - \cos^2(\psi) \right)^{1/2} d\psi \\
&= \frac{kP_c}{\mu} \frac{1}{\eta_f(\tilde{t})} (\psi_2 - \psi_1).
\end{aligned}
\tag{2.3.10}
$$

Here, we have assumed that the front velocity, η_f, is independent of ψ.* Since the liquid motion occurs in a 2D plane, the above result is per unit length in the direction normal to the plane surface. The local velocity $\tilde{v}$ will decrease with the increase of η in an expanding domain and is lowest at the front where $\eta = \eta_f$. The volumetric flux U conserves because as the velocity decreases the front area increases to exactly compensate for that. Both, however, will change with time. For fully open entrance $(\psi_1 = 0, \psi_2 = \pi)$ one obtains

$$
U(\tilde{t}) = \frac{kP_c}{\mu} \frac{\pi}{\eta_f(\tilde{t})}.
\tag{2.3.11}
$$

2.3.1 Asymptotic Results for Small and Large η_f

For short times, η_f is small and we can further simplify the solution (2.3.9) (also setting $\psi = \pi/2$) to read

$$
\frac{{\eta_f}^2}{2} = \tilde{t}.
\tag{2.3.12}
$$

This expression is formally identical to the LW result [54,55]

$$
\frac{L(t)^2}{2a^2} = \tilde{t},
\tag{2.3.13}
$$

which describes the position of the front $L(t)$ in porous domain with constant cross-section.† Hence for short times and small η_f the effect of the expansion is negligible.

---

* This assumption is often inaccurate as we will discuss in the derivation of Eq. (4.3.22) and observe in Figures E.1a and E.2.   † We derive the Lucas–Washburn equation using potential flow in Eq. (3.3.25).

It is also important to stress that the short times discussed here are reflecting only the effect of the porous media geometry and are still long in comparison to the time-scale of any inertial fluid motion. Inertia (if present) occurs on a time scale that is much faster (about at fraction of a second) and practically absent for pores with radii below 10 μm, or for even larger pores if the wetting contact angle is less than 0°.[64]

The asymptotic result for large η_f is obtained by realizing that $\sinh(2\eta_f) \rightarrow \exp(2\eta_f)/2$ and $\cosh(2\eta_f) \rightarrow \exp(2\eta_f)/2$. At long times the asymptotic result for (2.3.9) is

$$\frac{1}{8}\eta_f \exp(2\eta_f) - \frac{1}{16}\exp(2\eta_f) = \tilde{t}. \qquad (2.3.14)$$

As will be shown below, Eq. (2.3.14) is identical to the long time asymptotic results of Hyväluoma *et al.*,[61]

$$\left(\frac{r_f}{r_0}\right)^2 \ln\left(\frac{r_f}{r_0}\right)^2 - \left(\frac{r_f}{r_0}\right)^2 + 1$$

$$\approx \left(\frac{r_f}{r_0}\right)^2 \ln\left(\frac{r_f}{r_0}\right)^2 - \left(\frac{r_f}{r_0}\right)^2 = 4\frac{kP_c}{\mu r_0^2}t. \qquad (2.3.15)$$

r_f is the position of the expanding liquid front and r_0 is the radius of the entrance, which in their analysis must be circular. Using the relationship between polar and elliptical coordinates defined by

$$r^2 = x^2 + y^2 = a^2\left(\cosh^2(\eta)\cos^2(\psi) + \sinh^2(\eta)\sin^2(\psi)\right), \qquad (2.3.16)$$

one can write Eq. (2.3.15) in terms of η_f. Thus tracing the position of the liquid front along the y-axis we obtain

$$\frac{r_f^2}{r_0^2} = \frac{a^2}{r_0^2}\sinh^2(\eta_f) + 1. \qquad (2.3.17)$$

The term 1 on the right hand side of the above equation is added to ensure that $r_f/r_0 \geq 1$. Inserting (2.3.17) into (2.3.15) describes the position of the liquid front (along the y-axis) as a function of time

$$\left(\sinh^2(\eta_f) + \frac{r_0^2}{a^2}\right)\ln\left(\sinh^2(\eta_f) + \frac{r_0^2}{a^2}\right) - \sinh^2(\eta_f) = 4\frac{kP_c}{\mu r_0^2}t = 4\tilde{t}. \qquad (2.3.18)$$

The factor r_0^2/a^2 can be found from the condition that entrances for both circular and elliptical cases are the same. For $0 \leq \psi \leq \pi$ this condition reads

$$2a = \pi r_0 \text{ or } \frac{a}{r_0} = \frac{\pi}{2}. \qquad (2.3.19)$$

For large η_f we have

$$\cosh^2(\eta_f) \to \frac{1}{4}\exp(2\eta_f), \quad \sinh^2(\eta_f) \to \frac{1}{4}\exp(2\eta_f), \qquad (2.3.20)$$

and

$$\frac{r_f^2}{r_0^2} = \frac{a^2}{r_0^2}\frac{1}{4}\exp(2\eta_f)\left(\cos^2(\psi) + \sin^2(\psi)\right) = \frac{a^2}{r_0^2}\frac{\exp(2\eta_f)}{4}. \qquad (2.3.21)$$

Then the right hand side of Eq. (2.3.15) becomes

$$\frac{a^2}{r_0^2}\frac{\exp(2\eta_f)}{4}\ln\left(\frac{a^2}{r_0^2}\frac{\exp(2\eta_f)}{4}\right) - \frac{a^2}{r_0^2}\frac{\exp(2\eta_f)}{4}$$

$$= \frac{a^2}{r_0^2}\left(\frac{\exp(2\eta_f)}{4}\left[2\eta_f + \ln\left(\frac{a^2}{4r_0^2}\right)\right] - \frac{\exp(2\eta_f)}{4}\right)$$

$$\approx \frac{a^2}{r_0^2}\left[\frac{\eta_f\exp(2\eta_f)}{2} - \frac{\exp(2\eta_f)}{4}\right], \qquad (2.3.22)$$

since $2\eta_f \gg \ln\left(a^2/4r_0^2\right)$. Introducing the above expression in Eq. (2.3.15) makes it identical to (2.3.14). For very large η_f and one may use the approximation

$$x\ln x - x \approx \ln(x!) \approx \ln[\Gamma(x + 1)], \qquad (2.3.23)$$

which allows to write the left hand sides of Eq. (2.3.15) in a more compact form;

$$\frac{1}{8}\eta_f\exp(2\eta_f) - \frac{1}{16}\exp(2\eta_f) \approx \frac{1}{16}\ln\left[\Gamma\left(e^{2\eta_f} + 1\right)\right]. \qquad (2.3.24)$$

2.4 Exact Solution in Three–Dimensional Expansion

For flow in 3D porous media, a general grasp of the geometry can be obtained from Figures 2.1a and 2.1b if the graphs are revolved around their vertical axis of symmetry
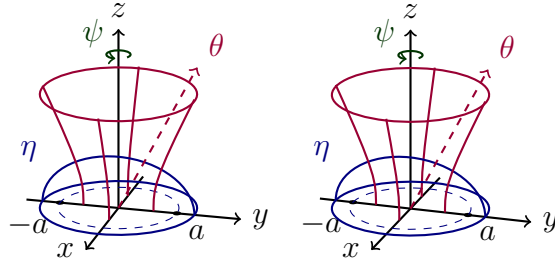
Figure 2.3. Oblate spheroid coordinates, used to describe the flow in an expanding 3D porous domain. (Stereoscopic images) The points $-a$ and a are the foci of the oblate surface corresponding to η. Only systems with axial symmetry are considered.

(the z-axis in Figure 2.3). The coordinates that are relevant to such system are defined by[31] (see also Figure 2.3)

$$x = a\cosh(\eta)\sin(\theta)\cos(\psi), \tag{2.4.1a}$$

$$y = a\cosh(\eta)\sin(\theta)\sin(\psi), \tag{2.4.1b}$$

$$z = a\sinh(\eta)\cos(\theta). \tag{2.4.1c}$$

Note that the variable ψ is different from the one used in the elliptic 2D case discussed above (see Figure 2.3 and compare it to Figure 2.2). The Laplace equation for the flow potential, Eq. (2.2.4), has the form[31]

$$
\begin{aligned}
\nabla^2\varphi = &\frac{1}{a^2\left(\cosh^2(\eta) - \sin^2(\theta)\right)}\left(\frac{\partial^2\varphi}{\partial\eta^2} + \tanh(\eta)\frac{\partial\varphi}{\partial\eta} + \frac{\partial^2\varphi}{\partial\theta^2}\right.\\
&\left. + \cot(\theta)\frac{\partial\varphi}{\partial\theta}\right) + \frac{1}{a^2\cosh^2(\eta)\sin^2(\theta)}\frac{\partial^2\varphi}{\partial\psi^2} = 0.
\end{aligned}
\tag{2.4.2}
$$

Since we consider an axis-symmetric domain, $\frac{\partial^2\varphi}{\partial\psi^2} = 0$, the last term can be omitted. Additionally, we assume there is no flow across the surface corresponding to $\theta = \pi/2$ and $\theta = -\pi/2$, hence there is no change with θ and all derivatives with respect to the polar angle are zero. Therefore Eq. (2.4.2) can be significantly simplified to

$$\frac{\partial^2\varphi}{\partial\eta^2} + \tanh(\eta)\frac{\partial\varphi}{\partial\eta} = 0. \tag{2.4.3}$$

This equation describes concentric oblate surfaces that correspond to the flow potential $\varphi(\eta)$. The boundary conditions for capillary driven flow are identical to those given by Eq. (2.3.4)

$$\varphi|_{\eta=0} = \varphi_0 = -\frac{k}{\mu} P_{\rm c}, \tag{2.4.4a}$$

$$\varphi|_{\eta=\eta_f} = 0. \tag{2.4.4b}$$

The solution for the flow potential is then

$$\varphi = \varphi_0 \left(1 - \frac{\arctan[\tanh(\eta/2)]}{\arctan[\tanh(\eta_f/2)]} \right). \tag{2.4.5}$$

Note that for $\eta_f \to \infty$ the above expression becomes

$$\varphi = \varphi_0 \left(1 - \frac{4\arctan[\tanh(\eta/2)]}{\pi} \right). \tag{2.4.6}$$

which means that in the 3D case we have a finite asymptotic result for infinite domains which is not true for the one and two dimensional cases.

The liquid velocity profile in the 3D porous region has only an η-component, which is

$$
\begin{aligned}
v_\eta &= \frac{1}{a \left(\cosh^2(\eta) - \sin^2(\theta) \right)^{1/2}} \frac{\partial \varphi}{\partial \eta} \\
&= \left(\frac{kP_{\rm c}}{a\mu} \right) \frac{1}{2\cosh(\eta) \left(\cosh^2(\eta) - \sin^2(\theta) \right)^{1/2} \arctan[\tanh(\eta_f/2)]}.
\end{aligned}
\tag{2.4.7}
$$

The velocity of the front is

$$
\begin{aligned}
v_f &= \frac{1}{a \left(\cosh^2(\eta) - \sin^2(\theta) \right)^{1/2}} \left[\frac{\partial \varphi}{\partial \eta} \bigg|_{\eta=\eta_f} \right] \\
&= \left(\frac{kP_{\rm c}}{a\mu} \right) \frac{1}{2\cosh(\eta_f) \left(\cosh^2(\eta_f) - \sin^2(\theta) \right)^{1/2} \arctan[\tanh(\eta_f/2)]}.
\end{aligned}
\tag{2.4.8}
$$

The velocity is formally expressed in terms of the spatial and temporal variables by

$$v_f = a \left(\cosh^2(\eta_f) - \sin^2(\theta) \right)^{1/2} \frac{\mathrm{d}\eta_f}{\mathrm{d}t}. \tag{2.4.9}$$

Hence, combining (2.4.8) and (2.4.9) one derives

$$\int_0^{\eta_f(\tilde{t})} \left(\cosh^2(\eta_f') - \sin^2(\theta)\right) \arctan\left[\tanh\left(\frac{\eta_f'}{2}\right)\right] \cosh(\eta_f') \, \mathrm{d}\eta_f' = \frac{kP_c}{2\mu a}t = \frac{\tilde{t}}{2}. \tag{2.4.10}$$

After integration we obtain a relationship between the front position η_f and scaled time $\tilde{t}$

$$\frac{1}{3}\arctan[\tanh(\eta_f/2)]\left[2 + 3\cos(2\theta) + \cosh(2\eta_f)\right]\sinh(\eta_f)$$
$$-\frac{1}{6}\left[1 + 3\cos(2\theta)\right]\ln[\cosh(\eta_f)] - \frac{1}{12}\left[\cosh(2\eta_f) - 1\right] = \tilde{t}. \tag{2.4.11}$$

The front velocity is then obtained by introducing the obtained time dependence of η_f in Eq. (2.4.8) or (2.4.9). Assuming η_f is not a function of θ, the volumetric flux is obtained from

$$U(\tilde{t}) = \iint\limits_A \mathbf{v} \cdot \mathbf{n} \, \mathrm{d}A,$$

$$= \frac{kP_c}{\mu a}\frac{a^2}{\arctan\left[\tanh\left(\eta_f(\tilde{t})/2\right)\right]}\int_0^{2\pi}\mathrm{d}\psi\int_0^{\theta_0}\sin(\theta)\,\mathrm{d}\theta,$$

$$= \frac{2\pi akP_c}{\mu}\frac{(1 - \cos(\theta_0))}{\arctan\left[\tanh\left(\eta_f(\tilde{t})/2\right)\right]}. \tag{2.4.12}$$

For full open entrance $(\theta_0 = \pi/2)$, this reduces to

$$U(\tilde{t}) = \frac{2\pi akP_c}{\mu}\frac{1}{\arctan\left[\tanh\left(\eta_f(\tilde{t})/2\right)\right]}. \tag{2.4.13}$$

2.4.1 Asymptotic Results for Small and Large η_f

For short times and small values of η_f and $\theta = 0$, Eq. (2.4.11) simplifies to

$$\frac{\eta_f^2}{2} = \tilde{t}. \tag{2.4.14}$$

The long-time, large η_f, asymptotic result can be derived for Eq. (2.4.14) using the same arguments as above [see Eq. (2.3.14)] and also noting that $\arctan\left[\tanh\left(\eta_f(\tilde{t})/2\right)\right] \rightarrow$

$\pi/4$. The result is

$$\frac{\pi}{4}\frac{\exp(3\eta_f)}{12} = \tilde{t}. \tag{2.4.15}$$

For large η_f the front shape should approach that of an expanding sphere. The latter can be derived from Eq. (2.2.4) written in the form

$$\frac{1}{r^2}\frac{\mathrm{d}}{\mathrm{d}r}\left(r^2\frac{\mathrm{d}\varphi}{\mathrm{d}r}\right) = 0, \tag{2.4.16}$$

together with the following boundary conditions

$$\varphi|_{r=r_0} = \varphi_0 = -\frac{k}{\mu}P_{\mathrm{c}}, \tag{2.4.17a}$$

$$\varphi|_{r=r_f} = 0. \tag{2.4.17b}$$

Then the solution for the potential is (see also Ref.[60])

$$\varphi = \varphi_0\frac{r_f r_0}{r_f - r_0}\left(\frac{1}{r} - \frac{1}{r_f}\right). \tag{2.4.18}$$

It is interesting to point out that in the case of 3D radial flow, there is a finite solution for $\varphi(r)$ even if r_f is at infinity. In this case

$$\varphi = \varphi_0\frac{r_0}{r}. \tag{2.4.19}$$

The radial velocity is then

$$v_r = \frac{\partial\varphi}{\partial r} = -\varphi_0\frac{r_f r_0}{r_f - r_0}\frac{1}{r^2} = \frac{r_f r_0}{r_f - r_0}\frac{kP_{\mathrm{c}}}{\mu}\frac{1}{r^2}. \tag{2.4.20}$$

At $r = r_f$

$$v_f = \frac{\mathrm{d}r_f}{\mathrm{d}t} = \frac{r_0}{r_f(r_f - r_0)}\frac{kP_{\mathrm{c}}}{\mu} \tag{2.4.21}$$

Hence the time-dependent position of the moving front is given by

$$\int_{r_0}^{r_f(\tilde{t})}\frac{r_f'\left(r_f' - r_0\right)}{r_0^3}\,\mathrm{d}r_f' = \frac{1}{3}\frac{r_f^3(\tilde{t})}{r_0^3} - \frac{1}{2}\frac{r_f^2(\tilde{t})}{r_0^2} + \frac{1}{6} = \frac{a^2}{r_0^2}\tilde{t}. \tag{2.4.22}$$

The radial coordinate in 3D oblate spheroid coordinates is

$$
\begin{aligned}
r^2 &= x^2 + y^2 + z^2, \\
&= a^2 \left(\cosh^2(\eta) \sin^2(\theta) \cos^2(\psi) + \cosh^2(\eta) \sin^2(\theta) \sin^2(\psi) + \sinh^2(\eta) \cos^2(\theta) \right), \\
&= a^2 \left(\cosh^2(\eta) \sin^2(\theta) + \sinh^2(\eta) \cos^2(\theta) \right).
\end{aligned} \tag{2.4.23}
$$

At the front $\eta = \eta_f$ and for large η_f, we use the approximations $\cosh^2(\eta_f) \to \frac{1}{4}\exp(2\eta_f)$ and $\sinh^2(\eta_f) \to \frac{1}{4}\exp(2\eta_f)$. Hence

$$
\frac{r_f^2}{r_0^2} = \frac{a^2}{r_0^2}\frac{\exp(2\eta_f)}{4}, \tag{2.4.24}
$$

and Eq. (2.4.22) becomes

$$
\frac{1}{3}\frac{r_f^3(\tilde{t})}{r_0^3} - \frac{1}{2}\frac{r_f^2(\tilde{t})}{r_0^2} + \frac{1}{6} = \frac{a^3}{3r_0^2}\frac{\exp(3\eta_f)}{8} - \frac{a^2}{2r_0^2}\frac{\exp(2\eta_f)}{4} + \frac{1}{6}
$$
$$
= \frac{a^2}{r_0^2}\tilde{t}, \tag{2.4.25}
$$

or

$$
\frac{a}{r_0}\frac{\exp(3\eta_f)}{24} - \frac{\exp(2\eta_f)}{8} + \frac{r_0^2}{6a^2} = \tilde{t}. \tag{2.4.26}
$$

Keeping only the leading order term in (2.4.27) and expressing the ratio a/r_0 using Eq. (2.3.19) we obtain

$$
\frac{\pi}{2}\frac{\exp(3\eta_f)}{24} = \tilde{t}, \tag{2.4.27}
$$

which is identical to (2.4.15).

2.5 Results and Discussion

2.5.1 Transport in Two–Dimensional Expansions

Two effects govern the liquid transport in an expanding 2D porous region. Both of them follow from the mass conservation of the incompressible liquid. The first
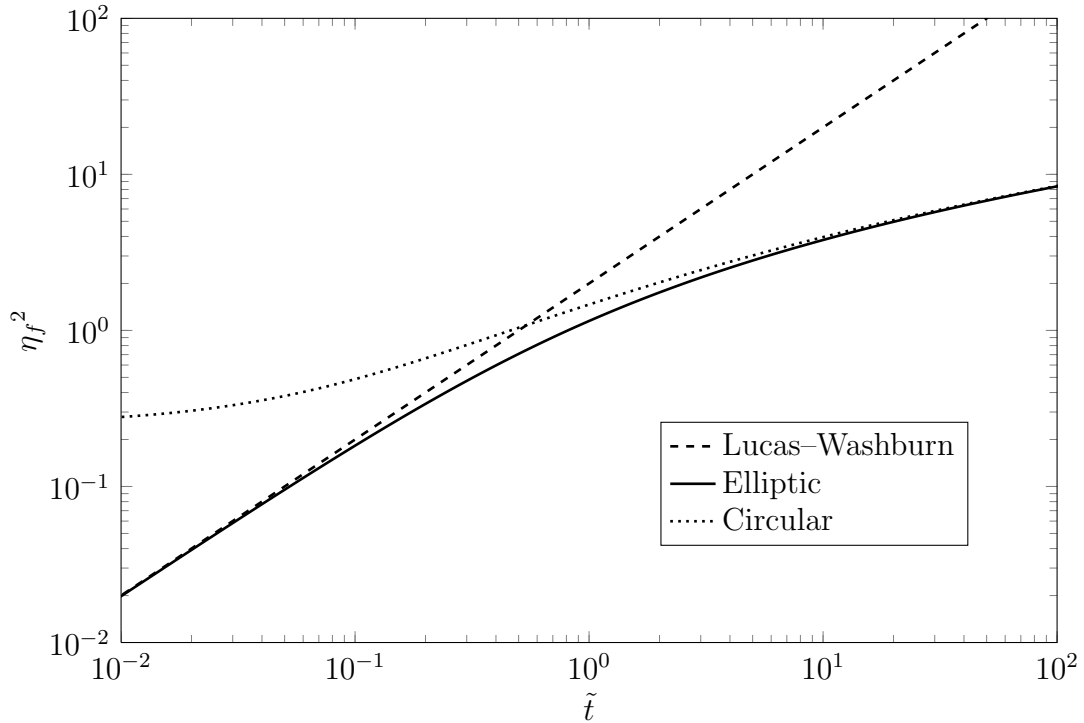
Figure 2.4. Position of the liquid front in an expanding 2D porous material as a function of time [see Eq. (2.3.9)] (solid line). The dashed line is corresponds to the non-expanding LW result [see Eq. (2.3.12)]. The dotted line represents the result for an expanding circular front [see Eq. (2.3.15)].

one follows from the mass conservation and is due to the liquid distribution over an ever-increasing space (or area). This effect leads to an apparent decrease in the velocity of the moving front. At the same time the liquid travels less distance per unit time which lowers the friction resistance while the capillary force increases due to the expansion of the front. The combination of the two effects slows down the linear velocity and facilitates the bulk flow rate in an expanding porous material. Figures 2.4 and 2.5 show the dependence of the liquid front position and linear velocity of capillary driven liquid flow in two dimensional porous regions. The solid lines correspond to the case depicted in Figure 2.1a (the entrance has finite dimensions). The plot was derived from Eq. (2.3.9) setting $\psi = \pi/2$ *i.e.*, the flow along the y-
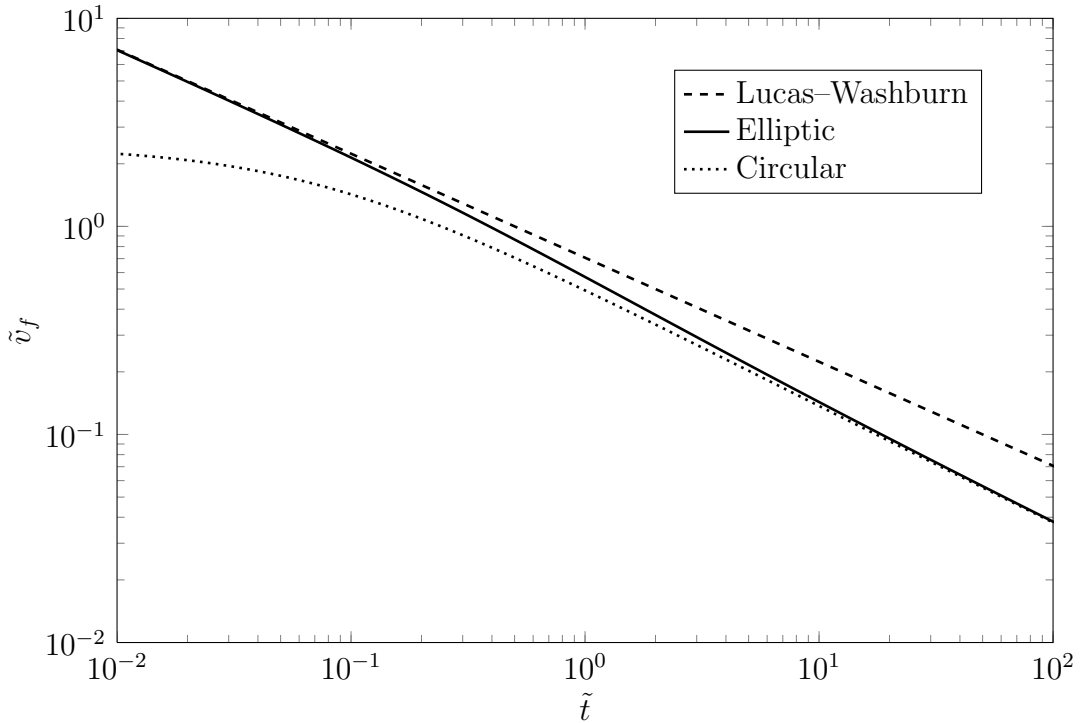
Figure 2.5. Velocity of the liquid front for capillary motion in expanding 2D porous material. The solid line corresponds to the flow depicted in Figure 2.1a [see also Eqs. (2.3.7) and (2.3.9)]. The dashed line shows the LW while the dotted show the 2D radial flows.

axis is traced (see Figure 2.2). It is compared to the LW power-law case[54,55] of non-expanding porous material which maintains constant cross sectional dimension [dashed line, see also Eqs. (2.3.12) and (2.3.13)], as well as to the case of radial flow[61] [see Eq. (2.3.15)]. At short times the front position shows a power law increase similar to the LW solution. This is due to the fact that the effect of the expansion is weak for short distances, the liquid has not spread too much, and the streamlines are almost parallel. As time progresses, however, the expansion effect increases and the distance traveled by the front in the expanding porous domain decreases in comparison with the non-expanding LW case because liquid has also moved to the sides to form the elliptically shaped front. For long times the front becomes less elliptical and more circular and the solution for the front position asymptotically approaches that for
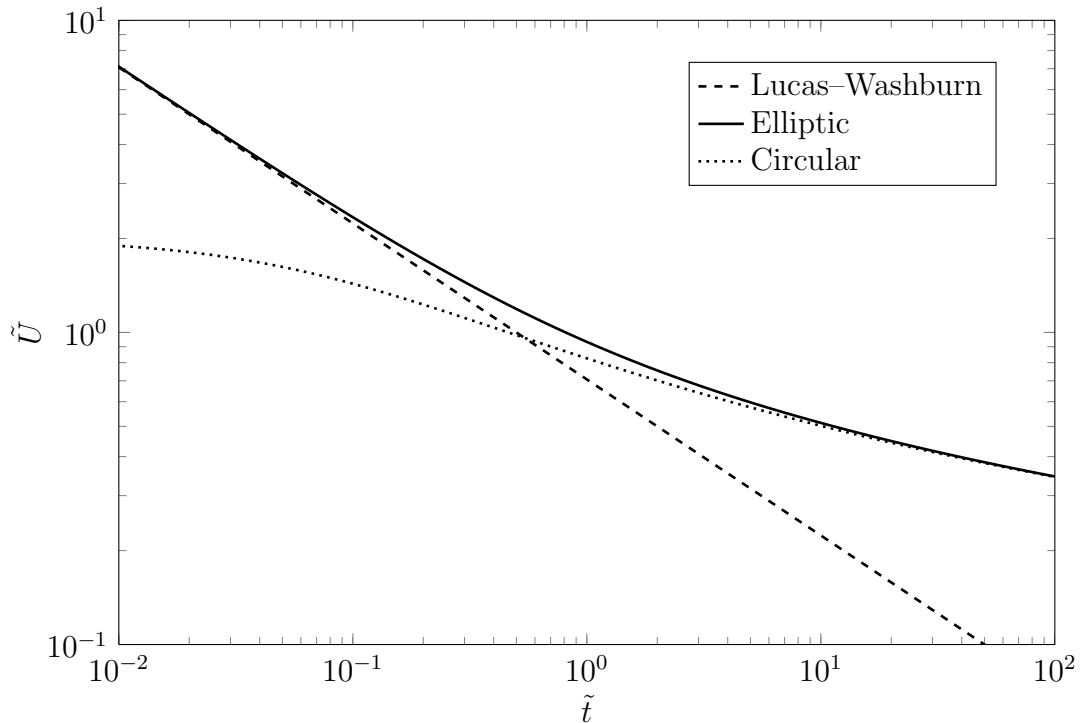
Figure 2.6. Bulk flow rate vs. time for expanding 2D porous materials. The solid line corresponds to the flow depicted in Figure 2.1a [see Eq. (2.3.11) and (2.3.9)]. The dashed line shows the LW while the dotted—the 2D radial flows for large η_f.

an expanding circle given by the dotted line in Figure 2.4 [see Eq. (2.3.14) and the discussion thereafter]. Hence, the LW[54,55] solution and the circular expansion result obtained by Hyväluoma *et al.*[61] represent the limiting cases of no expansion and maximum expansion in 2D. Our result given by Eq. (2.3.9) describes the entire time behavior including two limiting cases as well as the intermediate case, and as seen from Figure 2.4. The latter applies to a range of more than two orders of magnitude of the scaled time.

The time dependence of the linear velocity of the liquid front is shown in Figure 2.5. The solid line corresponds to our solution given by Eq. (2.3.7) in combination with (2.3.9). The dashed line is the LW result[54,55] and the dotted line is that for the

radial flow when r_f/r_0 or, equivalently, η_f are large.[61] Clearly the velocity drops with time for all the cases but at different rates. If the porous region does not expand, then the reason for the velocity decrease is due to the increase of the length of liquid penetration. This length contributes to the viscous resistance and hence, slows down the motion. If the liquid travels in an expanding material (like the examples outlined in Figure 2.1) the front motion is also slowed by the fact that liquid is diverted sideways into the available expanding space. The effect of the expansion is strongest in the case of pure radial flow. At short times our solution is close to that for a non-expanding medium and asymptotically approaches the one for radial flow for very long times.

It is interesting to examine the dependence of the bulk (volumetric) flow rate since it is a measure of the ability of the porous material to absorb liquid. An important practical application exploiting this ability is to drive fluid in devices and material using capillary action instead of an external power source.[50] The solid line in Figure 2.6 shows the change of the bulk flow rate with time calculated from Eq. (2.3.11). Since we are considering a 2D domain, the bulk flow rate is calculated per unit length in direction normal to the plane of the flow. Again for comparison both the non-expanding LW and the radial expanding cases (for large η_f) are shown. Both are obtained in a similar way by multiplying the liquid velocity at the front by its length. Clearly an expanding porous material has better capabilities of absorbing liquids; as it is evident in the plots, the bulk flow rate decreases much slower with time in comparison with the non-expanding case.

2.5.2 Transport in Three–Dimensional Expansions

The effect of expansion is stronger when it occurs in three dimensions. The reason is that there is more space available for the liquid to occupy as it moves forward
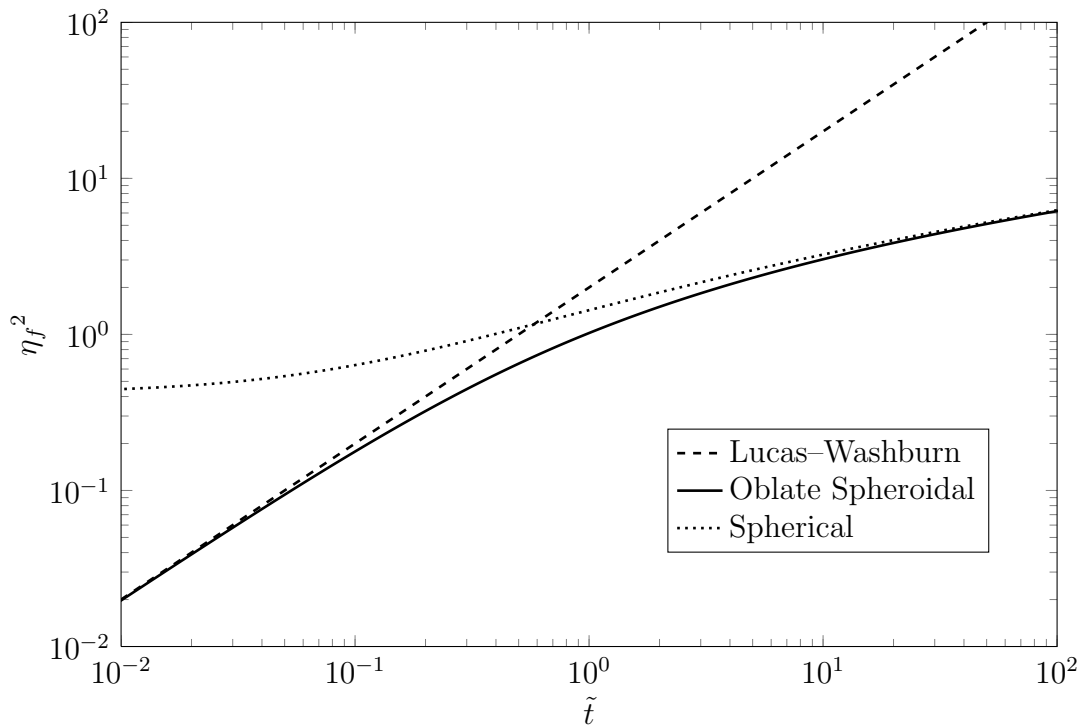
Figure 2.7. Liquid front position as a function of the elapsed time in a 3D expanding porous material. The solid line corresponds to the solution in oblate spheroid coordinates, the dashed line is the LW non-expanding case and the dotted line is the solution for spherical expansion at large η_f.

driven by capillary pressure. The calculations presented below are for fully opened medium where $\theta = \pi/2$ (see Figure 2.3). The entrance has a circular shape. The flow along the y-axis is traced, which corresponds to $\theta = 0$. Figure 2.7 shows the position of the fluid front as a function of the elapsed time. The solid line corresponds to the solution in oblate spheroid coordinates given by Eq. (2.4.11) (*i.e.* the fluid enters the porous material through a circular entrance with finite dimension) and it is compared to the non expanding case (dashed line) and the expansion in spherical symmetry for large r_f/r_0 [or η_f—see Eq. (2.4.27)]. At short times the expansion effect is insignificant while at long times the behavior approaches that of an expanding spherical front. Similarly to the 2D case, our solution interpolates between these two
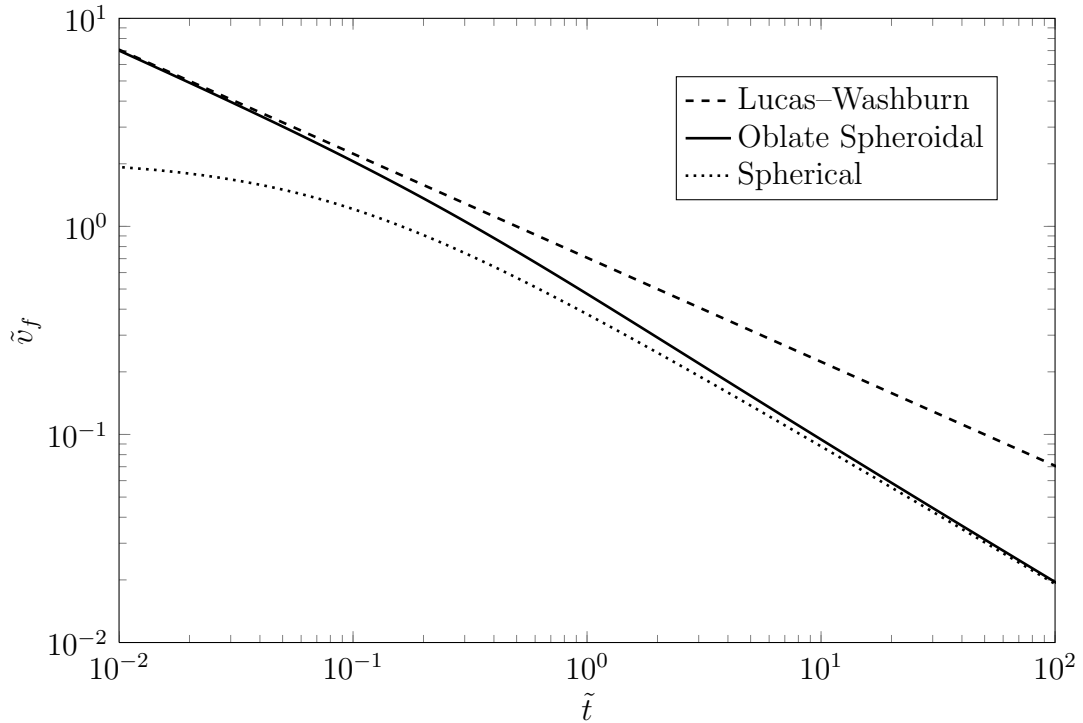
Figure 2.8. Linear velocity of the moving liquid front in 3D porous material. The solid line represents the solution for an oblate spheroid front, the dashed line is for the LW solution and the dotted line corresponds to the asymptotic case of an expanding spherical front.

limiting cases and provides a correct description for the cases where the liquid enters the 3D expanding porous material through an entrance with a finite size.

The linear velocity of the advancing liquid front is shown in Figure 2.8. The effect of the expansion on the front velocity resembles 2D (see Figure 2.5) but more pronounced because of the spreading of the liquid over larger front area. That leads to greater reduction of the velocity of the moving liquid front.

The bulk volumetric velocity is presented in Figure 2.9. It should be emphasized that the 3D expanding case allows for a solution where fluid will keep entering the porous material through the circular entrance. This is also evident from Eq. (2.4.13)
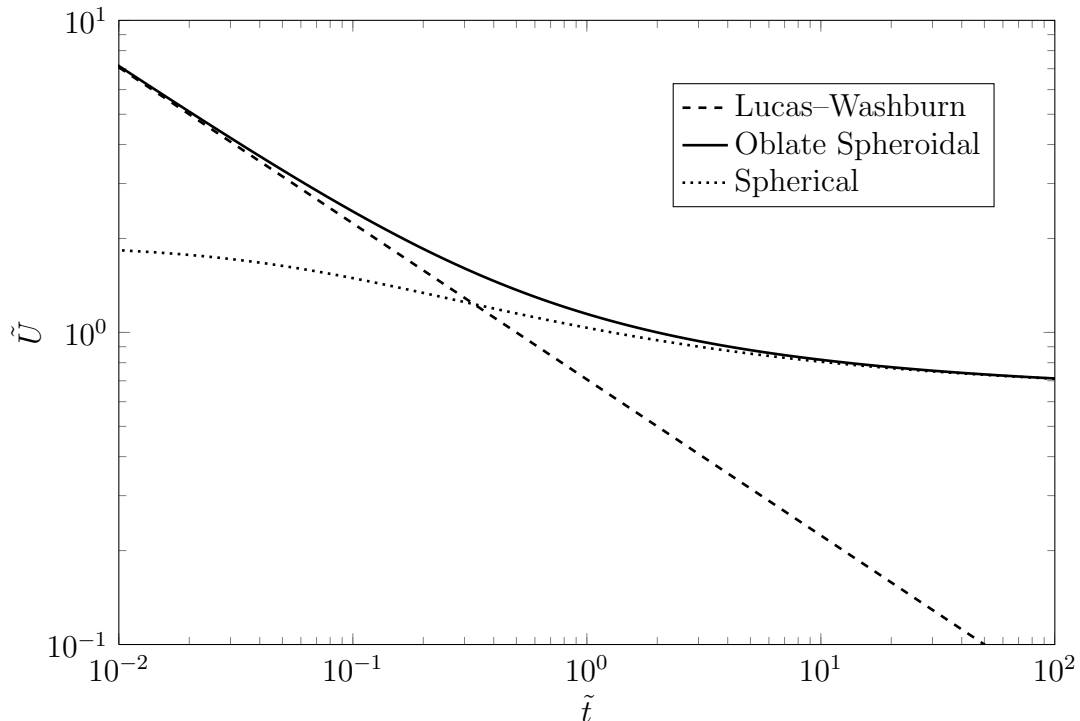
Figure 2.9. Bulk flow in 3D porous medium. The solid line the result for oblate spheroid symmetry, the dashed line corresponds to the LW case and dotted line represents the spherical case.

which for time and $\eta_f \to \infty$ becomes

$$\tilde{U}_\infty = \frac{\mu U_\infty}{2\pi a k P_\text{c}} = \frac{4}{\pi}. \tag{2.5.1}$$

This result implies that 3D porous media can be used as capillary pumps to drive fluids in devices. This cannot be accomplished if the porous material does not expand, or the expansion is two dimensional (see also the discussion below). The actual rate of drawing liquid in, however, will depend on parameters such as the average pore size, liquid viscosity, and pore wetting ability and may turn out in many cases to be too low (see experimental results in Xiao, *et al.*[60]).

Since the asymptotic result, Eq. (2.5.1), follows from the dimensionality of the system, one may expect that similar relationship to exist for the pure radial (spherical)

transport (see Figure 2.9). Indeed using equation (2.4.20) we can find the linear velocity at the entrance where $r = r_0$. To obtain the bulk flow rate one needs to multiply the result by the area of the entrance which we assume to be a hemispherical in order to better compare to the oblate spheroid case discussed above. Thus the asymptotic $(r_f \to \infty)$ expression reads

$$\tilde{U}_\infty = \frac{\mu U_\infty}{2\pi akP_{\rm c}} = 1. \tag{2.5.2}$$

Hence, if the system is 3D stationary solutions are possible, which is generally the case for Laplace equations in infinite or semi-infinite spaces and is known for similar processes like heat transfer or diffusion.[11]

2.5.3 Effect of Expansion Dimensionality

The dimensionality of the porous media is extremely important for the flow rate. There is no expansion in the case of 1D transport (which is represented by the LW case[54,55]) and the linear velocity (as well as the bulk flow rate) drop as $1/\sqrt{t}$. At the other extreme, the 3D case allows for a solution even for $\eta_f \to \infty$ [see Eq. (2.5.1) above]. Figure 2.10 shows a comparison for the time dependent position of the moving liquid front for 1D, 2D (elliptical) and 3D (oblate spheroid) cases. The 1D case exhibits the farthest liquid penetration while in 2D and 3D the distance is much shorter. The rate of liquid motion also decreases with the dimensionality of the flow (see Figure 2.11). This is due to distribution of the advancing liquid over greater space. The cross sectional area that the fluid moves through does not change in 1D, increases linearly with distance in 2D, and quadratically in 3D. Since the liquid is incompressible it can cover shorter distances per unit time for the two and particularly the three dimensional cases. It is, however, very different for the bulk flow rate (see Figure 2.12). The volume absorbed per unit time by the porous domain decreases the fastest for the 1D flow. The decrease in the bulk flow rate for the 2D expanding
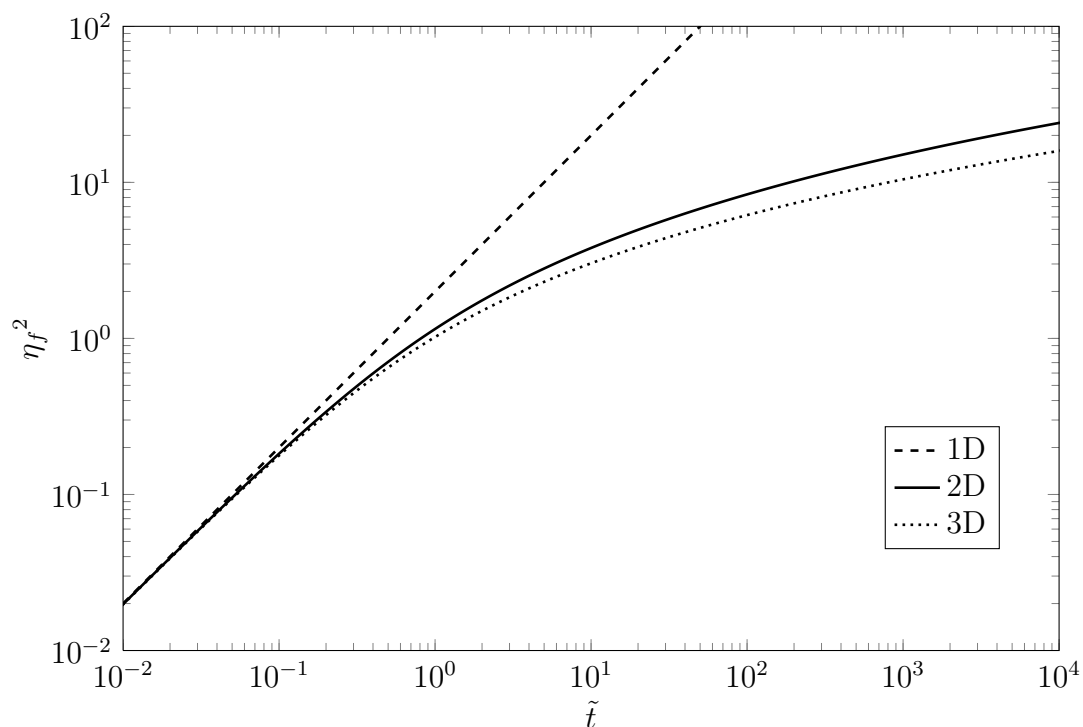
Figure 2.10. Liquid front position vs. time in 1D (dashed line), 2D (solid line), and 3D (dotted line).

case is lower and for 3D it levels off to a steady state [see Eq. (2.5.1) above]. The reason is the bulk flow rate is slowed down by the viscous resistance which increases with the length of the traveled path. The latter is greatest in 1D, shorter in 2D and shortest in 3D.*

---

* The solutions presented in Figures 2.10 and 2.12 will be revisited in Figure 3.2, were we broaden the applicability of the data from purely asymptotic comparisons into physically applicable results.
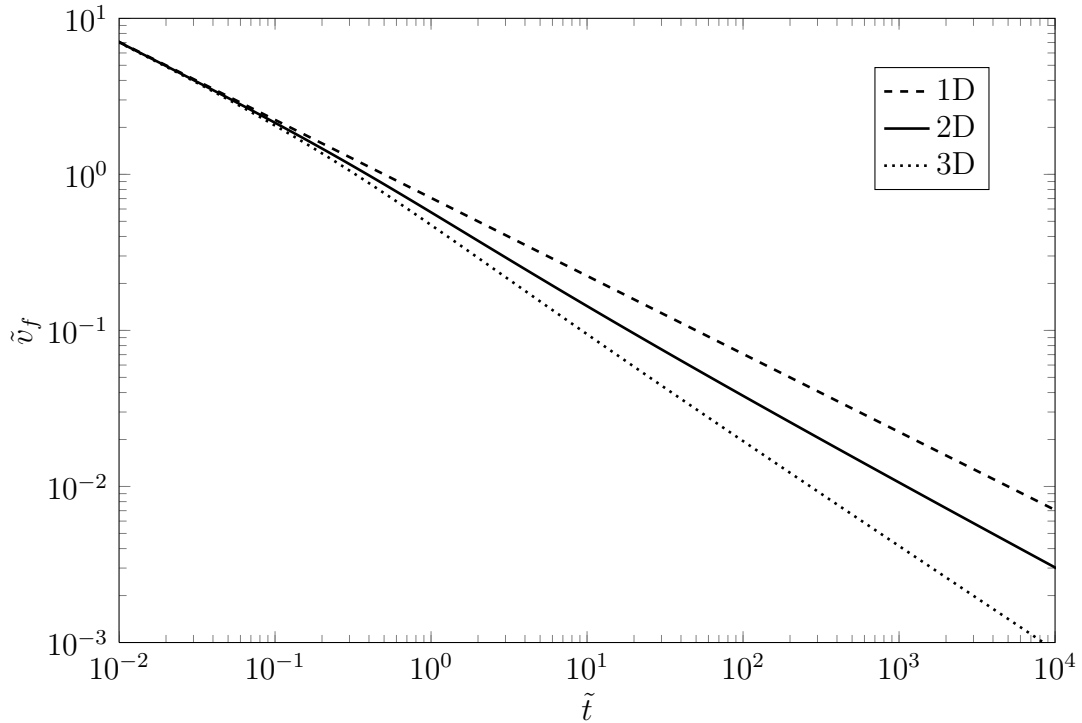
Figure 2.11. Linear velocity of the liquid front vs. time in 1D (dashed line), 2D (solid line), and 3D (dotted line).

2.6   Conclusions

We derived solutions for potential capillary driven liquid flow in 2D and 3D expanding porous media. The selection of suitable coordinate systems allows for simplification of the mass balance expressions to ordinary differential equations that can be exactly solved. The obtained solutions for expanding 2D and 3D porous materials are different from the well-known Lucas–Washburn solution describing liquid motion in non-expanding material geometries. The functional forms of the time dependence of the front position and velocity are more complicated if the porous domain is expanding. At the same time and the liquid linear velocity is lower, which is due to spreading of the incompressible liquid over an ever-increasing domain.
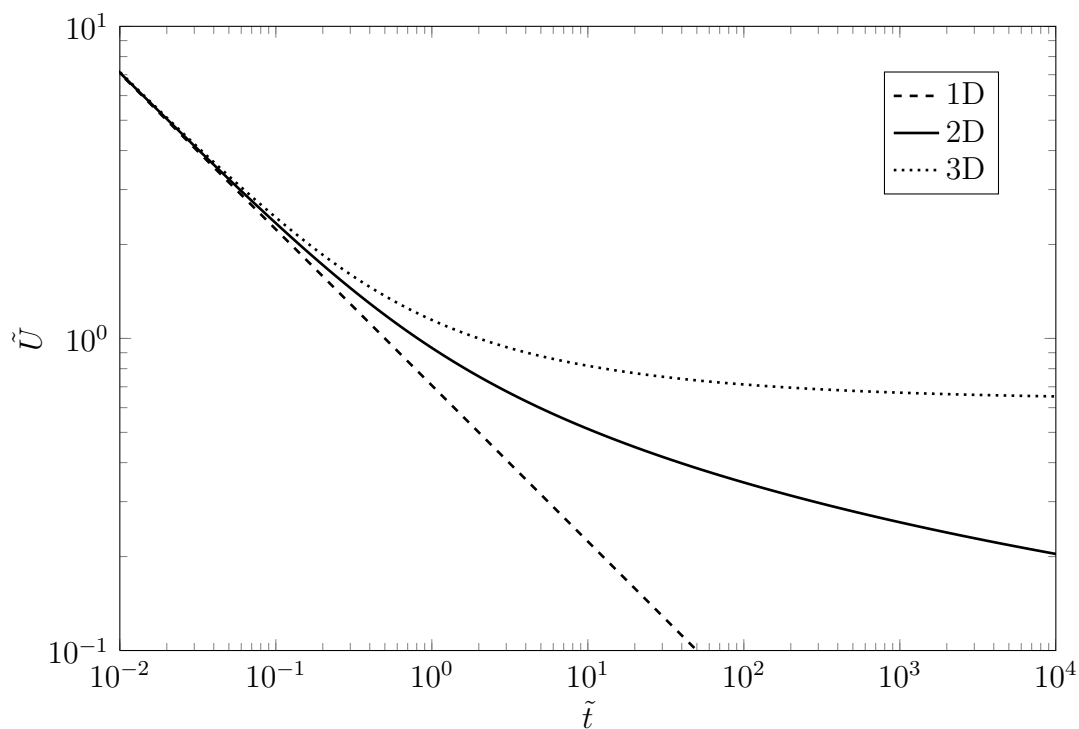
Figure 2.12. Bulk liquid flow vs. time in 1D (dashed line), 2D (solid line), and 3D (dotted line).

The bulk flows display a qualitative difference in 1D, 2D and 3D. It decreases the fastest if the porous domain does not expand, less in 2D expanding domain and least in 3D. In fact, the 3D case can reach a steady state for the bulk flow into the porous material. This makes it suitable to use in driving fluids through devices using capillary forces and without the need of an external power source.

Chapter 3

Evaporation Influences on Wicking in Thin Porous Strips

3.1 Introduction

Wicking, the capillary suction of liquids into previously dry porous media, is a complex and on-going area of study with numerous physical applications. Several examples in engineering include microfluidic devices,[17,50] medical diagnostics,[48,49] textiles,[67] and building materials.[57,58] In hydrogeology, porous media is foundational to aquifer analysis,[68] soil studies,[4] and contaminant transport.[69]

Capillary imbibition in a thin porous strip of constant cross section may be influenced by evaporation through three distinct types of surface. The largest surface of the strip, which we call the normal surface, dominates the evaporation due to total surface area. The evaporation along the thin edge, alternatively termed the side boundary, of the medium also occurs directly into the air. Thirdly, the liquid may undergo evaporation through the interface of the moving wet front. In this chapter, we show from theoretical arguments that the effects on a fully saturated capillary

flow of the normal and side evaporation modes are analogous, even though the side evaporation gives more complicated front behavior, while the front evaporation effect is both physically and dynamically different from the other two, but similar to restraint of the wicking by gravity.

In general, capillary transport in porous media occurs with unsaturated capillary flow,[63] which is modeled theoretically by the Richards equation.[70] However, the Green–Ampt[71] theory (GAT) considers fully saturated liquid imbibition where the liquid saturation is modeled with a Heaviside step function. The one-dimensional (1D) solution to this problem both in porous media and in single capillaries is known as the Lucas–Washburn Equation (LWE) and relates the wetted length to the square root of the time of imbibition.[54,55] In many instances the GAT is a sufficient approximation to Richards infiltration with only small deviations due to the diffuse interface throughout the volume in the Richards model.[72] The Green–Ampt theory may be further applied to expanding or contracting flows which give power laws other than the Lucas–Washburn relation.[23,60,61,73]

Gravity also has a significant influence on capillary motion. In a three-dimensionally (3D) expanding flow the gravity significantly deform the front shape from a sphere in the direction of the gravitational force.[59,62] The solution of 1D capillary rise against gravity may be given by the Lambert W function.[74–76] Gravitational effects may be ignored for wicking in the plane orthogonal to the gravity vector, and is often insignificant relative to evaporation.

Capillary flow with evaporation is a growing area of interest. Philip[77] discussed evaporation from a pond which is simultaneously percolating into dry soils. Hohenbichler *et al.*[78] described the steady flow into a narrow cylinder of liquid which is undergoing isothermal evaporation and shows significant front curvature in the evaporation dominated zone of the flow. Lockington *et al.*[79] developed an approximate solution to unsaturated capillary flow in a 1D medium with evaporation. Fries *et*

al.[80] gave the solution of a Green–Ampt model for capillary rise with evaporation and gravity restraint. Barry *et al.*[81] compared the Lockington and Fries solutions and suggested modifications to Fries results due to the Green–Ampt model. In recent work, we have considered normal surface evaporation from a thin medium with two-dimensional (2D) expanding capillary flow and shown a dimensionless quantity, called the evaporation capillary number (ECN), determines the time behavior of the flow.[82]* Other significant works have investigated the fluid evaporation from drying media.[83–85] In addition, evaporation has been commonly discussed coupled with heat transfer properties in the medium.[86,87]

Evaporation and its effects on capillary flow is open to further study. Evaporation is fundamentally complicated because of the coupled physical phenomena involved. Each of the three modes of evaporation are physically a result of evaporation through a capillary meniscus around the wet boundary of the entire system. This means that the contribution of pore scale processes to the bulk properties need intensive study.[84] Unsaturated flow theory provides degrees of freedom in the models which can reproduce many physical aspects of the imbibition.[79] Coupling unsaturated flow in the porous medium with computational fluid dynamics in the surrounding atmosphere would significantly resolve nonlinear behavior of the evaporation. Side and front evaporation are mostly uninvestigated and can benefit from a variety of Green–Ampt models to characterize their effects on the expanding flows in porous media.[78,85]

In this chapter, we analyze the effects of evaporation on capillary flow using the Green–Ampt theory. The analysis is conducted at time scales where the viscous friction of the liquid dominates the inertia of the liquid in the absorption rate.[88,89] This allows us to apply Darcy's law to describe the velocity by the pressure.[64] The evaporation occurs slowly and isothermally, so there is a constant rate over each of the surfaces of the medium. The liquid and gas phases are immiscible and without

---

* This is Chapter 4, which was completed and submitted for publication almost simultaneously with this chapter.

trapped gas.[83] Nonlinear behaviors such as swelling of the medium[90] and viscous fingering of the wet front are considered negligible.[91] We derive general expressions of the front position and inlet flux, or bulk velocity, for capillary flow in porous media when all three modes of evaporation and restraint by gravity are present. Each of these phenomena are discussed individually and compared to capillary flow and among each other. The developed solutions are analytical or readily calculated with common numerical integration schemes from a first order nonlinear ordinary differential or integral equation. This avoids the increased numerical difficulties involved with tracking phase interfaces in computational fluid dynamics simulations.[50]

The content of this chapter is organized as follows. The next section details the general potential flow method of Green–Ampt theory in porous media with evaporation. In Section 3.3, we derive the general solution of the velocity potential for capillary, gravity, and evaporation forces, and give specific front position solutions for each phenomenon. Section 3.4 describes the results for each of the phenomena with comparisons to other results and phenomena to show limitations and differences in the GAT approach to evaporation. We describe related open problems and summarize our findings in Section 3.5. In appendix 3.A, we compare our solutions with results from Fries *et al.*[80], show agreement between the models, and suggest an additional dimensionless quantity relevant to the analysis.*

---

* Further results and relevant information are given in the supplemental sections D.1 and D.2.

3.2 Theory

3.2.1 The Richards Equation and Green–Ampt Theory

The Richards equation for unsaturated flow in porous media with evaporation is given by

$$\frac{\partial \Theta}{\partial t} = -\boldsymbol{\nabla} \cdot \mathbf{v} - f(\Theta), \tag{3.2.1}$$

where the fluid velocity, $\mathbf{v}$, may be related to the saturation, Θ, by $\mathbf{v} = D(\Theta)\boldsymbol{\nabla}\Theta$, $D(\Theta)$ is the capillary diffusivity, and $f(\Theta)$ is the evaporation rate out of the volume of the medium as a function of the saturation.[79] Gravity will be accounted for as a hydrostatic pressure acting on a boundary, similar to capillary pressure, as we detail later. Now, in the Green–Ampt model, we have a step change in saturation at some boundary, Γ_j, going to a constant full saturation of liquid, $\Theta = 1$. Substituting,

$$0 = -\boldsymbol{\nabla} \cdot \mathbf{v} - f(1).$$

If we define a constant evaporation rate throughout the saturated domain, $Q = f(1)$, we rearrange to find[92]

$$\boldsymbol{\nabla} \cdot \mathbf{v} = -Q, \tag{3.2.2}$$

At the boundary of the liquid wetted domain we will have the balance of mass of the interface

$$\frac{\mathrm{d}\mathbf{x}_{\Gamma_j}}{\mathrm{d}t} = \mathbf{v}_{\Gamma_j} - \mathbf{q}_{\Gamma_j}, \tag{3.2.3}$$

where the left hand side describes the change of position of the boundary, $\mathbf{x}_{\Gamma_j}$, with time, t; the liquid velocity due to forces acting on the liquid, $\mathbf{v}_{\Gamma_j}$, is calculated on the boundary from the solution of Eq. (3.2.2); and mass is exchanged through the boundary by a loss flux, $\mathbf{q}_{\Gamma_j}$. This loss is of the form $\mathbf{q}_{\Gamma_j} = q_{\Gamma_j}\mathbf{n}_{\Gamma_j}$, where positive values of q_{Γ_j} represents a loss from the saturated domain and negative values are gains, such as from the liquid reservoir and $\mathbf{n}_{\Gamma_j}$ is the outward normal vector calculated by $\mathbf{n}_{\Gamma_j} = \mathbf{x}_{\Gamma_j}/|\mathbf{x}_{\Gamma_j}|$.

3.2.2 Potential Flow Theory

The macroscopic flow in porous media is irrotational,[65] so we may describe the velocity by a velocity potential, φ,

$$\mathbf{v} = \boldsymbol{\nabla}\varphi. \tag{3.2.4}$$

Substituting into Eq. (3.2.2), we have a Poisson equation inside the liquid-filled domain;

$$\nabla^2\varphi = -Q. \tag{3.2.5}$$

The internal liquid velocity contributes to the boundary by the potential, $\mathbf{v}_{\Gamma_j} = [\boldsymbol{\nabla}\varphi|_{\Gamma_j}$, and the boundary equation (3.2.3) becomes

$$\frac{\mathrm{d}\mathbf{x}_{\Gamma_j}}{\mathrm{d}t} = [\boldsymbol{\nabla}\varphi|_{\mathbf{x}_{\Gamma_j}} - q_{\Gamma_j}\mathbf{n}_{\Gamma_j}. \tag{3.2.6}$$

3.2.3 Closure of the Boundary Conditions

In the system of interest, we define three types of boundaries: inlets, fronts, and sides. The inlets allow liquid to flow into the medium but are fixed in space. The liquid front is a free moving boundary driven by the fluid potential. Finally, the side boundaries are the stationary edges of the porous medium through which liquid may be lost.

Inlet from the Liquid Reservoir

The velocity potential is closely related to the pressure in the liquid by Darcy's law[5,56,93]

$$\mathbf{v} = -\frac{k}{\mu}\boldsymbol{\nabla}P, \tag{3.2.7}$$

where k is the permeability and μ is the liquid dynamic viscosity. If k and μ are constant, then

$$\varphi = -\frac{k}{\mu}P. \tag{3.2.8}$$

In porous media, the principal driving pressure is from the capillary force which, in the micro-scale, is given by the Young–Laplace equation,

$$P_c = \gamma \cos(\alpha) \left(\frac{1}{R_1} + \frac{1}{R_2} \right), \tag{3.2.9}$$

where γ is the surface tension at the gas-liquid interface, α is the contact angle of solid wetting, and R_1 and R_2 are the principal radii of curvature of the pore cross-section.[66] We designate a portion of the boundary as the inlet, where liquid enters the domain from a reservoir. The pressure at the inlet may be set to a combination of the capillary, P_c, and restraining hydrostatic pressure of magnitude, $\rho g h_f$;

$$P_i = P_c - \rho g h_f,$$

where P_i is the inlet pressure, ρ is the density of the liquid (the gas contribution is assumed negligible), g is the magnitude of the local gravitational acceleration, and h_f is the height of liquid from the inlet to the front. Thus, the velocity potential at the inlet, φ_i, is prescribed by

$$\varphi_i = -\frac{k P_c}{\mu} + \frac{k \rho g h_f}{\mu}. \tag{3.2.10}$$

The inlet itself does not move, so the boundary equation, Eq. (3.2.6), is reduced to $[\boldsymbol{\nabla}\varphi|_{\mathbf{x}_i} = q_i \mathbf{n}_{\mathbf{x}_i}$. The gradient of the potential and the normal vector are known, so q_i is the remaining variable. Defining the total volumetric flux of liquid into the domain or the bulk velocity—textbf,

$$U = - \iint_{\mathbf{x}_i} q_i \, \mathrm{d}\mathbf{x}_i,$$

where the negative sign gives a positive value of U for inward flow. The bulk velocity is calculated from the potential,

$$U = - \iint_{\mathbf{x}_i} [\boldsymbol{\nabla}\varphi|_{\mathbf{x}_i} \cdot \mathbf{n}_{\mathbf{x}_i} \, \mathrm{d}\mathbf{x}_i. \tag{3.2.11}$$

The Moving Wet Front

At the front of the liquid, there is no significant gravitational force and the difference in the capillary pressure from our definition at the inlet is such that the capillary pressure does not contribute. This means that the the front pressure, $P_f = 0$, and correspondingly, we have as a boundary condition for the front potential,

$$\varphi_f = 0. \tag{3.2.12}$$

When frontal evaporation is included, we must use the full form of Eq. (3.2.6) to determine the front position,

$$\frac{\mathrm{d}\mathbf{x}_f}{\mathrm{d}t} = [\boldsymbol{\nabla}\varphi|_{\mathbf{x}_f} - q_f \mathbf{n}_{\mathbf{x}_f}. \tag{3.2.13}$$

If there is no evaporation loss the motion of the front is simply calculated from $\mathrm{d}\mathbf{x}_f/\mathrm{d}t = [\boldsymbol{\nabla}\varphi|_{\mathbf{x}_f}$. This differential equation must be integrated over time to determine the position of the wet front and thereby the solution of all other variables.

Side Boundaries of the Medium

The porous medium also has boundaries which do not contact the reservoir and are thus either insulated, so there is no mass transport through the boundary, or open to the atmosphere, and thereby losing mass by a side evaporation flux, q_s. These side boundaries at positions $\mathbf{x}_s$ are fixed such that Eq. (3.2.6) reduces to a boundary condition for the potential;

$$[\boldsymbol{\nabla}\varphi|_{\mathbf{x}_s} = q_s \mathbf{n}_{\mathbf{x}_s}. \tag{3.2.14}$$

An insulated side wall gives a no-flux boundary condition, $[\boldsymbol{\nabla}\varphi|_{\mathbf{x}_s} = \mathbf{0}$.

Thus, potential flow models of Green–Ampt theory which incorporate gravity and evaporation require first the analytical or computational solution of the velocity potential, Eq. (3.2.5), from the boundary conditions, Eq. (5.2.3), (3.2.12), and (3.2.14),
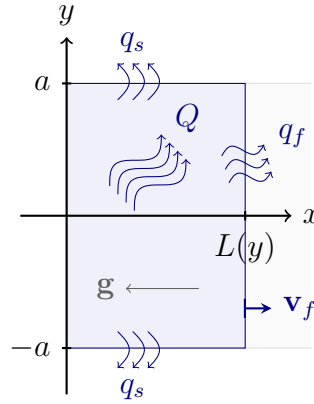
Figure 3.1. Wicking in a porous medium of constant cross section restrained by gravity and influenced by evaporation from the surface, sides, and front. The medium is $2a$ width and saturated to length L. Gravity restrains the flow with magnitude g in the negative x-direction. Evaporation flux through the sides occur with magnitude q_s.

where all parameters in these equations are known. Then, the front position as a free boundary is determined as a function of time by Eq. (3.2.13), and the bulk velocity may be solved from Eq. (3.2.11).

3.3   Derivation of Analytical Model

In this section, we detail the application of the potential flow method in a medium with constant cross-section with combined capillary, gravity, and evaporation effects. The total velocity potential is solved in the Cartesian coordinate system from which we produce the general front position and bulk velocity equations. Several reduced solutions of the equation of the front are given which illustrate analytical similarities between normal and side evaporation as well as between front evaporation and gravity.

3.3.1 The Velocity Potential

The velocity potential equation, Eq. (3.2.5), is expressed in Cartesian coordinates

$$\frac{\partial^2 \varphi}{\partial x^2} + \frac{\partial^2 \varphi}{\partial y^2} = -Q. \tag{3.3.1}$$

Here we assume that the thickness in the z-direction, denoted δ, is very thin relative to the x- and y-directions and plays no direct role in the flow. For the total velocity potential, the boundary conditions (BC) apply each of the individual physical boundary phenomena,

$$[\varphi]_{x=0} = -\frac{kP_{\rm c}}{\mu} + \frac{k\rho g}{\mu}L, \tag{3.3.2a}$$

$$[\varphi]_{x=L} = 0, \tag{3.3.2b}$$

$$\left[\frac{\partial \varphi}{\partial y}\right]_{y=0} = 0, \tag{3.3.2c}$$

$$\left[\frac{\partial \varphi}{\partial y}\right]_{y=a} = q_s. \tag{3.3.2d}$$

where L is the position of the front along the x-direction and a is half the inlet width. Each of these boundary conditions are the simplified Cartesian forms of the inlet BC, Eq. (5.2.3); the front pressure BC, Eq. (3.2.12); the assumed symmetry along the center of flow; and the side evaporation BC, Eq. (3.2.14), respectively. These effects on the medium are illustrated in Figure 3.1. The centerline of the flow is along $y = 0$ and $y = \pm a$ are the boundaries of the domain. Note that the capillary force expression is negative in magnitude to indicate that it is a driving force, while the gravity and side evaporation terms resist the flow and hence are positive.

The total velocity potential, φ, may be split into sub-potentials for each of the physical phenomena, so we apply linear superposition because Eq. (3.3.1) is a linear differential equation with linear boundary conditions, Eq. (3.3.2).[28] The sub-potential for each phenomenon is solved for individually and combined to determine the total

potential. Thus, we define the total potential,

$$\varphi = \xi + \gamma + \zeta + \omega, \tag{3.3.3}$$

where we denote the capillary, gravity, normal surface, and side boundary potentials by ξ, γ, ζ, and ω, respectively. The capillary potential, ξ, is determined by retaining $-kP_{\mathrm{c}}/\mu$ as the only non-homogeneous term in Eqs. (3.3.1) and (3.3.2). Similarly, the gravity potential, γ, is the solution with only $k\rho gL/\mu$ as a boundary condition. The normal surface evaporation potential, ζ, solves Eq. (3.3.1) when Q is finite for homogeneous boundary conditions. Finally, the side boundary evaporation potential, ω, solves the system when q_s is the non-homogeneous term. The boundary conditions of the system, Eq. (3.3.2), indicate the side evaporation sub-potential is dependent on both the x- and y-direction, while all others are dependent only on x. All the velocity potentials are made dimensionless by the magnitude of the capillary potential at the inlet kP_{c}/μ; for example, $\tilde{\varphi} = (\mu/kP_{\mathrm{c}})\varphi$, $\tilde{\xi} = (\mu/kP_{\mathrm{c}})\xi$, *etc.* We use the capillary force because the magnitude depends only on the porous medium and is naturally present throughout all of our subsystems of interest. As shown in Eq. (3.2.13), the evaporation from the front interface is only incorporated when the actual motion of the front itself is considered, so we do not need an expression of a front evaporation potential.

Capillary Potential

Purely capillary-driven flow is described by the system,

$$\frac{\mathrm{d}^2\xi}{\mathrm{d}x^2} = 0, \tag{3.3.4}$$

with the boundary conditions,

$$[\xi]_{x=0} = -\frac{kP_{\mathrm{c}}}{\mu}, \tag{3.3.5a}$$

$$[\xi]_{x=L} = 0. \tag{3.3.5b}$$

The ordinary differential equation integrates to a linear expression, $\xi = c_{\xi,1}x + c_{\xi,0}$, where we consider $c_{\alpha,i}$ an arbitrary constant in all derivations. Substituting the boundary conditions we obtain the solution,

$$\tilde{\xi} = -\left(\frac{\tilde{L} - \tilde{x}}{\tilde{L}}\right), \tag{3.3.6}$$

where dimensionless lengths are defined, $\tilde{L} = L/a$, $\tilde{x} = x/a$, and $\tilde{y} = y/a$. In the literature, the pressure head is represented by L and is often used as the characteristic length scale because $L_{ss} = P_c/\rho g$ is the maximum height of wicking.[80] We choose a instead because it enables analysis in a wider variety of geometries and is constant over the time of the wicking.[23]

Gravity Potential

We solve for the gravity potential, γ, with the differential equation,

$$\frac{d^2\gamma}{dx^2} = 0, \tag{3.3.7}$$

and the boundary conditions,

$$[\gamma|_{x=0} = \frac{k\rho g}{\mu}L, \tag{3.3.8a}$$

$$[\gamma|_{x=L} = 0. \tag{3.3.8b}$$

The linear expression, $\gamma = c_{\gamma,1}x + c_{\gamma,0}$ is again the form of the solution, and the boundary conditions supply the result;

$$\tilde{\gamma} = \text{Bo}_a\left(\tilde{L} - \tilde{x}\right), \tag{3.3.9}$$

where we have defined a time invariant Bond number,

$$\text{Bo}_a = \frac{\rho g a}{P_c}. \tag{3.3.10}$$

The Bond number is the ratio of the gravitational to capillary forces and is usually defined by the hydraulic head $\text{Bo} = \rho g L / P_\text{c} = \text{Bo}_a \tilde{L}$, however a is constant, and therefore Bo_a is a constant with time. Also, we will find Bo_a is a more natural quantity for comparison with evaporation. Observe that the right hand side of Eq. (3.3.9) increases in magnitude with increasing front length, $\tilde{L}$, while the capillary potential in Eq. (3.3.6) contains $\tilde{L}$ in the denominator and does not increase. For this reason the capillary potential is easily limited by the contribution to the total potential of the other phenomena as the length of wicking is increased.

Normal Surface Evaporation Potential

The normal surface evaporation potential, ζ, is determined by the non-homogeneous linear differential equation,

$$\frac{\partial^2 \zeta}{\partial x^2} = Q, \tag{3.3.11}$$

with the homogeneous boundary conditions,

$$[\zeta|_{x=0} = 0, \tag{3.3.12a}$$

$$[\zeta|_{x=L} = 0. \tag{3.3.12b}$$

We integrate the differential equation to find the solution form, $\zeta = -Q(\frac{1}{2}x^2 + c_{\zeta,1}x + c_{\zeta,0})$. The boundary constraints at the inlet and the front give the result,

$$\tilde{\zeta} = \frac{1}{2}\mathfrak{N}_\text{n}\left(\tilde{L}\tilde{x} - \tilde{x}^2\right), \tag{3.3.13}$$

where we define the normal surface evaporation-capillary number (ECN)

$$\mathfrak{N}_\text{n} = \frac{\mu a^2 Q}{k P_\text{c}}. \tag{3.3.14}$$

We will detail this and other forms of the ECN shortly.*

---

* The potential given in Eq. (3.3.13) is discussed in §4.3.3 with further details.

Side Boundary Evaporation Potential

The potential for the side boundary evaporation, ω, is described by the 2D Laplace equation

$$\frac{\partial^2 \omega}{\partial x^2} + \frac{\partial^2 \omega}{\partial y^2} = 0, \tag{3.3.15}$$

with boundary conditions,

$$[\omega]_{x=0} = 0, \tag{3.3.16a}$$

$$[\omega]_{x=L} = 0, \tag{3.3.16b}$$

$$\left[\frac{\partial \omega}{\partial y}\right]_{y=0} = 0, \tag{3.3.16c}$$

$$\left[\frac{\partial \omega}{\partial y}\right]_{y=a} = q_s. \tag{3.3.16d}$$

The potential, ω, may be split into the product of functions, $\omega(x, y) = X(x)Y(y)$, by separation of variables. In the x-direction the solution is necessarily of the form, $X = c_{x,1} \cos(\sqrt{\lambda}x) + c_{x,2}\sin(\sqrt{\lambda}x)$, where λ is the eigenvalue of the differential equation $\mathrm{d}^2 X/\mathrm{d}x^2 + \lambda X = 0$. When the homogeneous Dirichlet boundary conditions of the x-direction are applied the cosine term is dropped and the eigenvalues are determined, $\sqrt{\lambda_n} = n\pi/L$, where n is a positive integer. This indicates the solution is the infinite series

$$X(x) = \sum_{n=1}^{\infty} c_{x,n} \sin\left(n\pi\frac{x}{L}\right). \tag{3.3.17}$$

The solution in the y-direction is determined by the differential equation $\mathrm{d}^2 Y_n/\mathrm{d}y^2 - \lambda_n Y_n = 0$. The form of the solution is given by $Y_n = c_{y,1n}\cosh(n\pi y/L) + c_{y,2n}\sinh(n\pi y/L)$; applying the third boundary condition indicates that the sinh term must be dropped. Recombining X and Y, we have a form of solution for the side evaporation potential,

$$\omega = \sum_{n=1}^{\infty} c_{\omega,n} \cosh\left(n\pi\frac{y}{L}\right) \sin\left(n\pi\frac{x}{L}\right). \tag{3.3.18}$$

Finally, the fourth boundary condition is applied to determine the coefficients, $c_{\omega,n}$. By orthogonality of the sine term, the system is invertible, and we find that the coefficient, $c_{\omega,k} = \{4/[(2k-1)^2\pi^2]\}\{Lq_s/\sinh[(2k-1)\pi a/L]\}$, where $n = 2k-1$ indicates that only odd integers give non-zero values in the solution terms. Thus, the solution of the potential for the side boundary evaporation may be arranged in the form

$$\tilde{\omega} = \mathfrak{N}_{\mathrm{s}}\tilde{L}\sum_{k=1}^{\infty}\left(\frac{4}{(2k-1)^2\pi^2}\right)\frac{\cosh\left((2k-1)\pi\frac{\tilde{y}}{\tilde{L}}\right)}{\sinh\left((2k-1)\pi\frac{1}{\tilde{L}}\right)}\sin\left((2k-1)\pi\frac{\tilde{x}}{\tilde{L}}\right). \qquad (3.3.19)$$

where we have non-dimensionalized q_s to give the side boundary ECN,

$$\mathfrak{N}_{\mathrm{s}} = \frac{\mu a q_s}{kP_{\mathrm{c}}}. \qquad (3.3.20)$$

Note that $\mathfrak{N}_{\mathrm{s}}$ depends on the diffusive contribution of the evaporation in the form of aq_s as apposed to a^2Q in $\mathfrak{N}_{\mathrm{n}}$. Eq. (3.3.19) shows that side evaporation effects the potential in both the x- and y-directions.

The Total Velocity Potential

We arrive at the total velocity potential of the system by substituting the solutions given in Eqs. (3.3.6), (3.3.9), (3.3.13), and (3.3.19) into Eq. (3.3.3);

$$\tilde{\varphi} = -\left(\frac{\tilde{L}-\tilde{x}}{\tilde{L}}\right) + \mathrm{Bo}_a\left(\tilde{L}-\tilde{x}\right) + \frac{1}{2}\mathfrak{N}_{\mathrm{n}}\left(\tilde{L}\tilde{x}-\tilde{x}^2\right)$$

$$+ \mathfrak{N}_{\mathrm{s}}\tilde{L}\sum_{k=1}^{\infty}\left(\frac{4}{(2k-1)^2\pi^2}\right)\frac{\cosh\left((2k-1)\pi\frac{\tilde{y}}{\tilde{L}}\right)}{\sinh\left((2k-1)\pi\frac{1}{\tilde{L}}\right)}\sin\left((2k-1)\pi\frac{\tilde{x}}{\tilde{L}}\right). \qquad (3.3.21)$$

3.3.2 The Front Velocity Equation

The velocity in the x-direction will determine how the system behaves over time. From Eq. (3.2.4), the velocity is the gradient of the potential. Thus,

$$\tilde{v}_x = \frac{\mathrm{d}\tilde{\varphi}}{\mathrm{d}\tilde{x}}, \tag{3.3.22a}$$

$$= \frac{1}{\tilde{L}} - \mathrm{Bo}_a + \frac{1}{2}\mathfrak{N}_\mathrm{n}\left(\tilde{L} - 2\tilde{x}\right)$$

$$+ 4\mathfrak{N}_\mathrm{s}\sum_{k=1}^{\infty}\left[\frac{1}{(2k-1)\pi}\right]\frac{\cosh\left[(2k-1)\pi\frac{\tilde{y}}{\tilde{L}}\right]}{\sinh\left[(2k-1)\pi\frac{1}{\tilde{L}}\right]}\cos\left[(2k-1)\pi\frac{\tilde{x}}{\tilde{L}}\right], \tag{3.3.22b}$$

where dimensionless velocity is defined $\tilde{v} = (\mu a/kP_\mathrm{c})v$.

From Eq. (3.2.13), the position of the front is the time derivative of the velocity at the front, $x = L$, given by Eq. (3.3.22b) minus any evaporation loss through the front interface. For simplicity, we realize that, with exception of contributions of the side evaporation, the normal vector at the front, $\mathbf{x}_f$, lies along x itself, so the flow is principally in x and we reduce Eq. (3.2.13) to a scalar differential equation. Thus, the front position as a function of time is given by the solution of a nonlinear ordinary differential equation;

$$\frac{\mathrm{d}\tilde{L}}{\mathrm{d}\tilde{t}} = \frac{1}{\tilde{L}} - \mathrm{Bo}_a - \mathfrak{N}_\mathrm{f}\left(\mathbf{n}_{\tilde{L}} \cdot \hat{\mathbf{i}}\right) - \frac{1}{2}\mathfrak{N}_\mathrm{n}\tilde{L}$$

$$- 4\mathfrak{N}_\mathrm{s}\sum_{k=1}^{\infty}\left[\frac{1}{(2k-1)\pi}\right]\frac{\cosh\left[(2k-1)\pi\frac{\tilde{y}}{\tilde{L}}\right]}{\sinh\left[(2k-1)\pi\frac{1}{\tilde{L}}\right]}. \tag{3.3.23}$$

where $\tilde{t} = (kP_\mathrm{c}/\mu a^2)t$ is the dimensionless time and $\mathbf{n}_{\tilde{L}} \cdot \hat{\mathbf{i}}$ is the projection of the vector normal to the front interface in the x-direction. Additionally, the front interface ECN is

$$\mathfrak{N}_\mathrm{f} = \frac{\mu a q_f}{kP_\mathrm{c}}. \tag{3.3.24}$$

This equation cannot be solved directly for all five physical phenomena combined because the term for the side boundary evaporation is not analytically invertible.

Below, we detail the solution of the equation for capillary force together with each of the other phenomena individually.

3.3.3   Special Solutions of the Front Velocity Equation

Capillary Flow or the Lucas–Washburn Equation

The solution of Eq. (3.3.23) for only capillary flow is the central result with which all the following will be compared. Dropping all other terms, we have the relation, $\mathrm{d}\tilde{L}/\mathrm{d}\tilde{t} = 1/\tilde{L}$. The equation may be rearranged and integrated to give the solution for capillary flow under the Green–Ampt assumption;

$$\tilde{L} = \sqrt{2\tilde{t}}. \tag{3.3.25}$$

This solution is referred to as the Lucas–Washburn equation (LWE).[23] In some instances, it is easier to compare the LWE to other solutions when it is in the form, $\tilde{L}^2 = 2\tilde{t}$; we consider both as equivalent forms and reference them identically.

Capillary Flow Restrained by Gravity

The first two terms of the right hand side of Eq. (3.3.23) give capillary flow with the gravitational contribution;

$$\frac{\mathrm{d}\tilde{L}}{\mathrm{d}\tilde{t}} = \frac{1}{\tilde{L}} - \mathrm{Bo}_a. \tag{3.3.26}$$

Rearranged into the form, $\int_0^{\tilde{L}} \tilde{L}/(1 - \mathrm{Bo}_a\tilde{L})\,\mathrm{d}\tilde{L} = \int_0^{\tilde{t}} \mathrm{d}\tilde{t}$, we may integrate the system to obtain the solution,

$$\mathrm{Bo}_a\tilde{L} + \ln\left|1 - \mathrm{Bo}_a\tilde{L}\right| = -\mathrm{Bo}_a^2\tilde{t}. \tag{3.3.27}$$

This solution agrees with the result by Fries *et al.*[80], which can also be expressed by the Lambert W function.[74,75]

Capillary Flow with Normal Surface Evaporation

The solution for the case of capillary wicking with gravity and normal surface evaporation is given by Fries *et al.*[80] In our recent work,[82] this case was fully derived in the appendix under the potential flow model. Simplifying Eq. (3.3.23) to only the capillary and normal surface evaporation terms, we have the reduced front position equation,

$$\frac{\mathrm{d}\tilde{L}}{\mathrm{d}\tilde{t}} = \frac{1}{\tilde{L}} - \frac{1}{2}\mathfrak{N}_{\mathrm{n}}\tilde{L}. \tag{3.3.28}$$

Integrating from times 0 to $\tilde{t}$ and positions 0 to $\tilde{L}$, we find the solution

$$\frac{1}{2}\mathfrak{N}_{\mathrm{n}}\tilde{L}^2 = 1 - \exp\left(-\mathfrak{N}_{\mathrm{n}}\tilde{t}\right). \tag{3.3.29}$$

We show in the appendix that this is equivalent to Fries' solution when gravity is neglected.*

Capillary Flow with Side Boundary Evaporation at Asymptotically Large Times

The total front position equation, Eq. (3.3.23), may also be reduced to account for capillary flow with only evaporation from the side boundaries of the medium;

$$\frac{\mathrm{d}\tilde{L}}{\mathrm{d}\tilde{t}} = \frac{1}{\tilde{L}} - 4\mathfrak{N}_{\mathrm{s}}\sum_{k=1}^{\infty}\left[\frac{1}{(2k-1)\pi}\right]\frac{\cosh\left[(2k-1)\pi\frac{\tilde{y}}{L}\right]}{\sinh\left[(2k-1)\pi\frac{1}{L}\right]}. \tag{3.3.30}$$

This nonlinear ordinary differential equation, like Eq. (3.3.23), is not known to have an analytical solution. Nevertheless, we may consider simplifying the effects of the side evaporation for asymptotic analysis. From physical intuition we expect the side evaporation should be phenomenologically the same as normal surface evaporation. These are both approximations of empirical media where all vapors pass through the side, but often the evaporating capillary interface is at some depth from the surface.

---

* See Eq. (3.A.5).

However, the normal surface evaporation model assumes a loss of liquid through the volume of the porous medium, while side evaporation explicitly considers the loss at the boundary only. In any case, it seems reasonable that normal and side evaporation should be asymptotically analogous. If we consider the limit as $a \to \delta$, we expect that the form of the two solutions should become the same; this is equivalent to $L \gg a$. In the limit of large L, curvature of the front interface will become negligible relative to the wicking distance, L, and so there is no longer any significant variation in y and the system reduces significantly.

We return to Eq. (3.3.30) and set $\tilde{y} = 1$;

$$\frac{d\tilde{L}}{d\tilde{t}} = \frac{1}{\tilde{L}} - 4\mathfrak{N}_s \sum_{k=1}^{\infty} \left[\frac{1}{(2k-1)\pi}\right] \coth\left[(2k-1)\pi\frac{1}{\tilde{L}}\right]. \qquad (3.3.31a)$$

If we define $z = \tilde{L}/[(2k-1)\pi]$, then in the limit of $z \to \infty$, $\coth(1/z) \approx z + 1/(3z) + \cdots$. Substituting for only the highest order term of the approximation and simplifying,

$$\frac{d\tilde{L}}{d\tilde{t}} = \frac{1}{\tilde{L}} - \mathfrak{N}_s \tilde{L} \sum_{k=1}^{\infty} \frac{4}{(2k-1)^2\pi^2}.$$

Finally, the summation reduces by the relation $\sum_{k=1}^{\infty} 4/[(2k-1)^2\pi^2] = 1/2$,

$$\frac{d\tilde{L}}{d\tilde{t}} = \frac{1}{\tilde{L}} - \frac{1}{2}\mathfrak{N}_s \tilde{L}. \qquad (3.3.31b)$$

This is precisely the form of the differential equation for the normal surface evaporation as given in Eq. (3.3.28), with only the change in the dimensionless quantity representing the evaporation effect from normal surface evaporation to side evaporation. This result gives validity to the assumption that the normal surface evaporation is a simplified approach to the more physically motivated phenomenon of side boundary evaporation. Naturally, the equivalence of Eqs. (3.3.28) and (3.3.31b) indicates the solution for side evaporation will approximate Eq. (3.3.29) when curvature of the front interface is suppressed.

Capillary Flow with Front Interface Evaporation

Eq. (3.3.23) shows that the frontal evaporation affects the motion of the front identically to the gravitational force in the Green–Ampt approximation of wicking. The reduced equation is $d\tilde{L}/d\tilde{t} = 1/\tilde{L} - \mathfrak{N}_f$, which is directly analogous to Eq. (3.3.26). Here the normal vector projected on the x-direction unit vector is unity, or $\mathbf{n}_{\tilde{L}} \cdot \hat{\mathbf{i}} = 1$. The solution of capillary flow with evaporation through the front interface is,

$$\mathfrak{N}_f \tilde{L} + \ln\left|1 - \mathfrak{N}_f \tilde{L}\right| = -\mathfrak{N}_f^2 \tilde{t}. \tag{3.3.32}$$

Thus, the time dependent contribution of front evaporation is similar to gravity and varies with $\mathfrak{N}_f^2 \tilde{t}$.

3.3.4 The Bulk Velocity

In Eq. (3.2.11), the bulk velocity is defined as the volumetric flux through the inlet of the medium, or expressed in Cartesian coordinates,

$$U = \left[\int_{-a}^{a} \int_{0}^{\delta} v_x \, dz \, dy\right]\bigg|_{x=0}. \tag{3.3.33}$$

Substituting the velocity given in Eq. (3.3.22b) into Eq. (3.3.33) we reach the expression,

$$\tilde{U} = \int_{-1}^{1} \left\{ \frac{1}{\tilde{L}} - \text{Bo}_a + \frac{1}{2}\mathfrak{N}_n \tilde{L} + \mathfrak{N}_s \sum_{k=1}^{\infty} \left[\frac{4}{(2k-1)\pi}\right] \frac{\cosh\left[(2k-1)\pi\frac{\tilde{y}}{\tilde{L}}\right]}{\sinh\left[(2k-1)\pi\frac{1}{\tilde{L}}\right]} \right\} d\tilde{y}, \tag{3.3.34}$$

where $\tilde{U} = (\mu/kP_c\delta)U$. This is the bulk velocity for the general case of $\tilde{L} = \tilde{L}(\tilde{y})$. For sufficiently far front advancement and small $\mathfrak{N}_s$, we may assume $\tilde{L}$ is a constant in the y-direction. Then we find the explicit form of the bulk velocity;

$$\tilde{U} = \frac{2}{\tilde{L}} - 2\text{Bo}_a + \mathfrak{N}_n \tilde{L} + \mathfrak{N}_s \tilde{L}. \tag{3.3.35}$$

The summation in the side boundary evaporation term reduces by a mathematical relation in the manner similar to Eq. (3.3.31b). We observe that the magnitude of the normal surface evaporation and the side boundary evaporation are identical, which also suggests that these mechanisms are essentially the same in the limit of large front advancement. The frontal evaporation is not calculated in $\tilde{v}_x$, Eq. (3.3.22b), because the phenomenon is introduced in the front interface material balance, so evaporation through the front interface influences the bulk velocity only indirectly by slowing the movement of the front in time.

3.3.5   Numerical Computation of Solutions

The data produced in the results is primarily computed by numerical integration of the nonlinear differential equations. The front position and bulk velocity equations in the general case with all physical phenomena are given in Eqs. (3.3.23) and (3.3.34), respectively. In several simplified cases, the solution is easier to compute; the Lucas–Washburn equation (3.3.25) and the solution for normal evaporation, Eq. (3.3.29), are both explicit functions of the time, while the gravity and front evaporation solutions, Eqs. (3.3.27) and (3.3.32), respectively, are implicit. For each of these individual solutions, the analytical bulk velocity given in Eq. (3.3.35) is accurate. The front position for capillary flow with side evaporation, Eq. (3.3.30), and the corresponding bulk velocity from Eq. (3.3.34) can only be solved by numerical integration. A fourth order Runge–Kutta method[32] is applied to the nonlinear differential equation of the front with an initial condition, $\tilde{L} = 0.04$ at time $\tilde{t} = 10^{-3}$ because the hyperbolic function terms are numerically unstable for smaller $\tilde{L}$ which therefore restricts the side evaporation results to small ECN, $\mathfrak{N}_{\mathrm{s}} < 1$. This is not a real problem because higher evaporation rates may be unphysical for the side evaporation model. The equation is then integrated along constant values of $\tilde{y}$ out to large times, *e.g.* $\tilde{t} = 10^5$. The bulk velocity in Eq. (3.3.34) is integrated over the y-direction with cubic splines

at each time step.

3.4 Results

3.4.1 The Evaporation–Capillary Number and Physical Significance

In the derivations above, we found three forms of the ECN as defined in Eqs. (3.3.14), (3.3.20), and (3.3.24);

$$\mathfrak{N}_{\mathrm{n}} = \frac{\mu a^2 Q}{k P_{\mathrm{c}}}, \qquad \mathfrak{N}_{\mathrm{s}} = \frac{\mu a q_s}{k P_{\mathrm{c}}}, \qquad \mathfrak{N}_{\mathrm{f}} = \frac{\mu a q_f}{k P_{\mathrm{c}}}.$$

In a physical system the evaporation rates—and by extension the evaporation numbers—are all related. The side and front evaporation rates, q_s and q_f, are in units of length per time, while the normal surface evaporation rate, Q, is in units of inverse time, so the units of the evaporation rates are equivalent for $aQ[=]q_s[=]q_f$. Given the wetted porous domain of dimensions $L \times 2a \times \delta$, we may relate the magnitudes of each ECN by the surfaces through which they occur. The normal surface evaporation and the side evaporation occur on boundaries exposed to the open air, and as such the mass flux by evaporation is assumed to be similar from the two different sides. The normal evaporation will occur through a surface of dimension $L \times 2a$ and the side evaporation will occur through two surfaces of $L \times \delta$. Setting the mass loss rates through respective surfaces of evaporation equal, we find $\delta Q = q_s$. For small inlet hight, $\delta/a \ll 1$, the evaporation rate $aQ \gg q_s$, and by extension

$$\mathfrak{N}_{\mathrm{n}} \gg \mathfrak{N}_{\mathrm{s}}.$$

This qualitatively supports the fact that in a thin, 2D-like porous medium the normal surface evaporation is the dominant mode of mass loss.

When we compare the side evaporation versus the frontal evaporation, we must consider that the frontal evaporation is diffusing into the porous medium while the side evaporation is going out to exterior air. This leads to the reasonable observation that $q_f < q_s$ because the frontal evaporation will be slowed by vapor transport in the medium, and consequently,

$$\mathfrak{N}_f < \mathfrak{N}_s.$$

However, consider that the front evaporation will have much greater surface area initially, but have a relatively decreasing ratio to the side evaporation as the imbibition progresses. In expanding flows, the surface areas of both will grow, but in narrowing flows the front surface area will decrease while the side increases. Thus, the geometry of the flow and the porous medium will contribute along with the evaporation numbers in determining which of the two phenomena is more influential to the flow behavior. In summary, for a given physical system of 2D-like nature the evaporation numbers will generally follow an order of relative strength such that,

$$\mathfrak{N}_n \gg \mathfrak{N}_s > \mathfrak{N}_f. \tag{3.4.1}$$

Formally, we define the general evaporation-capillary number as,

$$\mathfrak{N} = \frac{\text{characteristic mass flux of evaporation}}{\text{characteristic mass flux of wicking}}. \tag{3.4.2a}$$

A clear example of this definition is the side boundary ECN, $\mathfrak{N}_s = (\rho q_s)/(\rho k P_c/\mu a)$, which is rearranged from Eq. (3.3.20); the numerator of the side boundary ECN shows the mass flux loss due to phase change, ρq_s, while the denominator is the characteristic mass flux of the capillary flow in the porous medium, $\rho k P_c/\mu a$. Similarly, the ECN is the rate of diffusive transport through evaporation over diffusive transport though wicking; for example, the front interface ECN, Eq. (3.3.24), can be arranged in the form $\mathfrak{N}_f = (a q_f)/(k P_c/\mu)$. Alternatively, we may define the ECN as a ratio of time scales;

$$\mathfrak{N} = \frac{\text{time-scale of wicking}}{\text{time-scale of evaporation}}. \tag{3.4.2b}$$

The normal surface ECN, Eq. (3.3.14), may be equivalently defined $\mathfrak{N}_n = (\mu a^2/kP_c)/(1/Q)$, which is the time scale of the fluid propagation in the porous medium, $\mu a^2/kP_c$, divided by the timescale of the normal evaporation, $1/Q$. In the following results, the time-scale relation, Eq. (3.4.2b), will often be more useful for analysis of the systems, even though we consider the mass flux, Eq. (3.4.2a), to be the natural definition of the quantity. In any case these definitions are equivalent.

The authors have found no dimensionless quantities or trivial combination of other numbers in the literature which are equivalent to the ECN.*Philip[77] observed the ratio of the evaporation rate from a pond to the permeability of a soil principally effects the time to loss of surface water. This was not a dimensionless quantity, though similar to the ECN, it does effectively consider mass transport due to evaporation versus the porous medium. Lockington *et al.*[79] used the evaporation rate directly to make the time dimensionless, and the influx is normalized by the square root of the capillary diffusivity and the evaporation rate. In both papers, the independent parameter of the evaporation number was not exploited because of the assumed 1D geometry. The capillary force in the denominator of the ECN suggests alternative relations to the Bond number, Eq. (3.3.10), or the Capillary number, $Ca = \mu v/\sigma$, where σ is the surface tension. For analyzing vertical wicking with evaporation, Fries *et al.*[80] utilized both Bond and Capillary numbers to non-dimensionalize the height and the time. They defined a dimensionless quantity, Φ, called the "related maximum height," as the ratio of the maximum height of capillary flows under the influence of gravity with evaporation versus without, so the quantity determines the deviation in the flow from the ideal case of wicking against gravity. It may be shown (see the chapter Appendix 3.A.3) that Φ is purely a function of the ratio, $Bo_a^2/\mathfrak{N}_n$. Other dimensionless numbers in mass transfer such as the Schmidt and Sherwood numbers cannot be directly used with Ca to give the ECN because they are defined for single

---

* This chapter is the first published result with the ECN[24], however Chapter 4 was the first place we wrote about the ECN.

(a) Liquid front position
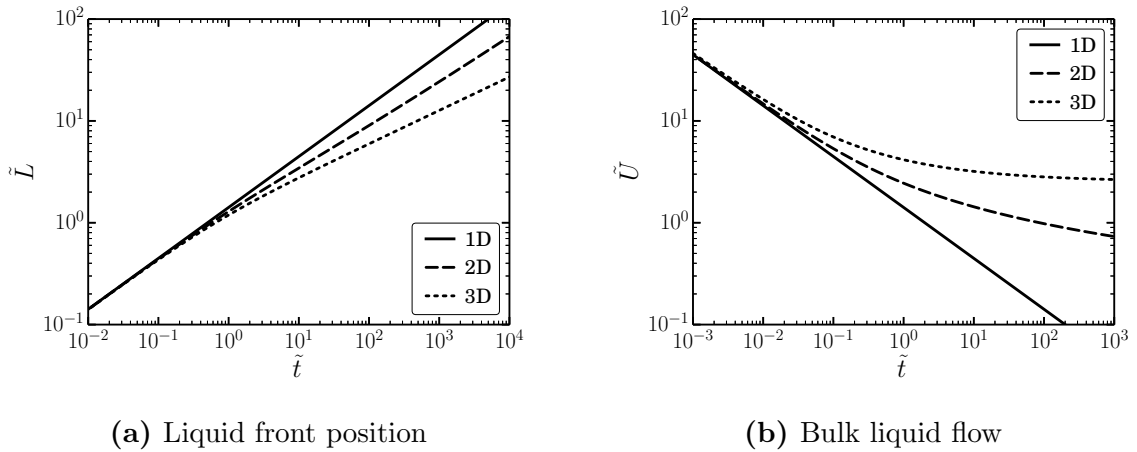
(b) Bulk liquid flow

Figure 3.2. Liquid wicking in porous media for 1D (solid line), 2D (dashed line), and 3D (dotted line) flows. (a) Liquid front position, $\tilde{L}$, versus time, $\tilde{t}$. (b) Bulk liquid flow, $\tilde{U}$, versus time; the bulk flow has been normalized to the same inlet cross-sectional area for all three cases.

phase diffusion.[30] In total, these examples support the need for a quantity such as the ECN in analysis of flows in porous media. Thus, we suggest that the evaporation-capillary number is a beneficial, new dimensionless number in fluid mechanics and porous media.

3.4.2 Capillary Flow

The capillary flow behavior predicted by the Lucas–Washburn law, Eq. (3.3.25), is the solution which we compare all other phenomena in wicking in porous media. The first phenomenon of interest is the geometry, where we observe how flow into fully 2D or 3D expanding domains effects the propagation of the front length and the bulk velocity.* Figure 3.2 shows the front positions and bulk velocities for the LW (1D), 2D, and 3D flows. We observe in Figure 3.2a, the front position for the LWE, $\tilde{L}^2 = \tilde{t}/2$,

---

* The results summarized here are from Chapter 2, in particular we are modifying Figures 2.10 and 2.12. This is published in the literature as Ref.[23].

advances more rapidly than the others, where in the limit of large advancement, the 2D case propagates as $\tilde{L}^2 \ln\left(\tilde{L}\right) \sim \tilde{t}$ and 3D as $\tilde{L}^3 \sim \tilde{t}$.* In Figure 3.2b, we observe that the volumetric flow of the fluid into the medium for the LW case decreases as $\tilde{U} = 1/\sqrt{2\tilde{t}}$, which is much more rapid than 2D and 3D. In fact, the bulk velocity for the 3D flow approaches a finite steady state. Hall[57] demonstrated both by the theory of conformal mappings and by experiment that the inflow deviates from the Lucas–Washburn prediction for 2D and 3D flows. This geometric steady state is a useful result wherein the parameters of the medium may be tuned such that a sufficient amount of fluid can be driven into it indefinitely for application in passive fluid-driven technologies. In other words, fluid may be drawn indefinitely by the capillary force alone into a 3D porous medium with a small inlet. Philip[59] also showed this finite steady-state in 3D by an assumed moisture profile solution of the Richards equation. However, this property is desirable in engineering porous media is even better enhanced by evaporation, as we now detail.

3.4.3 Capillary Flow with Normal Surface Evaporation

The normal surface evaporation is the predominant form of evaporation in a thin porous strip as we observed in the discussion of Eq. (3.4.1). As such we will use it as our starting point to compare with the other physical phenomena of evaporation and gravity. We may assess the validity of our Green–Ampt model of capillary flow influenced by evaporation with the work by Lockington *et al.*[79] They developed an approximate analytical solution of the unsaturated flow equation, Eq. (3.2.1), for a 1D medium with power law saturation, Θ^n, where n is the power law index. Making their solutions for the front position and inlet velocity nondimensional [Lockington equations (29) and (31)], we see in Figure 3.3 the comparison between the saturated

---

* These relationships may be observed in Eqs. (2.3.13), (2.3.15), and (2.4.25), but we give the full details of this power law analysis in §4.4.4, which is published in Ref.[82].

(a) Front position

(b) Bulk flow
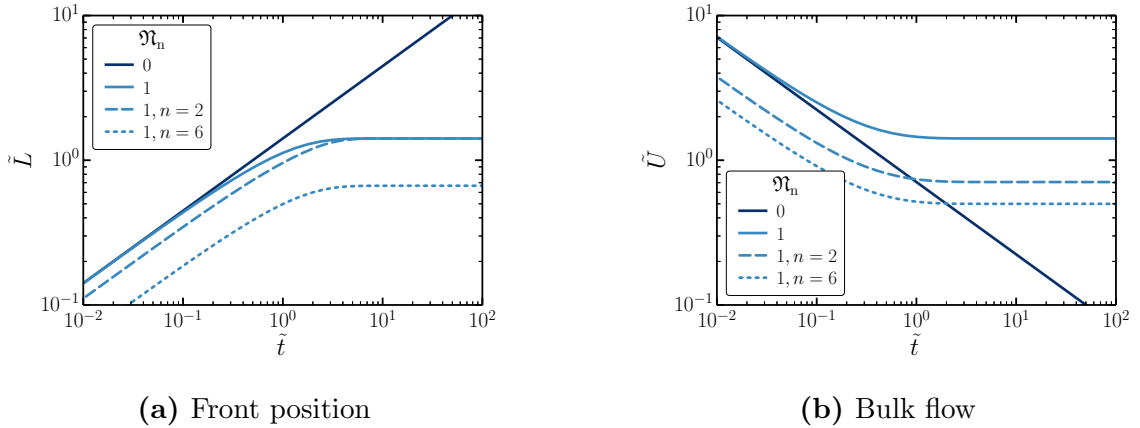
Figure 3.3. Wicking behavior of liquid with normal surface evaporation in a thin porous strip for fully and partially saturated flows. The Lucas–Washburn solution is the dark solid line, the fully saturated solution at $\mathfrak{N}_n = 1$ is given by the light solid line, and the partially saturated solutions at $\mathfrak{N}_n = 1$ for diffusivity exponents $n = 2$ and $n = 6$ are given with the light dashed and dotted lines, respectively. (a) Liquid front position, $\tilde{L}$, versus time, $\tilde{t}$. (b) Bulk liquid flow, $\tilde{U}$, versus time.

and unsaturated flow models. We consider $n = 2$ and $n = 6$ because Lockington suggests these are the lower and upper bounds of n in common porous media.*

Figure 3.3a gives the front positions for the LWE as well as the saturated and unsaturated models at $\mathfrak{N}_n = 1$. The shape of the front behavior and bulk velocity curves are the same for all ECN just transposed in space and time—so the choice of $\mathfrak{N}_n = 1$ is arbitrary—and the discussion is equally applicable to any $\mathfrak{N}_n$. The front positions for both of the unsaturated flow solutions are noticeably shorter than the LWE prior to evaporation taking effect. This indicates that the Green–Ampt (GA) model over-predicts the front position. However, as evaporation occurs, the $n = 2$ case merges with the saturated flow steady state. The $n = 6$ case has a much lower steady state from the other two. Figure 3.3b shows the bulk velocity for these four cases. The bulk flow for the two unsaturated cases, $n = 2$ and 6 are near to each

---

* The mathematical details relating our solution to Lockington's is given in the supplementary material §D.2.

other, but are substantially lower than the GA model.[*]

The differences between the steady state behavior of the GAT and unsaturated models may be shown quantitatively. We set the velocity in Eq. (3.3.28) equal to zero and rearrange to get the steady state front position as a function of the ECN,

$$\tilde{L}_{\text{ss, norm}} = \sqrt{\frac{2}{\mathfrak{N}_{\text{n}}}}. \tag{3.4.3}$$

Lockington gives [equation (32)] an expression for the front position, which in our notation is

$$\tilde{L}_{\text{ss, unsat}} = \frac{\sqrt{n+2}}{n}\sqrt{\frac{2}{\mathfrak{N}_{\text{n}}}}. \tag{3.4.4}$$

When $n = 2$ the two steady state front positions are the same, and for $n = 6$ the unsaturated case is smaller by $1/\sqrt{2}$. Similarly, the bulk velocities are related $\tilde{U}_{\text{ss, unsat}} = 1/\sqrt{n+2}\,\tilde{U}_{\text{ss, norm}}$ [see Eq. (3.3.35) and Lockington equation (13)]. This shows that for all positive values of n the steady state bulk velocity in the unsaturated case is less than the saturated case. For $n = 2$, half as much liquid is flowing into the medium as predicted by GAT, while for $n = 6$ it is only a factor of $1/2\sqrt{2} \approx 0.35$. Thus, the GAT over-predicts both the wet front position and the bulk flow rate into the medium by potentially significant proportions. This is in keeping with the discussion in Barry *et al.*[81]. Nevertheless, the essential power-law behavior of the Green–Ampt model agrees with the unsaturated flow results as given by Lockington *et al.*

3.4.4 Capillary Flow with Side Boundary Evaporation

The evaporation from the side boundaries of a porous strip resembles the normal surface evaporation. Figure 3.4a shows the front position for intermediate to small ECN in both cases. We observe the flows follow the LWE and branch away due to

---

[*] For more details, see supplemental Figure D.1 which plots the steady state front positions and bulk velocities versus ECN.

(a) Front position

(b) Front shape
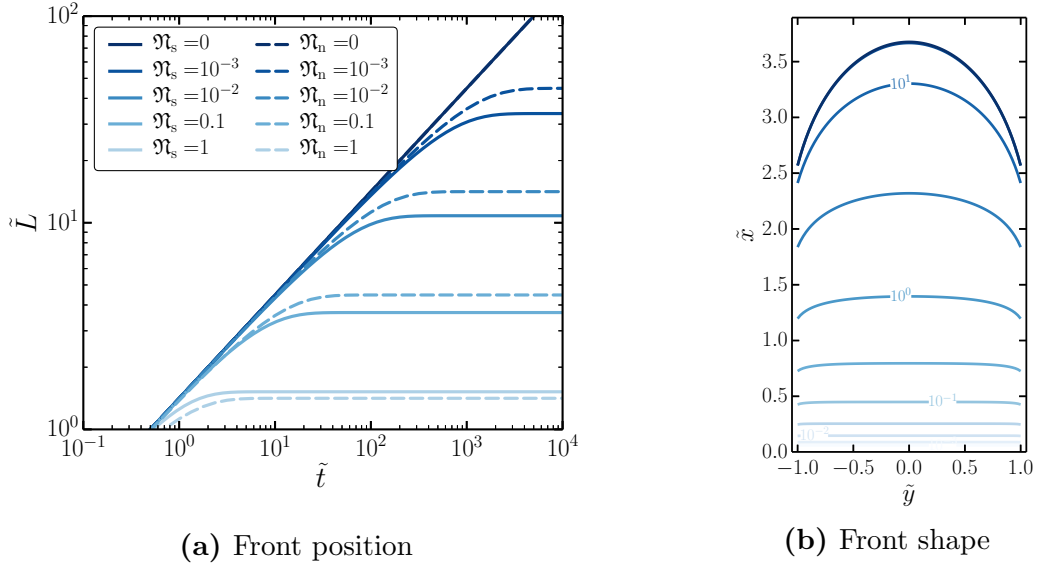
Figure 3.4. Behavior of the liquid front position for side boundary evaporation from a thin porous strip. (a) Front position, $\tilde{L}$, versus time, $\tilde{t}$, for side (solid lines) and normal surface (dashed lines) evaporation. Side evaporation data is calculated along the centerline, $\tilde{y} = 0$. The solutions with evaporation are shown for evaporation numbers, $\mathfrak{N}_s$ and $\mathfrak{N}_n$, equal to $0, 10^{-3}, 10^{-2}, 0.1$, and 1, from darkest to lightest. (b) Development of the liquid front shape, $\tilde{L}(\tilde{y}, \tilde{t})$, over time of an imbibing liquid with evaporation, $\mathfrak{N}_s = 0.1$. Contour lines correspond to front position at dimensionless times, $\tilde{t} = 10^{-3}, 10^{-2.5}, \ldots, 10^2$, from lightest lines to darkest.

evaporation in a similar way around $\mathfrak{N}_n \tilde{t} = 0.3$. However, the side evaporation comes to steady state somewhat more rapidly than the normal surface evaporation. This is consistent for $\mathfrak{N}_s < 0.1$, but is not accurate for $\mathfrak{N}_s \sim 1$. We will discuss these features of side evaporation more in the next paragraph. In Figure 3.4b, the wet front shape is illustrated at dimensionless times up to 100 for a system where $\mathfrak{N}_s = 0.1$. The computed front interface progressively curves over time from a straight flow into an approximately parabolic shape at steady state. This is the natural evolution of the front shape given by the differential equation, Eq. (3.3.30); no perturbation methods need to be applied to deform the front. The curvature occurs because the evaporation through the sides causes liquid loss near the edges, but allows fluid near the center to penetrate deeper into the medium. All steady states of the side evaporation model

(a) Front position

(b) Bulk flow
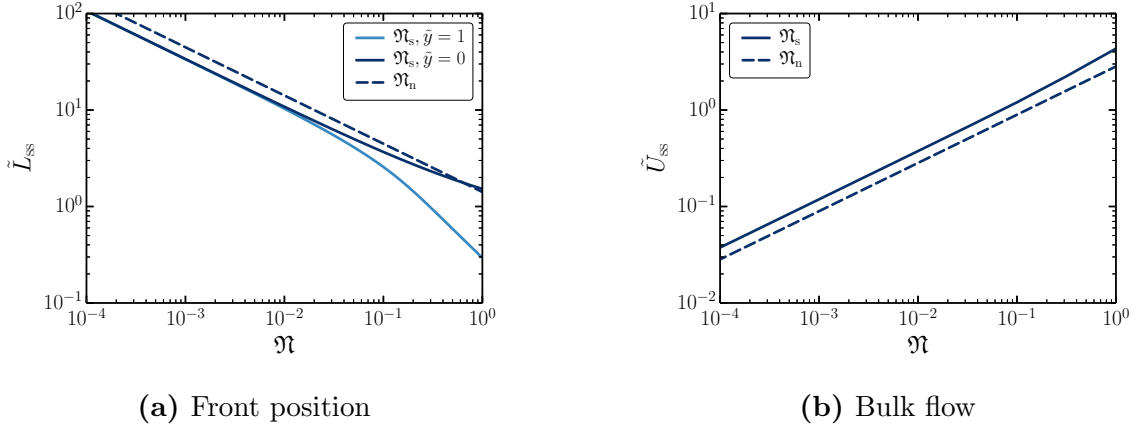
Figure 3.5. Steady state behavior versus ECN for side and normal evaporation in a thin porous strip. Side boundary evaporation is plotted with the solid line and normal surface evaporation with the dashed line. (a) Plot of steady state front position, $\tilde{L}_{ss}$, versus ECN, $\mathfrak{N}$. The dark solid line is calculated along the center-line, $\tilde{y} = 0$, and the light solid line is along the boundary, $\tilde{y} = 1$. (b) Plot of steady state bulk velocity, $\tilde{U}_{ss}$, versus ECN, $\mathfrak{N}$.

have a curved front shape.*

The steady state behavior of the side evaporation is compared with the normal surface evaporation in Figure 3.5. The plot of front position steady state, Figure 3.5a, shows the power law behavior of the normal and side evaporation modes are the same in the limit of small ECN. These power laws differ proportionally by a constant of approximately 1.4 for $\mathfrak{N} < 10^{-2}$, with the side evaporation smaller than the surface evaporation. The front position at the side and the center line of the flow converge asymptotically in the same limit; however, they are still sufficiently different to exhibit a curved front shape. In deriving Eq. (3.3.31b), we assumed that the front curvature was negligible. As we see in Figure 3.4b, this is a reasonable assumption for $\mathfrak{N}_s \tilde{t} < 0.1$, but for later times the curvature is important. This means that Eq. (3.3.31b) explains how the side and normal evaporations match as the evaporation is just beginning to effect the flow, as is observed in Figure 3.4a, but does not give precise steady-

---

* See Figure D.2b for another example, in addition to the bulk velocity plot in Figure D.2a.

state values of the side boundary front position. Thus, the proportional difference between the side and normal evaporation modes is because of the curvature of the side evaporation front, and we may still consider the normal evaporation a practical approximation of the side evaporation. The steady bulk velocity, Figure 3.5b, is greater for the side evaporation. This is due to the front position being less than the normal evaporation case, so the fluid pressure gradient is stronger.

To our knowledge, an equivalent to the side evaporation model has not been utilized in the literature. Hohenbichler *et al.*[78] considered a thermodynamic model of evaporation in a cylindrical porous medium with evaporation. They found curved steady state front shapes of the liquid by using the Antoine equation and coupling with the heat input into the system. Their work indicates that in a physical system where side evaporation is relevant, it cannot be completely decoupled from front evaporation. Hohenbichler computes a front shape with considerable curvature, but the shape is significantly different from the one shown in Figure 3.4b. This is because of their assumed non-constant properties at the boundary of the porous medium, and the different implementation of the evaporation phenomenon.

3.4.5 Capillary Flow with Front Interface Evaporation

Figure 3.6 compares the flow behavior for front interface evaporation to normal surface evaporation. The front position is plotted in Figure 3.6a, where we see the front evaporation separates earlier from the Lucas–Washburn flow than the surface evaporation. This causes the steady state front position of the front evaporation to be smaller than similar flows in normal evaporation. From Eq. (3.3.23) we may show the steady state front position is inversely proportional to the front ECN;

$$\tilde{L}_{\text{ss, front}} = 1/\mathfrak{N}_{\text{f}}. \tag{3.4.5}$$

(a) Front position

(b) Bulk flow
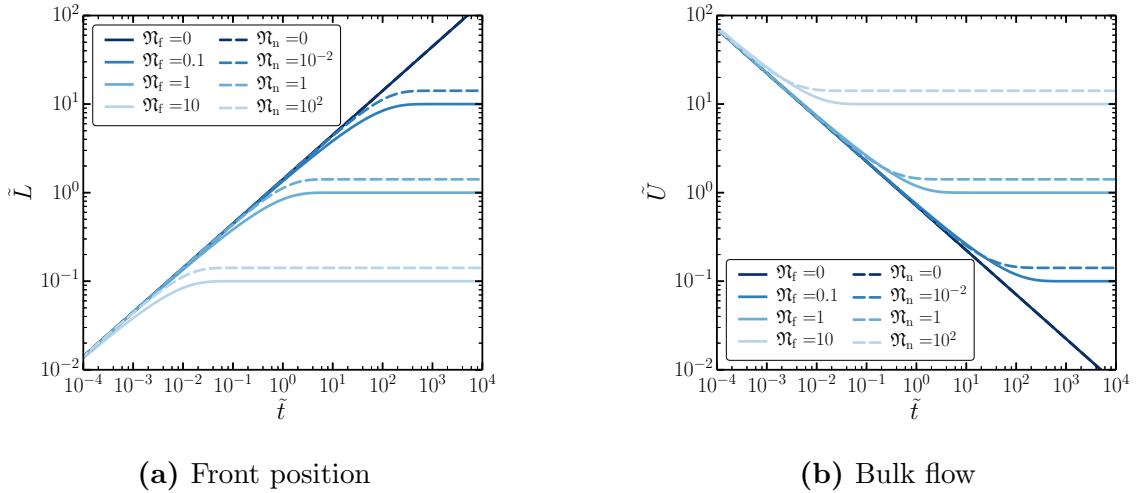
Figure 3.6. The time dependent behavior of front interface evaporation and normal surface evaporation in a thin porous strip. Front evaporation data is shown by solid lines and normal evaporation by dashed lines. Data is computed for both ECN: $\mathfrak{N}_{\mathrm{f}}$ at values of 10, 1, 0.1, and 0, and $\mathfrak{N}_{\mathrm{n}}$, at values of 10^2, 1, 10^{-2}, and 0 from shades of lightest to darkest. (a) Plot of front position, $\tilde{L}$, versus time, $\tilde{t}$. (b) Plot of bulk velocity, $\tilde{U}$, versus time, $\tilde{t}$.

In Figure 3.6b, we see the front evaporation does produce a steady state bulk velocity even though it was not explicitly included in the calculation of the bulk velocity directly in Eq. (3.3.34). In both figures the normal ECN varied more widely than the front ECN to give a similar effect on the steady state. We will discuss this in more detail later.

Philip[77] discussed evaporation from a freshly filled, dry lakebed and found solutions of similar shape to the data shown in Figure 3.6a when plotted on a non-logarithmic scale. His model is of evaporation taking place from the back of the medium in the fluid reservoir, while simultaneously affecting the flow potential of the front. However, Philip only considers the solution out to the point in time where the reservoir is empty because the physical system fundamentally changes beyond that time. Sadeghi *et al.*[85] detail steady state shapes of the saturation profile in a porous medium with front evaporation. They find the saturation function varies significantly
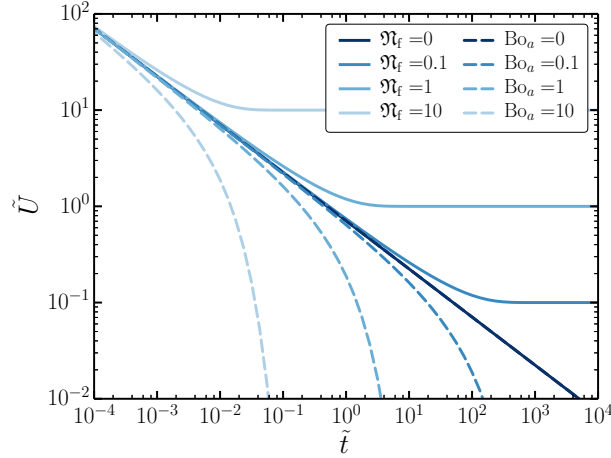
Figure 3.7. Comparison of bulk velocity, $\tilde{U}$, versus time, $\tilde{t}$, for front interface evaporation and gravity in a thin porous strip. The time dependent bulk velocity is given for front evaporation by solid lines and for gravity by dashed lines. Data is computed for both the ECN, $\mathfrak{N}_f$, and modified Bond number, Bo_a, at values of 10, 1, 0.1, and 0 from shades of lightest to darkest.

over the soil by considering a Brooks and Corey[94] power law model. This indicates that the saturated flow front evaporation model is based on an approximation which does not hold completely to steady state.

3.4.6 Capillary Flow Restrained by Gravity

As noted with Eq. (3.3.32) above, the solutions of front position for front evaporation and gravity restraint are identical for fully saturated liquid wetting. When plotted the effect of gravity on the front position is the same as the data of the front evaporation shown in Figure 3.6a except for equivalent values of Bo_a instead of $\mathfrak{N}_f$.* The steady state value of the liquid front with gravity restraint is given by $\text{Bo} = 1$, or equivalently,

$$\tilde{L}_{\text{ss, grav}} = 1/\text{Bo}_a. \tag{3.4.6}$$

---

* See Figure D.3 in the supplemental results given in Appendix D.

(a) Normal surface evaporation　　　**(b)** Side boundary evaporation
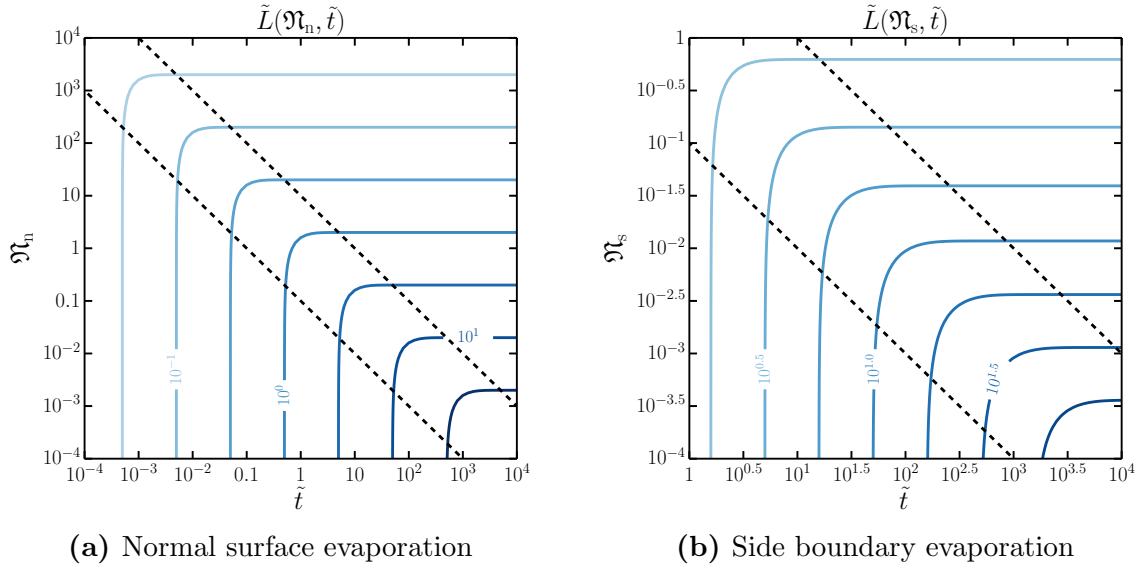
Figure 3.8. Contour plot of front position, $\tilde{L}$, over ECN and time, $\tilde{t}$, for a thin porous strip. Dotted black lines distinguish regimes of flow behavior; the lower left section is dominated by capillary flow and upper right is at steady state. (a) Dotted lines in the lower left and upper right correspond to $\mathfrak{N}_n\tilde{t} = 0.1$ and $\mathfrak{N}_n\tilde{t} = 10$, respectively. (b) Dotted lines in the lower left and upper right correspond to $\mathfrak{N}_s\tilde{t} = 0.1$ and $\mathfrak{N}_s\tilde{t} = 10$, respectively. This figure is similar to the lower right quadrant of (a).

The effects of gravity on the steady state behavior of the bulk velocity are completely different from the front evaporation, as we observe in Figure 3.7. The lines of bulk velocity go to a finite steady state for the front evaporation, but gravity resistance causes a sharp drop in the bulk flow rate around $\mathrm{Bo}_a\tilde{t} = 0.1$. By $\mathrm{Bo}_a\tilde{t} = 10$, the bulk flow rate has been reduced to about 0.1% of the Lucas–Washburn value. Thus, the front evaporation gives a finite steady influx at large times, while the gravity reduces the incoming flow to zero.

3.4.7　Comparison of All Phenomena

We observed in Figure 3.4a that the normal surface evaporation and the side boundary evaporation have similar behaviors. In Figure 3.8 we show the front position for both

(a) Front interface evaporation   **(b)** Gravity
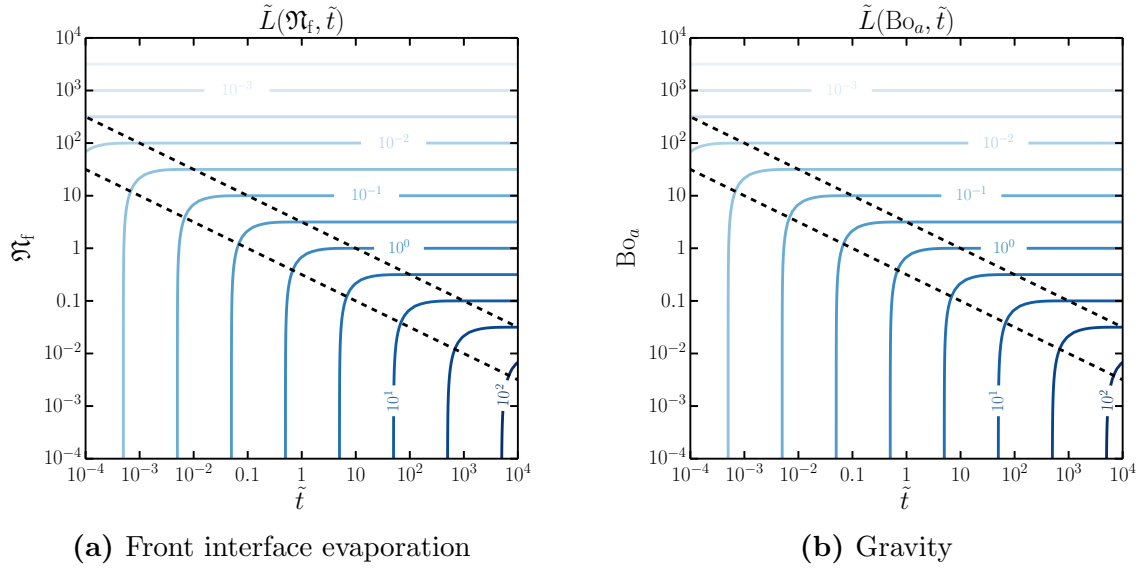
Figure 3.9. Contour plot of front position, $\tilde{L}$, over dimensionless control quantity and time, $\tilde{t}$, for a thin porous strip. Dotted black lines distinguish regimes of flow behavior; the lower left section is dominated by capillary flow and upper right is at steady state. (a) Dotted lines in the lower left and upper right correspond to $\mathfrak{N}_f^2\tilde{t} = 0.1$ and $\mathfrak{N}_f^2\tilde{t} = 10$, respectively. (b) Dotted lines in the lower left and upper right correspond to $\mathrm{Bo}_a^2\tilde{t} = 0.1$ and $\mathrm{Bo}_a^2\tilde{t} = 10$, respectively. The figures, (a) and (b), are essentially identical.

these phenomena as a contour plot over ECN and time.* In the bottom left corner of Figures 3.8a and 3.8b the flow is driven entirely by capillary pressure and the evaporation number has no effect on the front position. In the upper right corner of the two figures the flow has reached steady state wherein the front position only varies with ECN, but not in time. The diagonal band between the upper left and bottom right constitutes the regime in which both evaporation and capillary force are effecting the flow. This regime lies approximately in the similar ranges of $0.1 < \mathfrak{N}_n\tilde{t} < 10$ for surface evaporation and $0.1 < \mathfrak{N}_s\tilde{t} < 10$ for side evaporation. Thus, we see a power-law relation where the time to steady state will be related to inverse ECN for both normal and side evaporations, or $\tilde{t}_{ss} \sim 1/\mathfrak{N}_{n,ss}$.

---

* The equivalent contour plots for the front velocity and bulk velocity are given in Figures D.4 and D.5.

The front evaporation shows a significant difference from the other two evaporation modes. In Figure 3.9a the transition region between capillary dominance and evaporative steady state is in the power behavior $0.1 < \mathfrak{N}_\mathrm{f}^2 \tilde{t} < 10$. This means that the time to steady state is now related to the inverse *square* ECN. From Figure 3.9b, we similarly observe the transition region from capillary flow to hydrostatic front position is $0.1 < \mathrm{Bo}_a^2 \tilde{t} < 10$. In the analytical solution of the frontal position with frontal evaporation, Eq. (3.3.32), we find that the evaporation number squared times time is the natural expression to equate with the frontal motion. This is in contrast with Eq. (3.3.29) for normal evaporation, where the right hand side is only to the first power. Therefore, the effect on capillary flow behavior by the front evaporation is fundamentally different from normal evaporation, but similar to restraint by gravity.

3.5 Conclusion

A physical study of the effects of the modes of evaporation on capillary flow in porous media may be further extended to more complex geometries and flows. The normal surface evaporation in a 2D medium may be contrasted to 1D flow.*The front interface evaporation model may be readily extended into 2D and 3D flows by use of the capillary potentials.† However, capillary flows with side boundary evaporation become very challenging in 2D and 3D expanding flows because solving the two-dimensional potential equation becomes non-trivial, so a semi-analytical method may not be practical, particularly for the 3D case. The model of unsaturated flow with evaporation given by Lockington *et al.*[79] should also be applied computationally to 2D and 3D flows to show more accurate physical behaviors of wicking with evaporation. Nevertheless, the semi-analytical models of fully saturated flow are useful in constraining how the wicking is affected by changes in geometry and additional physical phenomena such as evaporation.

---

* See chapter 4   † See chapter 2 or Ref.[23].

We have shown variations in flow behavior due to evaporative effects on fluid imbibition by using analytical and semi-analytical solutions of the GAT capillary flow model. The defined evaporation-capillary number has significant influence on the flow of the infiltrating liquid. It determines when the capillary motion is effected by the evaporation and the ultimate steady state front position and bulk velocity. Normal surface evaporation and side boundary evaporation both show similar time-dependent effects with the ECN, particularly in the limit of small ECN. Front interface evaporation behaves analogously to restraint by gravity in influencing the motion of the front with time; the evaporation noticeably effected the behavior over a longer period of time, and required a smaller change in magnitude than normal evaporation to significantly effect the dynamics. We also noted that flow geometry, such as 2D and 3D, can significantly reduce the front saturation length while simultaneously increasing the flow of liquid into the medium. These results clearly show the potential to use evaporation and domain shape to design media to drive liquids which only require passive energy from the surroundings to function.

3.A Relation of 1D Velocity Potential Method Solution to Fries' Solution

In this appendix, we compare our velocity potential solution to the solution given by Fries *et al.*[80] through arguments of hydraulic pressure head effects of capillary, gravity, and normal evaporation on the changing height of the liquid.

3.A.1 Fries Equation for Wicking with Gravity and Evaporation

Fries finds the solution for both gravity and evaporation acting on the wicking liquid. The governing differential equation for the motion of the front interface, h, is [Fries equation (27)]

$$\dot{h} = \frac{a}{h} - b - ch, \tag{3.A.1}$$

where the coefficients are

$$a = \frac{2\sigma \cos(\theta_s)}{\phi\mu} \frac{K}{R_s}, \tag{3.A.2a}$$

$$b = \frac{\rho g K}{\phi\mu}, \tag{3.A.2b}$$

$$c = \frac{\dot{m}_e (W + T)}{\rho W T \phi}, \tag{3.A.2c}$$

$$\Psi = -4ac - b^2. \tag{3.A.2d}$$

On the right hand side, the first term accounts for the capillary transport, the second term gives the gravity contribution, and the last gives the evaporation effect; this is analogous to Eq. (3.3.23) with only the first, second, and fourth terms in the right hand side. The Young–Laplace equation, Eq. (3.2.9), accounts for the capillary pressure when there is a single porous radius, $R_s = R_1 = R_2$ in Eq. (3.A.2a); surface tension, σ; contact angle, θ_s, and permeability, $k = K/\phi$. Fries' coefficient for the evaporation, Eq. (3.A.2c), directly considers the mass loss rate out of the system due to evaporation, $\dot{m}_e$; the density of the liquid, ρ; the width and thickness of the medium, W and T, respectively; and the void volume of the medium, ϕ. Fries implicit solution of Eq. (3.A.1) is [Fries equation (38)]

$$t = \frac{1}{2c}\left[-\ln\left(\frac{-ch^2 - bh + a}{a}\right)\right] - \frac{b}{2c\sqrt{-\Psi}}\ln\left[\frac{(-2ch - b - \sqrt{-\Psi})(-b + \sqrt{-\Psi})}{(-2ch - b + \sqrt{-\Psi})(-b - \sqrt{-\Psi})}\right]. \tag{3.A.3}$$

This solution only applies if there is a finite evaporation rate.

3.A.2 Wicking with Evaporation Only

Our solution for the normal surface evaporation, Eq. (3.3.29), is related to a reduced form of Fries' implicit solution of the wicking front, Eq. (3.A.3), when gravity is ignored, $b = 0$;

$$t = \frac{1}{2c}\left[-\ln\left(\frac{-ch^2 + a}{a}\right)\right]. \tag{3.A.4}$$

The equation may be arranged,

$$\frac{c}{a}h^2 = 1 - e^{-2ct}, \tag{3.A.5}$$

which is equivalent to Eq. (3.3.29) when

$$L = h, \tag{3.A.6a}$$

$$Q = 2c, \tag{3.A.6b}$$

$$\frac{kP_c}{\mu} = a. \tag{3.A.6c}$$

Thus, Fries' solution agrees with our analytical expression for the normal surface evaporation.

3.A.3 The Related Maximum Height and the ECN

Fries suggests a parameter, Φ, called the "related maximum height," to compare the ratio of the maximum height with capillary, gravity and evaporation over the height without evaporation [Fries equation (41)];

$$\Phi = \frac{b}{a}\left(-\frac{b}{2c} + \sqrt{\frac{b^2}{4c^2} + \frac{a}{c}}\right), \tag{3.A.7a}$$

$$= \sqrt{\left(\frac{b^2}{2ac}\right)^2 + 2\frac{b^2}{2ac}} - \frac{b^2}{2ac}. \tag{3.A.7b}$$

In the second form, we have rearranged the expression to show that it is purely dependent on a single quantity, $b^2/(2ac)$. This is rearranged to an expression in terms of the modified Bond number and the normal surface ECN,

$$\frac{b^2}{2ac} = \frac{(Wb/a)^2}{2cW/a}, \tag{3.A.8a}$$

$$= \frac{\mathrm{Bo}_a^2}{\mathfrak{N}_\mathrm{n}}. \tag{3.A.8b}$$

The ratio suggests another dimensionless number which we define

$$\mathfrak{E}_\mathrm{g} = \mathrm{Bo}_a^2/\mathfrak{N}_\mathrm{n}. \tag{3.A.9}$$

Thus, the related maximum height is reduced to,

$$\Phi = \sqrt{\mathfrak{E}_\mathrm{g}^2 + 2\mathfrak{E}_\mathrm{g}} - \mathfrak{E}_\mathrm{g}. \tag{3.A.10}$$

Ultimately, this gives an alternative means of using the results by Fries *et al.*[80]

Chapter 4

Time-Dependent Effects of Normal Surface Evaporation on Capillary–Driven Flow in Expanding Geometries

4.1   Introduction

Evaporation in porous media has significant effects on the behavior of capillary-driven flows, but is still not very well understood. Often, evaporation is considered from the perspectives of coupled multiple phases, heat transfer, and species diffusion, which are conjointly very difficult to model and test experimentally, particularly within a porous solid matrix.[30,86] However, for certain systems these complex phenomena may be reduced to simpler source and sink terms in the liquid saturated portion of the porous medium.[79,80]

Capillary-driven flows define a broad and extensively investigated topic, which

has a significant impact on numerous fields of study.[8,51,56] The wicking process in porous media is an important research area in medical and energy technologies,[48–50] thin layer chromatography, and hydrophysical phenomena.[47,57,59,62] Phase changes in porous media such as evaporation and condensation affect the advancement of fluid in porous media for many different systems.[80,87] Design of capillary-driven devices requires quantitative knowledge of the effects of evaporation on the absorption of liquids into unsaturated porous media. Capillary driven flows do not require an external input of energy and as such they are "free," which makes them attractive for a variety of engineering applications.[21,22] A class of new microfluidic devices, for example, use capillarity to drive motion of the liquid through the unit, but they require a steady, finite flow rate for continuous and predictable wicking.[17] Evaporation allows the capillary media to be designed and adaptively tuned to the desired flow rate through the device.

An easy way to control capillary driven flows in porous materials can be achieved by designing their macroscopic shape. For example the flow rate in expanding porous media exhibits a very different time behavior from the simple $v \sim 1/\sqrt{t}$ dependence predicted by the Lucas and Washburn (LW) analysis.[54,55] Several studies have considered expanding flows into two- (2D) and three-dimensional (3D) porous domains.[23,50,60,61,73]

In general, continuum two phase flows in porous media can be successfully analyzed by using a continuity equation for unsaturated capillary flow.[4,68,70–72]

Recently, the phenomenology and potential effects of evaporation in connection with capillary flows have increasingly been analyzed. Lockington *et al.*[79] developed an approximate analytical solution for 1D capillary diffusion under evaporation. Fries *et al.*[80] compared the solution for saturated wicking with evaporation and gravity to experiments in a metallic weave, but found that the theory noticeably over-predicted the distance of infiltration relative to experiment. Barry *et al.*[81] suggested that capillary

diffusion and evaporation can explain the discrepancy with the theoretical predictions given by determining the front position via absorbed mass. Villarrubia *et al.*[17] observed a steady-state flow of water due to evaporation into porous paper after an initial wicking behavior similar to the LW equation in a quasi-2D medium. Liu *et al.*[95] extended Fries' methods into 2D radial flow to study convergence between inner and outer wetting flows.

In this paper, we present analytical solutions to the flow behavior of a liquid wicking into an expanding two-dimensional porous system which is undergoing isotropic evaporation from the surface normal to the 2D porous medium. Hence, a particular focus of the our study is on the interplay between the evaporation effect and the shape of the porous material. We consider 2D domains where the evaporation from surface normal to the plane of the medium dominates the overall mass loss. The evaporation losses across the side boundaries can be ignored; in most cases this loss is insignificant because of the vanishingly small contact area with the surroundings. We show that the evaporation has an increasing effect on the liquid motion over time, wherein the flow transitions from purely capillary dominated flow, to a transitional flow regime, to evaporation dominated steady state. The relative contributions of evaporation and capillary imbibition is conveniently described by a dimensionless characteristic (evaporation-capillary) number (see also Ref[24]). Simplified solutions are obtained for long times, when the system reaches a steady state, as well as for short times, which correspond to the initial stage of liquid transport in the porous medium.

The paper is organized as follows: in the next section, we outline potential flow theory for capillary driven motion with evaporation; the solutions of wicking with normal surface evaporation for various shapes of the porous media are developed in Sec. 4.3; Sec. 4.4 details the asymptotic analysis; and Sec. 4.5 summarizes the conclusions.

4.2 Governing Equations for the Flow in Porous Media with Evaporation

The mass balance equation for incompressible flow of liquid through a porous medium with evaporation rate, $Q > 0$, is

$$\boldsymbol{\nabla} \cdot \mathbf{v} = -Q, \tag{4.2.1}$$

where the linear liquid velocity, $\mathbf{v}$, is measured over a length scale significantly greater than the size of the individual pores.[92]The sink term, Q, is defined as the fractional mass loss rate (vaporized mass rate over liquid phase mass) from the liquid-filled domain of the porous medium and has units of inverse time.* This evaporation model restricts the system to a very thin or effectively two-dimensional porous layers because the evaporation occurs as mass leaving the liquid domain in the direction normal to the plane of the 2D medium. The plane is orthogonal to gravity or the Bond number—the ratio of the gravitational to capillary force—is significantly less than one.[89] In the alternative case of $Q < 0$, capillary condensation would occur. However, it affects the saturation throughout the medium and results in a diffuse wetting front, so this model is not practical for condensation.[96]

The flow of liquid in porous media is irrotational,[65] so the velocity may be expressed as the gradient of a velocity potential, φ,

$$\mathbf{v} = \boldsymbol{\nabla}\varphi. \tag{4.2.2}$$

By the Darcy law, $\mathbf{v} = -(k/\mu)\boldsymbol{\nabla}P$, the potential is directly related to the driving pressure, P,

$$\varphi = -\frac{k}{\mu}P, \tag{4.2.3}$$

---

* See the discussion in Chapter 3 in the development of Eq. (3.2.5) for more mathematical details, here we focus on some of the assumptions relating specifically to normal surface evaporation.

where k is the constant isotropic permeability of the medium and μ is the dynamic viscosity of the liquid.[56,90,93,97,98] The pressure gradient driving the liquid motion is due to the capillary pressure drop at the front of the advancing domain. This effectively simplifies the behavior of the system to three parameters: the permeability, which is intrinsic to the solid medium; the viscosity, which characterizes the flow of liquid; and the capillary pressure, $P = P_\text{c}$. We apply the linear Darcy law which is valid for incompressible pore networks,[56] and at times significantly greater than the brief inertially-dominated flow regime.[64,88,99]

The potential and the velocity, equations (4.2.1) and (4.2.2), combine to into a Poisson equation for the potential,[4]

$$\nabla^2 \varphi = -Q. \tag{4.2.4}$$

The velocity potential in Eq. (4.2.4) is solved assuming the potential at the inlet is $\varphi_0 = -kP_\text{c}/\mu$ and $\varphi_f = 0$ at the front. For the side boundaries, the flux of the velocity potential is set to zero. Once the potential is solved, the velocity of the liquid is found using Eq. (4.2.2). Mass is conserved at the frontal interface, such that the wet front is moved by the potential driving force of the liquid velocity,[54,55]

$$\mathbf{v}_f = \frac{\mathrm{d}\mathbf{x}_f}{\mathrm{d}t}, \tag{4.2.5}$$

where $\mathbf{v}_f$ and $\mathbf{x}_f$ are the velocity and position vectors, respectively, of the liquid at the front boundary.* The motion is relatively slow and in a small domain, so we assume the liquid saturated portion is isothermal.[78] The secondary fluid in the system is normally air, which is sufficiently immiscible with most liquids and low enough in density to assume the motion of the liquid phase is independent of the gas phase. We consider the evaporation to be homogenous across the wetted portion of the domain and the liquid saturated portion of the domain does not have any trapped gas.[93] Eq. (4.2.5) is solved to find the dependence of the front position with respect to time.

* We show the derivation of this expression in Eq. (3.2.13).

Finally, the bulk velocity—the volumetric flow rate into the medium—is computed from the integral of the liquid velocity normal to a complete cross-section of the flow, particularly the inlet. We refer to these steps generally as the Lucas–Washburn approach or method as it extends their single-pore techniques to a general porous medium.[23] Eqs. (4.2.4) and (4.2.5) are the governing equations of the infiltrating liquid system.

4.3 Capillary Driven Flow with Evaporation in Thin Porous Media

In this section, we derive solutions of wicking with evaporation for 2D-like domains with circular and flat inlets and a 1D-like domain of constant rectangular cross section. We solve the total velocity potential to determine the front velocity equation from which the equations of motion for the wetting front position and the bulk velocity are determined. A characteristic dimensionless number is introduced to simplify the asymptotic comparison between the solutions and to consider the time-dependent effects of the wicking.

4.3.1 Capillary Flow Through a Semicircular Inlet with Surface Evaporation

The radial flow in a 2D porous domain in absence of evaporation was recently solved by Hyvaluoma et al.[61] We extend the analysis by accounting for evaporation losses by introducing a sink term Q in the mass balance equation Eq. (4.2.4) in polar coordinates (see also Fig. 4.1)

$$\frac{\mathrm{d}^2\varphi}{\mathrm{d}r^2} + \frac{1}{r}\frac{\mathrm{d}\varphi}{\mathrm{d}r} = -Q, \tag{4.3.1}$$
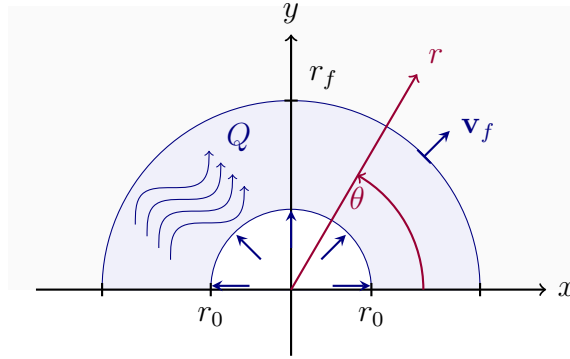
Figure 4.1. Expanding flow through semicircular inlet into saturated domains with evaporation loss, Q, from the normal surface described by polar coordinates.

with the boundary conditions

$$\varphi|_{r=r_0} = -\frac{k}{\mu} P_{\text{c}}, \tag{4.3.2a}$$

$$\varphi|_{r=r_f} = 0. \tag{4.3.2b}$$

The radius of the circular inlet is r_0 while r_f is the radius of the front of the saturated domain. The polar angle, θ, varies from 0 to π. The porous material is considered to be of thickness δ, small enough to ignore any variations in z-direction. The side boundaries are subject to no flux conditions.

The solution of (4.3.1) with boundary conditions (4.3.2) and constant Q reads

$$\tilde{\varphi} = -\frac{\ln(\tilde{r}_f) - \ln(\tilde{r})}{\ln(\tilde{r}_f)} \tag{4.3.3}$$
$$- \frac{1}{4} \frac{\mu a^2 Q}{k P_{\text{c}}} \frac{(\tilde{r}^2 - 1)\ln(\tilde{r}_f) - (\tilde{r}_f^2 - 1)\ln(\tilde{r})}{\ln(\tilde{r}_f)}.$$

The dimensionless potential is defined $\tilde{\varphi} = (\mu/kP_{\text{c}})\varphi$ and $\tilde{r} = r/r_0$ or r/a with dimensionless forms of other length variables defined in the same manner. Examining Eq. (4.3.3), we observe a dimensionless group, which we refer to as the evaporation-

capillary number, or for brevity, the evaporation number,

$$\mathfrak{N}_{\mathrm{n}} = \frac{\mu a^2 Q}{k P_{\mathrm{c}}}. \tag{4.3.4}$$

The subscript 'n' indicates the evaporation mechanism is through the surface *normal* to the thin medium.* $\mathfrak{N}_{\mathrm{n}}$ is a measure of the relative strength of the mass loss rate by evaporation, Q, over mass transport into the medium, $k P_{\mathrm{c}}/\mu a^2$, by capillary forces and is found in the general case by proper scaling of Eq. (4.2.4). Alternatively, $\mathfrak{N}_{\mathrm{n}}$ may be considered as the ratio of the characteristic time of capillary motion to the characteristic time of the evaporation loss. From this perspective it is evident that the quantity, $\mathfrak{N}_{\mathrm{n}}$, estimates which mode of transport dominates the time-dependent behavior of the flow. Large $\mathfrak{N}_{\mathrm{n}}$ indicates that the flow is mostly driven by the evaporation of the flat surface, while small $\mathfrak{N}_{\mathrm{n}}$ means that the flow is governed by the capillary pressure drop [see Eq. (4.3.2)].

The velocity in the radial direction is found by differentiating the potential with respect to r,

$$\tilde{v}_r = \frac{1}{\tilde{r} \ln(\tilde{r}_f)} - \frac{1}{4} \mathfrak{N}_{\mathrm{n}} \frac{\tilde{r}^2 \ln(\tilde{r}_f^2) - (\tilde{r}_f^2 - 1)}{\tilde{r} \ln(\tilde{r}_f)}. \tag{4.3.5}$$

Then the velocity at the liquid front, v_f, is found by substituting $r = r_f$, so

$$\tilde{v}_f = \frac{1}{\tilde{r}_f \ln(\tilde{r}_f)} - \frac{1}{4} \mathfrak{N}_{\mathrm{n}} \frac{\tilde{r}_f^2 \ln(\tilde{r}_f^2) - (\tilde{r}_f^2 - 1)}{\tilde{r}_f \ln(\tilde{r}_f)}. \tag{4.3.6}$$

where $\tilde{v} = (\mu a/k P_{\mathrm{c}})v$. This expression for the front velocity is equivalent to equation (5) in the recently published work of Liu *et al.*[95] At steady state the front velocity is zero, so for 2D flow geometry and in the limits of large front radius and small $\mathfrak{N}_{\mathrm{n}}$, $\tilde{r}_{f,\mathrm{ss}}^2 \ln(\tilde{r}_{f,\mathrm{ss}})/2 \approx 1/\mathfrak{N}_{\mathrm{n}}$. Following the general LW approach and using Eq. (4.2.5), the evolution equation of the frontal radius is determined by $\mathrm{d}r_f/\mathrm{d}t = v_f$. This equation

---

* The evaporation-capillary number as defined for the side and front boundaries are given in Eqs. (3.3.20) and (3.3.24), respectively. We discuss the nature of the ECN in greater detail in §3.4.1.

is integrable and gives an implicit solution of the dependence of the frontal wetted radius with time

$$\ln\left\{1 - \frac{1}{4}\mathfrak{N}_{\mathrm{n}}\left[\tilde{r}_f^2 \ln\left(\tilde{r}_f^2\right) - \left(\tilde{r}_f^2 - 1\right)\right]\right\} = -\mathfrak{N}_{\mathrm{n}}\tilde{t}, \tag{4.3.7}$$

where $\tilde{t} = (kP_{\mathrm{c}}/\mu a^2)t$. Expanding the left hand side and keeping only the two lowest-order terms in $\mathfrak{N}_{\mathrm{n}}$ with their highest-order terms in the front radius,

$$\frac{1}{2}\left\{\tilde{r}_f^2 \ln(\tilde{r}_f) + \frac{1}{4}\mathfrak{N}_{\mathrm{n}}\tilde{r}_f^4[\ln(\tilde{r}_f)]^2 + \cdots\right\} = \tilde{t}. \tag{4.3.8}$$

The expression for the front position, Eq. (4.3.7), may be rearranged,

$$2\tilde{r}_f^2 \ln(\tilde{r}_f) - \left(\tilde{r}_f^2 - 1\right) = \frac{4}{\mathfrak{N}_{\mathrm{n}}}\left(1 - \mathrm{e}^{-\mathfrak{N}_{\mathrm{n}}\tilde{t}}\right). \tag{4.3.9}$$

In the limit of $\mathfrak{N}_{\mathrm{n}} \to 0$ or for short times, this result agrees with the solution without evaporation given in Hyvaluoma *et al.*[61] Comparing the leading terms on both sides reduces Eq. (4.3.9) to

$$\tilde{r}_f^2 \ln(\tilde{r}_f) \approx \tilde{t} - \frac{1}{2}\mathfrak{N}_{\mathrm{n}}\tilde{t}^2, \tag{4.3.10}$$

with errors of the order of $\tilde{r}_f^2$ and $\mathfrak{N}_{\mathrm{n}}^2\tilde{t}^3$. Conversely, for $\tilde{t} \to \infty$, Eq. (4.3.9) matches the steady state result given in Liu *et al.*[95]

The volumetric flux through the inlet into the medium (*i.e.* bulk velocity) is computed for polar geometry by

$$U = \left[\int_0^\delta \int_0^\pi v_r \, r \, \mathrm{d}\theta \, \mathrm{d}z\right]\Bigg|_{r=r_0}. \tag{4.3.11}$$

The final form of the bulk velocity is determined by integrating the radial velocity over the angular direction;

$$\tilde{U} = \frac{\pi}{\ln(\tilde{r}_f)}\left\{1 + \frac{1}{4}\mathfrak{N}_{\mathrm{n}}\left[\tilde{r}_f^2 - \ln(\tilde{r}_f)^2 - 1\right]\right\}. \tag{4.3.12}$$

where the dimensionless bulk velocity is defined $\tilde{U} = (\mu/kP_{\mathrm{c}}\delta)U$. For simplicity in the form of the solution, we have alternatively chosen δ as the length scale in $\tilde{U}$ instead of a.
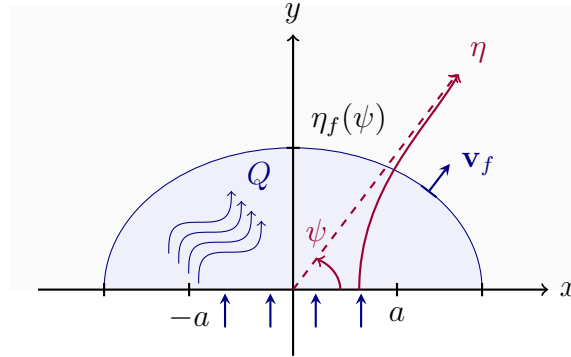
Figure 4.2. Expanding flow through linear inlet into saturated domains with evaporation loss described by elliptic coordinates.

4.3.2   Expanding Capillary Flow Through a Linear Inlet with Evaporation

A porous medium with a flat, discrete-sized inlet into a thin half-plane is conveniently described by elliptic coordinates.[23] This choice follows from the fact that the equipotential curves corresponding to a finite line source (or sink) are ellipses. The sudden expansion depicted in Fig. 4.2 can be formally considered as a line source supplying the liquid into a half-plane, which is the 2D porous domain. This also implies that the side boundary conditions correspond to absence of flux or symmetry [see Fig. 4.1 and Eqs. (4.3.15) below]. The model has some interesting implications, when evaporation is present, that are unique to this particular shape and are discussed below.

The elliptic coordinate system is defined as[31]

$$x = a \cosh(\eta) \cos(\psi), \tag{4.3.13a}$$

$$y = a \sinh(\eta) \sin(\psi). \tag{4.3.13b}$$

The fluid motion occurs primarily in the η-direction, while the angular variable, ψ,

accounts for small variations in the expansion near the inlet. The inlet width into the medium is equal to the distance between the two foci of the elliptical coordinate system, $2a$. As in the radial flow case above the porous medium is 2D, hence the z-axis has no effect on the overall transport. The evaporation of the surface is accounted for by the sink term Q.

The mass balance equation (4.2.4), for elliptic geometry may be expressed in the form[31]

$$\frac{1}{a^2 \left[\cosh^2(\eta) - \cos^2(\psi)\right]} \left(\frac{\partial^2 \varphi}{\partial \eta^2} + \frac{\partial^2 \varphi}{\partial \psi^2}\right) = -Q. \tag{4.3.14}$$

The boundary conditions of the system account for capillary-driven motion, and no flux through the edges of the medium

$$\left.\frac{\partial \varphi}{\partial \psi}\right|_{\psi=0} = 0, \tag{4.3.15a}$$

$$\left.\frac{\partial \varphi}{\partial \psi}\right|_{\psi=\pi} = 0, \tag{4.3.15b}$$

$$\varphi|_{\eta=0} = \varphi_0 = -\frac{k}{\mu}P_{\mathrm{c}}, \tag{4.3.15c}$$

$$\varphi|_{\eta=\eta_f} = 0. \tag{4.3.15d}$$

The solution for the velocity potential in dimensionless form is (see Ref.[100] for details)

$$\tilde{\varphi} = -\frac{\eta_f - \eta}{\eta_f} - \frac{1}{4}\mathfrak{N}_{\mathrm{n}} \left[\frac{\eta - \eta_f + \eta_f \cosh(2\eta) - \eta \cosh(2\eta_f)}{2\eta_f}\right.$$
$$\left. + \frac{\sinh(\eta_f - \eta)\sinh(\eta)}{\cosh(\eta_f)} \cos(2\psi)\right]. \tag{4.3.16}$$

This potential is then used to derive the velocity of liquid propagation in the porous materials that includes both capillary and evaporation effects. The first term accounts for the capillary pressure driven transport, while the second one is for the evaporation loss.

The velocity of liquid propagation can be expressed as the potential gradient,[31]

or

$$\boldsymbol{\nabla}\varphi = v_\eta \hat{\mathbf{e}}_\eta + v_\psi \hat{\mathbf{e}}_\psi \tag{4.3.17a}$$

$$= \frac{1}{a\left[\cosh^2(\eta) - \cos^2(\psi)\right]^{1/2}} \left[\frac{\partial\varphi}{\partial\eta}\hat{\mathbf{e}}_\eta + \frac{\partial\varphi}{\partial\psi}\hat{\mathbf{e}}_\psi\right]. \tag{4.3.17b}$$

Hence the two components of the velocity are

$$\tilde{v}_\eta = \frac{1}{\left[\cosh^2(\eta) - \cos^2(\psi)\right]^{1/2}} \left\{ \frac{1}{\eta_f} \right.$$
$$-\frac{1}{4}\mathfrak{N}_{\mathrm{n}}\left[\frac{2\eta_f\sinh(2\eta) - \cosh(2\eta_f) + 1}{2\eta_f}\right. \tag{4.3.18}$$
$$\left.\left. + \frac{\sinh(\eta_f - 2\eta)}{\cosh(\eta_f)}\cos(2\psi)\right]\right\},$$

and

$$\tilde{v}_\psi = \frac{-1}{\left[\cosh^2(\eta) - \cos^2(\psi)\right]^{1/2}}$$
$$\times \frac{1}{2}\mathfrak{N}_{\mathrm{n}}\frac{\sinh(\eta_f - \eta)\sinh(\eta)}{\cosh(\eta_f)}\sin(2\psi). \tag{4.3.19}$$

The velocity components are scaled as described above. We are interested in the front velocity where $\eta = \eta_f$. Examining Eq. (4.3.19) shows that at the front $v_\psi = 0$, and the velocity $\tilde{v}_f$ has components only along η_f. Restating Eq. (4.2.5) for the elliptic coordinate system, then the front velocity,

$$\tilde{v}_f = \left[\cosh^2(\eta_f) - \cos^2(\psi)\right]^{1/2}\frac{\mathrm{d}\eta_f}{\mathrm{d}\tilde{t}} \tag{4.3.20a}$$

$$= \frac{1}{\left[\cosh^2(\eta_f) - \cos^2(\psi)\right]^{1/2}} \left\{ \frac{1}{\eta_f} \right.$$
$$-\frac{1}{4}\mathfrak{N}_{\mathrm{n}}\left[\frac{2\eta_f\sinh(2\eta_f) - \cosh(2\eta_f) + 1}{2\eta_f}\right. \tag{4.3.20b}$$
$$\left.\left. - \tanh(\eta_f)\cos(2\psi)\right]\right\}.$$

Following the spirit of the LW approach, Eq. (4.3.20b) must be numerically integrated to give the time-dependent position of the front $\eta_f(\tilde{t})$.*

---

* See §E.1.4 for details. Also, we may compare this solution to Eq. (2.3.7), which yields the analytical solution Eq. (2.3.9) for 2D flow with capillary force only.

Both the fluid front velocity $\tilde{v}_f$ and position η_f are not elliptic in shape. Hence, this case is different from the simple 1D and 2D circular cases where the both the velocity and the time-dependent front position have the same shape as the equipotential lines. More detailed analysis shows that while the shape of the liquid front for expanding flow through a linear inlet is not elliptic for short times and small η_f, it approaches one for longer times, which also agrees with experimental observations.[100] The deviation from elliptic shape for $\eta_f \geq 2$ is less than 5% and rapidly decreases further with the advancement of the liquid front.

The bulk velocity is calculated via

$$U = \left[\int_0^\delta \int_0^\pi \mathbf{v} \cdot \mathbf{n}\, a \left[\cosh^2(\eta) - \cos^2(\psi) \right]^{1/2} \mathrm{d}\psi\, \mathrm{d}z \right]\Bigg|_{\eta=0}, \qquad (4.3.21)$$

where $\mathbf{n}$ is the unit vector normal to the inlet, which in this case is $\hat{\mathbf{e}}_\eta$. When the velocity from Eq. (4.3.18) is substituted and the expression simplified, we find the bulk velocity in integral form,

$$\tilde{U} = \int_0^\pi \frac{1}{\eta_f} + \frac{1}{4}\mathfrak{N}_{\mathrm{n}} \left[\frac{\cosh(2\eta_f) - 1}{2\eta_f} + \tanh(\eta_f) \cos(2\psi) \right] \mathrm{d}\psi, \qquad (4.3.22)$$

The integration over the angular variable is not straight-forward because the frontal position is a weak function of the angle, $\eta_f = \eta_f(\psi, t)$, and may only be fully solved numerically. This arises principally from the angular dependence of the inverse squared metric coefficient in front of the expression for integrating the position over time in Eq. (4.3.20b). If we assume η_f is constant with respect to ψ, the equation simplifies;

$$\tilde{U} = \frac{\pi}{\eta_f} + \frac{\pi}{8}\mathfrak{N}_{\mathrm{n}} \left[\frac{\cosh(2\eta_f) - 1}{\eta_f} \right]. \qquad (4.3.23)$$

This equation is only useful qualitatively in the limit of large η_f, and invalid for the early times of expansion where the angular dependence is especially strong.[100*]

---

* This solution for $\mathfrak{N}_{\mathrm{n}} = 0$ agrees with the bulk velocity for capillary flow given in Eq. (2.3.11), indicating that the limitations on the angular variable which we consider here are important in capillary flow as well.

4.3.3 Capillary Flow with Normal Surface Evaporation in a Non-Expanding Porous Media

Before comparing the 2D expanding flow solutions found above, it is instructive to revisit the known solution for capillary flow through a medium of constant cross section with normal surface evaporation. This case does not involve any expansion of the porous medium, which makes the flow effectively 1D. The problem of finding the time dependence of the front position was first solved by Fries *et al.*[80] (see also Ref[24]). The solution for the front position may be presented in the form,

$$\tilde{L}^2 = \frac{2}{\mathfrak{N}_{\mathrm{n}}} \left[1 - \exp\left(-\mathfrak{N}_{\mathrm{n}} \tilde{t}\right) \right]. \tag{4.3.24}$$

As the exponential term goes to zero at longer time, the steady state value of the front position becomes $\tilde{L}_{\mathrm{ss}} = \sqrt{2/\mathfrak{N}_{\mathrm{n}}}$. Similar to the 2D polar case with Eq. (4.3.10), the solution may be expressed as a series in the time variable;

$$\frac{1}{2}\tilde{L}^2 = \tilde{t} - \frac{1}{2}\mathfrak{N}_{\mathrm{n}}\tilde{t}^2 + \cdots . \tag{4.3.25}$$

Rearranging Eq. (4.3.24) into the implicit form of the length variable,

$$\ln\left(1 - \frac{1}{2}\mathfrak{N}_{\mathrm{n}}\tilde{L}^2 \right) = -\mathfrak{N}_{\mathrm{n}}\tilde{t}.$$

We expand the logarithm in the same manner as Eq. (4.3.8) to achieve the series approximation in the spatial variable;

$$\frac{1}{2}\left(\tilde{L}^2 + \frac{1}{4}\mathfrak{N}_{\mathrm{n}}\tilde{L}^4 + \cdots \right) = \tilde{t}. \tag{4.3.26}$$

The bulk velocity for the porous strips of constant cross section $2a$ by δ is[24]

$$\tilde{U} = \frac{2}{\tilde{L}} + \mathfrak{N}_{\mathrm{n}}\tilde{L}. \tag{4.3.27}$$

As $\tilde{L}$ increases, the first term decreases and the evaporation becomes the primary driver of liquid infiltration. The time-dependent bulk flow-rate can be derived by
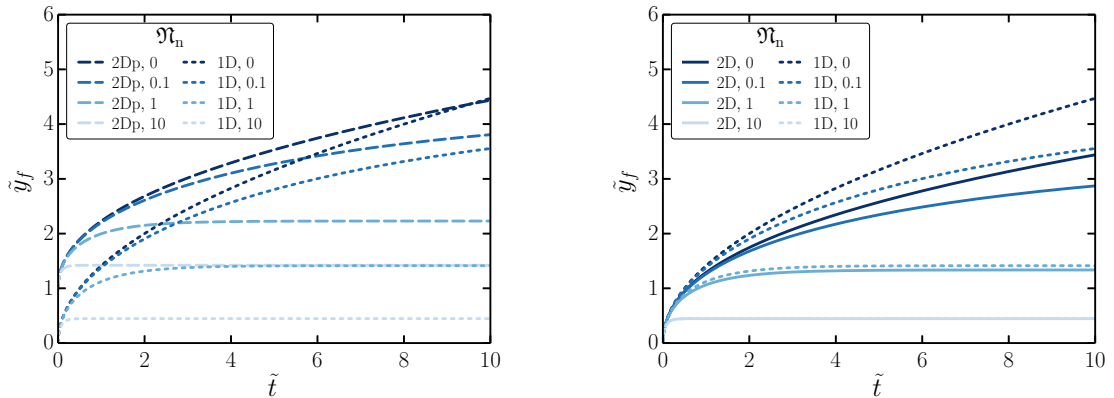
(a) Flow through circular inlet (2Dp) described by polar coordinates in Figure 4.1.

(b) Flow through linear inlet (2D) described by elliptic coordinates in Figure 4.2.

Figure 4.3. Front position, $\tilde{y}_f$, versus time, $\tilde{t}$, compared to flow through constant cross section (1D).

substituting Eq. (4.3.24) into (4.3.27). At steady state ($\tilde{t} \to \infty$), the bulk velocity becomes particularly simple,

$$\tilde{U}_{ss} = \sqrt{8\mathfrak{N}_n}. \tag{4.3.28}$$

4.4 Results and Discussion

4.4.1 Time Dependence of Propagation Length in the Presence of Evaporation

The LW solution for 1D capillary flow in absence of evaporation predicts that the distance of liquid imbibition $L \sim \sqrt{t}$. If the porous materials has a varying cross-section then this simple law is no longer valid.[23,60,61] The evaporation effects further complicate the physical picture and also have an impact on the overall time behavior. Here we present results on the capillary driven liquid penetration in 2D expanding

porous with surface evaporation.

Fig. 4.3 illustrates notable differences and similarities in early time dependent behavior of the front position solutions for the three cases given above. Fig. 4.3a compares the solution in the Cartesian (1D) and polar (2D radial) solutions, Eq. (4.3.24) and (4.3.7), respectively. The position along the y-axis is tracked, hence the front in the figures is denoted by $\tilde{y}_f$. The 2D radial flow has a circular inlet, and begins at $\tilde{y} = 1$, while the 1D flow, begins at a flat inlet where $\tilde{y} = 0$. This makes the solutions disjointed at early times, when plotted together (see Fig. 4.3a). Additionally, the later time behaviors (with lower evaporation numbers) do not become similar because the effects of the expansion on the 2D flow reduce the rate of front advancement relative to the LW result.

In Fig. 4.3b the 2D elliptic coordinate solution, Eq. (4.3.20b), is compared to the 1D solution, Eq. (4.3.24). Here we observe much better agreement, particularly for high evaporation numbers because the expansion is insignificant for the 2D elliptic solution at small values of the front position. For $\mathfrak{N}_n = 10$, the two solutions are indistinguishable, and for $\mathfrak{N}_n = 1$ the they are still very close. Small numbers, $\mathfrak{N}_n < 1$, lead to increased deviation between the 1D and 2D solutions. This is because the liquid penetrates further in the porous material and curves due to the expansion in the 2D case. This effect leads to the observed discrepancy between the 1D and 2D cases.

Fig. 4.4 presents data for larger values of $\mathfrak{N}_n$ and much longer times. Fig. 4.4a shows the front position along the y-axis for both the 2D expansion (elliptic) and 1D (Cartesian) cases. We again observe the front position data match almost perfectly for large $\mathfrak{N}_n = 100$, and they are very similar for $\mathfrak{N}_n = 1$. At longer times and small $\mathfrak{N}_n$, the discrepancies between the 2D and 1D cases are even greater that in Fig. 4.3b, particularly when the evaporation is low (*i.e.*, $\mathfrak{N}_n = 0.01$).
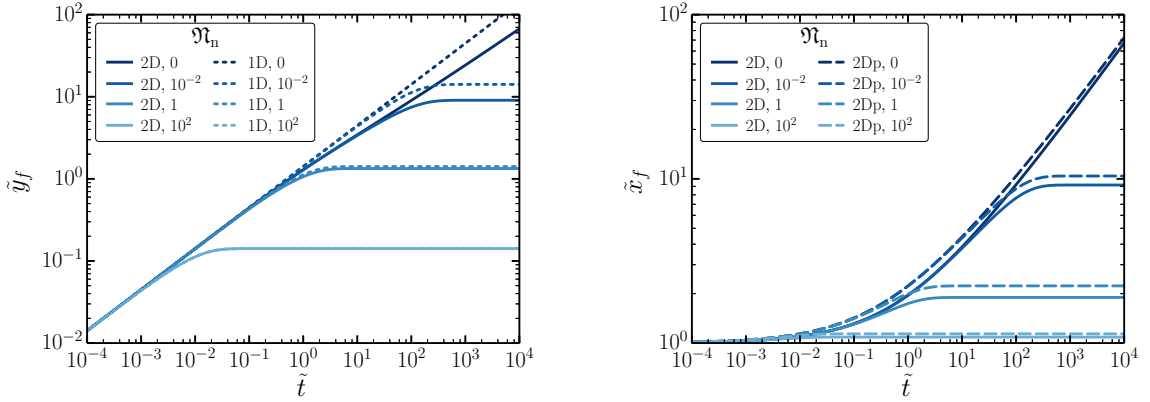
(a) Comparison of 1D and 2D with linear inlet.

(b) Comparison of lateral flow for 2D linear and 2D circular inlets.

Figure 4.4. Logarithmic comparison of front positions versus time, $\tilde{t}$, for 1D and 2D cases. The front position is tracked along the y-axis in (a) and x-axis in (b).

Figure 4.4b plots the elliptic and 2D polar solutions of the front position along the x-axis because the polar front starts at $\tilde{r}_f = 1$ as elliptic does along $\psi = 0$ and π. The front positions begin close together at early times $\tilde{t} < 0.01$ and are slightly different for high evaporation number, $\mathfrak{N}_{\mathrm{n}} = 100$. On the opposite scale, at small evaporation numbers and large times, such as $\mathfrak{N}_{\mathrm{n}} = 0.01$ or 0 and $\tilde{t} > 10^3$, the elliptic and polar solutions asymptotically agree. In the intermediate range of $\tilde{t} \sim 1$ and $\mathfrak{N}_{\mathrm{n}} \sim 1$, the solutions are noticeably separated due to the subtle difference of the inlet shape between the elliptic and polar models. Ultimately, we observe that the length of the propagation of the liquid derived with the elliptic geometry gives the correct qualitative asymptotic behaviors both with and without the evaporation
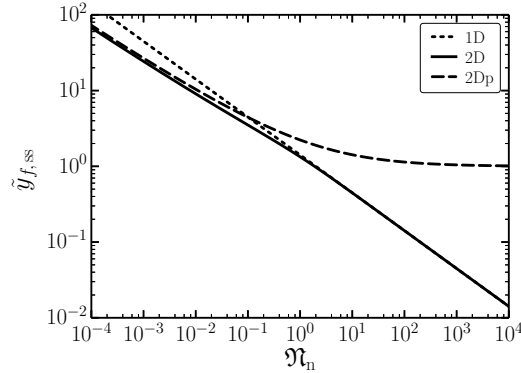
Figure 4.5. Steady state front position along the y-axis, $\tilde{y}_f$, versus evaporation number, $\mathfrak{N}_n$, for linear inlet (2D), circular inlet (2Dp), and constant cross section (1D).

effects.[*]

The steady state front position versus evaporation number is shown in Fig. 4.5, which illustrates how far the liquid propagates into the medium depending on the relative evaporation loss (*i.e.* the $\mathfrak{N}_n$ number). The flat linear inlet case (elliptic) interpolates between the 1D Cartesian and 2D radial flow solutions. The steady state front position for elliptic coordinates appears to match asymptotically with the polar case for $\mathfrak{N}_n < 0.01$, and is very close to the Cartesian data for $\mathfrak{N}_n > 10$. For evaporation numbers between these two values, the elliptic propagation length is less than both of the asymptotic cases. Particularly for large $\mathfrak{N}_n$, where the 1D Cartesian case is relevant, the bottom right side of Fig. 4.5 shows the steady state position of

---

[*] The solutions of the front position in Chapter 2 may be numerically shown to match the results above in the limit of no evaporation, *i.e.* $\mathfrak{N}_n = 0$. However, Figure 2.10, which gives the 1D, 2D, and 2D polar solutions of the front position over time, presents the data in the elliptic variable, η_f^2, for asymptotic comparison between the three cases. So, this prior result is not visually comparable to Figures 4.4a and 4.4b of in this chapter where the data is relevant asymptotically, relatable to dimensional physical systems, and thereby directly applicable to physical analysis and device design. This is similar to Figure 3.2.
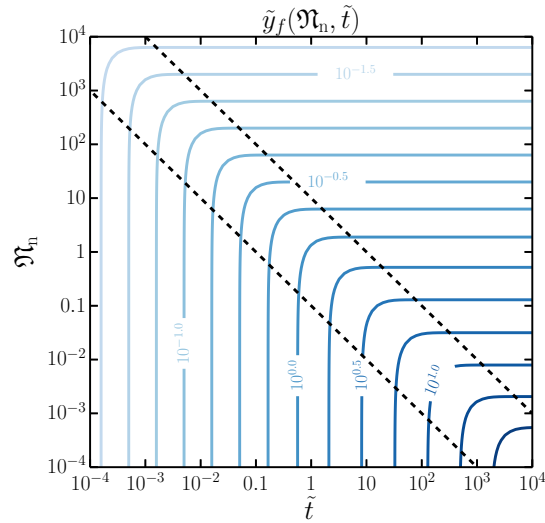
Figure 4.6. Contour plot of frontal position, $\tilde{y}_f$, over evaporation number, $\mathfrak{N}_n$, and time, $\tilde{t}$, for the elliptic solution. Dashed black lines distinguish regimes of flow behavior; $\mathfrak{N}_n\tilde{t} = 0.1$ and $\mathfrak{N}_n\tilde{t} = 10$ are plotted in the lower left and upper right, respectively. The lower left section is dominated by capillary flow and upper right is at steady state.

the front varies as the inverse square root of the evaporation number; $\tilde{y}_{f,\,\mathrm{ss}} \sim 1/\sqrt{\mathfrak{N}_n}$ or $\mathfrak{N}_n\tilde{y}_{f,\,\mathrm{ss}}^2 \sim 1$. This is in agreement with Eq. (4.3.24) at steady state. In the limit of small $\mathfrak{N}_n$, the front advancements for the radial and elliptic flows are less than in the 1D case. This observation agrees with the steady state form of Eq. (4.3.6); $\tilde{y}_{f,\,\mathrm{ss}}^2 \ln(\tilde{y}_{f,\,\mathrm{ss}}) \sim 1/\mathfrak{N}_n.$*

4.4.2 Regimes of Capillary Flow Behavior

Three regimes can be identified in the time-dependent behavior of the capillary driven frontal fluid motion in the presence of evaporation. These are clearly visible in Fig. 4.6, where the data from Fig. 4.4a are essentially revisualized as a contour plot of the magnitude of the front position as it varies over the evaporation number and the time. The contours exhibit three distinctly patterned zones: vertical lines, horizontal

---

* See Eq. (E.1.17b) for the explanation.

lines, and transitional curves from vertical to horizontal. Each represent different flow regimes of the liquid front. The first regime (see the vertical lines) indicates that the front position is very weakly dependent on the evaporation number. This is the capillary force dominated regime, $\mathfrak{N}_n \tilde{t} \ll 1$, where the fluid motion is asymptotically identical to the infiltration by capillary forces only. The second zone (horizontal lines) is for longer time scales, $\mathfrak{N}_n \tilde{t} \gg 1$, where the evaporation effects become much greater than the capillary forces and the fluid saturated medium has reached a steady state. The lines are horizontal because the front position is no longer advancing with time. Between these two regimes is the transition zone (approximately between $0.1 < \mathfrak{N}_n \tilde{t} < 10$) where the flow behavior is a mixture of capillary and evaporation effects, with evaporation becoming dominant as time increases.

The relationship between the evaporation number $\mathfrak{N}_n$ and time is shown analytically in Eqs. (4.3.9) and (4.3.24), where the implicit function of the front position is proportional to $[1 - \exp(-\mathfrak{N}_n \tilde{t})]/\mathfrak{N}_n$. This illustrates that it is the product $\mathfrak{N}_n \tilde{t}$ that determines the time behavior in the presence of surface evaporation. The first order asymptotic expansion of this expression is in the form $\tilde{t}(1 - \frac{1}{2}\mathfrak{N}_n \tilde{t})$, which is valid for early times or small evaporation rate [see Eqs. (4.3.25) and (4.3.10)]. For $\mathfrak{N}_n \tilde{t} = 0.1$ this means the magnitude of the front position is reduced by 5%. As illustrated in Figure 4.4, the solution of the behavior of the front in elliptic coordinates matches the Cartesian and polar solutions asymptotically.[100] Thus, in all three cases the front position of the liquid is determined by $\mathfrak{N}_n \tilde{t}$, or equivalently in dimensional form, by the product of the evaporation rate and the wetting time, Qt.

4.4.3 Rate of Liquid Absorption

The bulk velocity is defined as the amount of water the porous medium is absorbing per unit time. Figure 4.7a plots the bulk velocity versus time for liquid penetrating

(a) Bulk flowrate vs. time for flat inlet.

(b) Steady state bulk velocity.
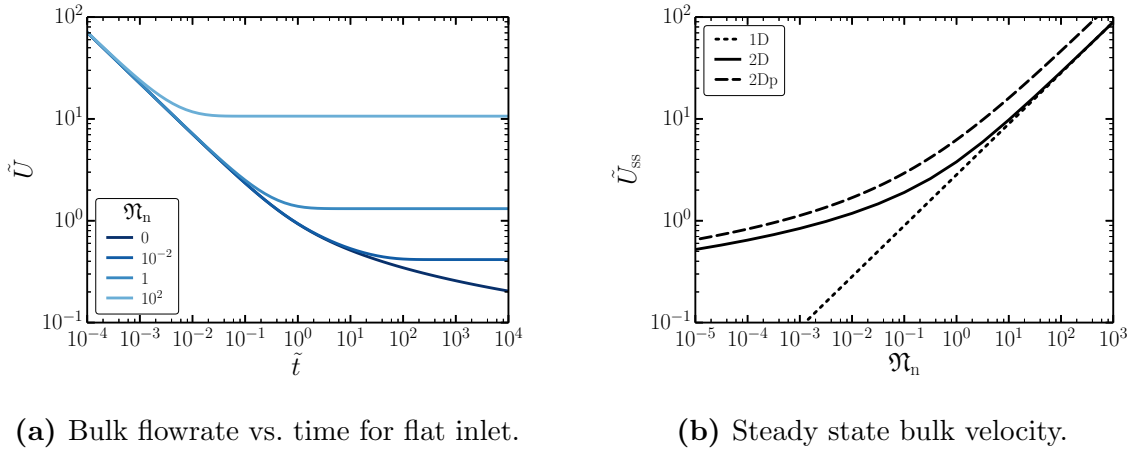
Figure 4.7. Bulk flow-rate behavior with time (a) and with evaporation number at steady state (b).

an expanding 2D porous medium as described by Eq. (4.3.22).* In absence of surface evaporation, the bulk velocity exhibits a fast initial drop, but declines less rapidly in 2D at later times.†

In the presence of evaporation, the bulk velocity always reaches a finite steady state. Figure 4.7b gives the specific relationship between the steady state bulk velocity and the evaporation number for the three geometries: expanding flow from a linear source (elliptic case), 1D non-expanding flow (the LW case), and radial (polar). All three cases show similar behavior at high evaporation numbers. The steady state radial flow is greater than the other two systems by a factor of $\pi/2$ because of the larger circular inlet. For high evaporation numbers, $\mathfrak{N}_n > 10$, the bulk velocity varies as $\tilde{U}_{ss} \sim \sqrt{\mathfrak{N}_n}$, which resembles the power law for the 1D non-expanding case [see

---

* In the supplemental material, Figure E.6 gives the contour plot showing the capillary dominated and steady state regimes. † The results for the zero evaporation rate limit in Fig. 4.7a gives a more accurate physical value of the bulk velocity with time than in Figures 2.6 and 2.12. In Chapter 2, the data for the 2D elliptic was calculated from Eq. (2.3.11) which, similar to Eq. (4.3.23), did not take into account the dependence of η_f on ψ.

Eq. (4.3.28)]. In the limit of low evaporation numbers, the expanding flow cases are asymptotically similar and exhibit much higher bulk flow rates into the medium than in a non-expanding strip. This figure may be used to determine the evaporation rate required for a desired bulk velocity, and coupled with Fig. 4.4a can estimate the necessary size of the porous domain. Thus, Figures 4.4a and 4.7b together provide a practical resource for engineering and design of thin media used in driving liquids, see for example Refs. [17,21]

4.4.4 Power Law Behavior of Capillary Flows

Power law relations have played an important role in the study of wicking in porous media. Here we consider a generic coordinate system where the principal direction of flow is the y-axis and the variables are in dimensionless form to simplify the comparison of various results in the literature. We are interested in the simplest characteristic relation for capillary driven flows in porous media between the position of the liquid front, $\tilde{y}_f$, and the time of contact with the liquid, $\tilde{t}$, while potentially including evaporation effects given by the evaporation-capillary number, $\mathfrak{N}_n$.

Power law behavior was first proposed by Bell and Cameron[53] who showed experimentally $\tilde{y}_f^n \sim \tilde{t}$, where n was generally measured to be slightly greater than two for 1D non-expanding flows. In studies of capillary rise, Lucas[54] and Washburn,[55] theoretically demonstrated that the capillary wetting length varied with the square root of the time, or

$$\frac{1}{2}\tilde{y}_f^2 = \tilde{t}, \tag{4.4.1}$$

which is known as the Lucas–Washburn equation. In porous media with constant cross-section, the capillary-driven flow modeled by Green–Ampt theory[71] is related to the LW equation by considering the porous medium as capillary networks, so the LW equation is applicable in the context of porous media.[8]

Flows into porous media of higher dimensional shapes and varying cross-section can be asymptotically modeled using similar relationships. The solution of Hyväluoma *et al.*[61] shows that in the case of 2D radial expansion and large advancement of the liquid, the wet front moves with time according to

$$\frac{1}{2}\tilde{y}_f^2 \ln(\tilde{y}_f) \approx \tilde{t}. \qquad (4.4.2)$$

Similarly, the result by Xiao *et al.*[60] for capillary driven flow in a 3D spherical system indicates the asymptotic behavior for large liquid advancement is

$$\frac{1}{3}\tilde{y}_f^3 \approx \tilde{t}. \qquad (4.4.3)$$

The full 2D and 3D solutions include a second order term in $\tilde{y}_f$ similar to the LW equation which dominates the behavior at very early times.

In Sec. 4.3 above, we derived reduced solutions for the 1D and 2D capillary flows with evaporation. The first order effect of the evaporation to the Lucas–Washburn relation is given in Eq. (4.3.26),

$$\frac{1}{2}\left(\tilde{y}_f^2 + \frac{1}{4}\mathfrak{N}_n\tilde{y}_f^4\right) \approx \tilde{t}, \qquad (4.4.4)$$

where the term $\mathfrak{N}_n\tilde{y}_f^4/4$ accounts for the surface evaporation. This polynomial gives the initial evaporation effect for $\mathfrak{N}_n\tilde{t} < 1$, but is inaccurate in the steady-state limit.

For 2D expanding flows the approximate power law is [cf. Eq. (4.3.8)]

$$\frac{1}{2}\left\{\tilde{y}_f^2 \ln(\tilde{y}_f) + \frac{1}{4}\mathfrak{N}_n\tilde{y}_f^4[\ln(\tilde{y}_f)]^2\right\} \approx \tilde{t}. \qquad (4.4.5)$$

This shows the evaporation influences the frontal motion of the flow more strongly than for the 1D case because the first order evaporation term is of higher order in front position, so the initial effect of the evaporation grows more rapidly.

4.5   Conclusions

The effects of the domain geometry and evaporation from porous media on capillary flow was explored in the framework of Green–Ampt theory with potential flow. The prescribed model of evaporation from the surface of a porous medium shows several important phenomena in the time-dependent and steady state behaviors of the liquid infiltration. Capillary forces initially drive the liquid into the unsaturated medium, but the liquid advancement is slowed by the evaporation when the expansion becomes sufficiently large. A steady state is reached when the evaporation loss flux is equal to the flow by capillary imbibition of incoming liquid. A dimensionless number, termed the evaporation-capillary number, $\mathfrak{N}_n$ was introduced that reflects the relative contributions of capillary driven flow and evaporation on the overall liquid transport. The evaporation begins to slow the flow observably around $\mathfrak{N}_n \tilde{t} = 0.1$, and the fluid motion reaches steady state near $\mathfrak{N}_n \tilde{t} = 10$. An asymptotic power law behavior of evaporating liquid wicking into a 2D domain in the form $\tilde{y}_f^2 \ln(\tilde{y}_f) + \tilde{y}_f^4 [\ln(\tilde{y}_f)]^2/4 \sim \tilde{t}$ is derived for large expansions and moderate evaporation losses. The rate of volumetric flux of liquid imbibed into the medium is significantly higher for evaporation from a fanning domain shape than from a strip of constant cross section, which gives a fanning porous medium a greater capacity to drive fluids through microfluidic devices. The theory of flow behavior in an effectively two-dimensional medium presented in this paper gives a useful standard for determining to what extent a proposed domain geometry improves the bulk flow rate characteristics in an engineered porous medium.

Chapter 5

Wicking in Expanding Flow Geometries with Evaporation and Restraint by Gravity

5.1 Introduction

Several phenomena have significant effects on capillary flows in porous media including evaporation, restraint by gravity, and the geometry of the porous domain.[23] There are three modes of evaporation losses from porous materials related to the interface through which the evaporation occurs; these are normal surface, side boundary, and front interface evaporation. Each of these modes have distinct effects on the imbibition rate of liquid into dry porous media.[24] Novel technologies are being developed which make use of capillary flows to drive a reacting fluid in small microfluidic and fuel cell devices.[17,48] This requires accurate predictive models of the fluid rate of liquid advancement and bulk flow into the porous medium. In this chapter, we present the semi-analytical solutions for capillary flow in two- and three-dimensional geometries

when effected by front evaporation, side evaporation, and restraint by gravity.

The effect of the 2D polar and 3D hemi-spherical geometries on unsaturated wicking are given by Hyväluoma *et al.*[61] and Xiao *et al.*[60], respectively. These solutions and the 1D Lucas–Washburn equation[54,55] are compared in Ref.[23] along with the derived solutions expansions with flat inlets.* Phillip[59] considers the 2D and 3D expanding geometries when the capillary flow has a continuous wetting interface. In all the studies, it has been observed that a greater dimensionality of the expansion reduces the rate of advancement of the wet front, but increases the volumetric flow into the porous medium.

The modes of normal, side, and front evaporation are introduced in Ref.[24], where it was shown that the normal and side evaporation are related in the limit of large front length.† No prior work on side or front evaporation from 2D or 3D expanding flows in porous media is known. In soils the evaporation, capillarity, and gravitational effects all contribute to the moisture profile.[83,85] It is clear that the general steady state front saturation profile of a system with front evaporation is continuous and the therefore the GAT is limited to shorter times.[84,96]

Green and Ampt[71] observed that the discrete capillary front held more closely for downward infiltration than upward wicking due to pore-scale variations in capillary diffusion. Philip[59] illustrated that gravity deforms the front shape over sufficient length scales and reduces the symmetry of the front shape, which may also be shown by the contour shape of the liquid saturation of the medium.[101] Barry *et al.*[74] determined the solution of 1D imbibition in the presence of gravity in the form of the Lambert W function. This solution was reproduced in the formulation of capillary rise by Fries and Dryer.[75,76] Other work has added evaporation to the restraint gravity acting on wicking.[67,80] For sufficiently large pore sizes, the inertia affects the wetting behavior.[89] Milczarek *et al.*[102] have shown that the wetting of some granular media

---

* This is discussed in Ch. 2 and revisited in Sec. 3.4.2.   † See Ch. 3.

deviates from the LWE.

We assume the porous medium itself does not expand during wetting, the evaporation rate is a constant, and the process is isothermal. Fingering instabilities are ignored because the gravity is acting opposite to the flow.[91] Normal surface evaporation in expanding geometries has already been addressed, and is not physically relevant to fully 3D porous media.* The evaporation capillary number and modified Bond numbers signify the relative strength of the evaporation and gravity to the capillary force, respectively. In particular, we quantify the initial effect of the phenomenon on the rate of advancement of the wet front and the fluid uptake by the medium, as the Green–Ampt model is relevant for timescales smaller than steady state.

The material in this chapter is laid out as follows. In the next section, Sec. 5.2, we outline the expressions of capillary wicking with restraint by gravity and mass losses by front and side evaporation. Secs. 5.3 and 5.4 present the derivation of the general equations for 2D and 3D expanding flows, respectively. In Sec. 5.5 we discuss the simultaneous effects of the dimensionality and the restraining physics. Finally, we summarize the results in Sec. 5.6.

5.2   Governing Equations

In this section, we review the governing equations for capillary wicking in porous media with side and front evaporation and with restraint by gravity.† The potential flow formulation of Green–Ampt theory begins with the conservation of mass equation, $\nabla \cdot \mathbf{v} = 0$, or the velocity, $\mathbf{v}$, is equal into and out of a control volume. For flow in

---

* See Ch. 4.   † A more detailed discussion is given in Sec. 3.2.

porous media the velocity may be given as the gradient of a velocity potential, φ;

$$\mathbf{v} = \boldsymbol{\nabla}\varphi. \tag{5.2.1}$$

Substituting into the conservation equation

$$\nabla^2\varphi = 0. \tag{5.2.2}$$

Here we assume that there is no mass loss due to normal surface evaporation.

From the Darcy law, we may relate the internal pressure to the velocity potential $\varphi = -\frac{k}{\mu}P$, where k is the permeability, μ the viscosity, and P the pressure. Combining the capillary pressure, P_{c}, and the hydrostatic pressure, we find an expression for the velocity potential at the inlet,

$$\varphi_i = -\frac{kP_{\mathrm{c}}}{\mu} + \frac{k\rho g h_f}{\mu}, \tag{5.2.3}$$

where ρ is the density difference between the liquid and gas, g is the magnitude of the local gravity, and h_f is the correlated height of the liquid front from a given reference point. The mass balance equation at the front interface is

$$\frac{\mathrm{d}\mathbf{x}_f}{\mathrm{d}t} = [\boldsymbol{\nabla}\varphi|_{\mathbf{x}_f} - q_f\mathbf{n}_{\mathbf{x}_f}, \tag{5.2.4}$$

where $\mathbf{x}_f$ is the position of the front at time, t; q_f is the rate of loss through the front interface, and $\mathbf{n}_{\mathbf{x}_f}$ is the vector normal to the front interface. For insulated side boundaries, $[\boldsymbol{\nabla}\varphi|_{\mathbf{x}_s} = \mathbf{0}$. However, when there is evaporation occurring at the boundary,

$$[\boldsymbol{\nabla}\varphi|_{\mathbf{x}_s} = q_s\mathbf{n}_{\mathbf{x}_s}, \tag{5.2.5}$$

where q_s is the rate of loss of fluid through the side boundary. The bulk flow rate entering the medium, U, is found by integrating the velocity at the inlet

$$U = -\iint_{\mathbf{x}_i} [\boldsymbol{\nabla}\varphi|_{\mathbf{x}_i} \cdot \mathbf{n}_{\mathbf{x}_i}\,\mathrm{d}\mathbf{x}_i. \tag{5.2.6}$$
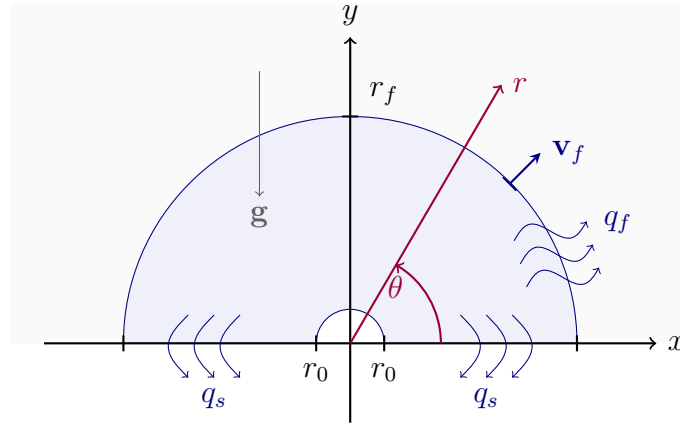
Figure 5.1. Wicking in a porous medium with 2D expanding capillary flow and evaporation through the sides and front interface with restraint by gravity.

5.3 Solutions for Two–Dimensional Expansion

Two dimensional expanding flows in porous media is most simply described by polar coordinates as given in[31]

$$x = r\cos(\theta), \tag{5.3.1a}$$

$$y = r\sin(\theta). \tag{5.3.1b}$$

Figure 5.1 shows the coordinate system as well as the layout of the porous domain.[*] The thickness of the porous medium in the z-direction, δ, is small so we only consider behavior in the plane. The gravity restrains the flow along the center axis into the half-plane of the porous domain. The liquid enters the domain through a circular inlet of radius r_0 and the domain is saturated with liquid out to the radius of the front, r_f. Side evaporation causes a loss of fluid through the sides along the x-axis at a rate of q_s and fluid is also lost through the front at a rate of q_f. A system with a flat inlet may be described by elliptic coordinates.

[*] The differential operators used are summarized in Apx. A.

5.3.1   General Derivation

Within the wetted porous domain, the mass of the liquid is conserved as indicated in Eq. (5.2.2); in polar coordinates this is

$$\frac{\partial^2 \varphi}{\partial r^2} + \frac{1}{r}\frac{\partial \varphi}{\partial r} + \frac{1}{r^2}\frac{\partial^2 \varphi}{\partial \theta^2} = 0. \tag{5.3.2}$$

The boundary conditions account for the capillary force (third equation, the side evaporation (first two equations), and the restraining force of gravity (second RHS term in third equation);

$$\left[-\frac{1}{r}\frac{\partial \varphi}{\partial \theta} \right]_{\theta=0} = -q_s, \tag{5.3.3a}$$

$$\left[\frac{1}{r}\frac{\partial \varphi}{\partial \theta} \right]_{\theta=\pi} = -q_s, \tag{5.3.3b}$$

$$\left[\varphi \right]_{r=r_0} = \varphi_0 + \frac{k\rho g}{\mu} r_f \sin(\theta), \tag{5.3.3c}$$

$$\left[\varphi \right]_{r=r_f} = 0. \tag{5.3.3d}$$

Using linear superposition, this system is solved by splitting the total velocity potential $\varphi = \xi + \gamma + \omega$, where ξ, γ, and ω are the capillary, gravity, and side evaporation potentials, respectively. It is readily shown that the capillary potential is

$$\tilde{\xi} = -\frac{\ln(\tilde{r}_f) - \ln(\tilde{r})}{\ln(\tilde{r}_f)}. \tag{5.3.4}$$

The gravity potential is more challenging because of the dependence of the non-homogenous boundary condition on θ, so the solution is a Fourier series;[*]

$$\tilde{\gamma} = -\frac{4}{\pi}\mathrm{Bo}_a\tilde{r}_f \sum_{j=1}^{\infty} \frac{1}{(2j)^2 - 1} \frac{\tilde{r}_f^{4j} - \tilde{r}^{4j}}{\tilde{r}_f^{4j} - 1} \frac{1}{\tilde{r}^{2j}} \cos(2j\theta). \tag{5.3.5}$$

---

[*] See the derivations of Eqs. (F.1.11) and (F.1.23) for the process of determining the gravity and side evaporation potentials, respectively.

Similarly, the side evaporation potential is a series

$$
\begin{aligned}
\tilde{\omega} = -2\mathfrak{N}_{\mathrm{s}} \sum_{n=1}^{\infty} & \frac{[1-(-1)^n \tilde{r}_f]\ln(\tilde{r}_f)}{n^2\pi^2 + (\ln(\tilde{r}_f))^2} \sin\left(n\pi \frac{\ln(\tilde{r})}{\ln(\tilde{r}_f)}\right) \\
& \times \left[\coth\left(n\pi \frac{\pi/2}{\ln(\tilde{r}_f)}\right)\cosh\left(n\pi \frac{\theta}{\ln(\tilde{r}_f)}\right) - \sinh\left(n\pi \frac{\theta}{\ln(\tilde{r}_f)}\right)\right].
\end{aligned}
\tag{5.3.6}
$$

The combined potential is

$$
\begin{aligned}
\tilde{\varphi} = & -\frac{\ln(\tilde{r}_f)-\ln(\tilde{r})}{\ln(\tilde{r}_f)} - \frac{4}{\pi}\mathrm{Bo}_a \tilde{r}_f \sum_{j=1}^{\infty} \frac{1}{(2j)^2-1}\frac{\tilde{r}_f^{4j}-\tilde{r}^{4j}}{\tilde{r}_f^{4j}-1}\frac{1}{\tilde{r}^{2j}}\cos(2j\theta) \\
& - 2\mathfrak{N}_{\mathrm{s}} \sum_{n=1}^{\infty} \frac{[1-(-1)^n \tilde{r}_f]\ln(\tilde{r}_f)}{n^2\pi^2 + (\ln(\tilde{r}_f))^2} \sin\left(n\pi \frac{\ln(\tilde{r})}{\ln(\tilde{r}_f)}\right) \\
& \times \left[\coth\left(n\pi \frac{\pi/2}{\ln(\tilde{r}_f)}\right)\cosh\left(n\pi \frac{\theta}{\ln(\tilde{r}_f)}\right) - \sinh\left(n\pi \frac{\theta}{\ln(\tilde{r}_f)}\right)\right].
\end{aligned}
\tag{5.3.7}
$$

In general this combined potential is precise at a given instant for only the capillary potential and either gravity or side evaporation but not both.

The velocity in the radial direction is found from the derivative of the potential,

$$
\begin{aligned}
\tilde{v}_r = \frac{1}{\tilde{r}}\Bigg\{ & \frac{1}{\ln(\tilde{r}_f)} - \frac{4}{\pi}\mathrm{Bo}_a \tilde{r}_f \sum_{j=1}^{\infty} \frac{2j}{1-(2j)^2}\frac{\tilde{r}_f^{4j}+\tilde{r}^{4j}}{\tilde{r}_f^{4j}-1}\frac{1}{\tilde{r}^{2j}}\cos(2j\theta) \\
& - 2\mathfrak{N}_{\mathrm{s}} \sum_{n=1}^{\infty} \frac{n\pi[1-(-1)^n \tilde{r}_f]}{n^2\pi^2 + (\ln(\tilde{r}_f))^2} \cos\left(n\pi \frac{\ln(\tilde{r})}{\ln(\tilde{r}_f)}\right) \\
& \times \left[\coth\left(n\pi \frac{\pi/2}{\ln(\tilde{r}_f)}\right)\cosh\left(n\pi \frac{\theta}{\ln(\tilde{r}_f)}\right) - \sinh\left(n\pi \frac{\theta}{\ln(\tilde{r}_f)}\right)\right]\Bigg\}.
\end{aligned}
\tag{5.3.8}
$$

Substituting for the front radius, we get the front velocity inside the wetted domain,

$$
\begin{aligned}
\tilde{v}_f = \frac{1}{\tilde{r}_f}\Bigg\{ & \frac{1}{\ln(\tilde{r}_f)} - \frac{8}{\pi}\mathrm{Bo}_a \sum_{j=1}^{\infty} \frac{2j}{1-(2j)^2}\frac{\tilde{r}_f^{2j+1}}{\tilde{r}_f^{4j}-1}\cos(2j\theta) \\
& - 2\mathfrak{N}_{\mathrm{s}} \sum_{n=1}^{\infty} \frac{(-1)^n n\pi[1-(-1)^n \tilde{r}_f]}{n^2\pi^2 + (\ln(\tilde{r}_f))^2} \\
& \times \left[\coth\left(n\pi \frac{\pi/2}{\ln(\tilde{r}_f)}\right)\cosh\left(n\pi \frac{\theta}{\ln(\tilde{r}_f)}\right) - \sinh\left(n\pi \frac{\theta}{\ln(\tilde{r}_f)}\right)\right]\Bigg\} - \mathfrak{N}_{\mathrm{f}}.
\end{aligned}
\tag{5.3.9}
$$

The bulk velocity is

$$
\tilde{U} = \int_0^\pi \frac{1}{\ln(\tilde{r}_f)} - \frac{4}{\pi} \mathrm{Bo}_a \tilde{r}_f \sum_{j=1}^\infty \frac{2j}{(2j)^2 - 1} \frac{\tilde{r}_f^{4j} + 1}{\tilde{r}_f^{4j} - 1} \cos(2j\theta)
$$

$$
- 2\mathfrak{N}_\mathrm{s} \sum_{n=1}^\infty \frac{n\pi \left[1 - (-1)^n \tilde{r}_f\right]}{n^2\pi^2 + (\ln(\tilde{r}_f))^2} \left[\coth\left(n\pi \frac{\pi/2}{\ln(\tilde{r}_f)}\right) \cosh\left(n\pi \frac{\theta}{\ln(\tilde{r}_f)}\right) - \sinh\left(n\pi \frac{\theta}{\ln(\tilde{r}_f)}\right)\right] \mathrm{d}\theta.
$$

$$(5.3.10)$$

Without side evaporation and gravity, the bulk velocity is simply

$$
\tilde{U} = \frac{\pi}{\ln(\tilde{r}_f)}.
\tag{5.3.11}
$$

This is valid for front evaporation because that is accounted for only in the front velocity equation and therefore does not directly affect the bulk velocity.

5.3.2   Front Evaporation

When we reduce the full front equation (5.3.9) to only capillary flow and front evaporation, $\mathrm{d}\tilde{r}_f/\mathrm{d}\tilde{t} = 1/[\tilde{r}_f \ln(\tilde{r}_f)] - \mathfrak{N}_\mathrm{f}$, the equation can be put into integral form

$$
\int_1^{\tilde{r}_f} \frac{\tilde{r}_f \ln(\tilde{r}_f)}{1 - \mathfrak{N}_\mathrm{f} \tilde{r}_f \ln(\tilde{r}_f)} \, \mathrm{d}\tilde{r}_f = \tilde{t}.
\tag{5.3.12}
$$

The integral in the left hand side is not analytic. But we may expand the integral to the first order evaporation term,

$$
\frac{1}{2} \tilde{r}_f^2 \ln(\tilde{r}_f) + \mathfrak{N}_\mathrm{f} \frac{1}{3} \tilde{r}_f^3 \left[\ln(\tilde{r}_f)\right]^2 \approx \tilde{t}.
\tag{5.3.13}
$$

The velocity equation reduces in the steady state for pure front evaporation to

$$
\tilde{r}_{f,\,\mathrm{ss}} \ln(\tilde{r}_{f,\,\mathrm{ss}}) = \frac{1}{\mathfrak{N}_\mathrm{f}}.
\tag{5.3.14}
$$

5.3.3 Gravity

From Eq. (5.3.9), the first order effect of the gravity on the capillary flow along the x-axis (orthogonal to the gravity vector) is

$$\frac{\mathrm{d}\tilde{r}_f}{\mathrm{d}\tilde{t}} = \frac{1}{\tilde{r}_f \ln(\tilde{r}_f)} + \frac{16}{3\pi}\mathrm{Bo}_a \frac{1}{\tilde{r}_f^2} \qquad (5.3.15)$$

Conversely, along the y-axis (opposite to gravity)

$$\frac{\mathrm{d}\tilde{r}_f}{\mathrm{d}\tilde{t}} = \frac{1}{\tilde{r}_f \ln(\tilde{r}_f)} - \frac{16}{3\pi}\mathrm{Bo}_a \frac{1}{\tilde{r}_f^2}. \qquad (5.3.16)$$

We see that along the x-axis the gravity is increasing the flow rate, but is decreasing it along the front. When we assume that the gravity has not yet deformed the front shape, *i.e.* the front radius is independent of θ, the entire gravity term goes to zero in the integral for the bulk velocity from Eq. (5.3.10). So, the gravity cannot be having any influence on the bulk flow if there is no curvature to the front shape.

5.3.4 Side Evaporation

When gravity is dropped and the front shape is assumed to be constant with θ, the bulk velocity simplifies from the integral into the form,

$$\tilde{U} = \frac{\pi}{\ln(\tilde{r}_f)} - 4\mathfrak{N}_\mathrm{s} \sum_{n=1}^{\infty} \frac{[1 - (-1)^n \tilde{r}_f] \ln(\tilde{r}_f)}{n^2\pi^2 + (\ln(\tilde{r}_f))^2}. \qquad (5.3.17)$$

5.4 Solutions for Three–Dimensional Expansion

Similarly to the 2D-like porous medium discussed in the previous section, we now have a porous medium of a half space domain with a hemispherical inlet of radius r_0, as shown in Fig. 5.2. Gravity restrains the flow with magnitude g in the negative z-direction, which is normal to the plane of the half-space. Evaporation flux through
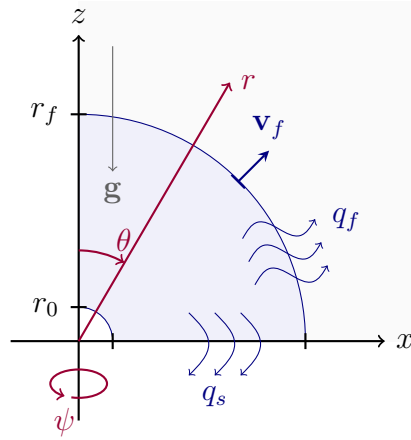
Figure 5.2. Wicking in a porous medium with 3D expanding capillary flow and evaporation through the front interface.

the sides occurs with magnitude q_s and evaporation also occurs through the front at a rate q_f. The front length, r_f, is the distance that the liquid has reached into the domain.

This system is naturally described by spherical coordinates system as defined by[31]

$$x = r \sin(\theta) \cos(\psi), \tag{5.4.1a}$$

$$y = r \sin(\theta) \sin(\psi), \tag{5.4.1b}$$

$$z = r \cos(\theta). \tag{5.4.1c}$$

For a half-space with a flat, circular inlet one may alternatively use oblate spheroid coordinates.*

---

* See Apx. A for further details on these coordinate systems which were also used in Ch. 2.

5.4.1 General Derivation

The Laplace equation for the velocity potential within the wetted region is

$$\frac{\partial^2 \varphi}{\partial r^2} + \frac{2}{r}\frac{\partial \varphi}{\partial r} + \frac{1}{r^2}\frac{\partial^2 \varphi}{\partial \theta^2} + \frac{\cot(\theta)}{r^2}\frac{\partial \varphi}{\partial \theta} = 0. \tag{5.4.2}$$

The boundary conditions are of the form,

$$\left[-\frac{1}{r}\frac{\partial \varphi}{\partial \theta}\right]_{\theta=0} = 0, \tag{5.4.3a}$$

$$\left[\frac{1}{r}\frac{\partial \varphi}{\partial \theta}\right]_{\theta=\frac{\pi}{2}} = 0, \tag{5.4.3b}$$

$$[\varphi]_{r=r_0} = \varphi_0 + \frac{k\rho g}{\mu} r_f \cos(\theta), \tag{5.4.3c}$$

$$[\varphi]_{r=r_f} = 0. \tag{5.4.3d}$$

The total velocity potential is split up into the capillary and gravity potentials, respectively, $\tilde{\varphi} = \tilde{\xi} + \tilde{\gamma}$. The capillary potential is

$$\tilde{\xi} = -\frac{\tilde{r}_f - \tilde{r}}{\tilde{r}_f - 1}\frac{1}{\tilde{r}}. \tag{5.4.4}$$

The gravity potential is*

$$\gamma = -\mathrm{Bo}_a \tilde{r}_f \sum_{n=0}^{\infty} \frac{(-1)^n (4n+1)}{(2n-1)(2n+2)} \frac{(2n)!}{2^{2n}(n!)^2} \frac{\left(\frac{\tilde{r}_f}{\tilde{r}}\right)^{2n+1} - \left(\frac{\tilde{r}}{\tilde{r}_f}\right)^{2n}}{\tilde{r}_f^{2n+1} - \tilde{r}_f^{-2n}} \mathrm{P}_{2n}(\cos(\theta)). \tag{5.4.5}$$

The side evaporation potential is

$$\tilde{\omega} = -2\mathfrak{N}_s \sum_{n=1}^{\infty} \frac{n\pi\left[(-1)^n \tilde{r}_f^{3/2} - 1\right]}{(n\pi)^2 + \left[\ln\left(\tilde{r}_f^{3/2}\right)\right]^2} \frac{\mathrm{P}_{n\pi/\ln(\tilde{r}_f)-1/2}(\cos(\theta))}{[n\pi/\ln(\tilde{r}_f)+1/2]\,\mathrm{P}_{n\pi/\ln(\tilde{r}_f)+1/2}(0)} \frac{\sin\left(n\pi\frac{\ln(\tilde{r})}{\ln(\tilde{r}_f)}\right)}{\sqrt{\tilde{r}}}. \tag{5.4.6}$$

---

* See the derivations of Eqs. (F.1.34) and (F.1.46) for details.

Recombining the separated potentials

$$
\tilde{\varphi} = -\frac{\tilde{r}_f - \tilde{r}}{\tilde{r}_f - 1}\frac{1}{\tilde{r}} - \mathrm{Bo}_a\tilde{r}_f \sum_{n=0}^{\infty} \frac{(-1)^n(4n+1)}{(2n-1)(2n+2)}\frac{(2n)!}{2^{2n}(n!)^2}\frac{\left(\frac{\tilde{r}_f}{\tilde{r}}\right)^{2n+1} - \left(\frac{\tilde{r}}{\tilde{r}_f}\right)^{2n}}{\tilde{r}_f^{2n+1} - \tilde{r}_f^{-2n}}\,\mathrm{P}_{2n}(\cos(\theta))
$$

$$
- 2\mathfrak{N}_s \sum_{n=1}^{\infty} \frac{n\pi\left[(-1)^n\tilde{r}_f^{3/2} - 1\right]}{(n\pi)^2 + \left[\ln\left(\tilde{r}_f^{3/2}\right)\right]^2}\frac{\mathrm{P}_{n\pi/\ln(\tilde{r}_f)-1/2}(\cos(\theta))}{[n\pi/\ln(\tilde{r}_f) + 1/2]\,\mathrm{P}_{n\pi/\ln(\tilde{r}_f)+1/2}(0)}\frac{\sin\left(n\pi\frac{\ln(\tilde{r})}{\ln(\tilde{r}_f)}\right)}{\sqrt{\tilde{r}}}.
$$

$$(5.4.7)$$

Differentiating the potential in the radial direction,

$$
\tilde{v}_r = \left(\frac{\tilde{r}_f}{\tilde{r}_f - 1}\right)\frac{1}{\tilde{r}^2} + \mathrm{Bo}_a\frac{\tilde{r}_f}{\tilde{r}} \sum_{n=0}^{\infty} \frac{(-1)^n(4n+1)}{(2n-1)(2n+2)}\frac{(2n)!}{2^{2n}(n!)^2}\frac{(2n+1)\left(\frac{\tilde{r}_f}{\tilde{r}}\right)^{2n+1} + 2n\left(\frac{\tilde{r}}{\tilde{r}_f}\right)^{2n}}{\tilde{r}_f^{2n+1} - \tilde{r}_f^{-2n}}\,\mathrm{P}_{2n}(\cos(\theta))
$$

$$
- \mathfrak{N}_s \sum_{n=1}^{\infty} \frac{n\pi\left[(-1)^n\tilde{r}_f^{3/2} - 1\right]}{(n\pi)^2 + \left[\ln\left(\tilde{r}_f^{3/2}\right)\right]^2}\frac{\mathrm{P}_{n\pi/\ln(\tilde{r}_f)-1/2}(\cos(\theta))}{[n\pi/\ln(\tilde{r}_f) + 1/2]\,\mathrm{P}_{n\pi/\ln(\tilde{r}_f)+1/2}(0)}\frac{\frac{2n\pi}{\ln(\tilde{r}_f)}\cos\left(n\pi\frac{\ln(\tilde{r})}{\ln(\tilde{r}_f)}\right) - \sin\left(n\pi\frac{\ln(\tilde{r})}{\ln(\tilde{r}_f)}\right)}{\tilde{r}^{3/2}}.
$$

$$(5.4.8)$$

Including the front evaporation effect, the front velocity is

$$
\tilde{v}_f = \frac{\mathrm{d}\tilde{r}_f}{\mathrm{d}\tilde{t}} = \frac{1}{\tilde{r}_f^2 - \tilde{r}_f} - \mathfrak{N}_f + \mathrm{Bo}_a \sum_{n=0}^{\infty} \frac{(-1)^n(4n+1)^2}{(2n-1)(2n+2)}\frac{(2n)!}{2^{2n}(n!)^2}\frac{\mathrm{P}_{2n}(\cos(\theta))}{\tilde{r}_f^{2n+1} - \tilde{r}_f^{-2n}}
$$

$$
- 2\mathfrak{N}_s \frac{1}{\tilde{r}_f^{3/2}\ln(\tilde{r}_f)} \sum_{n=1}^{\infty} \frac{(n\pi)^2\left[\tilde{r}_f^{3/2} - (-1)^n\right]}{(n\pi)^2 + \left[\ln\left(\tilde{r}_f^{3/2}\right)\right]^2}\frac{\mathrm{P}_{n\pi/\ln(\tilde{r}_f)-1/2}(\cos(\theta))}{[n\pi/\ln(\tilde{r}_f) + 1/2]\,\mathrm{P}_{n\pi/\ln(\tilde{r}_f)+1/2}(0)}.
$$

$$(5.4.9)$$

The bulk velocity is taken from the radial velocity at the inlet

$$
\tilde{U} = 2\pi \int_0^{\pi/2} \left(\frac{\tilde{r}_f}{\tilde{r}_f - 1} + \mathrm{Bo}_a\tilde{r}_f \sum_{n=0}^{\infty} \frac{(-1)^n(4n+1)}{(2n-1)(2n+2)}\frac{(2n)!}{2^{2n}(n!)^2}\frac{(2n+1)\tilde{r}_f^{2n+1} + 2n\tilde{r}_f^{-2n}}{\tilde{r}_f^{2n+1} - \tilde{r}_f^{-2n}}\,\mathrm{P}_{2n}(\cos(\theta))\right.
$$

$$
\left. - 2\mathfrak{N}_s \frac{1}{\ln(\tilde{r}_f)} \sum_{n=1}^{\infty} \frac{(n\pi)^2\left[(-1)^n\tilde{r}_f^{3/2} - 1\right]}{(n\pi)^2 + \left[\ln\left(\tilde{r}_f^{3/2}\right)\right]^2}\frac{\mathrm{P}_{n\pi/\ln(\tilde{r}_f)-1/2}(\cos(\theta))}{[n\pi/\ln(\tilde{r}_f) + 1/2]\,\mathrm{P}_{n\pi/\ln(\tilde{r}_f)+1/2}(0)}\right)\sin(\theta)\,\mathrm{d}\theta.
$$

$$(5.4.10)$$

Without gravity and side evaporation, the bulk velocity simplifies to,

$$\tilde{U} = 2\pi \frac{\tilde{r}_f}{\tilde{r}_f - 1}. \tag{5.4.11}$$

This is also applicable to front evaporation.

5.4.2 Front Evaporation

The equation reduces to $\mathrm{d}\tilde{r}_f/\mathrm{d}\tilde{t} = 1/(\tilde{r}_f^2 - \tilde{r}_f) - \mathfrak{N}_\mathrm{f}$, which in integral form is,

$$\int_1^{\tilde{r}_f} \frac{\tilde{r}_f^2 - \tilde{r}_f}{\tilde{r}_f^2 - \tilde{r}_f - \frac{1}{\mathfrak{N}_\mathrm{f}}} \, \mathrm{d}\tilde{r}_f = -\frac{\tilde{t}}{\mathfrak{N}_\mathrm{f}} \tag{5.4.12}$$

Expanding the integral in powers of $\tilde{r}_f$, we find the early time first order perturbation of the front evaporation is

$$\frac{1}{3}\tilde{r}_f^3 + \mathfrak{N}_\mathrm{f}\frac{1}{5}\tilde{r}_f^5 \approx \tilde{t}. \tag{5.4.13}$$

At large times we readily find the front evaporation steady state is

$$\tilde{r}_{f,\mathrm{ss}}^2 - \tilde{r}_{f,\mathrm{ss}} = \frac{1}{\mathfrak{N}_\mathrm{f}}, \tag{5.4.14}$$

or for $\mathfrak{N}_\mathrm{f} \ll 1$, $\tilde{r}_{f,\mathrm{ss}} \approx 1/\sqrt{\mathfrak{N}_\mathrm{f}}$. Unlike with the solution in polar coordinates, there is an analytic expression for the integral. So the implicit solution for the capillary flow with front evaporation is

$$(\tilde{r}_f - 1) + \ln(1 - \mathfrak{N}_\mathrm{f}(\tilde{r}_f - 1)\tilde{r}_f)$$
$$- \frac{2(1 + 1/\mathfrak{N}_\mathrm{f})}{\sqrt{4/\mathfrak{N}_\mathrm{f} + 1}} \left[\tanh^{-1}\left(\frac{2\tilde{r}_f - 1}{\sqrt{4/\mathfrak{N}_\mathrm{f} + 1}} \right) - \tanh^{-1}\left(\frac{1}{\sqrt{4/\mathfrak{N}_\mathrm{f} + 1}} \right) \right] = -\frac{\tilde{t}}{\mathfrak{N}_\mathrm{f}}. \tag{5.4.15}$$

However, this solution is cumbersome, and we use the differential equation for analysis instead.

5.4.3 Gravity

The reduced solution of the bulk velocity for constant radius is,

$$\tilde{U} = 2\pi \left(\frac{\tilde{r}_f}{\tilde{r}_f - 1} - \frac{\mathrm{Bo}_a}{2} \frac{\tilde{r}_f^2}{\tilde{r}_f - 1} \right) \tag{5.4.16}$$

Unlike in the 2D case, this shows that the bulk velocity does depend on the gravity even when the gravity is not yet perturbing the front shape.

5.4.4 Side Evaporation

Similarly, when we assume that the front radius is independent of θ, we find an expression for the bulk velocity with side evaporation;

$$\tilde{U} = 2\pi \left[\frac{\tilde{r}_f}{\tilde{r}_f - 1} - \mathfrak{N}_s \sum_{n=1}^{\infty} \frac{n\pi \left[(-1)^n \tilde{r}_f^{3/2} - 1 \right]}{(n\pi)^2 + \left[\ln\left(\tilde{r}_f^{3/2} \right) \right]^2} \frac{\mathrm{P}_{n\pi/\ln(\tilde{r}_f)-3/2}(0) - \mathrm{P}_{n\pi/\ln(\tilde{r}_f)+1/2}(0)}{[n\pi/\ln(\tilde{r}_f) + 1/2] \, \mathrm{P}_{n\pi/\ln(\tilde{r}_f)+1/2}(0)} \right]. \tag{5.4.17}$$

This complex formula must be computed numerically to find useful information.

5.5 Results

5.5.1 Power Law Analysis

Front Evaporation

We may now consider front evaporation from a wetting interface moving in a medium of constant cross section.* We may contrast with the front evaporation effect with

---

* Here we are expanding the full 1D front evaporation capillary flow solution given in Eq. (3.3.32).

that of the normal surface evaporation.[*]

$$\frac{1}{2}\tilde{L}^2 + \mathfrak{N}_f\frac{1}{3}\tilde{L}^3 \approx \tilde{t}. \tag{5.5.1}$$

The first order effect of the front evaporation is cubic in the front length, while for normal evaporation the front length is to the fourth power; this indicates the front evaporation effects the capillary flow at an earlier time than for normal surface evaporation. As derived above in Eq. (5.3.13), with two dimensional radial expansion the lowest order effect of the evaporation is described by,

$$\frac{1}{2}\tilde{r}_f^2 \ln(\tilde{r}_f) + \mathfrak{N}_f\frac{1}{3}\tilde{r}_f^3 \left[\ln(\tilde{r}_f)\right]^2 \approx \tilde{t}. \tag{5.5.2}$$

For front evaporation we have uniform front shape in the radial direction. From Eq. (5.4.13), we have the power law for 3D radial capillary flow with front evaporation,

$$\frac{1}{3}\tilde{r}_f^3 + \mathfrak{N}_f\frac{1}{5}\tilde{r}_f^5 \approx \tilde{t}. \tag{5.5.3}$$

In all these cases, it appears that the first order evaporation term is one polynomial order lower than for the normal surface evaporation. This means that generally the front evaporation begins to affect the flow sooner, but that steady state is not reached as quickly.

Restraint by Gravity

The effect of the restraint of gravity on the liquid for media with constant cross section is similar to front evaporation;[†]

$$\frac{1}{2}\tilde{L}^2 + \mathrm{Bo}_a\frac{1}{3}\tilde{L}^3 \approx \tilde{t}. \tag{5.5.4}$$

The other power law behaviors for gravity and side evaporation are more difficult to determine because of the inherent series solution, usually of trigonometric functions.

---

[*] The power-laws for capillary flows and capillarity with normal evaporation are detailed in Sec. 4.4.4.   [†] As noted with Eq. (3.3.27).

Also, the power laws are not the same along the center axis of the flow versus along the side boundary. Thus, we will not discuss any further power series.

5.6   Conclusions

A significant amount of prospective work remains to be carried out on the theory of evaporation effects in capillary wicking. The general time-dependent behaviors need to be compared to the described theory. Analysis on the steady states front deformity of some models is needed. To the authors knowledge, no experiments have been conducted on the systems analyzed in this chapter. On earth's surface the gravitational effect may be significant enough to prohibit experiments on 3D side evaporation. As it is known that restraining gravity causes a more diffuse wetting front, some experiments need to be carried out constraining the applicability of the GAT-based 2D and 3D models above. Some physical challenges are posed to the front evaporation methodology used in this paper due to the effect that evaporation has on the capillary via capillary condensation, such that GAT may hold for a short time. Furthermore, each of these different phenomena should be investigated through the framework of partially saturated capillary wetting via the Richards equation. Some of these effects may be best understood via continuum simulations of partially saturated flow, or through three dimensional pore-scale computational models of two phase flow.

Front evaporation, side evaporation, and restraint by gravity affect the behavior of capillary flows in two and three-dimensional porous domains in distinct ways from normal surface evaporation and each other. The front evaporation effects the flow at an earlier time than normal evaporation, but takes longer to reach steady state. The restraint by gravity opposite to the central axis of the flow slows the flow in the center of the flow, but increases flow along the side boundaries. Side evaporation does the opposite, where the center axis is insignificantly effected by the evaporation, but the

front along the side boundaries goes to a steady state.

Chapter 6

Pitting Corrosion at Al-AlO$_3$ Interface

6.1 Introduction

The failure of aluminum mechanical parts due to corrosion demands significant further advancements in the understanding of species transport in the pitting corrosion process. Lattice Boltzmann methods can be used to investigate the transport of species through irregular sub-surface pores, with solid degradation and electrochemical effects. In this chapter, we present reduced computational models which help to improve understanding of the interworking physical and chemical mechanisms in the aluminum corrosion process for the purpose of providing insights on prevention and repair.

In many ways, corrosion is the cancer of materials—nearly insignificant damages suddenly lead to catastrophic failure of an entire system. Corrosion costs American organizations on the order of $60 billion per year in maintenance and repair of damaged vehicles and machinery. The United States military estimates that approxi-

mately 20% of their maintenance costs are directly related to corrosion. Corrosion is a frequent cause of mishaps for aircraft, ships, and land vehicles across the globe. Aluminum corrosion in particular is a significant economic drain in the aircraft industry and other light-weight metals applications such as fast naval vessels. Improvements in materials design and treatment techniques have the potential to increase the lifespan of such aircraft mechanical parts.[46]

Pitting corrosion leading to stress corrosion cracking in aluminum is a frequent cause of failure due to material fatigue. Pitting corrosion is an electrochemical reaction which slowly etches away aluminum from the bulk of the material under cracks located below the protective aluminum oxide surface.[103] In wet or humid environments, a liquid film may form over surface imperfections, so the corrosion rate is a function of vapor phase conditions such as humidity, pressure, and temperature. Salt in the film significantly increases the degradation rate via the action of hydrochloric acid in the micropore accelerating the dissolution of aluminum.[45] The electrolytes further accelerate the transport of the aluminum ion through diffusiophoresis. As the aluminum ion approaches the atmospheric boundary of the film, oxygen absorbed into aqueous phase precipitates the ions into a buildup of aluminum oxide normally outside the micropore. Thus, the aluminum ion concentration profile, and thereby the dissolution rate of the metal, is a function of the electrolyte conditions such as salt concentration, pH, pressure, temperature, and solvated oxygen.

When sufficiently large pits are formed due to corrosion or impact, both the mechanical strains on the metal as well as the chemical degradation may interact to induce stress corrosion cracking (SCC) along the crystal grain boundaries of the metal.[104] As the corrosion process continues, the excess solvated hydrogen ions in the micropore cause hydrogen embrittlement of the aluminum metal.[45,105] This describes a common pathway through which corrosion accelerates material fatigue.*

---

* In Apx. H we briefly cover some preliminary work of modeling SCC.

Corrosion can also be caused by microbial decomposition of the metals—both steel and aluminum—such as has been observed with the sunken H.M.S. Titanic. However, we focus only on chemical mechanisms of corrosion and the physical phenomena influencing the transport of species effecting the aluminum degradation reactions occurring near the surface.

Corrosion is a chaotic process which involves coupled chemical reactions, diffusion, surfaces features and chemistry, solid mechanics, and other nonlinear phenomena. Thus, self-consistent, full-scale computational models of corrosion are computationally challenging to find sensible, repeatable results. Ideally, all phenomena involved in the corrosion process should be done through *ab initio* simulations with only given atomic principles and a minimum of adjustable parameters, but scaled to the time and length scales involved in corrosion. Naturally, a single computational model is impractical both now and for the foreseeable future. Quantum density functional models of local atomic configurations can be used to accurately determine molecular scale behaviors. From this data, quantum-trained molecular dynamics simulations may be done on the small grain material physics, surface chemistry, and fluid properties to feed into the lattice Boltzmann method (LBM). In this configuration, the LBM would be applied to view mesoscale behaviors of the fluid transport processes and limitations which govern some of the physical and chemical interactions occurring at the small scales. Returning this information back to the molecular scale model would allow iteration of physical constraints between these methods to mutually improve the results demonstrated by each method. When the results have converged to giving regular statistics, the results could be compared with experimental data to determine if the statistically predicted pit growth rate matches.

In this chapter, we present models of several key transport phenomena involved in the corrosion process as the basis for future work in the multiscale computational analysis described above. We use the lattice Boltzmann method to illustrate some of

the emergent system asymmetries which develop from the physical transport mechanisms of multiphase condensation and electrokinetic effects in a corroded pit. We also investigate important chemical processes involved in the degradation of the aluminum such as the reaction in the fluid which solvates the aluminum ion and the resulting material loss to the solid metal. In future, each of these methods may be combined into a pore-scale holistic multiphysics model of the pit corrosion process. Through these models, we observe some elementary insights into the transport limitations involved in the aluminum corrosion process.

In the following section, we outline the computational methods used. In section 6.3, we present several simplified models of transport phenomena in pitting corrosion with a discussion of the simulation results. Section 6.4 discusses future work and the conclusions.

6.2   Methods

The lattice Boltzmann method is a mesoscale fluids model especially applicable to discrete porous domains. The method is a discretized form of the Boltzmann gas kinetic equation which arose through advancements in lattice gas cellular automata. Additional phenomena can easily be added to the LBM for the analysis of transport in corroding and porous systems.*
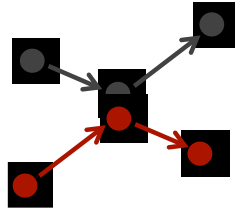
Figure 6.1. Motion of gaseous particles.

6.2.1 The Lattice Boltzmann Method

The Boltzmann Equation

The Boltzmann equation (BE) is a statistical description of the motion of particles through the distribution function of particles in the phase state, $f(t, \mathbf{x}, \mathbf{p})$, at given time, t, positions, $\mathbf{x}$, and momenta, $\mathbf{p}$;[10,12]

$$\left[\partial_t + \mathbf{v} \cdot \partial_\mathbf{x} + \mathbf{F}^{\text{ext}} \cdot \partial_\mathbf{p}\right] f = \int (f_{1'} f_{2'} - f_1 f_2)\, g\sigma(g, \Omega)\, \mathrm{d}\Omega\, \mathrm{d}\mathbf{p}_2, \tag{6.2.1}$$

where $\mathbf{v}$ is the velocity, $\mathbf{F}^{\text{ext}}$ any external force acting on the individual particles, Ω the solid angle of the collisions, g is the magnitude of the difference between the momenta, and σ is the collision cross section. At the mesoscale, the equation describes the collective effects of particles with differing momenta moving, coming into contact, and scattering while preserving the conservation laws of mass, momentum, and energy as exemplified in Figure 6.1. The left side of the equation is the advection term which describes the undisturbed movement of the gas-like particles in space, and the right side of the equation describes the collisions between particle pairs. For low velocity flows, the collision integral of the Boltzmann equation may be simplified to the deviation of the distribution function from the statistical equilibrium distribution or $-(f - f^{\text{eq}})/\tau$, which is referred to as the Bhatnagar–Gross–Krook (BGK) collision operator; this is commonly used with the LBM.[106]

---

* For more extensive background and details on the implementations of the LBM, see Apx. C.

The Boltzmann and the lattice Boltzmann equations (which we discuss below) both bridge atomistic and continuum scales.[13] At the molecular scale, the Liouville equation describes the phase state of every individual particle in a given system.[9] The Boltzmann equation is readily found by integrating over a given control volume and limiting the series approximation of possible collisions. Both the BE and LBE recover the Navier–Stokes equations through the Chapman–Enskog expansion in the continuum limit.[107] Thus, the Boltzmann equation is more detailed description than the Navier–Stokes equations from a physical perspective.[30]

The Lattice Boltzmann Equation

The lattice Boltzmann method was developed to overcome computational difficulties of the Lattice Gas Cellular Automata (LGCA) method, which tracked the advection and collisions of individual gas-like particles restricted to lattice points and discrete velocities based on simple automated rules.[13] Both methods share the simple idea of discretizing the velocity space into a very small number of discrete velocities in a hydrodynamically consistent manner.[108] The physical space, limited by these discrete velocities, becomes a lattice for all points $\mathbf{x}$ in the simulation. The LBM is related to the LGCA in much the same manner that the Boltzmann equation builds on the Liouville equation; the LBM deals with statistical groups of particles (the distribution functions) while LGCA treats individual particles in the computation, averaging the statistical or macroscopic properties later.[109]

The lattice Boltzmann equation (LBE) with the BGK approximation (or the LBGK equation) is,[110]

$$f_\alpha(\mathbf{x} + \mathbf{e}_\alpha \delta_t, t + \delta_t) = f_\alpha(\mathbf{x}, t) - \frac{f_\alpha(\mathbf{x}, t) - f_\alpha^{\mathrm{eq}}(\mathbf{x}, t)}{\tau}, \qquad (6.2.2)$$

where f_α^{eq} is the equilibrium distribution function calculated from a quadratic approximation of the Maxwell–Boltzmann distribution, δ_t is the time step size, and τ is the
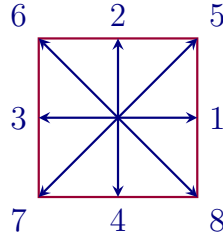
Figure 6.2. Two-dimensional discrete velocities of the D2Q9 lattice Boltzmann model.

relaxation time. The LBE governs the updating of the local distribution functions on the lattice by moving particles in the direction of their momenta each time step (*i.e.* the streaming step, LHS), while it also corrects the local deviation from equilibrium to relax the distribution functions (*i.e.* the collision step, RHS). The local density of the fluid is calculated as the zeroth velocity moment or sum of the local distribution functions, $\rho = \sum f_\alpha$, and the velocities are calculated through the first velocity moment, $\mathbf{j}$, of the distribution functions, where $\mathbf{u} = \frac{1}{\rho} \sum f_\alpha \mathbf{e}_\alpha$. The viscosity of the fluid is accounted for with relaxation time through the relation $\tau = \nu/c_s^2 + 1/2$, where c_s is the lattice sound speed.[111]

Implementation

Among the common computational methods in engineering, the lattice Boltzmann method presents a superior practical option for pore scale simulations. The simplicity of the lattice grid for the LBM is beneficial for ease of programming the computational domain. Figure 6.2 illustrates the nine discrete velocity vectors (the zeroth index vector is no velocity) of the D2Q9 LBM model, which is the standard model used for simulation of fluids in two-dimensional domains.[111] This common implementation of the LBE is second order in space and in time, where the time steps are restricted to small values relating to the pre-set value of the relaxation time.[13] Ultimately, this has

the effect of forcing the simulation to run for shorter timescales. Therefore, while the spatial resolution may increase and be readily parallelized, total time steps cannot be decreased, and thus many time dependent LBM simulations require ample time to run.

Within the lattice, the LBM computes the distribution functions locally and communication between the nodes only occurs during the streaming step. From this localization, solid nodes are easily implemented at any given point with the bounce back boundary condition, $f_{\alpha'} = f_{\alpha}^*$, where momentum is reflected instead of accepted from neighboring fluids. This allows any location to be solid or liquid indiscriminately with almost no extra computational cost and makes the method highly practical for modeling amorphous materials including porous media.

There are several common boundary conditions for the LBM.* The periodic boundary condition extends the streaming of the distribution functions back to the opposite sides of the domain as if the system is a torus or an infinite array of identical domains.[111] The Zou and He pressure and velocity BCs are derived from the conserved moments of the distribution functions and by assuming quasi-equilibrium.[112,113] Open outlet BCs are set by copying the distribution function from the neighboring column or row into the boundary node.

In this chapter, we assume that the length and time scales as well as the strength of the other phenomena are sufficiently large such that gravity may be ignored. All computational methods are carried out in lattice units and are not converted into dimensional units. As a result the timescales observed in some simulations are likely shorter for the action of a given physical phenomenon than would be the case in the ordinary unit systems for the corrosion model. However, given the appropriate physical constants and lattice conversion scales, the data in other physical variables may be converted from the original lattice units.

---

* The LBM boundary conditions are further outlined in Apx. C.2.3.

6.2.2 Additional Physical Models

Simulating pitting corrosion in the lattice Boltzmann method requires several additional physical and chemical phenomena to be incorporated into the methods to account for the primary complexities of the system. In particular, we are interested in multiphase models of the thin liquid film over the pore, the chemical processes involved in the dissolution of the metal, and the effects of the electrochemistry on the solute transport. The literature provides a number techniques to coupling the LBM with the required phenomena.* We conducted these simulations in MATLAB® instead of a compiled computational language to give flexibility in the process of building the new methods.

In humid environments a thin film may spontaneously condense over the pit. The condensation process may be modeled as a multiphase flow with surface adhesion. The Shan and Chen LBM uses a "pseudo-potential" to determine the density of the fluid, where the fluid is attracted to itself and liquids form as high densities.[114] Martys and Chen extend the model to include attractive forces between the solids and the liquids, resulting in sponaneous capillary wetting phenomena.[115,116] We have implemented these methods from the descriptions given in Sukop and Thorne.[111]

The loss of material from the metal is an interactive chemical process of multiple species. There are several multispecies transport methods for the LBM; we use the passive solute method, which is applicable to dilute species in a concentrated or liquid solvent.[111] The Yoshino and Inamuro modified boundary conditions are applied to improve the behavior of source conditions within the domain. We augment these LB multispecies methods with chemical reactions of any order by preserving the moments of the reaction collision operator.[116,117] We also represent reactive solid surfaces as a portion of the domain in which the reaction rate is dramatically higher in the solution

---

* These methods are discussed with more details and example tests of the method in Apx. C, sections C.2.4 and C.3.1–C.3.4.

when the lattice point is near solid lattice nodes then for nodes only surrounded by liquid nodes. An alternative model by Succi *et al.*[118] hybridizes the LBM with a Lax–Wendroff finite difference method to account for species reactions in solution.

The growth of the subsurface pit is modeled by a reaction-like dissolution process at the surface nodes of the metal. In the dissolution process, solid nodes progressively turn from solid to fully liquid. To account for this change, we must track the mixed phase state of the node and the rate of change between phases. For the variable solid content, we use the partial permeability LBM discussed in Sukop and Thorne[111] which both streams and bounces back quantities of the fluid based on the effective permeability of the node. For the receding solid surface, we devised a quadratic relation between the permeability and solid fraction. In this model, the solid is converted to liquid via a reaction equation which is a function of a limiting saturation concentration of the aluminum ion and the species saturation of the neighboring nodes. From this, the calculated fractional solid loss and the known density of the solid, the increase in solvated state concentration is computed via a mass balance. The neighboring nodes are accounted via an automatic rule to allow the dissolution to progress deeper into the metal as solid nodes turn completely to liquid. The solid oxide is simulated as a non-dissolving, ordinary bounce-back solid. Unlike the reactions described above, this dissolution process is independent of any other species in the solvent; this would be a useful future improvement to the model. Kang *et al.*[119,120] describes a similar surface dissolution reaction methods.

In electrolyte ion solutions, the Poisson equation governs the electric potential and the Boltzmann charged particle distribution describes the ions in the solution, resulting in the Poisson–Boltzmann equation.[121] This equation may be recast into a time dependent diffusion equation and solved on a D2Q9 lattice, resulting in a technique known as the lattice Poisson–Boltzmann Method (LPBM) which solves an LBE-like expression for the charge interactions.[122] The electric potential is found via the LPBM

and couples with the LBE via the force term and affects the fluid motion when an electric field is applied across the domain. We have developed an implementation of Wang's LPBM for coupled electrokinetic flows.[123] Other electrochemical models may be used with the LBM, including calculation of the electric potential through the known concentration of charged species.[124] The surface charge of the aluminum oxide layer also affects the charge in solution and can be more realistically computed via a charge regulating boundary conditions instead of the common Dirichlet condition.[125]

6.3   Results

In this section, we present the results of the several models of pitting corrosion discussed above.

6.3.1   Asymmetric Pitting Condensation

The corrosion process is accelerated by aqueous environments, which often form by direct fluid contact or through condensation of saturated vapor. Figure 6.3 shows the progression of condensation into an elliptic subsurface pit with narrow neck inlet and periodic boundary conditions. Initially, the domain is filled with super-saturated fluid—in other words, in the spinodal or two phase region of the phase diagram—with slight perturbations in the density to nucleate condensation (Fig. 6.3a). The fluid preferentially condenses onto the surfaces except in the middle of the pit where a droplet forms (b). Soon the droplet fully wets the inner wall and effectively trapped a bubble on the bottom of the pit (c). Although the simulation does not include gravity, the bubble rises and moves to the left to minimize the surface free energy of the system because the pit is slightly horizontally oblongated (d). In some simulations,

(a) Initial fluid density.

(b) Early condensation stage.

(c) Late condensation stage.

(d) Migrated bubble.
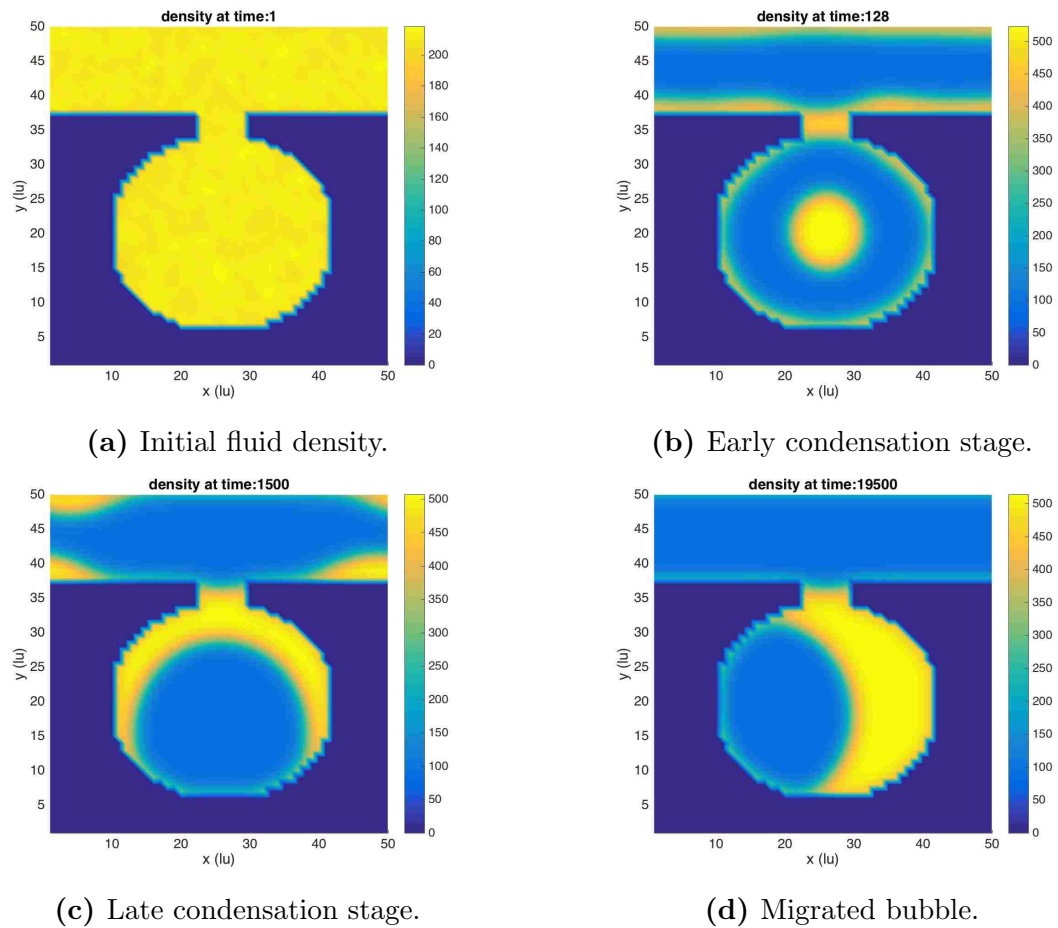
Figure 6.3. Condensation in a sub-surface pit. Lighter colors indicate higher fluid density: yellow is liquid, light blue or turquoise is gas, and dark blue is solid (no fluid).

the bubble goes both to the left and others to the right. Thus, we have observed an asymmetric behavior of the system arise purely as a result of the initial pressure perturbations.

(a) Velocity profile.

(b) Reactant concentration.

(c) Early product concentration.

(d) Developed product concentration.
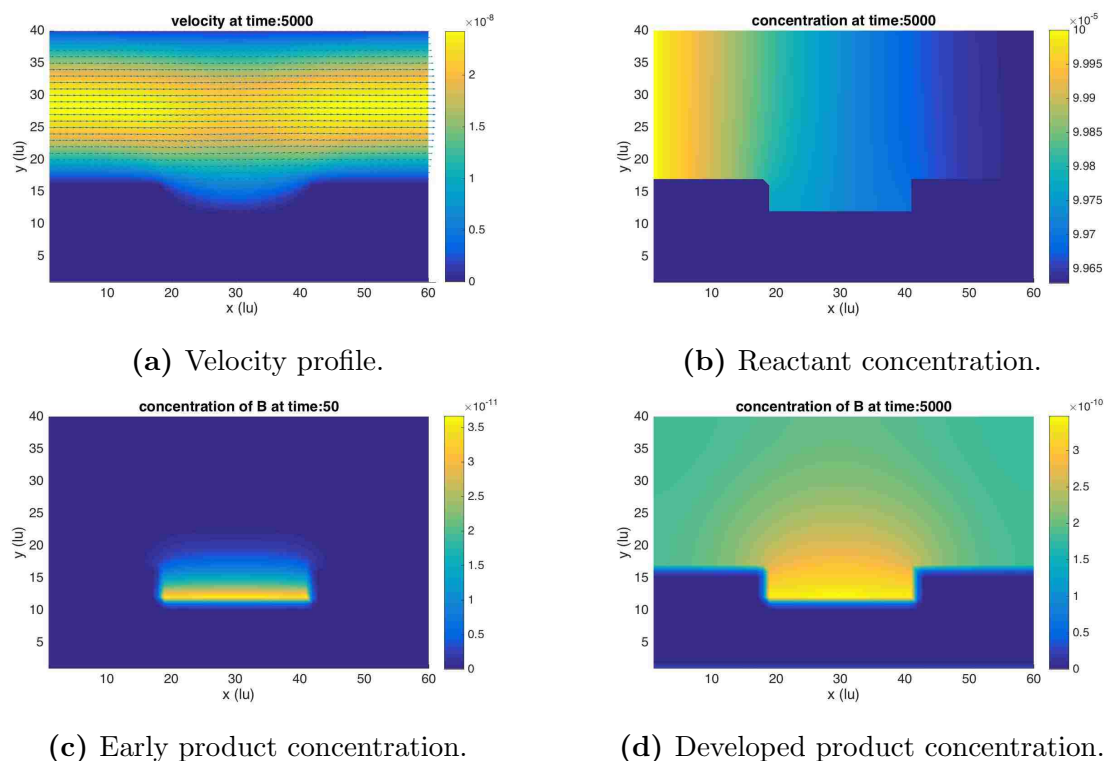
Figure 6.4. Surface reaction simulation of aluminum ion production in solution.

6.3.2   Reacting Transport Model of Solvating Aluminum

The dissolution of the aluminum metal is a function of the ionic species in the bulk fluid. In Figure 6.4 we consider the concentration of hydroxide ion and aluminum hydroxide ion as the $Al(OH)_3$ slowly builds up in the solution. A slow flow of bulk fluid moves from left to right (Fig. 6.4a), bringing with it the hydroxide ion at a pH of about 10 (b). An insignificant concentration gradient of OH^- is visible due to the density gradient over the total system from the compressibility of the LBM. A small nick in the oxide layer exposes some of the aluminum metal and generates the aluminum hydroxide ion at the surface as it is slowly reacted with the hydroxide (c). The two-species reaction model is driven by an effectively third order reaction which

(a) Initial ion concentration.

(b) Intermediate concentration.

(c) Concentration in developed pit.

(d) Initial phase state.

(e) Early pitting.

(f) Developed pit.
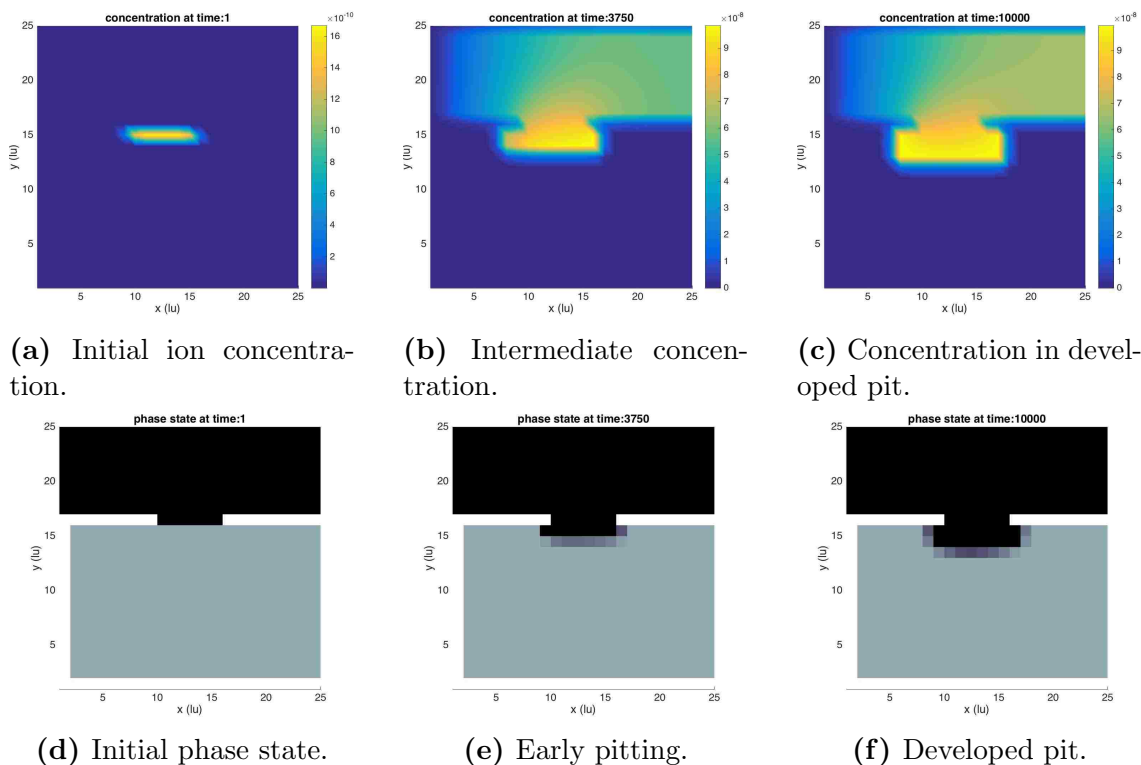
Figure 6.5. Solid dissolution process on an aluminum metal surface using a saturated ionic species limited model. Fluid shown in black, aluminum metal in gray, and oxide shown in white.

is intrinsically slow and not diffusion limited. However, we observe the aluminum ion disperse in the fluid and build up its concentration over time (d). This shows the importance of coupled interactions between the ions for the dissolution modeling.

6.3.3 Surface Dissolution and Degradation

The key interest in the simulation of the pitting corrosion process is the rate at which the metal is lost. In Figure 6.5, we apply the reaction-dissolution model to the early progression of a dissolving pit. In this model we have the bulk fluid and one explicitly tracked solute species, the dissolved metal ion. The fluid flows from left to right over

the surface which is mostly covered by the oxide and does not dissolve, and a shallow nick in the surface exposes a small amount of the pure aluminum metal (Fig. 6.5d). Initially, the bulk contains no dissolved ion except at the aluminum surface where a small amount of metal has been lost in the first time step (a). The dissolution rate is a function of solute concentration in fluid phase and is limited by the saturation concentration of the ion. So, we observe that the concentration of solute upstream is lower than for portions of the pit which are down-stream (b). This leads to faster degradation in the pit upstream (e). Thus, concentration differences near the surface change the dissolution rate of the solid and the dissolution progresses asymmetrically due to the flow of liquid in the bulk. As the corrosion progresses further, the flow over the pit affects the transport near the dissolving surface to a lesser degree and the ion is at saturated concentration almost uniformly over the exposed metal surface (c). This slows the over-all progression of the dissolution as the reaction becomes limited by the rate at which the ion can leave the mouth of the pit and reduces the rate of asymmetric growth (f).

6.3.4   Electrokinetic Transport in a Developed Pit

Electrolyte solutions involved in the pitting corrosion process have distinctive and important effects on aqueous solute transport. Figure 6.6 shows the lattice Poisson–Boltzmann simulation of the electric potential and the resulting electrokinetic flow. In Figure 6.6a, the LPBM-based potential in the small subsurface pit is computed for a pit with oxide layer over the entire surface. This is the result of the ion configuration due to the surface potential of the oxide and develops an electric double layer observed over the entire surface of the metal. When an electric field is applied across the domain from bottom left to upper right, this field interacts with the charged fluid near the surface to drive the electrokinetic flow shown in Figure 6.6b. In a corroding pit, a net electric field could be induced by the oxidation-reduction reaction across the cathodes
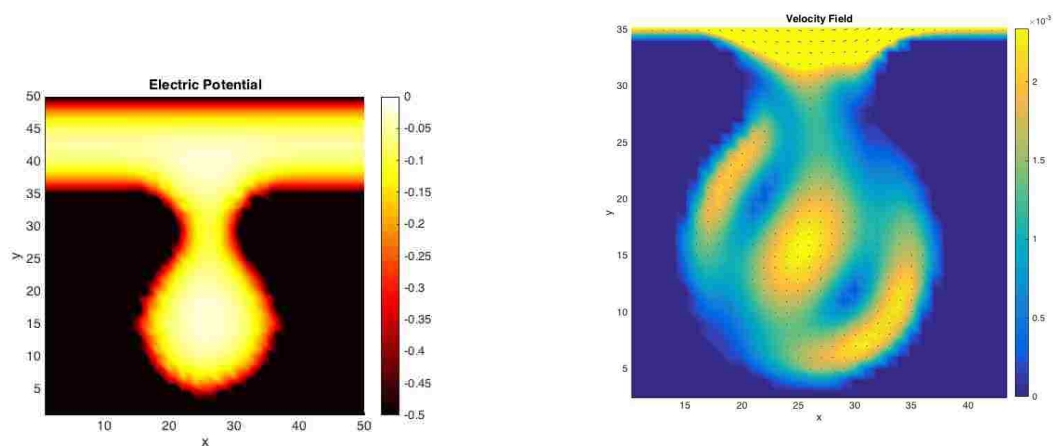
(a) Electric potential.

(b) Fluid velocity.

Figure 6.6. Electric field driven flow of brine. Electric field is imposed from upper left to lower right.

and anodes. In this case, we observe that the liquid in the pore swirls because of the induced flow. On the upper left and bottom right of the pit walls, the fluid flows down and to the left. However, these flows curve into each other near the bottom left of the pit and then swirl back around, resulting in the double vortex within the pit.

Changing the electric field from diagonal (as it is in Figure 6.6) to lateral (right to left) causes the fluid in the pit to flow in a single vortex as shown in Figure 6.7. The fluid motion due to the induced surface potential in the bulk and from the charged upper portion of the pit causes the fluid in the pit to move in a counter-clockwise vortex. However, at the very bottom of the pit the electric field effect on the ionic electric potential causes flow in the clockwise direction which resists the vortex of flow from the rest of the fluid.

As seen in both simulations, the electric field may significantly enhance transport in the pit. Furthermore, the location of the anodes and cathodes of the oxidation and reduction reactions can cause further asymmetry in the pitting due to the induced
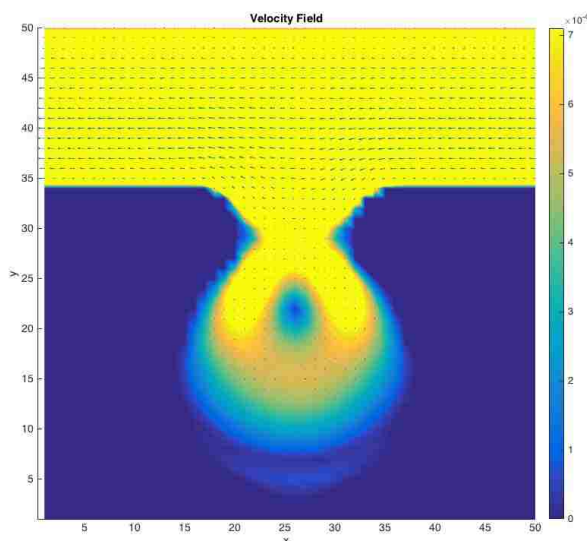
Figure 6.7. Lateral electric field driving swirling flow of brine in a developed pit.

ionic motion.

6.4 Conclusions

The long-term goal of this project is to model the progression of a corroding pit with all the essential transport processes and thereby to suggest methods of pit mitigation. All of the physical models discussed in the results above are important in the full system model. With further development, the combination of the methods will produce more relevant and useful models of the corrosion process in the aluminum subsurface pore. The implementations of each of the physical phenomena may be verified with analytical solutions or, in more complicated cases, finite element methods and would thus improve minor flaws in the current methodology. The methods may be further translated into a compiled computer language for numerical scalability and

efficiency, including a two-dimensional parallel decomposition of the domain. These improvements will allow the simulations to run for larger time and length scales. This compiled lattice Boltzmann code may be developed out of the numerical methods already built for analysis of biporous media as discussed in the following chapter.

Furthermore, several enhancements to the physical models will increase the scope of the analysis. Firstly, we can track the set of relevant species that is involved in the common corrosion process such as water, hydrogen and hydroxide ions, salt ions, aluminum hydroxide, aqueous oxygen, solid aluminum and aluminum oxide. The solvated ions experience significant electrochemical transport phenomena such as chemiosmotics, diffusiophoresis, and surface charge. This will require a revised electrochemical potential model beyond the LPBM, which calculates the electric potential based on the concentration of ionic species. From this full model of the chemistry, we desire to build fully coupled, first principles reaction models of the dissolution and precipitation in and around the pit. The whole process should accurately account for the reduction and oxidation reactions and their electrochemical effects on the flow. This will improve our understanding of the important rates and key dimensional scales involved in the process. On the whole, we would like to know how the electrolytes and electrokinetics accelerate or stabilize the corrosion process.

In conclusion, the work in this chapter has illustrated several techniques for investigating aluminum corrosion. The lattice Boltzmann method is a simulation technique which offers flexible approaches to numerous fluid processes and works with many of the important physics at the porescale. In some of the simulations, we observed how asymmetries in the system may develop due to underlying fluid and species process. In particular, random initial density fluctuations perturbing a supersaturated fluid caused condensation in the subsurface pit to form bubbles which migrate to one side or the other of the pit. Also, fluid motion over a pit undergoing dissolution can drive a higher material loss on the upstream side of the dissolving solid. Finally, we have

shown how an electric field may cause flows within the pit due to the motion of the ions in solution.

Chapter 7

Fluid Transport in Bimodal Porous Media

7.1 Introduction

Bimodal porous media is an emerging area of experimental and theoretical research. Biporous media are materials with two distinct internal pore sizes and have potential application in catalysts,[27] drug delivery,[18,126] and chemical separations.[127] Theoretical modeling is still largely in its infancy and the effective permeabilities of the media are not well understood. Of particular importance are the relationships between the different internal pore sizes, their relative fractions in the medium, and their interconnectivity. It is anticipated that each of these parameters influence the bulk fluid motion through the medium.

Recent work by Carroll, *et al.*[1] demonstrated a useful method for producing microspheres with two distinct internal pore sizes. This biporous material has pore sizes on the order of 5 nm and 50 nm (see figure 7.1a), where the distinct pores are a result of micro-emulsion templating in solutions before the particle is solidified. An

(a) Pore radius
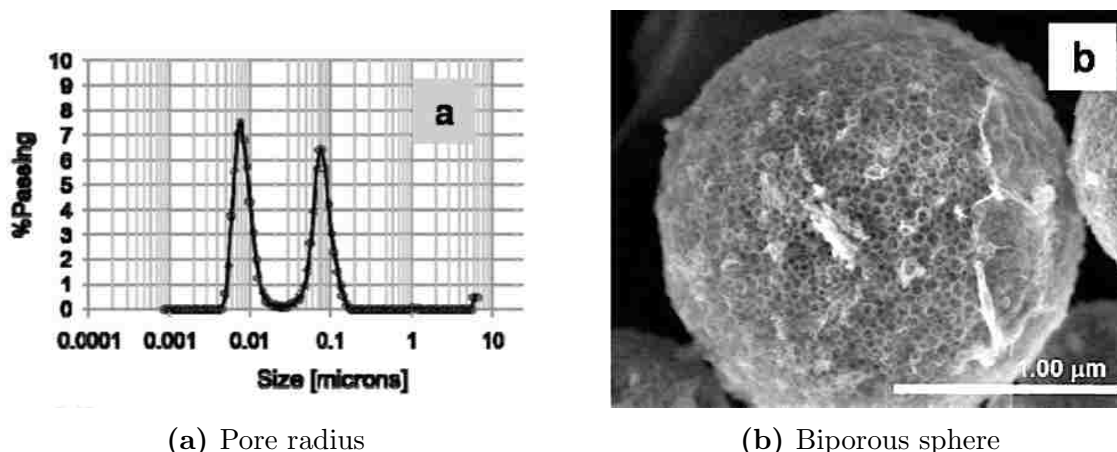
(b) Biporous sphere

Figure 7.1. Bimodal porous spherical particles. (Ref[1])

example particle is shown in figure 7.1b. Using a 'lost wax' technique these particles may be implanted with platinum for catalysts.[1,27] Additionally, these spheres may potentially be produced into monodisperse spheres using microfluidic devices and settled into a packed bed to further create a larger third level of porosity in the system.[128] Spherical porous particles are well-established as important materials in modern catalyst systems such as packed beds and slurries, and are being intensively researched for medical use in targeted drug-delivery.* A key relationship implicit in the continuum modeling of a porous medium is the connection between permeability with the pore radius, porosity, tortuosity an interconnectivity. The coefficient of permeability is a crucial material parameter in porous media models because it is the dominant term in determining the bulk fluid motion through the media over a given pressure drop. This is a complex system-dependent interaction; however, some experimental and algebraic models do exist.[8] It will suffice to observe that generally, as porosity (the volume of the object which is porous for liquid propagation) and pore radius increase, the permeability will also increase.

Understanding the species transport properties in bidisperse media will impact

---

* See also Figure 1.1e.

design and optimization. The relationship between the permeability and the pore size and tortuosity is well understood for monoporous materials, but has not yet received extensive treatment for biporous media and is especially unexplored for fluid transport on length scales nearing Knudsen diffusion (*i.e.*, molecular scale). Exploring the transport effects in this complex physical regime will enable better design and analysis of nano-porous structures.

The focus of this chapter is to analyze a computational tool which has practical and scalable application to the modeling of bimodal porous media used in engineering applications. The lattice Boltzmann method presents a very practical means of modeling the solid domain while still preserving the mesoscopic behavior of the fluid. We have produced a LBM code which is able to model two-dimensional biporous domains of arbitrary shaped solids.* The physical pore geometry of the particles of interest may be mimicked using internal pores of two distinct sizes.

The Darcy law approximates the pressure to volumetric flux through a porous medium with a linear permeability.[5,8] The applicability of the continuum porous flow approximation may be extended with Brinkman and Forschheimer terms.[20,129,130] These equations essentially retain additional terms of the Navier–Stokes equation in averaged porous media form.† Discrete porous media are also analyzed through other means. For example, the Kozeny–Carman equation gives the exact analytical expression for flow through a single pore with a driving pressure gradient.[56] The Darcy number for the porous particles as well as the Reynolds number for the flow help to characterize the fluid system.[131]

In the following section we summarize the methods used for computation, particularly the parallelization of the lattice Boltzmann method. Sec. 7.3 gives the results of simulation of biporous media and the parallel code, and Sec. 7.4 outlines areas for

---

* Some details on mono-disperse discrete pore modeling of 2D and 3D particles using finite element methods are given in Apx. I.   † For other details see Sec. I.2.

potential work and the conclusions.

7.2 Methods

7.2.1 Lattice Boltzmann Code

We have implemented the lattice Boltzmann method in the C++ compiled computer language with periodic boundary conditions from all sides of the domain.* The fluid is driven by gravity to simplify the structure and implementation of the code. The code has been functionalized and designed with parameter input capabilities, debugging, and final data output for post-processing. This code may be further augmented with additional physical methods to increase the applicability to kinds of biporous media applications (see Section 7.4 below).

Solid Lattice Domains

The great benefit of the LBM is the intrinsic flexibility in handling amorphous solid domains, which makes it widely applicable to porous materials. Several of the simulation domains (Figures 7.2a–c) were digitally hand-sketched and then converted into solid-liquid domain grids.These domains are all used for the scaling tests.

Biporous simulation domains were developed with slightly randomized sizes for the large and small pores and potentially a macro-particle. For example, the domain shown in Figure 7.2d was automatically generated in MATLAB®. Here, the large pores are placed in a hexagonal grid of circles with random size in a Gaussian distribution with a limit on maximum size (half the distance between the hexagonal lattice sites). The hexagonal layout mimics the natural close-packing of the spherical voids. The

---

* See Sec. 6.2.1 for the overview of the LBM with further details in Apx. C.

(a) $n = 50$

(b) $n = 100$

(c) $n = 200$

(d) $n = 200$
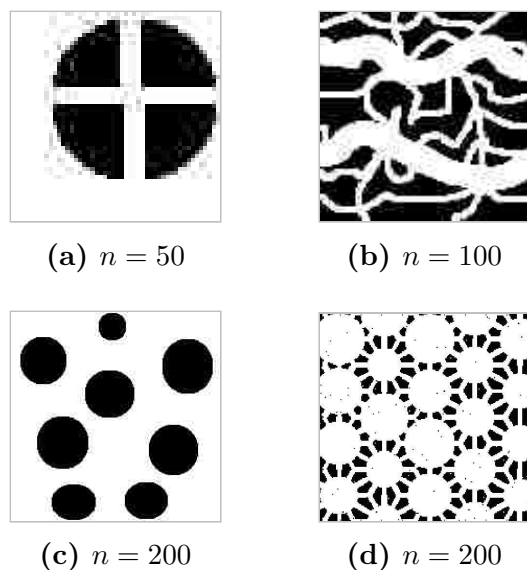
Figure 7.2. Square porous domains of width and length n used in scaling tests.

small pores are approximately a tenth the size of the large ones and twelve of them radiate out from the center of the large pores to connect with other large pores. To create a biporous particle, with larger domains the solid points can be removed outside a set particle radius, as shown for example in Figure 7.4 below. The particle radius is also chosen from a Gaussian distribution with a mean of approximately ten times greater than the large pores. Lastly, a small amount of random solid noise (on the order of one in every one thousand nodes) is peppered into the domain to mimic other small scale heterogenous behaviors may occur in a physical porous medium. This method generates a physically motivated 2D cross-sectional model of the 3D biporous particle. The particle would have approximately 5 nm small pores, 50 nm large pores, and would be about 500 nm in radius—all of these specifications corresponding to reasonable values observed with the real particles produced in the laboratory.[1]

7.2.2 Parallel Computation

Parallel programming allows computational resources to be used more efficiently by assigning portions of the problem to different processors. In general this significantly reduces the time a given problem takes to solve and conversely allows much bigger problems to be posed.

There are four central program design paradigms in modern parallel computing.[132] First, there are serial codes which execute a problem sequentially and entirely on a single processor. In some cases, a single serial application may be scripted to run multiple problems simultaneously on different processors, where each problem run is assigned to a different problem. This is a form of parallelism but is not a classical paradigm and is not used here.

Second, distributed memory parallelization is when the application itself is written such that different parts of the problem may be assigned a specific processor and the processor has its own allocated memory to store the data in for the sub-problem. Each of these processors communicate with each other via messages as prescribed by the program. The modern standard for distributed memory implementation are the Message Passing Interface (MPI) library functions.

Third, shared memory is similar to the distributed memory, except that the processors are all assumed to be working from the same set of memory and therefore explicit communication between processors is not required. This is very helpful in modern multi-core computers which commonly have 4–8 processors; however care must be taken in designing these codes to prevent processors from over-writing other processors work. Furthermore, shared memory on CPUs does not scale well beyond 32 processors, and for most applications is used on a smaller number. Common implementations of shared memory include OpenMP and pThreads. The pThreads is more customizable than OpenMP, but OpenMP is much easier to add to an existing

serial code.

Finally, graphics processing units (GPUs) are a designated processing component, separate from the central processing unit (CPU), that often has the ability to do numerous simple operations in a similar way to shared memory. Numerous computational methods, including LBM, have been ported to GPUs, however this generally requires a significantly different program design from CPU-based codes and will not be done with our codes because of the large resource investment in redevelopment. Hybrid parallelization methods may make use of a combination any two or more of the different paradigms.

There are several concepts used to analyze the performance of a parallel algorithm. Naturally, the time taken for a given problem to be computed is the central focus. Less time taken in parallel means that the problem is *scaling* with parallelization. When a given problem is parallelized and broken up across different processors the time it takes to run the parallelized program versus the original serial program is referred to as *strong scaling*. The case where the problem size itself is increased to match the number of processors is referred to as *weak scaling*.[132]

MPI Implementation

We are interested in optimizing a LBM code on large-scale distributed memory super-computers with shared memory multi-core processors in the individual compute nodes. The first step to accomplishing this is to incorporating the Message Passing Interface (MPI) into the LBM code because it should scale well with problem size for a 1D or 2D processor domain decomposition. Thus, the functions in the code were modified so that the processors only work on the local data within the boundaries for their cells. The streaming step of the LBE computation required communication of boundary conditions between computational cells. The communication was done

(a) Equal size decomposition **(b)** Optimized histogram decomposition
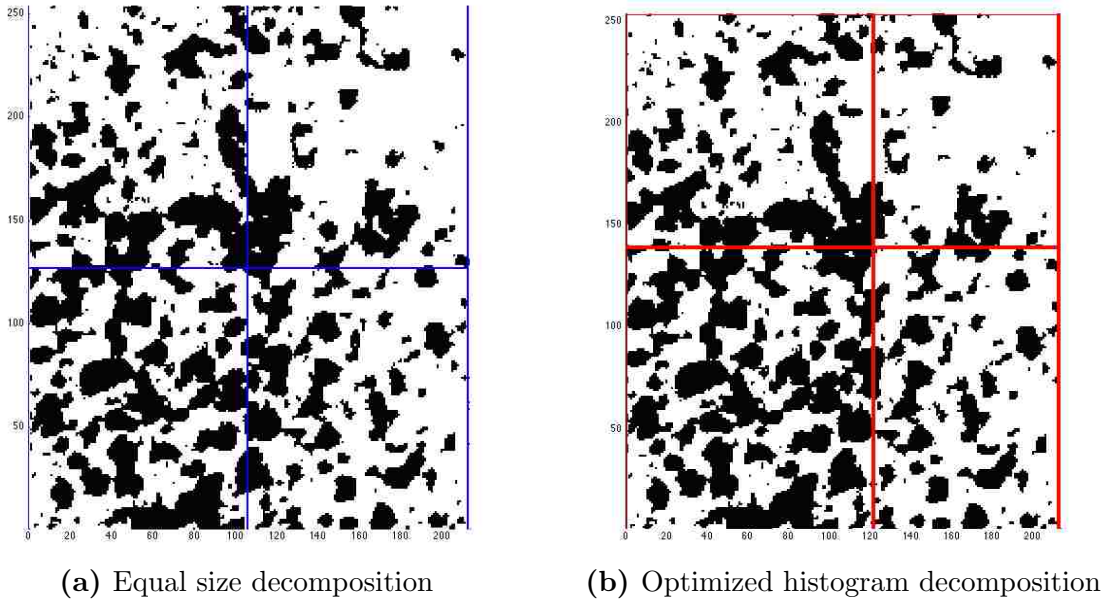
Figure 7.3. Parallel domain decomposition example

with blocking send and receive in step between neighboring cells and cells connected through the periodic boundary conditions in the same order as the lattice velocities, *e.g.* right first, above second, *etc* for the zeroth processor. This limits the number of processors along each dimension of the decomposition to even values, *i.e.* the total number of processors must be a multiple of four.

To further optimize the MPI method, we designed domain decomposition algorithm to pre-optimize the size of the sub-domains owned by each processor as is illustrated in Figure 7.3. Fig. 7.3a shows the domain split into four equal areas, each to be distributed to a single processor. In Figure. 7.3b the grid lines have been shifted such that processors with domains which are mostly solid gain more of the domain to even out the load. Because many possible domains may be weighted more heavily on one side or another due to inhomogeneities in the porous medium it was approximated that the liquid lattice sites cost 30 times more operations than the solid. From the optimized boundary lines, the computed domains were pre-set at beginning of

simulation. This was done by computing the histogram of fluid nodes from both x and y directions and then iterating the processor boundary locations such that these histograms were as nearly equally split in total area as possible. This histogram method allowed the boundaries to be iterated in each direction by simple rules. The method has not been compared to simulations using the naive approach of a simply gridded domain. This simple iterative method sets the values of the lattice domain edges which yield a more nearly even load balance.

OpenMP Implementation

The ultimate purpose in adding OpenMP to the numerical methods, is to conserve memory in a distributed memory system with multi-core nodes. Ideally, this would take advantage of the processors to naturally load balance and to reduce communication costs which would be necessary in a large-scale distributed memory simulation. This type of parallelization is also generally helpful for optimizing an already parallel code in machines with nodes of multiple cores or for some basic scale-up on a small machine with several cores. However, it is not as versatile as MPI.

The OpenMP shared memory capabilities are incorporated into the code through relatively simple and straightforward compiler flags which tell the compiler what parts can be run in parallel.[132] The majority of the computation of the lattice Boltzmann equation involves for-loops over the lattice sites, with all computation local to each lattice node. In this case the OpenMP flags have been added to the for-loop directly. The streaming step, where fluid is advected from one point to another, is the portion of the computation with interaction of computer memory between the lattice cells, and therefore is parsed into a three-banded routine with blocking between the bands to prevent over-writing of data from different threads. This may slow down the computation, but prevents data being overwritten by separate cores accessing and writing the data simultaneously.

Computational Speedup and Scaling

Speedup data is calculated from the raw timing data taken on specific machines for each test. First, the average runtime per cell per time step is calculated for each number of processors;

$$\hat{t}_p = \frac{\text{runtime}_p}{n^2 \, t_{\text{final}}}, \tag{7.2.1}$$

then the speedup was computed based on the speed of a single processor;

$$\text{speedup}_p = \frac{\hat{t}_p}{\hat{t}_1}. \tag{7.2.2}$$

This allows for comparison of algorithm performance and efficiency. Ideal speedup is when the measured speedup is the same as the number of processors.[133]

7.3   Results

7.3.1   Serial LBM

Anisotropic Flow

Figure 7.4 shows the result of one of the largest domains run on the C++ serial LBM code. The simulation demonstrates that the highest flow regions through an automatically generated biporous particle are near the edges of the particle, with significantly less flow through the center. This stems from the much higher velocity fluid flow around the outer edges of the particle and from the much higher viscous resistance of the thicker porous medium through the middle. Due to the periodic boundary conditions this model is effectively like a square packed bed of these particles, which is why the flow at the top and bottom of the domain is much greater. In effect it appears that only about an eighth to a sixth of the particle volume has significant
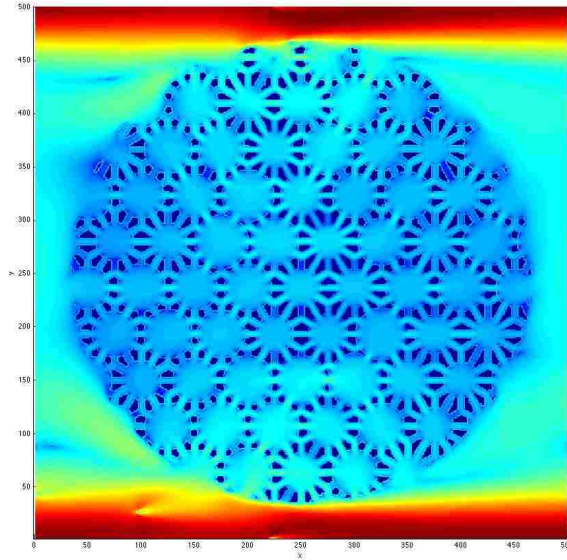
Figure 7.4. 2D LBM of biporous structure on a 500 by 500 grid. Fluid velocities shown in half-log, half-linear scale, where blue to yellow shows exponential increase in velocity, and yellow to red relates to linear increase.

flow through it. In this porous domain, the fluid flowing through the particle must always go through the small pores, bringing it into close contact with the pore surfaces, which is good for surface reactions.

Runtime

In figure 7.5 the runtime of the serial code is shown with differing sizes of edge lengths. The runtime of the serial code scales as approximately $n^{3.26}$ where n is the edge length in lattice units. This calculation may be higher than ideal as extra calculation and saving was being done on saving data during the simulation. However, there is also likely some factor of difficulty due to memory access issues for the larger domains. This scaling is somewhat worse than the anticipated n^3 for a two-dimensional sim-
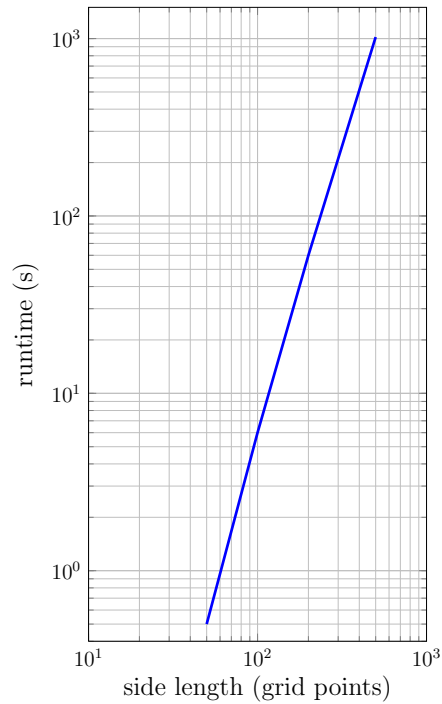
Figure 7.5. Runtime of serial lattice Boltzmann code to time of convergence

ulation, and this makes it more difficult to perform weak scaling tests of the code with good certainty. There is also the possibility this extra one-third factor is due to the extra number of time steps which the simulation takes to reach the convergence criterion. Because of this increase in cost with domain size, it is clear that for larger scale simulations the code needs to be parallelized to run the separate portions of the domain more quickly.

(a) Scaling of MPI LBM code   **(b)** Scaling of OpenMP LBM code
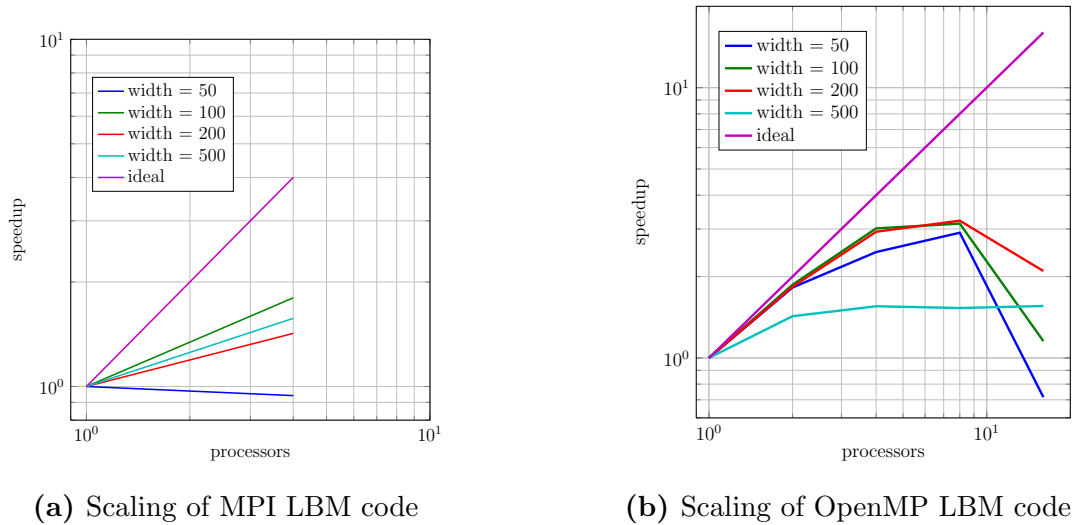
Figure 7.6. Parallel scaling of prototype lattice Boltzmann code.

7.3.2   Parallel LBM

MPI

Our current LBM MPI implementation has only had a small amount of strong scaling tests conducted on it. The parallel domain decomposition is limited to square arrangements of 4 or 16 processors due to data communication restraints. For the present the code has only been compiled on a machine with 8 cores, so we will simply compare a 4 processor set of runs with the MPI code to a similar serial version. In Figure 7.6a we observe that there is a minor improvement of the speedup for the 100–500 size runs. The 50×50 system likely is doing poorly due to too much communication overhead. The 100×100 domain is scaling the best with a 1.80 speedup for 4 processors; this is not a very significant improvement. It is encouraging that the 500 run is very close behind, though the 200 being slower than both seems anomalous. which is not near the benefits needed to run on around 100 processors with reasonable scaleup. On the data side, one concern with these runs is that the number of conver-

gence steps is slightly different for the MPI code from the serial; this is not the case with OpenMP implementation and does not make sense from a physical standpoint.

OpenMP

As shown in Figure 7.6b, the size 500 run does not have as much speedup as the other runs of size 50–200. It is suspected that the arrays are too large to fit in cache which leads to numerous expensive memory accesses due to the cache misses, however this is not as detrimental for the larger number of processors. Another noticeable feature of the graph is the fact that the 50, 100, and 200 runs drop massively in speedup at 16 processors. This is likely due to the fact that multithreading may be occurring and that the machines used likely do not have 16 processors. However, the 500 may already be maxed on the cache or memory access speeds so much that the multithreading does not slow the run down further. The max speedup achieved was 3.22 which was done on the size 200 run with 8 processors. However, this is only about a 40% efficiency which is not a good argument for implementing these more complicated algorithms.

Thus, we have demonstrated the capability to parallelize a lattice Boltzmann code which is a first step in preparing for large-scale simulations. Neither of these parallel codes performs ideally and require further optimization to improve their speed.*

7.4   Conclusions

In the future additional physical capabilities should be coupled with the current fluid flow methods to make the make the simulations become suitable to the full range of physics desired for this application. Firstly, the biporous models may be advanced

---

* Both parallel scaling tests of the MPI and OpenMP were run on UNM Department of Computer Science machines.

by varying the particle sizes, pore size distributions, and greater interconnectivity of the larger pores. Multiple particles may then be laid in square or hexagonal lattices of varying particle size. To further extend the physical analysis of the fluid system we can add pressure and velocity boundary conditions to compare the results more directly to Darcy's law. Porous media flows are most commonly driven by pressure differences across the flow domain and constant pressure boundary conditions may alternatively be applied on both sides of the domain to simulate this difference. The multiple relaxation time collision method for LBM improves the computationally determined permeability of the porous medium.[134]* The analysis of the flow should give the net velocity and pressure through and around the particles. Comparisons may be made to continuum equations, such as the Darcy equation and its variants, and to discrete pore models of two pores size to analyze changes in fluid motion due to the addition of the smallest pores. The relative volume fraction and size ratio of the pores will be compared among the different solutions to analyze their effects on the fluid permeation.

The fluids model may be augmented with multi-species capabilities to investigate diffusive transport in the highly irregular geometries both for drug delivery and catalysis applications. The multicomponent systems require more entire distribution function arrays for each species and appropriate manipulation routines and boundary conditions.[†] With heterogeneous catalysts, surface reaction models of chemical transformations would be critical and heat transfer models should be added later to account for the thermal processes.

The lattice Boltzmann code can be further optimized to advance the scale of simulations. The MPI implementation currently runs processor domains of specific processor numbers of square decompositions $4n^2$ (*e.g.* 4, 16, 36, ...), and should be

---

* See Apx. C.2.1 for details on the MRT method and pressure BCs.   † This is partially discussed in Sec. C.3.1, however the multi-species methods are currently implemented in MATLAB® only.

redesigned with communication methods which adapt to any domain grid layout. The goal would be to run lattice domains of upwards of 4000×4000 grids on up to 64 processors, which would require improvements in scaling and efficiency. The achievement of this goal would allow the simulation of a complete cross-section of a scale porous particle with two distinct small pore sizes and to model a small packed bed of slightly smaller particles. The optimization also be improved using blocked data structures of the domains one or two hundred lattice points square blocks. OpenMP can be used to further improve the optimization to hybridize the parallel implementation, though this is not the priority because the current OpenMP implementation was less successful than anticipated. Both the serial and parallel codes should be subjected to thorough verification and validation with, for example, the method of manufactured solution.

In this chapter we have shown the LBM is useful for complicated pore systems. Bimodal porous media present interesting possibilities for transport modeling particularly to understand fluid species behavior approaching surface contact. A parallel lattice Boltzmann code has been developed for OpenMP and MPI, though the methods could benefit from improvements in optimization. A bimodal particle shows flow passing heterogeneously through the object which implies much of the volume of the particle would not be as important for catalysis as the portions near the high-flow boundaries. This work may be extended to larger particles and higher flow resolution and comparisons with continuum models. The net permeability of biporous media should be measured as a function of connectivity and pore size. Multispecies and three dimensional simulations may be further added to understand species contact with the surfaces of particles.

Chapter 8

Summary and Conclusion

This dissertation investigated three topic areas covering the pore to continuum scales of fluid transport in porous media for application to materials design and engineering.

In this chapter, we summarize the results found in each topic, the future work, and the relation of the results to their applications. The following two sections—the first focused on theory and the second on computation—outline the key results presented in the dissertation. First, using semi-analytical models we have shown many significant effects of evaporation on capillary wetting in porous media. Second, we have applied the lattice Boltzmann method to pore-scale multiphysics models of pitting corrosion and heterogeneous flow behavior in bimodal porous media. In Sec. 8.3 we note significant topic areas which may advance the work. Finally, in Sec. 8.4 we conclude by outlining the general importance of the results to the associated engineering applications.

Metaphorically, we first look at each tree we have had a hand in growing, consider trees to be grown and nurtured, then observe the wider forest.

8.1 Capillary Wetting and Evaporation in Expanding Porous Domains

In Chapters 2 through 5, we investigated the theoretical implications of the effects of domain geometry and evaporation on the wicking of liquids into unsaturated porous media, and we produced the following results:[*]

1. **We developed a potential flow theory formulation of the Lucas–Washburn method of capillary wicking in porous media.**

   This formulation generalizes the domain shapes which may be analyzed, and facilitates incorporation of the source and sink terms which account for evaporation.[†] For example, we correctly analyzed expanding geometries with flat inlets (*i.e.* elliptic and oblate spheroid coordinates), when previously only circular inlets were easily solved (*i.e.* polar[61] and spherical[60] coordinates). The method produces semi-analytical solutions of the front position and bulk velocity, but is limited to Green–Ampt Theory[71] (GAT) applicable systems; in systems where this assumption fails, the wetting must be modeled with a continuous saturation function as given in the Richards equation.[70]

   All further results in this section rely on this formulation of the Lucas–Washburn method (LWM), so these limitations also constrain the derived results.[‡]

2. **The rate of advancement of the wet front is slower for capillary flow through higher dimensional expansions than through lower.**

---

[*] All results constitute original work by the author; although, some results are—to varying degrees—important redevelopments of others' work. The results include established physical facts, demonstrations of likely physical phenomena, or developed methodological capabilities. A brief note is given to clarify each result's implications and/or limitations.

[†] Sec. 2.2 first proposes the theory, which is generalized in Sec. 3.2. [‡] Some of these limitations are addressed by Result 7 below.

The Lucas–Washburn equation relates the length of the liquid penetration, $\tilde{y}_f$, to the square root of the wetting time, $\tilde{t}$, or $\tilde{y}_f^2/2 = \tilde{t}$. We have shown that while the flow behavior at very early times is similar to the LWE, in the large expansion limit, *e.g.* $\tilde{y}_f > 10$, the asymptotic power law relations for the capillary wicking go to $\tilde{y}_f^2 \ln(\tilde{y}_f)/2 \approx \tilde{t}$ for 2D radial flow and to $\tilde{y}_f^3/3 \approx \tilde{t}$ for 3D spherical.[*]

3. **Conversely, for a given inlet size, the magnitude of the flux into the porous domain increases with increasing dimensionality of the domain expansion.**

   The bulk velocity into a fully three-dimensional porous domain from a finite inlet has a finite constant steady rate of imbibition, in agreement with the conclusion of Philip[59] which was alternatively found for a continuous moisture profile. The Lucas–Washburn bulk velocity slowly goes to zero via $\tilde{U} \sim 1/\sqrt{\tilde{t}}$, while the magnitude of the bulk velocity for 2D flow lies between the 1D and 3D relationships.[†]

4. **In thin porous media there are three modes of evaporation: normal surface, side boundary, and front interface.**

   Each mode acts through three different kinds of surfaces and is mathematically formulated in distinct ways. Building on the work of Fries *et al.*[80], who considered the effect of restraint by gravity and normal surface loss from a wicking capillary porous medium, we showed that each mode of evaporation causes significant, but unique, deviations from Lucas–Washburn behavior in media of constant cross section.[‡]

---

[*] The solutions are presented in Ch. 2, while the power laws are detailed in Sec. 4.4.4; see also Figs. 2.10 and 3.2a and related discussions.   [†] See Figs. 2.12 and 3.2b with related discussion.   [‡] See Secs. 3.2 and 3.4.

5. **The ratio of the evaporation rate over the intrinsic capillary flow rate is a useful dimensionless quantity which we have called, for the first time, the *evaporation-capillary number.***

   The evaporation number governs the behavior of the system by determining when the evaporation begins to dominate the capillary flow. Each of the three evaporation modes has a specific expression of the evaporation number, but the ratio has the same fundamental meaning.*

   To our knowledge, this essential quantity has not been specifically noted in the related porous media and fluid mechanics literature.

6. **Normal surface evaporation is the predominant mode of evaporation in thin porous media.**

   In thin porous media, the ratio of the side height to the inlet width of the domain is very small, so the relative surface area through with normal evaporation occurs is much greater than for side and front evaporation.†

7. **The Lucas–Washburn method theoretical solution for capillary wicking with evaporation in a porous domain of constant cross section behaves with similar asymptotics to the related partially saturated wicking model, but often over-predicts the magnitude by a given proportion.**

   For wicking with a continuous saturation profile, we have observed that a capillary diffusivity proportional to a power-law saturation function of Θ^2 gives very similar results to the GAT model front position.[79] However, the magnitude of the bulk velocity is over-predicted by a factor of two because there is only half the volume of liquid in the medium, but the behavior has nearly the same profile.[81] Higher-order saturation functions have even lower predicted values, but

---

* See Secs. 3.4.1 and 4.3.1 for details.   † See the discussion in Sec. 3.4.1, particularly around Eq. (3.4.1).

still have very similar behavior profiles to the GAT model for both variables. Thus, we conclude that the overall time-dependent behavior profiles predicted by the GAT is sufficiently close to the Richards equation solution, but we recognize that the predicted magnitude may be too large by a factor of approximately two to four.*

Using a geometric analogy to the volumes of cones and hyper-cones, we hypothesize that for 2D and 3D expansions model with GAT the deviations may be by factors of three and four, respectively, for the second order saturation function and up to nine and sixteen for the highest orders, but that the general trends in behavior would be analogous and are therefore physically insightful.

8. **Normal surface evaporation and side boundary evaporation occur through the same fundamental physical mechanism, and in porous media of constant cross section, they behave analogously.**

   While side evaporation results in a curved wet front, in the limit of thin media and large fluid propagation, the characteristic behavior of the two modes only differ by a small fraction, and the curvature of the side evaporation becomes negligible in comparison to the total length of penetration. Additionally, the range of time from when the evaporation mode first influences the capillary flow to reaching evaporative steady state is well constrained by $0.1 < \mathfrak{N}\tilde{t} < 10$ for both normal and surface evaporation numbers.[†]

   Thus, we have shown it is reasonable to use normal evaporation as an approximation to what is ultimately evaporation through a domain side but through an infinitesimally thin system dimension.

9. **For capillary flow in a porous domain of constant cross section, the effects of front interface evaporation and restraint by gravity are analytically identical in the LWM.**

---

* See Sec. 3.4.3 and Fig. 3.3.   [†] See Secs. 3.3.3, 3.4.4 (particularly Fig. 3.5), and 3.4.7.

We have shown that the derived solutions for 1D capillary flow, the front evaporation and gravity solutions are the same. Of particular note, unlike with normal and side evaporation, for these two phenomena it is the dimensionless quantity squared, *i.e.* $0.1 < \mathfrak{N}_f^2 \tilde{t}$ or $\mathrm{Bo}_a^2 \tilde{t} < 10$, which determines the time range of non-steady state influence of the phenomenon, where Bo_a is the modified Bond number scaled with inlet size. This squared factor also shows that for small values of $\mathfrak{N}_f$ front evaporation is less significant than normal surface evaporation.[*]

In practice, both of these phenomena may degrade the assumption of a discontinuous front interface, however the result should hold for the early time effects of the phenomena on the capillary flow.

10. **In fan shaped media, both the expanding domain shape and the evaporation can affect the behavior of capillary flow.**

    In particular, the front goes to a stationary profile and the bulk velocity remains finite at that steady state. Additionally, the velocity of the flow inside the medium may be calculated given the front position and evaporation number.[†]

11. **The predicted front shape for 2D wicking out of a flat inlet agrees with the experimentally observed profile and behavior.**

    This is in contrast to Hall[57], who suggested theoretically that the shape was a pure ellipse. Instead, we observe the shape going from a LWE-like plug flow initially to a rectangle with rounded corners to a nearly circular shape at later times.[‡]

---

[*] See Secs. 3.3.3 and 3.4.7.   [†] See Ch. 4, particularly the discussion of Fig. 4.7. The solution for the 2D radial flow with evaporation agrees with the recent work by Liu *et al.*[95], but it was done prior to their publication and thus independently.   [‡] See Ch. 4 and the discussion of supplemental Figs. E.1 and E.2.

12. **We have plotted the steady state front positions and bulk velocities for fanning domains as a function of the evaporation number.**

    Given a desired steady state bulk velocity for a 1D or 2D fan shaped domain, the related evaporation number may be quickly determined. From the determined evaporation number the required size of the domain may be estimated by the corresponding steady state front position (provided that the over-prediction is accounted for as mentioned in Result 7).*

    This will be especially useful for design of porous domains used to drive microflows via capillary action as we discuss below in Sec. 8.4.

13. **Similar to pure capillary flow, the front motion is slowed by the normal surface evaporation more strongly with increasing dimensionality of the expanding domain.**

    Intuitively, this stems from the greater surface area increase that an advancement of the front represents for 2D than for 1D expansions. Alternatively, this is readily illustrated via the first order terms for the evaporation number in power series of the front position solutions for the 1D Cartesian and 2D radial coordinate systems. Adding each term to the left side of the corresponding expressions for capillary flow (see Result 2), for sufficiently low evaporation number and times at least an order of magnitude below the onset of the steady state, the first order perturbation of the evaporation to the LWE is $\frac{1}{8}\mathfrak{N}_{\mathrm{n}}\tilde{y}_f^4$, while for the 2D expansion the perturbation is $\frac{1}{8}\mathfrak{N}_{\mathrm{n}}\tilde{y}_f^4[\ln(\tilde{y}_f)]^2$. The perturbation for 2D wicking due to evaporation is a higher order expression and therefore has a stronger effect.†

14. **The effect of front evaporation on reducing front motion with increasing dimensionality follows the same general trend as normal evapo-**

---

* See Figs. 4.5 and 4.7b. † This comparison is fully detailed in Sec. 4.4.4; also see Figs. 4.3b and 4.4a.

ration but is relatively smaller.

We may intuit the trend in the effect on the front behavior by considering that the surface area through which the front evaporation occurs also increase in dimension along with the increasing degree of expansion (*i.e.* constant area, growing in 1D, and growing in 2D, for 1D, 2D and 3D expansions, respectively). Adding the first order asymptotic expansion of the front evaporation number series to the left side of the power laws for capillary flow (Result 2), for low evaporation numbers the Lucas–Washburn relation is slowed by $\frac{1}{3}\mathfrak{N}_{\mathrm{f}}\tilde{y}_f^3$, the 2D radial by $\frac{1}{3}\mathfrak{N}_{\mathrm{f}}\tilde{y}_f^3 \left[\ln(\tilde{y}_f)\right]^2$, and the 3D hemispherical by $\frac{1}{5}\mathfrak{N}_{\mathrm{f}}\tilde{y}_f^5$. These series approximation terms are lower order than the equivalent terms for normal evaporation which thus has a greater relative effect on the flow.[*]

15. **We have derived the semi-analytical GAT solutions for the effects of side evaporation and restraint by gravity on capillary flow in 2D and 3D expanding domains.**

    In future, we may prioritize generating results on these solutions. In the least, they provide constraints on the degree at which these phenomena may be affecting other results; for example, whether observed deviations from the ideal theoretical front position in the experiments of Xiao *et al.*[60] could be due to front evaporation, restraining gravity, or another source of error.[†]

    We anticipate that we will observe markedly distinct behaviors between the 2D effects of side and normal evaporation on the behavior, unlike with thin porous strips (as seen with Result 8).

---

[*] See Sec. 5.5.1.   [†] See Secs. 5.3 and 5.4—also the summary of derived potentials in Apx. B.1.

8.2 Pore-scale Simulations of Corrosion and Bi-porous Media

In Chapters 6 and 7, we used the lattice Boltzmann method (LBM) to simulate pore-scale phenomena involved in pitting corrosion of aluminum and transport in bimodal porous particles; we have demonstrated the following results:[*]

16. **We have produced our own implementations of the LBM.**

    The lattice Boltzmann method is a mesoscale (between continuum and atomistic) fluid simulation method which solves the Boltzmann kinetic equations on a Cartesian lattice. We have implementations of the 2D (D2Q9) method written in C++ and MATLAB®. The LBM has the particular benefit of handling amorphous porous media, and relative ease of programming.[†]

    At present, our simulations are only run in lattice units and not directly converted into physical units.

17. **We developed several modified and new implementations of physical phenomena to couple with the LBM.**

    Beyond the basic method, standard boundary conditions, and common physical phenomena coupled with the LBM, we have prototyped our own models of surface reactions, solid dissolution, and 2D extension of the lattice Poisson–Boltzmann method for electrokinetics flows.[‡]

18. **We have produced and tested parallel executable LB methods for prospective large-scale simulations of transport phenomena in porous materials.**

---

[*] We continue the numbering of the results from the previous section so all results are uniquely assigned.   [†] See Sec. 6.2.1 and Apx. C for more details.   [‡] For overview, see Sec. 6.2.2 and appendix Secs. C.3.2, C.3.3, and C.3.4 for specific details.

Implementations of the LBM with shared memory parallelism using OpenMP and distributed parallelism using MPI have been successfully run on small parallel machines. Though the current parallelized methods are functional, the code requires more LB methods development and gains in optimization before it would be used to simulate larger multiphysics porous transport problems.[*]

19. **We have built a set of various, simplistic LB models of physical pitting corrosion of aluminum surfaces.**

The transport of ionic species and oxidation/reduction chemistry are important to model and understand the aluminum pitting corrosion process, which is a large problem for materials science. So, we have begun to use the LBM to look into the important and highly complex transport phenomena involved in the pitting corrosion process.[†]

For more complete models of the process, we need to combine, advance, and optimize the different phenomenological models of corrosion transport.

20. **Condensation in metal subsurface pits may lead to asymmetry of the system.**

Using the Sukop and Thorne[111] description of the Shan–Chen multiphase LBM, we have observed in the process of a liquid condensing into a mirror-symmetric elliptic subsurface pore, that a spontaneously imbedded bubble migrates to either side of the pore to minimize the free energy of the system. As a result one side of the pit is exposed to air and the other to water, which can cause the pit to degrade asymmetrically. This demonstrates that multiphase processes are important for the analysis of the pit corrosion development.[‡]

21. **Exterior advection produces asymmetry in the development of a dissolving surface pit.**

---

[*] As discussed in Secs. 7.2.2 and 7.3.2.　[†] See Sec. 6.2.2 and Apx. **??**.　[‡] See Sec. 6.3.1 for details.

When the protective aluminum oxide coating is scratched off the surface of an aluminum part and the exposed aluminum comes into contact with a caustic solution, the aluminum metal may begin to dissolve. We have observed that when the solvent is flowing, and the dissolving ion has a small maximum saturation, the upstream portion of the exposed aluminum will dissolve more rapidly, thus promoting uneven growth of the pit.*

22. **Electrokinetic flows inside a subsurface pit may also drive asymmetric dissolution.**

    Applying the modified lattice Poisson–Boltzmann method,[122] when an electric field is imposed over an ionic fluid in a subsurface pit with charged walls, the field drives rotational motion of the fluid. This is one demonstration of the possible importance of the ionic character of the fluid in the dissolution process, although other effects such as diffusiophoresis or the electrochemical effects of the oxidation/reduction reactions may be more important to the net transport of the system.†

23. **We have designed a physically motivated model of bimodal porous particles.**

    We produced an automated domain generation algorithm which produces a 2D cross section of particles similar to those of Carroll *et al.*[1] These generated particle solid lattice domains are used by the LBM to simulate fluid flows in biporous particles.‡

    At present, the model has the small pores connecting the distinct large pores, but in future, the transport would have more interconnection between the large pores to make the domain more biporous in character.

24. **Fluid flows inhomogeneously inside biporous particles.**

---

* See Sec. 6.3.3. † See Sec. 6.3.4. ‡ See Sec. 7.2.1 for a description of the generation method.

In body force driven flows across a biporous particle cross section, the velocity around the edges perpendicular to the force gradient is much higher. This drives much more flow through the internal pores near these edges, while the total resistance to flow by pores along the middle of the particle prohibits significant fluid motion.* As a result, a significant fraction of the particle will only have diffusion-dominated transport in reactive processes.

However, this permeability behavior may be more prominent in body force driven flows. We expect the permeation through the center of the particle would improve with a prescribed pressure drop over the particle.

8.3 Prospective Work

There are several important directions for future investigation of the effects of evaporation on wicking. First, the theory would benefit from further validation with wetting paper in dry environments.† Furthermore, the accuracy of the LWM-based predictions should be checked with partially saturated flow models to consider the degree of likely over-prediction in magnitude of our theoretical results (see Result 7 above).

We would like to create methods with predictive capabilities for pitting corrosion rates and effects. This would include accurate models of stress corrosion cracking in aluminum,‡ interfacing our LBMs with results from simulations at the molecular scale,

---

* See Sec. 7.3.1, particularly Fig. 7.4.   † See Apx. G for discussion on three prototyping experiments. The theoretical prediction for the front position with active surface evaporation match reasonably closely with experiments. Also, the measured bulk velocity goes to a finite steady state due to the evaporation.   ‡ Preliminary results on SCC are outlined in Apx H. Due to preferential capillary condensation, narrower cracks and pores retain liquids better than wider ones. Exterior fluid advection has a negligible transport effect on solutes reaching or leaving the crack tip.

and quantitatively comparing the results for similarity to experiments on corrosion and fatigue.

Monoporous media provide a useful benchmark for checking the accuracy of permeability simulations, and should be further analyzed to compare with biporous media.* If feasible, the permeabilities of the original biporous particles will be measured for validation. Furthermore, the model may be combined with species diffusion, reactions, thermal, and other relevant catalytic or drug delivery methods to improve the analysis of the other important phenomena involved in the applications.

8.4   Conclusion

In this dissertation, we developed useful techniques of study and showed insightful details regarding fluid transport behaviors in three topic areas in porous media. These results will be beneficial to future design of media with optimal transport properties.

In Chapters 2 through 5, we significantly improved the theoretical basis for the analysis of the effects of evaporation and varied domain geometry on capillary wicking in porous media, and we observed the importance and variety of evaporation effects on behaviors of the system (Results 1 and 4). Several of the results have shown that the other conclusions derived by the methodology are generally sound for our particular applications and give proper constraints to their applicability (Results 7, 11, and 15).† In addition to deriving the specific equations for the motion of the front and the bulk velocity, we have shown the general trends in behavior of capillary

---

* Some preliminary results on monoporous media are given in Apx. I. We show the flux through a monoporous cylindrical particle in a low Reynolds number flow is proportional to the Reynolds number times the square root of the Darcy number. Flow through 2D and 3D monoporous particles are similar, while the flow profiles around them are distinct.   † See also the experimental work of Apx G.

flows, with and without evaporation from the surface and the front, as the system dimensionality is varied (Results 2, 3, 13, and 14).

We have substantially unified and improved the basic formulation of the evaporation effects on capillary wicking (Results 4 and 6); in particular, we have shown the important role the evaporation capillary number has in the system behavior (Result 5). Also, we have demonstrated important connections and differences between the modes of evaporation (Results 8, 9, and 14).

Finally, we have produced analytical relations and resources which will be beneficial in design of porous media used for passive driving of fluid via capillary action (Results 10 and 12). In practice, the most promising application of these results is in optimizing reactive transport processes in passive capillary driven fuel cell devices.[17,22]

Thus, we have presented a more rigorous understanding of the underlying theory of capillary flow in lab-scale engineering porous media, observed surprising physical behaviors, and increased in our capability to predict flow behaviors.

In Chapters 6 and 7, we laid practical groundwork for further computational analysis of pitting corrosion in aluminum and transport in biporous materials, and we have found a few elementary insights on the systems. We have assembled modeling and simulations resources catered to these applications (Results 16–19 and 23), and with some improvements to the methods, we expect these resources to yield groundbreaking insights into the engineering problems.

The costly damage to mechanical systems caused by the complex process of corrosion has been widely studied empirically, but many further advancements may be made in theoretical models. We focused particularly on the mitigation of pitting corrosion in aluminum mechanical parts (Result 19). We have observed three very different fluid processes that may cause spontaneous asymmetry in the developement the pit corrosion system (Results 20, 21, and 22). These results demonstrate the com-

plicated nature of the system and illustrates the need for more coupled multiphysics models of the pitting corrosion process.

Fundamental flow and transport modeling of bimodal porous media is an open area of research. Practical understanding of bimodal pore structure effects on the permeability of porous media is required for future advancements in biporous media applications such as catalysts and drug delivery particles[1] (Result 23). We have shown that the flow in an array of these biporous particles may not produce general flow through a significant fraction of the particle volume—potentially limiting their effectiveness (Result 24). A number of future modifications to the biporous simulations could show this is less significant.

In conclusion, this dissertation has presented significant results and useful preliminary capabilities in the three topic areas of porous media. We have demonstrated the importance of using analytical and computational models to understand fluid transport properties of porous media, and we believe that these results will improve the engineering of advanced materials.

Appendices
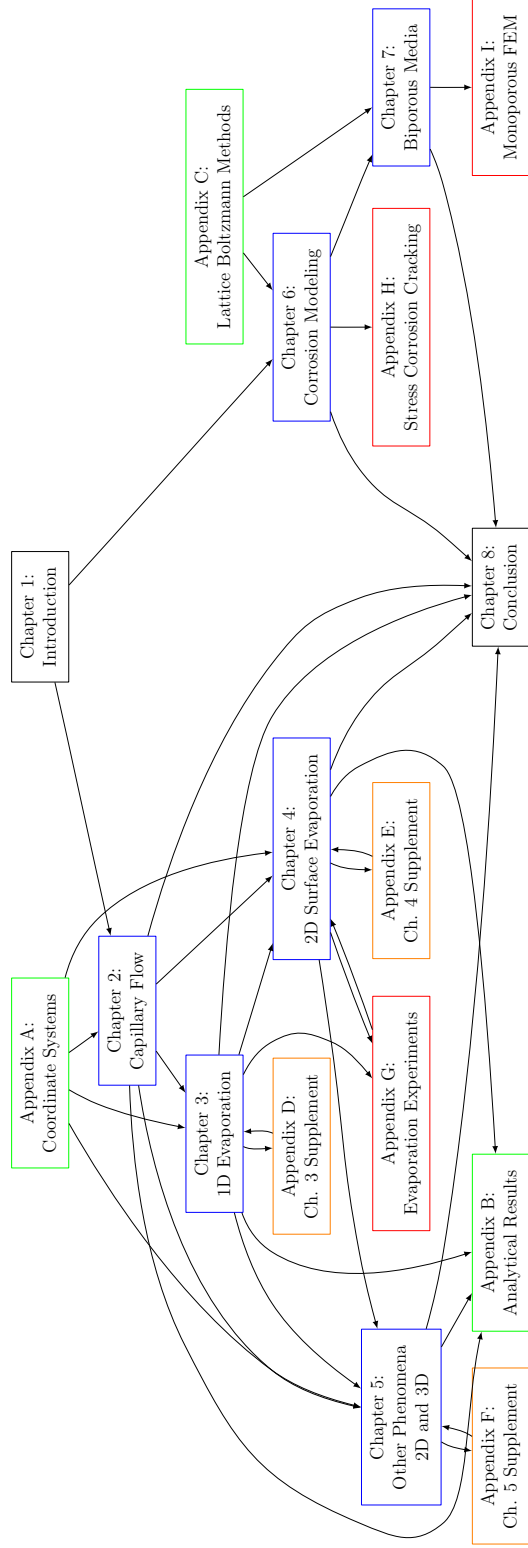
Connections between chapters and appendices

Appendix A

Coordinate Transforms

This appendix tabulates key mathematical expressions relating to the coordinate systems used in this dissertation. The method of coordinate transforms is summarized in the first section. In the second section, we present the major differential expressions—the differential length, gradient, laplacian, and divergence—in the five coordinate systems: Cartesian, polar, elliptic, spherical, and oblate spheroid.

A.1 General Curvilinear Coordinate Transforms

This section details the essential relations used to derive the differential expressions in a given coordinate system.coordinate system!transforms—(textbf Significant portions of the material in this appendix have been synthesized from the following textbooks, in order of importance:

- Moon and Spencer, *Field Theory Handbook*, 1989;[31]

- Bird, Stewart and Lightfoot, *Transport Phenomena*, 2nd edition 2006;[30]

- McQuarrie, *Mathematical Methods for Scientists and Engineers*, 2003.[29]

Appendix A. Coordinate Transforms

We only are considering coordinate systems where the metric tensor is diagonal.

A.1.1 Coordinate Systems

In transforming from cartesian coordinates, which we shall indicate by x_i with unit vectors $\hat{\mathbf{e}}_{x_i}$. Say $\hat{\mathbf{e}}_{u_i}$ is the unit vector in the u_i variable of the transformed space and N is the dimensions of the system; for most practical engineering purposes this is 2 or 3. For a three-dimensional system we may illustrate this,

$$x_1 = x_1(u_1, u_2, u_3), \tag{A.1.1a}$$

$$x_2 = x_2(u_1, u_2, u_3), \tag{A.1.1b}$$

$$x_3 = x_3(u_1, u_2, u_3). \tag{A.1.1c}$$

In vector notation, $\mathbf{x} = \mathbf{x}(\mathbf{u})$. The metric coefficients of the transform to our system are, (for $\mathbf{r} = \sum_{j=1}^{N} x_j \hat{\mathbf{e}}_{x_j}$),

$$h_{u_i} = \left| \frac{\partial \mathbf{r}}{\partial u_i} \right|, \qquad \text{or} \tag{A.1.2a}$$

$$= \sqrt{\sum_{j=1}^{N} \left(\frac{\partial x_j}{\partial u_i} \right)^2}. \tag{A.1.2b}$$

For convenience, we define

$$h = \prod_{i=1}^{N} h_{u_i} \tag{A.1.3}$$

which is the product of all the metric coefficients and is the coefficient of the total differential volume.

A.1.2 Unit Vectors

For a variety of applications it is helpful to know the specific form of the unit vectors in one coordinate system in terms of another coordinate system. The form of a

unit vector in the transformed coordinates in terms of the Cartesian (or original) coordinate system is,

$$\hat{\mathbf{e}}_{u_j} = h_{u_j} \sum_i \left(\frac{\partial u_j}{\partial x_i} \right) \hat{\mathbf{e}}_{x_i}, \tag{A.1.4a}$$

$$= \frac{1}{h_{u_j}} \sum_i \left(\frac{\partial x_i}{\partial u_j} \right) \hat{\mathbf{e}}_{x_i}. \tag{A.1.4b}$$

Expressing the Cartesian unit vectors in terms of the transformed coordinate unit vectors is similar;

$$\hat{\mathbf{e}}_{x_i} = \sum_j h_{u_j} \left(\frac{\partial u_j}{\partial x_i} \right) \hat{\mathbf{e}}_{u_j}, \tag{A.1.5a}$$

$$= \sum_j \frac{1}{h_{u_j}} \left(\frac{\partial x_i}{\partial u_j} \right) \hat{\mathbf{e}}_{u_j}. \tag{A.1.5b}$$

This second form can be used to determine the vector transform of a gravity vector acting on a liquid in a porous medium.

A.1.3 Differential Operators

There are several differential operators that are of major importance in differential equations because of their invariance. The differential length in a general orthonormal coordinate system is,

$$(\mathrm{d}s)^2 = \sum_{i=1}^{N} (h_{u_i})^2 (\mathrm{d}u_i)^2. \tag{A.1.6}$$

The general gradient of a scalar function is,

$$\boldsymbol{\nabla}\varphi = \sum_{i=1}^{N} \frac{1}{h_{u_i}} \frac{\partial \varphi}{\partial u_i} \hat{\mathbf{e}}_{u_i}. \tag{A.1.7}$$

The divergence operator on a vector in the transform space (*i.e.* vector values corresponding to the spacial variables in the transformed space) is,

$$\boldsymbol{\nabla} \cdot \mathbf{f} = \frac{1}{h} \sum_{i=1}^{N} \frac{\partial}{\partial u_i} \left(\frac{h}{h_{u_i}} f_{u_i} \right). \tag{A.1.8}$$

The Laplace operator, or simply Laplacian, is defined as $\nabla^2 = \boldsymbol{\nabla} \cdot \boldsymbol{\nabla}$ which is represented by

$$\nabla^2 \varphi = \frac{1}{h} \sum_{i=1}^{N} \frac{\partial}{\partial u_i} \left(\frac{h}{h_{u_i}^2} \frac{\partial \varphi}{\partial u_i} \right). \tag{A.1.9}$$

The advection operator is common in fluid dynamics and is part of the material derivative $(\frac{\mathrm{D}q}{\mathrm{D}t} = \frac{\partial q}{\partial t} + \mathbf{v} \cdot \boldsymbol{\nabla} q)$.

$$\mathbf{v} \cdot \boldsymbol{\nabla} q = \sum_{i=1}^{N} \frac{v_i}{h_{u_i}} \frac{\partial q}{\partial u_i}. \tag{A.1.10}$$

Several operators above are shown as operating on scalar quantities. In many cases these operators are inadequate forms to be applied to vector quantities. coordinate system!transforms—)textbf

A.2   Coordinate systems: Metrics and Operators

In this section, we define several important coordinate systems, their metric coefficients, and the major differential operators. We detail the Cartesian, cylindrical, elliptic cylindrical, spherical, and oblate spheroidal coordinate systems. The information is provided in the notation of Moon and Spencer.[31]

In the work in this dissertation primarily used standard Cartesian coordinates in the 1D flow solutions and in computational simulations, but relied significantly on elliptic cylinder and oblate spheroid coordinates for realistic extensions into 2D and 3D. Cylindrical and spherical coordinates were used primarily to derive solutions used for asymptotic verification of solutions in the other coordinates.

A.2.1 Cartesian

Definition of coordinates

$$x = x \tag{A.2.1a}$$

$$y = y \tag{A.2.1b}$$

$$z = z \tag{A.2.1c}$$

Metric coefficients

$$h_x = 1 \tag{A.2.2a}$$

$$h_y = 1 \tag{A.2.2b}$$

$$h_z = 1 \tag{A.2.2c}$$

Operators

$$(\mathrm{d}s)^2 = (\mathrm{d}x)^2 + (\mathrm{d}y)^2 + (\mathrm{d}z)^2 \tag{A.2.3}$$

$$\boldsymbol{\nabla}\varphi = \frac{\partial\varphi}{\partial x}\hat{\mathbf{e}}_x + \frac{\partial\varphi}{\partial y}\hat{\mathbf{e}}_y + \frac{\partial\varphi}{\partial z}\hat{\mathbf{e}}_z \tag{A.2.4a}$$

$$= \frac{\partial\varphi}{\partial x}\hat{\mathbf{i}} + \frac{\partial\varphi}{\partial y}\hat{\mathbf{j}} + \frac{\partial\varphi}{\partial z}\hat{\mathbf{k}} \tag{A.2.4b}$$

$$\boldsymbol{\nabla}\cdot\mathbf{f} = \frac{\partial f_x}{\partial x} + \frac{\partial f_y}{\partial y} + \frac{\partial f_z}{\partial z} \tag{A.2.5}$$

$$\nabla^2\varphi = \frac{\partial^2\varphi}{\partial x^2} + \frac{\partial^2\varphi}{\partial y^2} + \frac{\partial^2\varphi}{\partial z^2} \tag{A.2.6}$$

$$\mathbf{v}\cdot\boldsymbol{\nabla}q = v_x\frac{\partial q}{\partial x} + v_y\frac{\partial q}{\partial y} + v_z\frac{\partial q}{\partial z} \tag{A.2.7}$$

A.2.2   Cylindrical/Polar

Definition of coordinates

$$x = r\cos(\theta) \tag{A.2.8a}$$

$$y = r\sin(\theta) \tag{A.2.8b}$$

$$z = z \tag{A.2.8c}$$

Metric coefficients

$$h_r = 1 \tag{A.2.9a}$$

$$h_\theta = r \tag{A.2.9b}$$

$$h_z = 1 \tag{A.2.9c}$$

Operators

$$(\mathrm{d}s)^2 = (\mathrm{d}r)^2 + r^2\,(\mathrm{d}\theta)^2 + (\mathrm{d}z)^2 \tag{A.2.10}$$

$$\boldsymbol{\nabla}\varphi = \frac{\partial\varphi}{\partial r}\hat{\mathbf{e}}_r + \frac{1}{r}\frac{\partial\varphi}{\partial\theta}\hat{\mathbf{e}}_\theta + \frac{\partial\varphi}{\partial z}\hat{\mathbf{e}}_z \tag{A.2.11}$$

$$\boldsymbol{\nabla}\cdot\mathbf{f} = \frac{\partial f_r}{\partial r} + \frac{f_r}{r} + \frac{1}{r}\frac{\partial f_\theta}{\partial\theta} + \frac{\partial f_z}{\partial z} \tag{A.2.12}$$

$$\nabla^2\varphi = \frac{\partial^2\varphi}{\partial r^2} + \frac{1}{r}\frac{\partial\varphi}{\partial r} + \frac{1}{r^2}\frac{\partial^2\varphi}{\partial\theta^2} + \frac{\partial^2\varphi}{\partial z^2} \tag{A.2.13}$$

$$\mathbf{v}\cdot\boldsymbol{\nabla}q = v_r\frac{\partial q}{\partial r} + \frac{v_\theta}{r}\frac{\partial q}{\partial\theta} + v_z\frac{\partial q}{\partial z} \tag{A.2.14}$$

A.2.3   Elliptical Cylinder

Definition of coordinates

$$x = a\cosh(\eta)\cos(\psi) \tag{A.2.15a}$$

$$y = a\sinh(\eta)\sin(\psi) \tag{A.2.15b}$$

$$z = z \tag{A.2.15c}$$

Metric coefficients

$$h_\eta = a\sqrt{\cosh^2(\eta) - \cos^2(\psi)} \tag{A.2.16a}$$

$$h_\psi = a\sqrt{\cosh^2(\eta) - \cos^2(\psi)} = h_\eta \tag{A.2.16b}$$

$$h_z = 1 \tag{A.2.16c}$$

Note: h_η is equivalently $a\sqrt{\sinh^2(\eta) + \sin^2\psi}$.

Operators

$$(\mathrm{d}s)^2 = a^2\left(\cosh^2(\eta) - \cos^2(\psi)\right)\left[(\mathrm{d}\eta)^2 + (\mathrm{d}\theta)^2\right] + (\mathrm{d}z)^2 \tag{A.2.17}$$

$$\boldsymbol{\nabla}\varphi = \frac{1}{a\left(\cosh^2(\eta) - \cos^2(\psi)\right)^{1/2}}\left[\frac{\partial\varphi}{\partial\eta}\hat{\mathbf{e}}_\eta + \frac{\partial\varphi}{\partial\psi}\hat{\mathbf{e}}_\psi\right] + \frac{\partial\varphi}{\partial z}\hat{\mathbf{e}}_z \tag{A.2.18}$$

$$\boldsymbol{\nabla}\cdot\mathbf{f} = \frac{1}{a\left(\cosh^2(\eta) - \cos^2(\psi)\right)^{1/2}}\left[\frac{\partial}{\partial\eta}\left(\left(\cosh^2(\eta) - \cos^2(\psi)\right)^{1/2} f_\eta\right)\right.$$
$$\left. + \frac{\partial}{\partial\psi}\left(\left(\cosh^2(\eta) - \cos^2(\psi)\right)^{1/2} f_\psi\right)\right] + \frac{\partial f_z}{\partial z}$$

$$\nabla^2\varphi = \frac{\frac{\partial^2\varphi}{\partial\eta^2} + \frac{\partial^2\varphi}{\partial\psi^2}}{a^2\left(\cosh^2(\eta) - \cos^2(\psi)\right)} + \frac{\partial^2\varphi}{\partial z^2} \tag{A.2.19}$$

$$\mathbf{v} \cdot \boldsymbol{\nabla} q = \frac{v_\eta \frac{\partial q}{\partial \eta} + v_\psi \frac{\partial q}{\partial \psi}}{a \left(\cosh^2(\eta) - \cos^2(\psi)\right)^{1/2}} + v_z \frac{\partial q}{\partial z} \qquad (\text{A.2.20})$$

A.2.4 Spherical

Definition of coordinates

$$x = r \sin(\theta) \cos(\psi) \qquad (\text{A.2.21a})$$

$$y = r \sin(\theta) \sin(\psi) \qquad (\text{A.2.21b})$$

$$z = r \cos(\theta) \qquad (\text{A.2.21c})$$

Metric coefficients

$$h_r = 1 \qquad (\text{A.2.22a})$$

$$h_\theta = r \qquad (\text{A.2.22b})$$

$$h_\psi = r \sin(\theta) \qquad (\text{A.2.22c})$$

Operators

$$(\mathrm{d}s)^2 = (\mathrm{d}r)^2 + r^2 (\mathrm{d}\theta)^2 + r^2 \sin^2\theta (\mathrm{d}\psi)^2 \qquad (\text{A.2.23})$$

$$\boldsymbol{\nabla}\varphi = \frac{\partial \varphi}{\partial r} \hat{\mathbf{e}}_r + \frac{1}{r} \frac{\partial \varphi}{\partial \theta} \hat{\mathbf{e}}_\theta + \frac{1}{r \sin(\theta)} \frac{\partial \varphi}{\partial \psi} \hat{\mathbf{e}}_\psi \qquad (\text{A.2.24})$$

$$\boldsymbol{\nabla} \cdot \mathbf{f} = \frac{\partial f_r}{\partial r} + \frac{2}{r} f_r + \frac{1}{r} \frac{\partial f_\theta}{\partial \theta} + \frac{\cot(\theta)}{r} f_\theta + \frac{1}{r \sin(\theta)} \frac{\partial f_\psi}{\partial \psi} \qquad (\text{A.2.25})$$

$$\nabla^2 \varphi = \frac{\partial^2 \varphi}{\partial r^2} + \frac{2}{r} \frac{\partial \varphi}{\partial r} + \frac{1}{r^2} \frac{\partial^2 \varphi}{\partial \theta^2} + \frac{\cot(\theta)}{r^2} \frac{\partial \varphi}{\partial \theta} + \frac{1}{r^2 \sin^2(\theta)} \frac{\partial^2 \varphi}{\partial \psi^2} \qquad (\text{A.2.26})$$

$$\mathbf{v} \cdot \boldsymbol{\nabla} q = v_r \frac{\partial q}{\partial r} + \frac{v_\theta}{r} \frac{\partial q}{\partial \theta} + \frac{v_\psi}{r \sin(\theta)} \frac{\partial q}{\partial \psi} \tag{A.2.27}$$

A.2.5   Oblate Spheroid

Definition of coordinates

$$x = a \cosh(\eta) \sin(\theta) \cos(\psi) \tag{A.2.28a}$$

$$y = a \cosh(\eta) \sin(\theta) \sin(\psi) \tag{A.2.28b}$$

$$z = a \sinh(\eta) \cos(\theta) \tag{A.2.28c}$$

Metric coefficients

$$h_\eta = a \sqrt{\cosh^2(\eta) - \sin^2(\theta)} \tag{A.2.29a}$$

$$h_\theta = a \sqrt{\cosh^2(\eta) - \sin^2(\theta)} = h_\eta \tag{A.2.29b}$$

$$h_\psi = a \cosh(\eta) \sin(\theta) \tag{A.2.29c}$$

Operators

$$(\mathrm{d}s)^2 = a^2 \left(\cosh^2(\eta) - \sin^2(\theta) \right) \left[(\mathrm{d}\eta)^2 + (\mathrm{d}\theta)^2 \right]$$
$$+ a \cosh^2(\eta) \sin^2(\theta) \, (\mathrm{d}\psi)^2 \tag{A.2.30}$$

$$\boldsymbol{\nabla}\varphi = \frac{\frac{\partial \varphi}{\partial \eta} \hat{\mathbf{e}}_\eta + \frac{\partial \varphi}{\partial \theta} \hat{\mathbf{e}}_\theta}{a \left(\cosh^2(\eta) - \sin^2(\theta) \right)^{1/2}} + \frac{\frac{\partial \varphi}{\partial \psi} \hat{\mathbf{e}}_\psi}{a \cosh(\eta) \sin(\theta)} \tag{A.2.31}$$

Appendix A. Coordinate Transforms

$$\boldsymbol{\nabla} \cdot \mathbf{f} = \frac{1}{a\left(\cosh^2(\eta) - \sin^2(\theta)\right)^{1/2}}$$

$$\times \left[\frac{\frac{\partial}{\partial\eta}\left(\left(\cosh^2(\eta) - \sin^2(\theta)\right)^{1/2}\cosh(\eta)f_\eta\right)}{\cosh(\eta)} \right.$$

$$\left. + \frac{\frac{\partial}{\partial\theta}\left(\left(\cosh^2(\eta) - \sin^2(\theta)\right)^{1/2}\sin(\theta)f_\theta\right)}{\sin(\theta)} \right]$$

$$+ \frac{1}{a\cosh(\eta)\sin(\theta)}\frac{\partial f_\psi}{\partial\psi}$$

(A.2.32)

$$\nabla^2\varphi = \frac{\frac{\partial^2\varphi}{\partial\eta^2} + \tanh(\eta)\frac{\partial\varphi}{\partial\eta} + \frac{\partial^2\varphi}{\partial\theta^2} + \cot(\theta)\frac{\partial\varphi}{\partial\theta}}{a^2\left(\cosh^2(\eta) - \sin^2(\theta)\right)}$$

$$+ \frac{1}{a^2\left(\cosh^2(\eta) - \sin^2(\theta)\right)}\frac{\partial^2\varphi}{\partial\psi^2}$$

(A.2.33)

$$\mathbf{v}\cdot\boldsymbol{\nabla}q = \frac{v_\eta\frac{\partial q}{\partial\eta} + v_\theta\frac{\partial q}{\partial\theta}}{a\left(\cosh^2(\eta) - \sin^2(\theta)\right)^{1/2}} + \frac{v_\psi}{a\cosh(\eta)\sin(\theta)}\frac{\partial q}{\partial\psi}$$

(A.2.34)

Appendix B

Summary of Analytical Results

B.1   Chapters 2–5 Solutions

In this section, some important analytical results from the chapters on capillary flow in porous media (chs 2–5) are tabulated for reference and for easy comparison. The velocity potentials are given for capillary, normal surface and side evaporation, and gravity. We note the solution for the 3D oblate spheroid side evaporation potential has not been determined.

B.1.1   Velocity Potentials

All solved velocity potentials are enumerated below for the physical phenomena of capillary driven motion, wicking gravity effects, normal surface evaporation, and side evaporation for each of the six coordinate systems.* The systems employed in this work are standard Cartesian, elliptic, polar, oblate spheroid, and spherical. Cylindri-

---

* Front evaporation is not included because this phenomenon only influences the potential indirectly via the frontal mass balance equation.

cal is technically the same system as polar, but the direction of motion is in z not in r hence the usage is different. The first three coordinate systems include the normal surface evaporation, whereas the source term approach is not physically appropriate as a model of evaporation in the three latter coordinate systems.

The capillary potential is represented by ξ, the gravity potential by γ, the surface evaporation potential by ζ, and the side evaporation potential by ω. Hence, the potential for a system with any combination of these phenomena will be found by

$$\varphi = \xi + \gamma + \zeta + \omega. \tag{B.1.1}$$

Cartesian Coordinates

All of these potentials are derived in Chapter 3, and the phenomena are thoroughly compared to each other.

Capillary potential: The capillary potential for 1D-like flow gives rise to the Lucas–Washburn equation. We present its derivation in Eq. (3.3.6) and derive it alternatively in Eq. (E.1.14),

$$\tilde{\xi} = -\frac{\tilde{L} - \tilde{x}}{\tilde{L}}. \tag{B.1.2}$$

Gravity potential: The gravity potential is derived in Eq. (3.3.9), and is similarly linearly dependent on the spatial variable, however it does not drop off as the front length advances;

$$\tilde{\gamma} = \mathrm{Bo}_a \left(\tilde{L} - \tilde{x} \right). \tag{B.1.3}$$

Normal suface evaporation potential: The normal evaporation potential equation is derived around Eq. (3.3.13);

$$\tilde{\zeta} = -\frac{1}{2} \mathfrak{N}_\mathrm{n} \left(\tilde{x}^2 - \tilde{L}\tilde{x} \right). \tag{B.1.4}$$

Appendix B. Summary of Analytical Results

Some alternative discussion of the results of this equation are given in §4.3.3.

Side boundary evaporation potential: The derivation of the constant cross-section side evaporation potential culminates in Eq. (3.3.19), wherein the first potential with two-dimensional behavior is seen;

$$\tilde{\omega} = \mathfrak{N}_\mathrm{s}\tilde{L} \sum_{k=1}^{\infty} \left(\frac{4}{(2k-1)^2\pi^2} \right) \frac{\cosh\left((2k-1)\pi\frac{\tilde{y}}{\tilde{L}}\right)}{\sinh\left((2k-1)\pi\frac{1}{\tilde{L}}\right)} \sin\left((2k-1)\pi\frac{\tilde{x}}{\tilde{L}}\right), \qquad \text{(B.1.5)}$$

where sinh and cosh are the hyperbolic sine and cosine functions.

Elliptic Coordinates

The capillary potential for elliptic coordinates is derived in chapter 2, while the normal surface evaporation is effect is thoroughly detailed in chapter 4. The elliptic gravity and side evaporation potentials are not used in any of the results in this dissertation.

Capillary potential: The capillary potential is given originally in Eq. (2.3.5);

$$\tilde{\xi} = \frac{\eta - \eta_f}{\eta_f}. \qquad \text{(B.1.6)}$$

It is also used in Eq. (4.3.16).

Gravity potential: Here we give the restraining gravity potential for the elliptic coordinate system as one of several potentials which were not derived or used in this dissertation.

$$\tilde{\gamma} = \frac{4}{\pi}\mathrm{Bo}_a \sinh(\eta_f) \sum_{k=1}^{\infty} \frac{1}{1-(2k)^2} \left[\cosh(2k\eta) - \coth(2k\eta_f)\sinh(2k\eta)\right] \cos(2k\psi). \qquad \text{(B.1.7)}$$

Appendix B. Summary of Analytical Results

This is for the sake of thoroughness, ease of comparing the analytical solutions of other coordinate systems (such as in this case polar coordinates), and for any future extensions to the work by the authors or readers.

Normal suface evaporation potential: The normal surface evaporation potential in elliptic coordinates is given and described with Eq. (4.3.16), but is thoroughly derivedEq. (E.1.11);

$$\tilde{\zeta} = -\frac{1}{4}\mathfrak{N}_\mathrm{n}\left[\frac{\eta - \eta_f + \eta_f\cosh(2\eta) - \eta\cosh(2\eta_f)}{2\eta_f} + \frac{\sinh(\eta_f - \eta)\sinh(\eta)}{\cosh(\eta_f)}\cos(2\psi)\right].$$

(B.1.8)

This partial potential was the most critical to derive of this project.

Side boundary evaporation potential: The side evaporation potential for the elliptic coordinate system is;

$$\tilde{\omega} = -2\mathfrak{N}_\mathrm{s}\sum_{n=1}^{\infty}\frac{\eta_f\sinh(\eta_f)}{n^2\pi^2 + \eta_f^2}\left[\coth\left(n\pi\frac{\pi/2}{\eta_f}\right)\cosh\left(n\pi\frac{\psi}{\eta_f}\right) - \sinh\left(n\pi\frac{\psi}{\eta_f}\right)\right]\sin\left(n\pi\frac{\eta}{\eta_f}\right),$$

(B.1.9)

where coth is the hyperbolic cotangent function. This equation is not derived or used elsewhere.

Polar Coordinates

Section 5.3 applies the several velocity potentials for polar coordinates, with exception of the normal surface evaporation potential which is discussed in §4.3.1.

Capillary potential: The two-dimensional polar capillary potential was first considered, though not explicitly given, with the work in Sec. 2.3, but in §4.3.1 the

potential was derived with Eq. (4.3.3) as well as Eq (5.3.4);

$$\tilde{\xi} = \frac{\ln(\tilde{r}_f) - \ln(\tilde{r})}{\ln(\tilde{r}_f)}, \tag{B.1.10}$$

where $\ln(x)$ is the base-e logarithmic (*i.e.* natural log) function. This potential is closely analogous to the elliptic capillary potential, Eq. B.1.6.

Gravity potential: The restraining gravity potential for polar coordinates is derived in Eq. (F.1.11), and further described in Eq. (5.3.7);

$$\tilde{\gamma} = \frac{4}{\pi} \mathrm{Bo}_a \tilde{r}_f \sum_{j=1}^{\infty} \frac{1}{1 - (2j)^2} \frac{\tilde{r}_f^{4j} - \tilde{r}^{4j}}{(\tilde{r}_f)^{4j} - 1} \left(\frac{1}{\tilde{r}^{2j}} \right) \cos(2j\theta). \tag{B.1.11}$$

Normal suface evaporation potential: The polar normal surface evaporation potential is derived with Eq. (4.3.3);

$$\tilde{\zeta} = \frac{1}{4} \mathfrak{N}_\mathrm{n} \frac{\left(\tilde{r}_f^2 - 1\right) \ln(\tilde{r}) - (\tilde{r}^2 - 1) \ln(\tilde{r}_f)}{\ln(\tilde{r}_f)} \tag{B.1.12}$$

This equation has a very interesting symmetry between the quadratic and logarithmic terms.

Side boundary evaporation potential: The polar side evaporation potential is derived in Eq. (F.1.23), but it's application is discussed with Eq. (5.3.7);

$$\tilde{\omega} = -2\mathfrak{N}_\mathrm{s} \sum_{n=1}^{\infty} \frac{[1 - (-1)^n \tilde{r}_f] \ln(\tilde{r}_f)}{n^2 \pi^2 + (\ln(\tilde{r}_f))^2} \sin\left(n\pi \frac{\ln(\tilde{r})}{\ln(\tilde{r}_f)} \right)$$
$$\times \left[\coth\left(n\pi \frac{\pi/2}{\ln(\tilde{r}_f)} \right) \cosh\left(n\pi \frac{\theta}{\ln(\tilde{r}_f)} \right) - \sinh\left(n\pi \frac{\theta}{\ln(\tilde{r}_f)} \right) \right].$$

Cylindrical Coordinates

These potentials are not employed in this dissertation, however they can be used as a 1D-like asymptotic comparison to the 3D spherical and oblate spheroid solutions. Length scales are made dimensionless by the inlet radius, R.

Capillary potential: The capillary potential in cylindrical coordinates is readily found by a transformation of variables from Cartesian coordinates, Eq. (B.1.2);

$$\tilde{\xi} = -\frac{\tilde{L} - \tilde{z}}{\tilde{L}}. \tag{B.1.13}$$

Gravity potential: Similar to the capillary potential, the velocity potential for restraint by gravity is determined from transforming the coordinates of Eq. (B.1.3);

$$\tilde{\gamma} = \text{Bo}_a \left(\tilde{L} - \tilde{z} \right). \tag{B.1.14}$$

Side boundary evaporation potential: The side evaporation potential for loss of liquid through the side of a cylindrical porous medium was derived elsewhere;

$$\tilde{\omega} = \mathfrak{N}_{\text{s}} \tilde{L} \left(\frac{4}{\pi^2} \right) \sum_{k=1}^{\infty} \frac{1}{(2k-1)^2} \frac{\text{I}_0 \left((2k-1)\pi \frac{\tilde{r}}{\tilde{L}} \right)}{\text{I}_1 \left((2k-1)\pi \frac{1}{\tilde{L}} \right)} \sin \left((2k-1)\pi \frac{\tilde{z}}{\tilde{L}} \right), \tag{B.1.15}$$

where $\text{I}_k(x)$ is the modified Bessel function of the first kind.

Oblate Spheroid Coordinates

These potentials are useful for three dimensional expansions through flat circular inlets.

Capillary potential: The 3D oblate spheroid capillary potential is derived in Eq. (2.4.5);

$$\tilde{\xi} = -\frac{\arctan\left(\tanh\left(\frac{\eta_f}{2}\right)\right) - \arctan\left(\tanh\left(\frac{\eta}{2}\right)\right)}{\arctan\left(\tanh\left(\frac{\eta_f}{2}\right)\right)}, \tag{B.1.16}$$

where $\arctan(x)$ is the inverse tangent trigonometric function and $\tanh(x)$ is the hyperbolic tangent. It's resulting front velocity equation is further compared relative to Eq. (B.1.18).

Appendix B. Summary of Analytical Results

Gravity potential: The restraining gravity potential in oblate spheroid coordinates is

$$\tilde{\gamma} = -\text{Bo}_a \sinh(\eta_f) \sum_{n=0}^{\infty} \frac{(-1)^n(4n+1)}{(2n-1)(2n+2)} \frac{(2n)!}{2^{2n}(n!)^2}$$
$$\times \frac{\text{i}\,Q_{2n}(\text{i}\sinh(\eta_f))\,P_{2n}(\text{i}\sinh(\eta)) - P_{2n}(\text{i}\sinh(\eta_f))\,\text{i}\,Q_{2n}(\text{i}\sinh(\eta))}{\text{i}\,Q_{2n}(\text{i}\sinh(\eta_f))\,P_{2n}(0)}\,P_{2n}(\cos(\theta)).$$

$$(\text{B.1.17})$$

The functions P and Q are the Legendre functions of the first and second kinds, respectively. The collected terms $P_{2n}(\text{i}x)$ and $\text{i}\,Q_{2n}(\text{i}x)$ are real valued functions of x. This equation is not applied in any of the results in this dissertation.

Side boundary evaporation potential: The partial differential equation for the velocity potential in oblate spheroid coordinates does not yield a closed-form analytical solution, *i.e.* the root must be found for each eigenvalues in the infinite series.

Spherical Coordinates

The potentials for the spherical coordinate system are given in Sec. 5.4, with their applications.

Capillary potential: The capillary potential in spherical coordinates is first derived in Eq. (2.4.18), but also in Eq. (5.4.4);

$$\tilde{\xi} = -\frac{\tilde{r}_f - \tilde{r}}{\tilde{r}_f - 1}\frac{1}{\tilde{r}}.$$

$$(\text{B.1.18})$$

Gravity potential: The spherical restraining gravity potential is fully derived in Eq. (F.1.34), and detailed in Eq. (5.4.7);

$$\tilde{\gamma} = -\text{Bo}_a \tilde{r}_f \sum_{n=0}^{\infty} \frac{(-1)^n(4n+1)}{(2n-1)(2n+2)} \frac{(2n)!}{2^{2n}(n!)^2} \frac{\left(\frac{\tilde{r}_f}{\tilde{r}}\right)^{2n+1} - \left(\frac{\tilde{r}}{\tilde{r}_f}\right)^{2n}}{(\tilde{r}_f)^{2n+1} - \left(\frac{1}{\tilde{r}_f}\right)^{2n}}\,P_{2n}(\cos(\theta)). \quad (\text{B.1.19})$$

Side boundary evaporation potential: The side evaporation velocity potential for the spherical coordinate system is derived in Eq. (F.1.46) and further applied with Eq. (5.4.7);

$$\tilde{\omega} = -2\mathfrak{N}_{\mathrm{s}} \sum_{n=1}^{\infty} \frac{n\pi \left[(-1)^n \tilde{r}_f^{3/2} - 1\right]}{(n\pi)^2 + \left[\ln\left(\tilde{r}_f^{3/2}\right)\right]^2} \frac{\mathrm{P}_{n\pi/\ln\left(\tilde{r}_f\right)-1/2}(\cos(\theta))}{\left[n\pi/\ln(\tilde{r}_f) + 1/2\right] \mathrm{P}_{n\pi/\ln\left(\tilde{r}_f\right)+1/2}(0)} \frac{\sin\left(n\pi \frac{\ln(\tilde{r})}{\ln\left(\tilde{r}_f\right)}\right)}{\sqrt{\tilde{r}}}.$$

$$(\text{B.1.20})$$

Appendix C

Implementation of Lattice Boltzmann Methods

C.1 The Boltzmann Kinetic Equation

Statistical physics arose in part through the pioneering work of Ludwig Boltzmann in the 1870s. Boltzmann considered the effects of an ensemble of gas-like particles.[135] This was an important deviation from Newtonian mechanics where each gas could be modeled individually, however, Boltzmann realized the complexity (and unnecessary work) that this entailed.[9] His work ultimately proved that many macroscopic and thermodynamic relations can be derived directly from first principles.[10]

One of his key discoveries (along with the third law of thermodynamics and the arrow of time) was the Boltzmann transport equation;

$$\left[\partial_t + \mathbf{v} \cdot \partial_{\mathbf{x}} + \mathbf{F}^{\text{ext}} \cdot \partial_{\mathbf{p}}\right] f = \int \left(f_{1'} f_{2'} - f_1 f_2\right) g\sigma(g, \Omega) \, \mathrm{d}\Omega \, \mathrm{d}\mathbf{p}_2. \qquad (\text{C.1.1})$$

On the streaming (left) side of the equation, t is time, $\mathbf{v}$ is the microscopic velocity of the gas, $\mathbf{x}$ is the position, $\mathbf{F}^{\text{ext}}$ accounts for any external forces, $\mathbf{p}$ is the momentum,

f is the distribution function. On the collision side of the equation, $f_{1'}$ and $f_{2'}$ are the distribution functions of particles 1 and 2 at time $t + \delta_t$, respectively, while f_1 and f_2 is at time t (before collision), the The streaming portion of the equation accounts for the natural movement of un-inhibited particles through space including an external body forces. The collision integral adjusts for all possible collision angles and momenta that could change the distribution function.[13] Macroscopic physical variables are found by the moments of the distribution function;

$$\rho = m \int f \, \mathrm{d}\mathbf{v}, \tag{C.1.2a}$$

$$\mathbf{u} = \frac{m}{\rho} \int f\mathbf{v} \, \mathrm{d}\mathbf{v}, \tag{C.1.2b}$$

$$e = \frac{m}{\rho} \int f\frac{v^2}{2} \, \mathrm{d}\mathbf{v}, \tag{C.1.2c}$$

where ρ is the density, m is the unit mass, $\mathbf{u}$ is the macroscopic velocity, and e is the unit energy.

The Bhatnagar–Gross–Krook equation (BGK) in 1954 was an important development in the theory of statistical gas dynamics because its simplified approach to handling the collision operator.[106] BGK analyzed the collision as a deviation from the equilibrium distribution of the system;

$$\frac{\partial f}{\partial t} + \mathbf{v} \cdot \frac{\partial f}{\partial \mathbf{x}} + \mathbf{F}^{\text{ext}} \cdot \frac{\partial f}{\partial \mathbf{p}} = -\frac{f - f^{\text{eq}}}{\tau}. \tag{C.1.3}$$

The equilibrium, f^{eq} is calculated based on the thermodynamical properties of the system.

C.2 The Lattice Boltzmann Equation

The lattice Boltzmann method (LBM) is a computational technique for the simulation of fluid dynamics.* The method solves a discretized version of the Boltzmann equation

---

* The LBM is also discussed in Sec. 6.2.1.
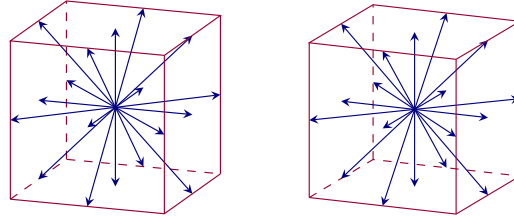
Figure C.1. Three-dimensional velocities of the D3Q19 Lattice Boltzmann model (stereoscopic images).

on a Cartesian lattice in space with an explicit time stepping routine to determine the fluid motion. These spatial properties allow the domains to be easily separated with only a small amount of edge communication necessary for each time step. Thus, LBM is very parallelizable for single-phase simulations of fluids even up to unsteady flow regimes and very irregular boundaries, such as porous media.*

The lattice Boltzmann method developed around 1988 as a probabilistic offshoot to a discrete fluid model called Lattice Gas Cellular Automata (LGCA). LGCA effectively models single particles on a discrete hexagonal lattice with only 6 possible velocities and a small number of collision rules. This method was fascinating because it showed full hydrodynamic phenomena as a deterministic result of the averaged locations and velocities of the discrete particles. The lattice Boltzmann method however emerged to correct limitations of LGCA such as difficult extension to three dimensions and failure at higher velocities. Furthermore, LBM was fit neatly in the theory as a continuum method with second-order convergence in space and time.

The lattice Boltzmann method contains several branches of core equations. The simplest form of the lattice Boltzmann equation (LBE) is the lattice–BGK equation which simplifies the calculation of the collision from a collision matrix into the deviation from the equilibrium distribution. This equation is suitable for many types of

---

* Parallel computation and LBM implementation is discussed in Sec. 7.2.2.
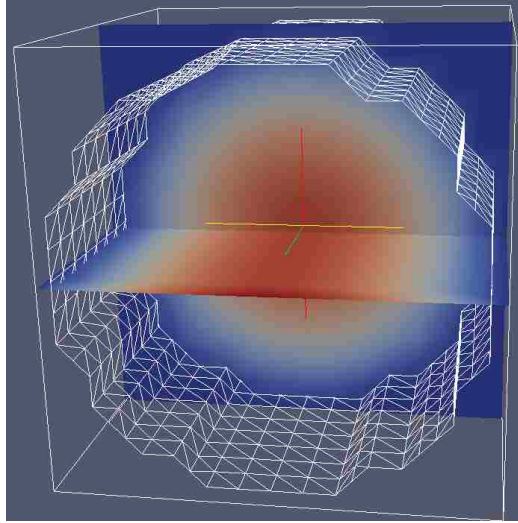
Figure C.2. 3D LBM simulation of single pore on 15 by 15 by 15 grid.

isothermal fluid flows especially laminar in porous media.[111] Below the equation is shown as a difference equation,

$$f_\alpha(\mathbf{x} + \mathbf{e}_\alpha \delta_t, t + \delta_t) = f_\alpha(\mathbf{x}, t) - \frac{f_\alpha(\mathbf{x}, t) - f_\alpha^{\text{eq}}(\mathbf{x}, t)}{\tau}, \qquad \text{(C.2.1)}$$

where $\mathbf{e}_\alpha$ are the discrete velocity vectors of the model. This difference equation form is easily codable because it will directly increment the local value. The commonly used three-dimensional lattice, D3Q19, is shown in Figure C.1. Note that $\mathbf{e}_0$ is no velocity—effectively the density of stationary fluid in the cell—and is at the center of the lattice cell. In Figure C.2 an example 3D simulation shown; it is the result of a modified MATLAB® code found online.

For our simulations we are using the two-dimensional nine velocity (D2Q9) model for the lattice Boltzmann equation. First, the domain must be initialized (some discussion on this shortly). In each time loop iteration we first calculate the macroscopic

variables which are determined from the moments of the distribution functions,

$$\rho = \sum_{i=0}^{8} f_\alpha,$$ (C.2.2a)

$$\mathbf{u} = \frac{1}{\rho} \sum_{i=0}^{8} f_\alpha \mathbf{e}_\alpha.$$ (C.2.2b)

Next, the equilibrium distribution is calculated from the quadratic approximation of the Maxwell–Boltzmann equilibrium;

$$f_\alpha^{\mathrm{eq}}(\mathbf{x}, t) = \omega_\alpha \rho(\mathbf{x}) \left(1 + 3 \frac{\mathbf{e}_\alpha \cdot \mathbf{u}}{c^2} + \frac{9}{2} \frac{(\mathbf{e}_\alpha \cdot \mathbf{u})^2}{c^4} - \frac{3}{2} \frac{\mathbf{u}^2}{c^2} \right).$$ (C.2.3)

where

$$\omega_\alpha = \begin{cases} \frac{4}{9}, & \alpha = 0; \\[2mm] \frac{1}{9}, & \alpha = 1, \ldots, 4; \\[2mm] \frac{1}{36}, & \alpha = 5, \ldots, 8, \end{cases}$$ (C.2.4)

are the weights of the different velocity directions, c is the speed of sound in the medium (usually $1/\sqrt{3}$). The collision step is calculated by recombining the streaming and equilibrium results,

$$f_\alpha(\mathbf{x}, t + \delta_t) = f_\alpha(\mathbf{x}, t) - \frac{f_\alpha(\mathbf{x}, t) - f_\alpha^{\mathrm{eq}}(\mathbf{x}, t)}{\tau}.$$ (C.2.5)

Finally, in the streaming step the distribution function values are transferred between the different neighboring lattice cells,

$$f_\alpha^{\mathrm{temp}}(\mathbf{x} + \mathbf{e}_\alpha \delta_t, t + \delta_t) = f_\alpha(\mathbf{x}, t + \delta_t),$$ (C.2.6)

and the distribution function is updated from the temporary distribution function.

The lattice is usually an equally spaced Cartesian grid. This limits the common LBM to systems where high resolution is not required in select subportions of the domain. Methods do exist to extend LBM domains to locally high-resolution, but are non-trivial to program and can defeat the purpose of computing over a simple lattice.

C.2.1 Alternative Collision Integration

Above we discussed the LBE with the Batnagar–Gross–Krook collision term, which is expressed

$$\Omega_{\text{BGK}} = -\frac{f_\alpha(\mathbf{x}, t) - f_\alpha^{\text{eq}}(\mathbf{x}, t)}{\tau}, \tag{C.2.7}$$

where Ω is the collision operator for the BGK. However, while this method is easy to implement, it does not perform well numerically for high advection flows, *e.g.* turbulent flows or some flows in complex porous media.*

The most common alternative method for is the multiple relaxation times (MRT) LBE. The MRT collision integral step is given generally by a collision matrix $\mathbf{S}$ operating on the deviation of the distribution functions from equilibrium,[†]

$$\boldsymbol{\Omega}_{\text{MRT}} = -\mathbf{S}\left[\mathbf{f}\left(\mathbf{x}, t\right) - \mathbf{f}^{\text{eq}}\left(\mathbf{x}, t\right)\right]. \tag{C.2.8a}$$

The Gram–Schmidt orthogonalization procedure is then applied to the collision matrix to find another matrix, $\mathbf{M}$, such that the collision matrix, $\hat{\mathbf{S}}$, is now diagonalized, or $\mathbf{S} = \mathbf{M}^{-1}\hat{\mathbf{S}}\mathbf{M}$, and the form of the collision integral becomes

$$= -\mathbf{M}^{-1}\hat{\mathbf{S}}\mathbf{M}\left[\mathbf{f}\left(\mathbf{x}, t\right) - \mathbf{f}^{\text{eq}}\left(\mathbf{x}, t\right)\right]. \tag{C.2.8b}$$

The MRT LBE is given by

$$\mathbf{f}\left(\mathbf{x} + \mathbf{e}\delta_t, t + \delta_t\right) = \mathbf{f}\left(\mathbf{x}, t\right) - \left[\mathbf{M}^{-1}\hat{\mathbf{S}}\right]\left[\mathbf{m}\left(\mathbf{x}, t\right) - \mathbf{m}^{\text{eq}}\left(\mathbf{x}, t\right)\right] + \mathbf{F}, \tag{C.2.9}$$

where the moments of the distribution functions are $\mathbf{m} = \mathbf{M}\mathbf{f}$. For the D2Q9, the equilibrium moments are given by the vector,[136]

$$\mathbf{m}^{\text{eq}} = \left[\rho \quad e^{(\text{eq})} \quad \varepsilon^{(\text{eq})} \quad j_x \quad q_x^{(\text{eq})} \quad j_y \quad q_y^{(\text{eq})} \quad p_{xx}^{(\text{eq})} \quad p_{xy}^{(\text{eq})}\right]^{\mathsf{T}}, \tag{C.2.10}$$

---

* Thus, the following discussion is important to the future work of Chapter 7.   † Here we use alternate vector notation where the distribution function f_α is represented by $\mathbf{f}$ and the tensor operation, $S_{\alpha\beta}f_\beta$, is $\mathbf{Sf}$.

where

$$e^{(\text{eq})} = -2\rho + \frac{3}{\rho}\left(j_x^2 + j_y^2\right), \tag{C.2.11a}$$

$$\varepsilon^{(\text{eq})} = \rho - \frac{3}{\rho}\left(j_x^2 + j_y^2\right), \tag{C.2.11b}$$

$$q_x^{(\text{eq})} = -j_x, \tag{C.2.11c}$$

$$q_y^{(\text{eq})} = -j_y, \tag{C.2.11d}$$

$$p_{xx}^{(\text{eq})} = \frac{1}{\rho}\left(j_x^2 - j_y^2\right), \tag{C.2.11e}$$

$$p_{xy}^{(\text{eq})} = \frac{1}{\rho}j_x j_y. \tag{C.2.11f}$$

Note that $\mathbf{j}$ is the momentum flux given by,

$$\mathbf{j} = \sum_\alpha f_\alpha \hat{\mathbf{e}}_\alpha. \tag{C.2.12}$$

The related collision moment matrix is

$$\mathbf{M} = \begin{bmatrix} 1 & 1 & 1 & 1 & 1 & 1 & 1 & 1 & 1 \\ -4 & -1 & -1 & -1 & -1 & 2 & 2 & 2 & 2 \\ 4 & -2 & -2 & -2 & -2 & 1 & 1 & 1 & 1 \\ 0 & 1 & 0 & -1 & 0 & 1 & -1 & -1 & 1 \\ 0 & -2 & 0 & 2 & 0 & 1 & -1 & -1 & 1 \\ 0 & 0 & 1 & 0 & -1 & 1 & 1 & -1 & -1 \\ 0 & 0 & -2 & 0 & 2 & 1 & 1 & -1 & -1 \\ 0 & 1 & -1 & 1 & -1 & 0 & 0 & 0 & 0 \\ 0 & 0 & 0 & 0 & 0 & 1 & -1 & 1 & -1 \end{bmatrix}. \tag{C.2.13}$$

The diagonalized collision matrix with the relaxation times is commonly defined,

$$\hat{\mathbf{S}} = \text{diag}\left(\begin{bmatrix} 1 & 1.1 & 1 & 1 & 1.2 & 1 & 1.2 & 1/\tau & 1/\tau \end{bmatrix}\right). \tag{C.2.14}$$

C.2.2 Body forces

There are several important physical conditions that may be added to a lattice Boltzmann model. In some systems the primary driving force is gravity. To incorporate gravity into the LBGK method, the velocity is calculated before the equilibrium step to include the acceleration due to gravity on the new velocity, or

$$\mathbf{u}^{\text{eq}} = \mathbf{u} + \frac{\tau \mathbf{F}}{\rho}, \qquad (\text{C.2.15})$$

where $\mathbf{F} = m\mathbf{g}$ in this case. The force may also be incorporated directly into the LBE as we will see below with the lattice Poisson–Boltzmann method.[*]

C.2.3 Boundary Conditions

Below we outline the boundary conditions which have been used in this dissertation.[†] Many of these boundary conditions are similar to those given in Sukop and Thorne.[111] Each condition is only described for a single boundary, though they can all be transformed to apply to all side boundaries of the domain. The boundary conditions are generally referred to by the cardinal directions of west, north, east, and south on the right, top, left, and bottom of the domain, respectively. We do not discuss any corner cases, which often involve adapting for two different kinds of boundary conditions simultaneously, nor is the free-slip boundary condition covered.

Solid bounce back boundary condition

The solid bounce back boundary condition is the condition applied at all solid point, wherein the solid interface affects the flow half-way between the liquid and solid lattice

---

[*] Gravity is the primary driving force in Ch. 7.   [†] These boundary conditions are also briefly summarized in Sec. 6.2.1.
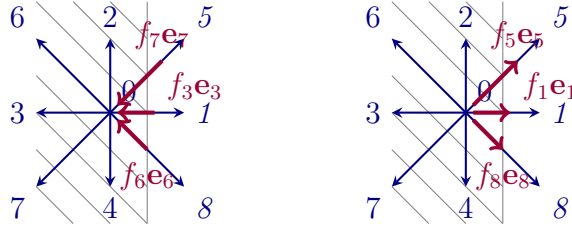
Figure C.3. 2D bounce back boundary condition.

nodes. The method simply reverses the direction of the distribution function $f_{\alpha'}$ from the previous direction prior to the collision f_{α}^*. As an equation,

$$f_{\alpha'} = f_{\alpha}^*. \tag{C.2.16}$$

For example, if we define in the algorithm some temporary variable f^{temp} at any solid node next to a liquid then we may exchange the opposite distribution functions during collision;[111]

$$f^{\text{temp}} = f_1, \tag{C.2.17a}$$

$$f_1 = f_3, \tag{C.2.17b}$$

$$f_3 = f^{\text{temp}}. \tag{C.2.17c}$$

Here velocity direction 1 is opposite to 3; this may be applied to all reflecting pairs of distribution functions.

Periodic boundary condition

The periodic boundary condition transfers information between opposite edges of the lattice. For example, at the north boundary of the domain, the distribution functions must be advected from the top nodes to the bottom ones. On internal lattice nodes, the distribution functions moving vertically are transferred from nodes

j to $j + 1$, where j is the lattice position in the y-direction. At the north boundary, however, information is moved from from ℓ_y to 1, where ℓ_y being the upper-most lattice point. Specifically, the distribution functions at a given point $\mathbf{x} = [i, \ell_y]$ on the north boundary are advected in the form,[111]

$$f_2([i, 1], t) = f_2([i, \ell_y], t), \tag{C.2.18a}$$

$$f_5([i + 1, 1], t) = f_5([i, \ell_y], t), \tag{C.2.18b}$$

$$f_6([i - 1, 1], t) = f_6([i, \ell_y], t). \tag{C.2.18c}$$

Conversely for a southern boundary, the formulas for the x-direction may be similarly determined by working with $i = 1$ and ℓ_x.

In parallel computation, the periodic boundary condition increases the total amount of communication by necessitating transfer of this information between upper/lower and left/right bounding computational cells. So using other boundaries which eliminate periodic conditions may reduce the run-time of parallel codes, and increase code design flexibility.

These first two boundary conditions are sufficient for a simulation of simple porous media flow. The following boundary conditions significantly increase the variety of simulations which are possible to be run.

Pressure boundary condition

In general, for a given non-corner boundary there are three distribution functions at each lattice node which are unknown because they are not received from neighboring nodes in the streaming process. Naturally, the three degrees of freedom must be constrained by three equations and three knowns; the equations are the density and the velocity expressions at the given node. This is true of both pressure and velocity boundary conditions, it is merely a variation of the three knowns which distinguishes the two boundary conditions.
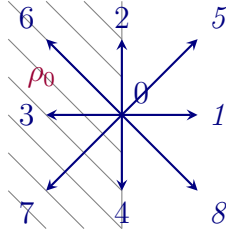
Figure C.4. 2D velocities for the pressure boundary condition applied to the west wall.

Now consider the pressure boundary condition, which for lattice Boltzmann simulations means a density boundary condition because pressure and the density are directly related.[111] So for a set density ρ_0, we also have the local density equation

$$\rho_0 = \sum_\alpha f_\alpha. \tag{C.2.19}$$

In addition the velocity is determined from

$$\mathbf{v} = \frac{1}{\rho} \sum_\alpha f_\alpha \mathbf{e}_\alpha. \tag{C.2.20}$$

Here we define the velocity at this boundary node to be $\mathbf{v} = v^* [\cos(\theta)\hat{\mathbf{i}} + \sin(\theta)\hat{\mathbf{j}}]$, where the angle θ is a prescribed direction of the flow as the common angle counterclockwise from the x-axis. The final constraint on f_α is most commonly provided by the Zou and He[112] non-equilibrium condition as we will exemplify below.

As an example, consider the west boundary of the domain, wherein the unknown distribution functions are f_1, f_5, f_8 as illustrated in Figure C.4. The non-equilibrium values of the distribution functions normal and anti-normal to the boundary are set equal;

$$f_1 - f_1^{\text{eq}} = f_3 - f_3^{\text{eq}}. \tag{C.2.21}$$

With the three previous equations the unknown distribution functions are solved via
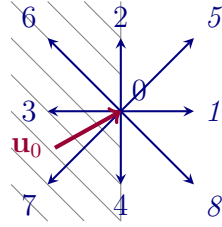
Figure C.5. 2D velocities for the velocity boundary condition applied to the west wall.

the effective fluid velocity, v^*,

$$v^* = \frac{\rho_0 - (f_0 + f_2 + f_4) - 2(f_3 + f_6 + f_7)}{\rho_0 \cos(\theta)}, \tag{C.2.22a}$$

$$f_1 = f_3 + \frac{2}{3}\rho_0 v^* \cos(\theta), \tag{C.2.22b}$$

$$f_5 = f_7 + \frac{1}{2}(-f_2 + f_4) + \frac{1}{2}\left[\frac{1}{3}\cos(\theta) + \sin(\theta)\right]\rho_0 v^*, \tag{C.2.22c}$$

$$f_8 = f_6 + \frac{1}{2}(f_2 - f_4) + \frac{1}{2}\left[\frac{1}{3}\cos(\theta) - \sin(\theta)\right]\rho_0 v^*. \tag{C.2.22d}$$

This boundary condition works for values of θ near the direction normal to the boundary surface, but fails when the angle is parallel to the boundary.

Velocity boundary condition

For the velocity boundary condition, we set

$$\mathbf{u}_0 = \begin{bmatrix} u_0 \\ v_0 \end{bmatrix}. \tag{C.2.23}$$

where u_0 and v_0 are the velocities in x- and y-directions.[111] The total velocity is alternatively related through $|\mathbf{u}_0| = \sqrt{u_0^2 + v_0^2}$ with $\theta = \arctan(v_0/u_0)$ similar to the pressure BC above. The nodal density equation,

$$\rho^* = \sum_\alpha f_\alpha, \tag{C.2.24}$$

and velocity equation,

$$\mathbf{u}_0 = \frac{1}{\rho^*} \sum_\alpha f_\alpha \mathbf{e}_\alpha, \tag{C.2.25}$$

once again are the relations which resolve the degrees of freedom. As shown in Figure C.5, for the west wall, we again have the unknowns f_1, f_5, f_8 and the intermediate variable, ρ^*. The Zou and He non-equilibrium balance is the same, $f_1 - f_1^{\text{eq}} = f_3 - f_3^{\text{eq}}$, and the resulting distribution functions for prescribed fluid velocity are[112]

$$\rho^* = \frac{(f_0 + f_2 + f_4) + 2(f_3 + f_6 + f_7)}{1 - u_0}, \tag{C.2.26a}$$

$$f_1 = f_3 + \frac{2}{3} u_0 \rho^*, \tag{C.2.26b}$$

$$f_5 = f_7 + \frac{1}{2}(-f_2 + f_4) + \frac{1}{2}\left(\frac{1}{3}u_0 + v_0\right)\rho^*, \tag{C.2.26c}$$

$$f_8 = f_6 + \frac{1}{2}(f_2 - f_4) + \frac{1}{2}\left(\frac{1}{3}u_0 - v_0\right)\rho^*. \tag{C.2.26d}$$

The no-flux condition normal to the boundary is determined by setting $u_0 = v_0 = 0$.

Open outlet boundary condition

In the open outlet boundary condition the edge nodes do not preserve information and effectively forget all information at each step as if the fluid particles simply left the domain without any future interaction. This is implemented by setting the values of the distribution functions at the boundary equal to that of the nearest neighboring node in the column or row next to the boundary. For example, if we are along the west boundary of a 2D domain then we are at the coordinate ℓ_x—the farthest node in the x-direction—and the next nearest node would then be at $\ell_x - 1$. So in the implementation, once the advection has been carried out on all the internal lattice nodes, we apply to the west boundary nodes the rule

$$f_\alpha([\ell_x, y], t) = f_\alpha([\ell_x - 1, y], t), \tag{C.2.27}$$

for all values of y and i at the given time t. This boundary condition is only useful in special cases, particularly in the multi-species models, because in the bulk fluid it can result in unphysical mass-loss through the boundary.

All of the above boundary conditions may also be applied to the multispecies methods discussed below in Sec. C.3.1.

C.2.4   Multiphase Fluids

Multiphase fluid systems (*e.g.* liquid water with vapor) occur in conjunction with numerous kinds of porous media such as soils, filters, and corroding pores.[61,69] For the LBM, multiphase systems require determination of the strength of interaction between the matter in neighboring cells. The Shan and Chen multiphase model, also known as the pseudo-potential method, uses an inter-particle force calculated by[137]

$$\mathbf{F}\left(\mathbf{x}, t\right) = -G\psi(\mathbf{x}, t) \sum_{\alpha=1}^{8} w_\alpha \psi(\mathbf{x} + \mathbf{e}_\alpha \delta_t, t) \mathbf{e}_\alpha. \tag{C.2.28}$$

The ideal gas equation of state is $P = c_s^2 \rho$.[11] In the pseudo-potential method, the equation of state is similar to the van der Waals equation of state;[66]

$$P = \frac{\rho}{3} + \frac{G}{6}\psi^2, \tag{C.2.29}$$

where the additional second term is the attractive/repulsive non-linear term. The form of the potential must be specified, and we use the exponential inter-particle potential

$$\psi(\rho) = \psi_0 \exp\left(\frac{-\rho_0}{\rho}\right), \tag{C.2.30}$$

although alternative potentials are used such as $\psi(\rho) = \rho$. The particle-wall force between solid points and fluid particles may be calculated in a similar way with the Martys and Chen model,[115,116]

$$\mathbf{F}_{\text{ads}}(\mathbf{x}, t) = -G_{\text{ads}}\psi(\mathbf{x}, t) \sum_\alpha w_\alpha s(\mathbf{x} + \mathbf{e}_\alpha \delta_t) \mathbf{e}_\alpha. \tag{C.2.31}$$

(a) Early time density variation.

(b) Surface and bulk condensation.

(c) Remaining droplets.

(d) Single equilibrium droplet.
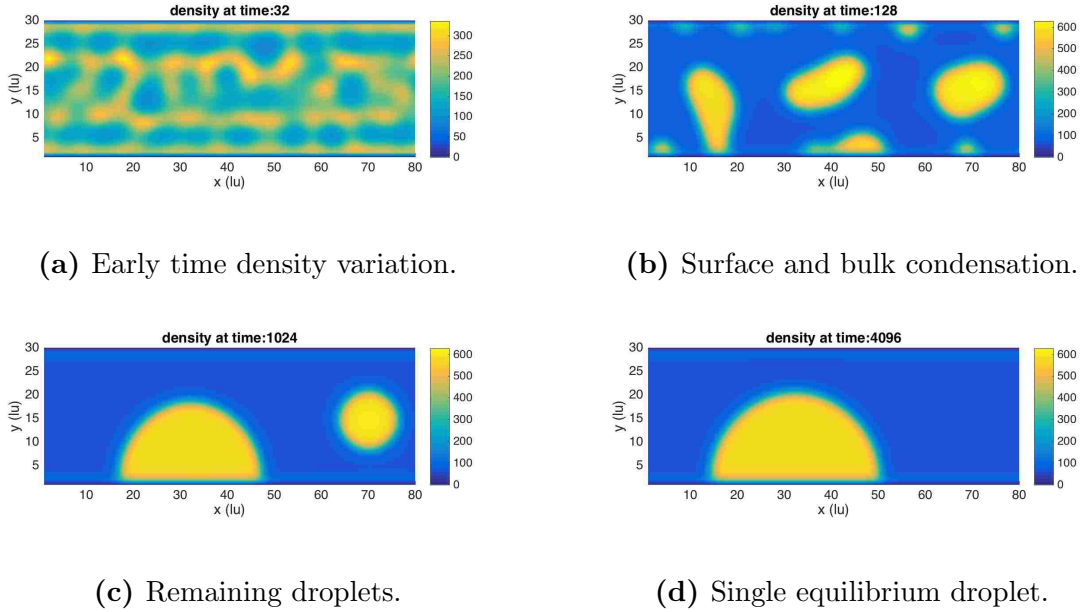
Figure C.6. Multi-phase droplet condensation model.

Other multiphase and fluid-solid interaction models exist, including the color gradient, free energy, and interface tracking models.[137] The interaction of values between neighboring cells which is critical in multiphase models especially near solid/liquid/gas interfaces, makes parallelizing the system more difficult due to higher communication load[111]*

In Figure C.6 we show an example simulation of this two phase model with hydrophilic behavior on the solid boundaries above and below (periodic BCs are applied on the left and right). Initial perturbations in the density (Figure C.6a) cause instabilities in the fluid which drive condensation both on the surface and in the bulk (b). Most of the droplets proceed to coalesce into a minimal number of droplets (c). Finally (d), fluid from the remaining drops continues to slowly evaporate and condense, which results in mass being added to the larger drop, eventually consuming

---

* These methods are further applied in Sec. 6.3.1.

the smaller.

C.3 Coupling Additional Physics to the Lattice Boltzmann Fluid Equation

C.3.1 Species transport

The dilute multispecies lattice Boltzmann method utilizes the lattice BGK equation for each additional species, σ,[111]

$$g_\alpha\left(\mathbf{x} + \mathbf{e}_\alpha \delta_{t,D_\sigma}, t + \delta_{t,D_\sigma}\right) - g_\alpha\left(\mathbf{x}, t\right) = -\frac{1}{\tau_{D_\sigma}}\left[g_\alpha\left(\mathbf{x}, t\right) - g_\alpha^{\text{eq}}\left(\mathbf{x}, t\right)\right]. \tag{C.3.1}$$

where g_α^σ is the non-solvent species distribution function, and the relaxation time is related to the diffusivity by $D_\sigma = (\tau_{D_\sigma} - 1/2)/3$. Here we are only considering a non-ionic species. Since we may assume that this dilute species is principally interacting with the solvent, the equilibrium calculation is simplified to

$$g_\alpha^{\sigma,\text{eq}} = w_\alpha C_\sigma\left(1 + 3\mathbf{e}_\alpha \cdot \mathbf{u}\right). \tag{C.3.2}$$

Here the species concentration (alternatively the density) is the zeroth moment of the species distribution function,

$$C_\sigma = \sum_{\alpha=0}^{8} g_{\sigma,\alpha}. \tag{C.3.3}$$

Because of the lower order of the equilibrium function, it is not necessary to use the more complex boundary conditions described above in Sec. C.2.3. Given a Dirichlet boundary condition with constant concentration, $\bar{C}_\sigma$, the effective concentration, C'_σ, at that boundary is[111]

$$C'_\sigma = \frac{\bar{C}_\sigma - \sum_{\alpha \in S_k} g_{\sigma,\alpha}}{\sum_{\alpha \in S_u} w_\alpha}, \tag{C.3.4}$$

(a) Velocity profile.   **(b)** Instantaneous concentration.
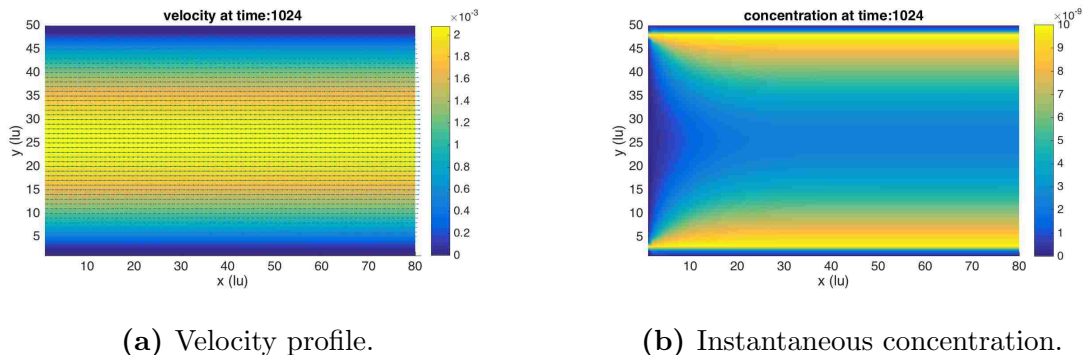
Figure C.7. LBM model of flow between plates with transient species diffusion from walls.

where S_k is the set of known distribution functions and S_u are the unknowns. The remaining distribution functions are then calculated $g_{\sigma,\alpha} = \omega_\alpha C'_\sigma$, where ω_α is given above in Eq. (C.2.4). This is equally applicable to an internal source condition.

In Figure C.7 we show an example simulation using the multispecies method coupled with net flow. Solid boundaries at the top and bottom resist flow, but are permeable to and diffusing a soluble species in the flowing solvent. A pressure differential across the domain drives the Poisuielle flow through the channel from right to left resulting in the ordinary parabolic velocity profile (Fig. C.7a). With a negligible concentration of the solute at the inlet and an open outlet on the right (b), we see the species building up in the channel, but the pure solvent at the inlet preventing the whole channel from being saturated.

C.3.2   Reacting Flows

Reacting fluids in the LBM are constrained by the ordinary conservation properties of mass and momentum. For a given reactive process, the collision operator is split

into the two terms of the reactive and non-reactive processes

$$\Omega^\sigma = \Omega^{\sigma,NR} + \Omega^{\sigma,R}. \tag{C.3.5}$$

The nonreactive operator, $\Omega^{\sigma,NR}$, (the equilibrium operator and force terms) are known from ordinary fluid processes, while the reacting collision operator, $\Omega^{\sigma,R}$ accounts for the additional effects on the distribution functions due to the reactions. The moments of on the reacting operator are also conserved because the operator itself conserves mass and momentum,

$$\sum_\sigma M_\sigma \sum_\alpha \Omega_\alpha^{\sigma,R} = 0, \tag{C.3.6a}$$

$$\sum_\sigma M_\sigma \sum_\alpha \Omega_\alpha^{\sigma,R} \mathbf{e}_\alpha = 0. \tag{C.3.6b}$$

As an example, consider the first order reaction

$$\mathrm{A} \to \mathrm{B}, \tag{C.3.7}$$

with a rate constant k. The ordinary kinetic equations are

$$\frac{\mathrm{d}C_A}{\mathrm{d}t} = -kC_A, \tag{C.3.8a}$$

$$\frac{\mathrm{d}C_B}{\mathrm{d}t} = kC_A. \tag{C.3.8b}$$

Adding the effective loss/gain of the reaction to the separate component LBEs, we have

$$g_\alpha^A(\mathbf{x} + \mathbf{e}_\alpha \delta_t, t + \delta_t) - g_\alpha^A(\mathbf{x}, t) = \frac{1}{\tau_A} \left[g_\alpha^A(\mathbf{x}, t) - g_\alpha^{A,\mathrm{eq}}(\mathbf{x}, t) \right] - kg_\alpha^A(\mathbf{x}, t), \tag{C.3.9a}$$

$$g_\alpha^B(\mathbf{x} + \mathbf{e}_\alpha \delta_t, t + \delta_t) - g_\alpha^B(\mathbf{x}, t) = \frac{1}{\tau_B} \left[g_\alpha^B(\mathbf{x}, t) - g_\alpha^{B,\mathrm{eq}}(\mathbf{x}, t) \right] + kg_\alpha^A(\mathbf{x}, t). \tag{C.3.9b}$$

Higher order reactions and systems of more parameters may also be implemented. Alternative methods of carrying out the reactions include coupling with a Lax–Wendroff method to handle the multiple species.[118]

Say we have a reacting process where the rate in the bulk fluid, k_f, differs from the rate at a catalytic wall, k_w. Then for a two dimensional model a given fluid node will have a given number solid neighbors at its sides, n_s, and at its corners, n_c. Weighting each of the neighboring nodes, the reaction rate k is computed as an effective average of these bounding rates,

$$k(\mathbf{x}) = \frac{\left[\left(\sum_{\alpha\neq0}\omega_\alpha\right) - \omega_c n_c(\mathbf{x}) - \omega_s n_s(\mathbf{x})\right] k_f + \left[\omega_c n_c(\mathbf{x}) + \omega_s n_s(\mathbf{x})\right] k_w}{\sum_{\alpha\neq0}\omega_\alpha}, \quad \text{(C.3.10)}$$

where the denominator normalizes the effects of the bounding nodes. For the D2Q9 method, the surface reaction reaction is then implemented with,

$$k(\mathbf{x}) = \frac{9}{5}\left\{\left[\frac{5}{9} - \frac{1}{36}n_c(\mathbf{x}) - \frac{1}{9}n_s(\mathbf{x})\right] k_f + \left[\frac{1}{36}n_c(\mathbf{x}) + \frac{1}{9}n_s(\mathbf{x})\right] k_w\right\}. \quad \text{(C.3.11)}$$

This is under the assumption that all reactions are based on collisions between neighboring nodes. For the case of local node being included then the formula is $\sum_\alpha \omega_\alpha = 1$ instead of $\sum_{\alpha\neq0}\omega_\alpha$. This model does not take into account solids which change the order of the reaction.*

To demonstrate the model in Figure C.8 the solid surface reaction model is applied for flow and diffusion around a circular particle. The domain is initially pure solvent and the reaction is first order. At first only a small amount of reactant enters the domain from the left side and slowly reacts with itself in the bulk causing a low concentration wave of product coming from the left (Fig. C.8a). When the reactant reaches the particle surface the reaction rate increases and the product is rapidly generated diffusing from the particle wall (b). Over time the product builds up around the particle and then diffuses throughout the bulk (c). The reaction takes place at such a small magnitude that the concentration of reactant appears virtually identical as with diffusion around a particle (d).

---

* This method is applied in Sec. 6.3.2.

(a) Early concentration of product.

(b) Beginning surface reaction.

(c) Late surface reaction.

(d) Concentration of reactant.
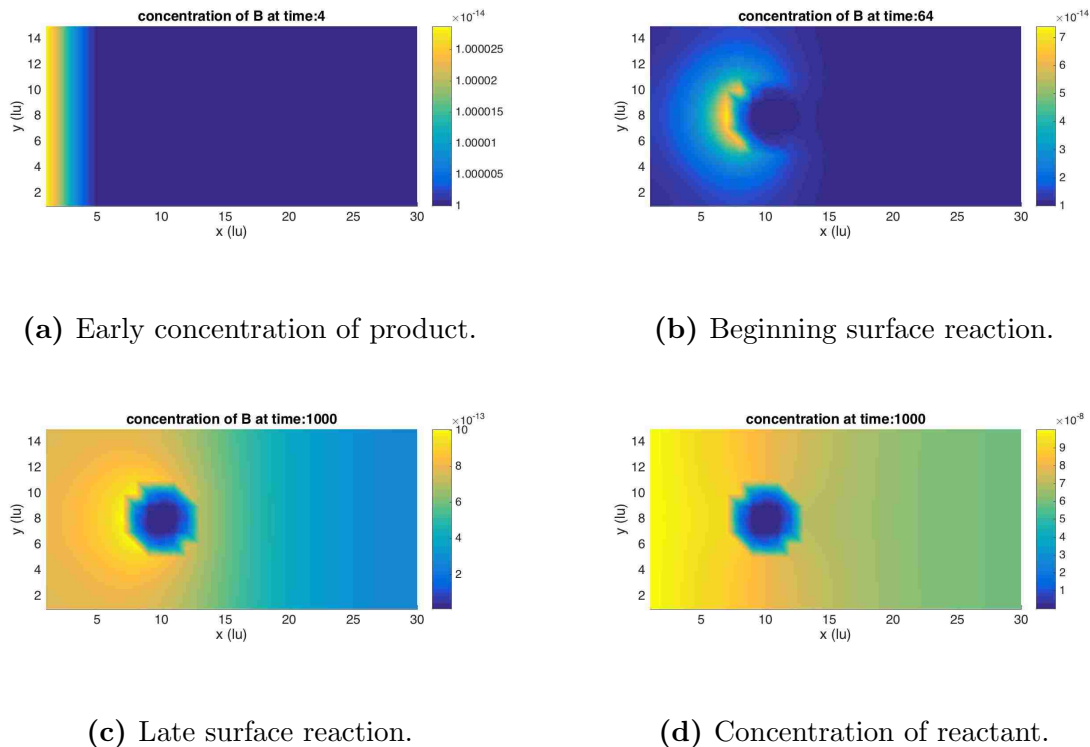
Figure C.8. Reaction-diffusion at a catalytic particle surface.

C.3.3 Solid Dissolution Partial Permeability Model

In our model of the dissolution process of a solid, the solid nodes turn to progressively turn into liquid nodes, with the solid matter transformed into solvated species. To account for partially liquid nodes, we used the partial fluid permeability model developed generally for porous media.[111] This effectively allows some fraction of particles to move like an ordinary fluid while others are bounced back. In place of the ordinary streaming step with bounce-back boundary condition we have an intermediate streaming function f_α^{**}, which then may be bounced back fractionally as a function

of the permeability of that node (which is a function of the solid fraction);

$$f_\alpha^{**}(\mathbf{x}, t + \delta_t) = f_\alpha^*(\mathbf{x}, t) + \frac{1}{\tau} \left[f_\alpha^{\text{eq}}(\mathbf{x}, t) - f_\alpha^*(\mathbf{x}, t) \right], \tag{C.3.12a}$$

$$f_\alpha(\mathbf{x}, t + \delta_t) = f_\alpha^{**}(\mathbf{x}, t + \delta_t) + k_{\text{perm}} \left[f_{\alpha'}^{**}(\mathbf{x} + \mathbf{e}_\alpha \delta_t, t + \delta_t) - f_\alpha^{**}(\mathbf{x}, t + \delta_t) \right]. \tag{C.3.12b}$$

The permeability and solid fraction relation is quadratic, $k_{\text{perm}} = n_{\text{s}}^2$, for dissolving surfaces and $n_{\text{s}} = 1$ is a solid node and zero if it is not. This quadratic relation is specifically for a solid boundary layer and not applicable for porous media, generally. The implementation of ordinary solid bounce-back boundary condition may still be used for non-dissolving solids.

The solid dissolution rate, Δn_{s}, is calculated as a first order function of the local fluid concentration and in neighboring lattice cites,

$$\Delta n_{\text{s}}(\mathbf{x}) = -k \sum_i \omega_\alpha \frac{C_s - C_i}{C_s} \left[1 - n_{\text{s}}(\mathbf{x}_{n,i}) \right], \tag{C.3.13}$$

for neighbor i and C_s is the saturated concentration of the species. The quantity of solid is then directly translated into an added local concentration of solvated species;

$$\Delta C_{\text{liq}} = \Delta n_{\text{s}} C_{\text{solid}}, \tag{C.3.14}$$

where C_{solid} is concentration of the solid (essentially ρ_{solid}). The neighboring nodes are used as a means to allow the dissolution can propagate deeper into the solid.*

In Figure C.9 the method is applied to a dissolving channel wall. The fluid flows through the channel in a laminar, parabolic flow profile (Fig. C.9a) which begins to remove solid from the wall (b). We see the flow dissolves the solid away at an approximately linear rate (c), until only the non-dissolving channel walls remain (d). This example of dissolution is similar to Kang's models of dissolving pores.[120]

---

* Sec. 6.3.3 discusses the application of this method to pitting corrosion.

(a) Early channel velocity.

(b) Early dissolution of first solid layer.

(c) Progressing solid dissolution.

(d) Cleared fluid channel.
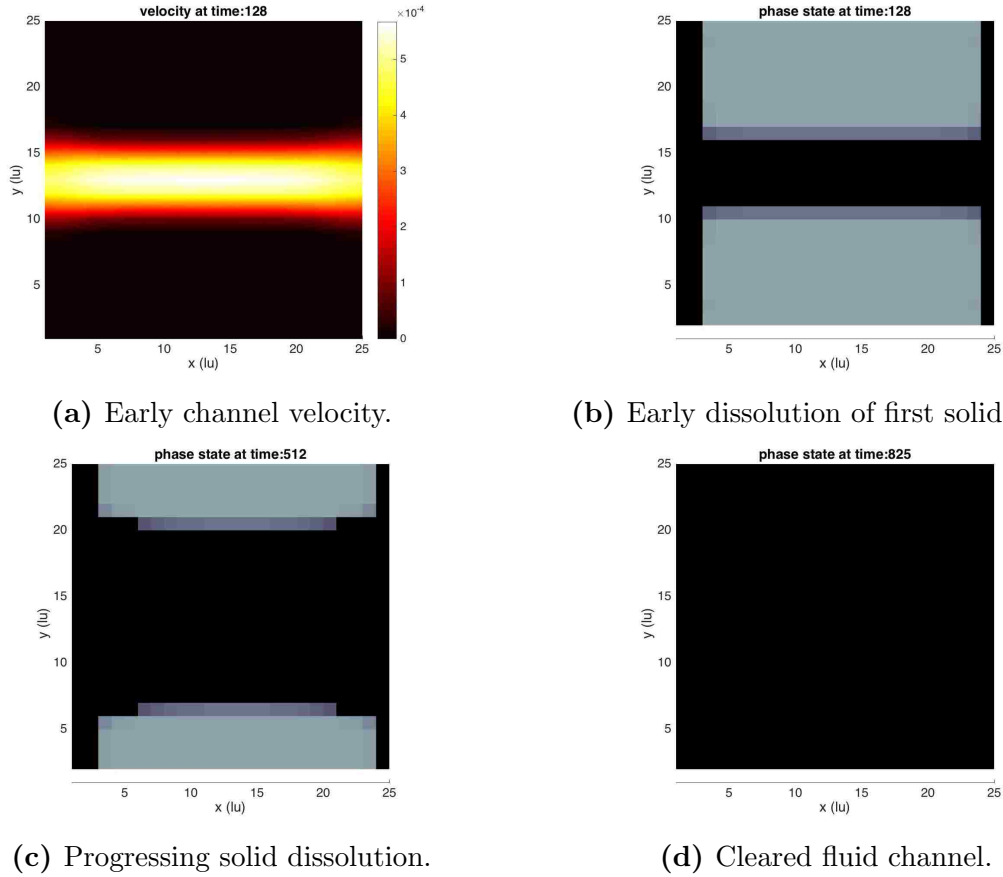
Figure C.9. Simulated dissolution of a soluble solid in a channel. Total white is a non-dissolvable solid, lightest gray is a fully dissolvable solid node, black is liquid, and other shades of gray are partially liquid solid nodes.

C.3.4 Electrochemistry

The electric potential has as significant effect on the behavior of charged and polar fluids. The Poisson equation describes the effective behavior of the electric potential in a dielectric medium,[121]

$$\nabla^2 \Psi = -\frac{1}{\varepsilon_r \varepsilon_0} \sum_\sigma e z_\sigma C_\sigma, \qquad (C.3.15)$$

where Ψ is the potential, ε_r is the relative permittivity, ε_0 is the vacuum permittivity, e is the charge of the electron, z_σ is the charge number of ion σ, and C_σ is the local concentration of the ion. Now according to Boltzmann statistics, for dilute electrolytes in solution the charge density is related to the potential via

$$C_\sigma = C_{\sigma,\infty} e^{-\frac{e z_\sigma \Psi}{k_b T}}, \tag{C.3.16}$$

where k_b is the Boltzmann constant, and T is the temperature. Substituting into the Poisson equation we get the non-linear Poisson–Boltzmann equation (PBE),

$$\nabla^2 \Psi = -\frac{1}{\varepsilon_r \varepsilon_0} \sum_\sigma z_\sigma e n_{\sigma,\infty} \exp\left(-\frac{z_\sigma e}{k_b T} \Psi\right), \tag{C.3.17}$$

where $n_{\sigma,\infty}$ is the number density of the ions in the bulk solution. This equation dictates the behavior of the electric potential in an ionic fluid.

To make a well-posed computational method, Lattice Poisson–Boltzmann Equation (LPBE)[123] is based on the convergence of a time-dependent form of the Poisson–Boltzmann Equation

$$\frac{\partial \Psi}{\partial t} = \nabla^2 \Psi + \frac{\rho_e}{\varepsilon_r \varepsilon_0}. \tag{C.3.18}$$

This describes a virtual diffusion of potential. Discretizing the electric potential into lattice vectors

$$\Psi = \sum_\alpha \left(h_\alpha + \frac{1}{2}\delta_{t,\Psi}\omega_\alpha h_{\text{RHS}}\right), \tag{C.3.19}$$

gives the LPBE

$$h_\alpha\left(\mathbf{x} + \mathbf{e}_\alpha \delta_{t,\Psi}, t + \delta_{t,\Psi}\right) - h_\alpha\left(\mathbf{x}, t\right) = -\frac{1}{\tau_\Psi}\left[h_\alpha\left(\mathbf{x}, t\right) - h_\alpha^{\text{eq}}\left(\mathbf{x}, t\right)\right] + \left(1 - \frac{0.5}{\tau_\Psi}\right)\delta_{t,\Psi}\omega_\alpha h_{\text{RHS}}. \tag{C.3.20}$$

The h_{RHS} accounts for the Boltzmann statistical charge density, which is a sink term in the above diffusion equation. (In principle, the LPBE may be modified to use other media such as semiconductors.) For the idealized case of 1:1 electrolyte solution the charge density is simplified to[122]

$$h_{\text{RHS}} = \frac{2 n_\infty z e}{\varepsilon_r \varepsilon_0} \sinh\left(\frac{z e}{k_b T} \Psi\right), \tag{C.3.21}$$

This is used as a first step because then the electrolytes do not need to be tracked individually. The equilibrium is calculated with

$$h_\alpha^{\text{eq}} = \bar{\omega}_\alpha \Psi, \tag{C.3.22}$$

where these integral weights are

$$\bar{\omega}_\alpha = \begin{cases} 0, & \alpha = 0; \\ 1/6, & \alpha = 1, \ldots, 4; \\ 1/12, & \alpha = 5, \ldots, 8, \end{cases} \tag{C.3.23}$$

We have found that the calculated electric potential computing via the LPBE usually converges significantly more quickly than the flow field determined by the LBE (*e.g.* in less than a hundred time steps, versus over a thousand).

We primarily employ a Dirichlet boundary condition much as described above in the species transport section, but with the alternative integral weights. The flux boundary condition can easily be added to the method for metals or insulating walls. The LPBE has not yet been coupled to a charge regulation boundary condition anywhere in the literature. The method could benefit from further advancements in simulating with different material and fluid characteristics. In addition, a future model of interest would assign charges to each of several dilute species modeled with the multicomponent LBM to determine the electric potential directly from the ionic species.

Once the electric potential is known, the potential and a given net electric field applied over the domain can significantly affect the fluid flow. The external force is given by $\mathbf{F}_{\text{ext}} = -\rho_e \nabla \Psi_{\text{ext}}$. The electric field couples with the LBE through the discrete force term,

$$f_\alpha(\mathbf{r} + \mathbf{e}_\alpha \delta_t, t + \delta_t) - f_\alpha(\mathbf{r}, t) = -\frac{1}{\tau_\nu} \left[f_\alpha(\mathbf{r}, t) - f_\alpha^{\text{eq}}(\mathbf{r}, t) \right] + \delta_t F_\alpha. \tag{C.3.24}$$
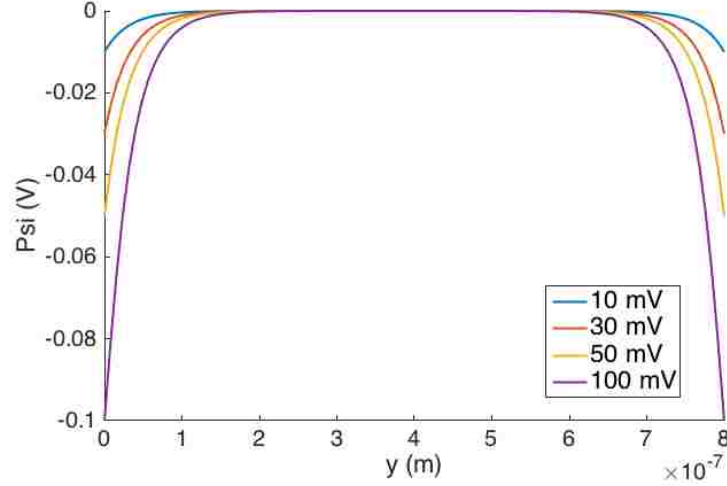
Figure C.10. Electrical potential profile in a narrow channel for changing surface potentials.

The discrete force term is calculated from

$$F_\alpha = \rho_e \mathbf{E} \cdot (\mathbf{e}_\alpha - \mathbf{u}) \, f_\alpha^{\text{eq}}/RT. \tag{C.3.25}$$

The LBE is otherwise computed as described previously.

In Figure C.10, we reproduce a figure given in Wang *et al.*[122] as example of the method. This figure shows the change of the profile of the electrical potential as the surface potential changes. Due to the nonlinearity of the Boltzmann statistics the charge mostly changes near the surface, but quickly goes to zero in the middle of the channel. This method is easily extended to a generalized 2D shaped domain.*

C.4 Summary

In this appendix we have outlined and developed the lattice Boltzmann methods employed in this dissertation. The LBM is a versatile computational method that is

---

* Sec. 6.3.4 applies the LPBM to pitting corrosion.

helpful to the study of porous media particularly through the simple implementation of solids in the fluid. The mesoscale fluids representation is readily augmented to account for multiphase fluid phenomena. Multiple species models with diffusion and bulk and surface reactions have been implemented. These models are further extended to account for dissolution of the solid into an unsaturated bulk fluid. The lattice Poisson–Boltzmann method accounts for electrochemical phenomena in the fluid.

Chapter Supplementary Material

Appendix D

Additional Details on Evaporation in a Thin Porous Strip

In this appendix, we give further results for evaporation in thin porous strips. The steady state front position behaves similarly for saturated and unsaturated models, while the bulk flow rate is significantly over-predicted by the fully saturated GAT model. Wicking with side evaporation causes significant curvature in the front shape which reduces the bulk flow rate relative to normal surface evaporation. The contour phase diagrams of the front velocity and bulk flow show very clear signatures of similar behavior between the phenomena of interest. Finally, we discuss the solutions by Lockington et al.[79] and their relevant dimensionless form used in the chapter.

(a) Front Position   **(b)** Bulk flow
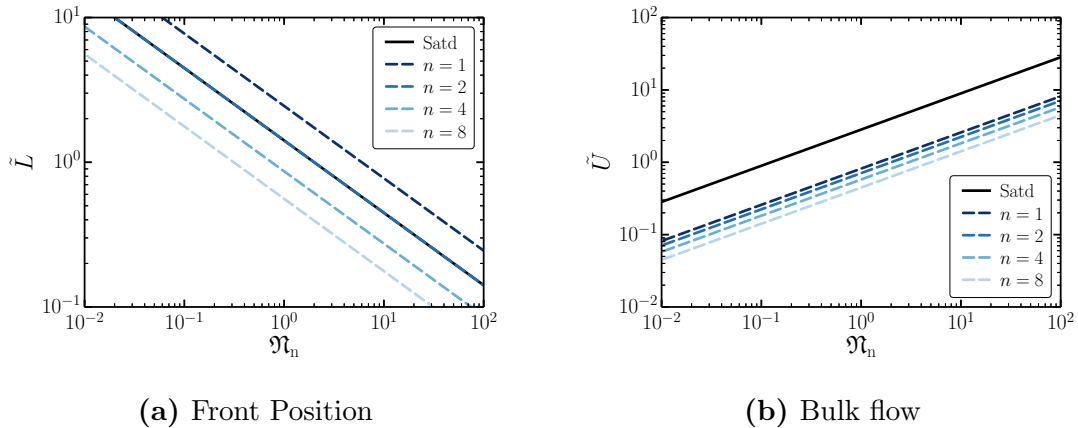
Figure D.1. Steady state behavior for saturated and unsaturated wicking with normal surface evaporation in a thin porous strip. Saturated flow is plotted with solid lines and unsaturated flows with dashed lines. Unsaturated flows are plotted for diffusivity exponents $n = 1, 2, 4$, and 8 from darkest to lightest. (a) Plot of steady state front position, $\tilde{L}_{ss}$, versus ECN, $\mathfrak{N}_n$. The saturated data is identical to the unsaturated for $n = 2$. (b) Plot of steady state bulk velocity, $\tilde{U}_{ss}$, versus ECN, $\mathfrak{N}_n$.

D.1 Supplementary Results

D.1.1 Capillary Flow with Normal Surface Evaporation

In Fig. D.1, the steady states for the saturated and unsaturated capillary flows with evaporation are shown. The plot of the steady state front position, Figure D.1a, shows that for $n = 2$, the capillary diffusion of second order, the front position predicted by the unsaturated method matches the fully saturated solution given in Eq. (3.3.29). Capillary diffusion of lower order will be under-predicted by the saturated normal evaporation model, while $n > 2$ over predicts the front position. All of the predicted fronts are a function of the square root of the inverse ECN. Figure D.1b shows that the two different models give the same power-law dependence of the bulk velocity on $\mathfrak{N}_n$; $\tilde{U} \sim \sqrt{\mathfrak{N}_n}$. However, in all cases the saturated model significantly over-predicts the magnitude of the absorbed liquid by approximately a factor of four or greater.

(a) Bulk liquid velocity

(b) Front Shape
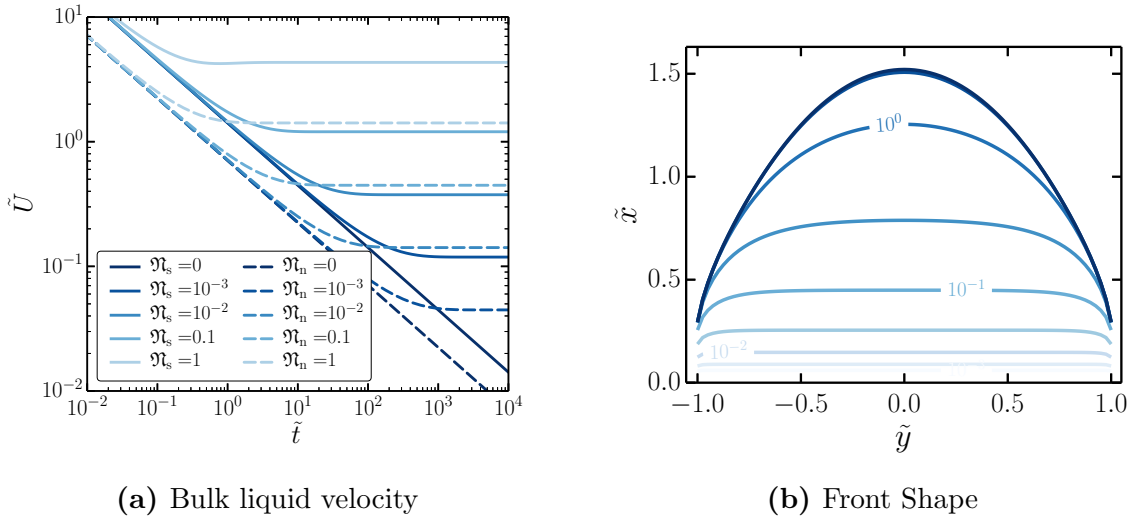
Figure D.2. Wicking behavior of side boundary evaporation from a thin porous strip. (a) Bulk velocity, $\tilde{U}$, versus time, $\tilde{t}$, for side (solid lines) and normal surface (dashed lines) evaporation. The solutions with evaporation are shown for evaporation numbers, $\mathfrak{N}_\mathrm{s}$ and $\mathfrak{N}_\mathrm{n}$, equal to $0, 10^{-3}, 10^{-2}, 0.1$, and 1, from darkest to lightest. (b) Development of the liquid front shape, $\tilde{L}(\tilde{y}, \tilde{t})$, over time of an imbibing liquid with evaporation, $\mathfrak{N}_\mathrm{s} = 1$. Contour lines correspond to front position at dimensionless times, $\tilde{t} = 10^{-3}, 10^{-2.5}, \ldots, 10^1$, from lightest lines to darkest.

D.1.2   Capillary Flow with Side Boundary Evaporation

Side evaporation is more mathematically complex than the other evaporation methods. Figure D.2, gives further results concerning the side boundary evaporation model in addition to that previously shown in Figures 3.4 and 3.5, where front shape and steady state behaviors where investigated. The bulk velocity, illustrated in Figure D.2a, is significantly greater for the side evaporation than for the normal surface evaporation. Figure D.2b shows the front shape for side evaporation when $\mathfrak{N}_\mathrm{s} = 1$, in contrast to Figure 3.4b where the ECN is 0.1. The steady state front shape is slightly more pointed, but nevertheless still looks similar to a flipped hyperbolic cosine function. In the steady state, the distance between the front along the x-axis and at $\tilde{y} = \pm 1$ slightly greater than 1, similar to the case of $\mathfrak{N}_\mathrm{s} = 0.1$. However,
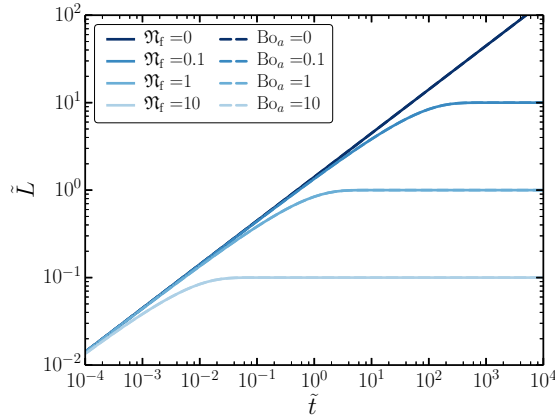
Figure D.3. Comparison of front position, $\tilde{L}$, versus time, $\tilde{t}$, for front interface evaporation and gravity in a thin porous strip. The time dependent front position for front evaporation is shown by solid lines and for gravity by dashed lines. Data is computed for both the ECN, $\mathfrak{N}_{\mathrm{f}}$, and modified Bond number, Bo_a, at values of 10, 1, 0.1, and 0 from shades of lightest to darkest; the darkest line is the Lucas–Washburn Equation. The data are identical, so only the front evaporation plot is visible.

the portion of the side through which the evaporation occurs is relatively small in comparison to the penetration length by a factor of about five, whereas with the lower evaporation they are only different by a factor of about 1.4.

D.1.3   Capillary Flow with Gravity

Figure D.3 shows the data for the 1D restraint by gravity solution perfectly overlays the solution for the front evaporation. This is calculated by the numerical solver using Eq. (3.3.26) and the equivalent expression for front evaporation, from the full differential equation, Eq. (3.3.23). This is the corresponding figure related to Fig. 3.7, where the bulk velocity is shown to be radically different for front evaporation versus gravity.

D.1.4   Comparison of All Phenomena

In Figures 3.8 and 3.9, we discussed differences between the behaviors of the front positions with time and ECN. Now in Figures D.4 and D.5, the data for the front velocity and bulk velocity is also considered. The front velocity for all the phenomena shown in Figure D.4, clearly shows that the lines of $\mathfrak{N}_\mathrm{n}\tilde{t} = \mathfrak{N}_\mathrm{s}\tilde{t} = 10$ and $\mathrm{Bo}_a^2\tilde{t} = \mathfrak{N}_\mathrm{f}^2\tilde{t} = 10$ marks the point when the front velocity, $\tilde{v}_f$, has become negligibly small. The front velocity is defined as $\boldsymbol{\nabla}\varphi(\tilde{x} = \tilde{L})$. The bulk velocity shown in Figure D.5 gives somewhat more varied results. The value of $\mathfrak{N}_\mathrm{n}\tilde{t} = \mathfrak{N}_\mathrm{s}\tilde{t} = 10$ seems to be far past the point at which the bulk velocity for the steady state of the normal and side evaporation occurs, as we see in Figures D.5a and D.5b, respectively. The contour plot for gravity, Figure D.5c, shows that the bulk velocity comes to a steady state as apposed to the case of the front velocity, in Figure D.5d.

D.2   Supplementary Information

D.2.1   Solution of 1D Capillary-Driven Flow under Evaporation with Partial Saturation

Lockington *et al.*[79] derive the solutions of the liquid saturation function in a wetting porous medium by capillary flow with arbitrary constant evaporation from the wetted medium. This is similar to our constant cross section model of 1D normal surface evaporation derived in Eq. 3.3.29, and analyzed in Section 3.4.3. Lockington considers a 1D Richards equation without gravity, but with an evaporation loss, k, which is linear with saturation, Θ, in Equation (5);

$$\frac{\partial \Theta}{\partial t} = \frac{\partial}{\partial x}\left(D(\Theta)\frac{\partial \Theta}{\partial x}\right) - k\Theta.$$

Appendix D. Additional Details on Evaporation in a Thin Porous Strip

He considers a power-law model for the capillary diffusivity in Equation (4)

$$D = D_0 \Theta^n,$$

where D is the capillary diffusivity, D_0 is the constant of capillary diffusivity (the diffusivity when in a fully saturated flow), and n is the power index of the saturation. Lockington suggests that n is usually between values of two to six in many physical systems. The model assumes an initially dry medium, which comes into contact with a fully wetted reservoir at $t = 0$.

An analytical solution for the steady state case may be found by setting the left hand side of (5) equal to zero; this gives the inlet velocity in Equation (13)

$$q = \sqrt{\frac{2kD_0}{n+2}}.$$

Lockington converts this into the simple form $\frac{q}{\sqrt{kD_0}} = \sqrt{\frac{2}{n+2}}$ for analysis in Figure 1 because this gives a simple function of a single variable, n. However, we are interested in the bulk velocity as it depends on the evaporation number. In dimensionless notation

$$\tilde{U} = \frac{1}{\sqrt{n+2}} \sqrt{2\mathfrak{N}_\mathrm{n}}. \tag{D.2.1}$$

where the inlet velocity is $\tilde{U} = aq/D_0$ and we have defined the evaporation–capillary number $\mathfrak{N}_\mathrm{n} = a^2 k/D_0$. The steady state solution for the GAT bulk velocity is $\tilde{U} = \sqrt{2\mathfrak{N}_\mathrm{n}}$, from which we get

$$\tilde{U}_{\mathrm{ss,\ unsat}} = 1/\sqrt{n+2}\,\tilde{U}_{\mathrm{ss,\ norm}}, \tag{D.2.2}$$

as mentioned in the text. The saturation function found by Lockington in the steady state is [Equation (12)]

$$\Theta^n = \left[1 - \frac{n}{\sqrt{2(n+2)}} \sqrt{\frac{k}{D_0}}\, x\right]^2$$

Appendix D. Additional Details on Evaporation in a Thin Porous Strip

which in our variables may be expressed,

$$\Theta^n = \left[1 - \frac{n}{\sqrt{2(n+2)}}\mathfrak{N}_{\mathrm{n}}^{1/2}\tilde{x}\right]^2 \tag{D.2.3}$$

This readily gives the steady state front position,

$$\tilde{L} = \frac{\sqrt{n+2}}{n}\sqrt{\frac{2}{\mathfrak{N}_{\mathrm{n}}}} \tag{D.2.4}$$

where $\tilde{L} = \tilde{x}_{\mathrm{F}}$ in Lockington's notation. We present this as Eq. (3.4.4). This is also derived from the time dependent solution later in equation (32). Eqs. (D.2.4) and (D.2.1) give the unsatured data for Fig. D.1.

Lockington furthermore gives an accurate analytical approximation to the time dependent solution of equation (5). He first determines a solution to the steady inflow [Equation (29)], which we give here in our dimensionless notation,

$$\tilde{q} = \sqrt{\mathfrak{N}_{\mathrm{n}}}\sqrt{\frac{1}{2(n+1)(n+2)}}$$

$$\times \frac{2(n+1)n_s - n - \dfrac{(n+2)^2}{2(n+1)[1+(n+1)u_s]}}{\left\{[1+(n+1)u_s](u_s-1) - \frac{1}{2}\left(\dfrac{n+2}{n+1}\right)^2\ln\left(\dfrac{1+(n+1)u_s}{n+2}\right)\right\}^{1/2}}, \tag{D.2.5}$$

where $u_s = \exp(kt)$. Then the saturation is given in equation (30) which yields the position of the wet front [equation (31)]

$$\tilde{L} = \frac{\sqrt{1 + \frac{2}{n} - \frac{2}{n}\frac{\mathfrak{N}_{\mathrm{n}}}{\tilde{q}^2}} - 1}{\tilde{q}\left(1 - \frac{\mathfrak{N}_{\mathrm{n}}}{\tilde{q}^2}\right)} \tag{D.2.6}$$

These two equations is used to calculate the unsaturated data given in our Fig. 3.3.

(a) Normal Surface Evaporation

(b) Side Boundary Evaporation

(c) Gravity

(d) Front Interface Evaporation
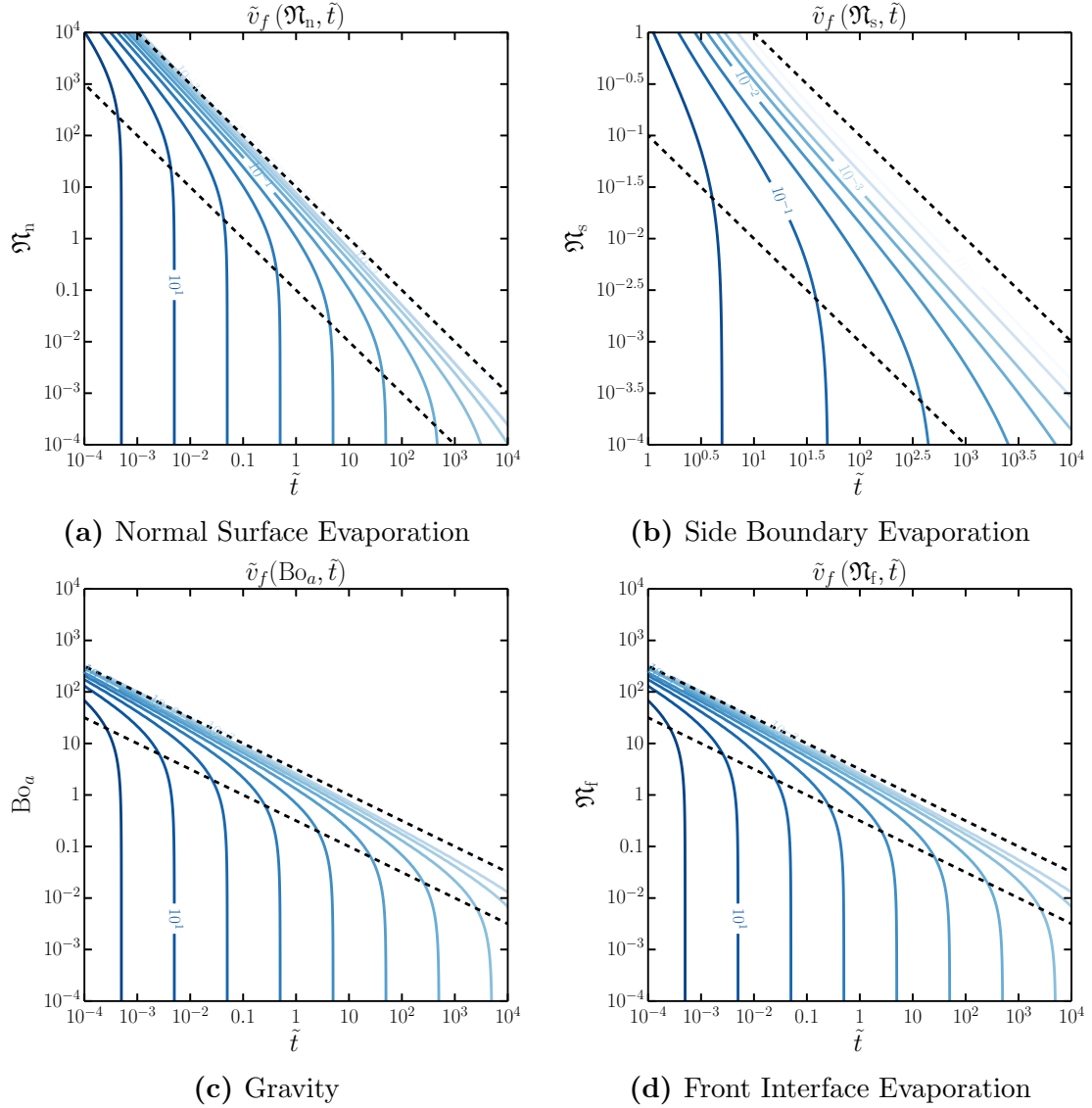
Figure D.4. Contour plot of front velocity, $\tilde{v}_f$, over corresponding dimensionless quantity and time for flow through thin porous strip. Dotted black lines distinguish regimes of flow behavior; the lower left section is dominated by capillary flow and upper right is at steady state. (a) Dotted lines in the lower left and upper right correspond to $\mathfrak{N}_n \tilde{t} = 0.1$ and $\mathfrak{N}_n \tilde{t} = 10$, respectively. (b) Dotted lines in the lower left and upper right correspond to $\mathfrak{N}_s \tilde{t} = 0.1$ and $\mathfrak{N}_s \tilde{t} = 10$, respectively. This figure is similar to the lower right quadrant of (a). (c) Dotted lines in the lower left and upper right correspond to $\mathrm{Bo}_a^2 \tilde{t} = 0.1$ and $\mathrm{Bo}_a^2 \tilde{t} = 10$, respectively. (d) Dotted lines in the lower left and upper right correspond to $\mathfrak{N}_f^2 \tilde{t} = 0.1$ and $\mathfrak{N}_f^2 \tilde{t} = 10$, respectively. The figures, (c) and (d), are essentially identical.

(a) Normal Surface Evaporation

(b) Side Boundary Evaporation

(c) Gravity

(d) Front Interface Evaporation
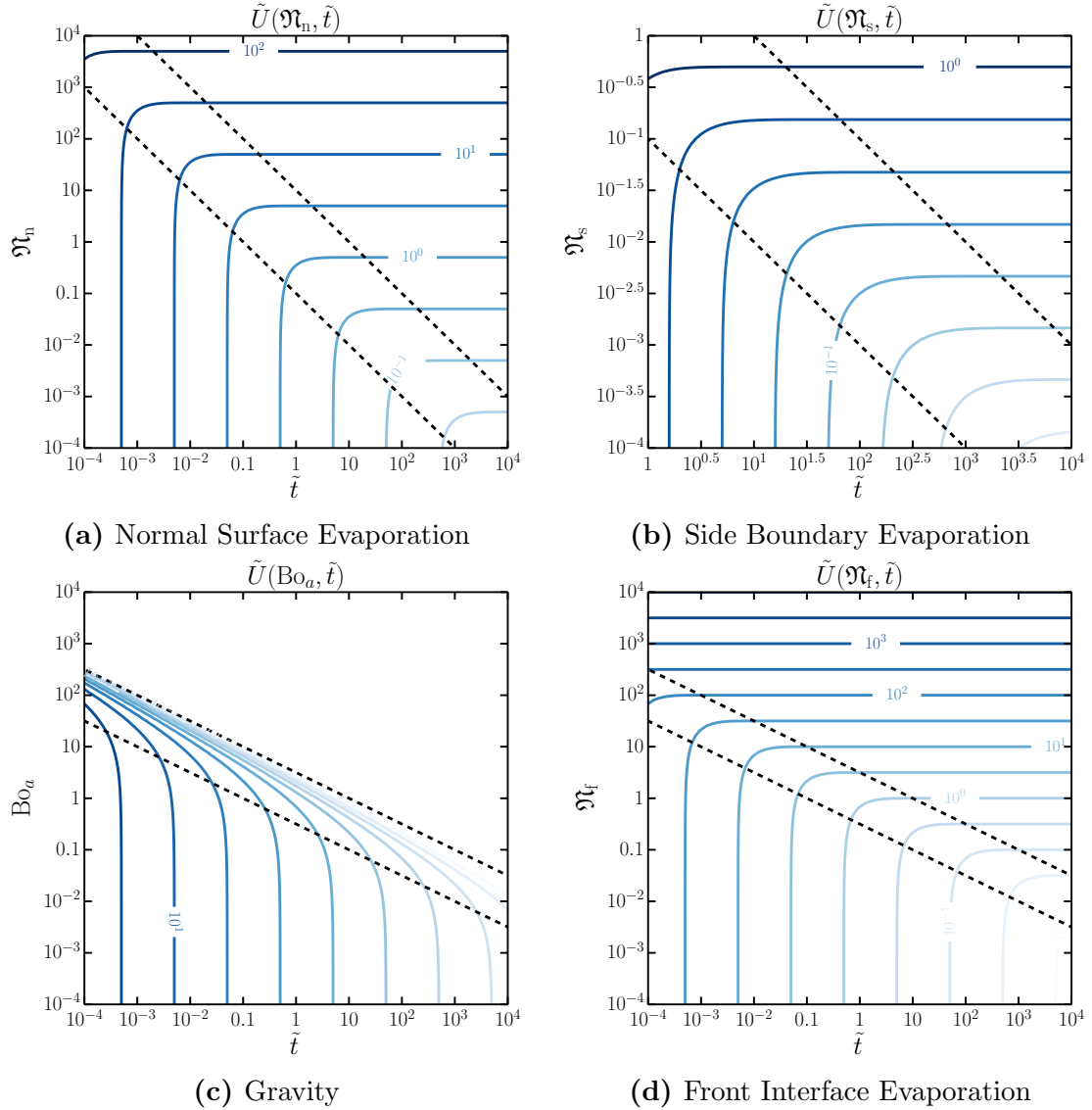
Figure D.5. Contour plot of bulk velocity, $\tilde{U}$, over corresponding dimensionless quantity and time for for flow through thin porous strip. Dotted black lines distinguish regimes of flow behavior; the lower left section is dominated by capillary flow and upper right is at steady state. (a) Dotted lines in the lower left and upper right correspond to $\mathfrak{N}_n\tilde{t} = 0.1$ and $\mathfrak{N}_n\tilde{t} = 10$, respectively. (b) Dotted lines in the lower left and upper right correspond to $\mathfrak{N}_s\tilde{t} = 0.1$ and $\mathfrak{N}_s\tilde{t} = 10$, respectively. (c) Dotted lines in the lower left and upper right correspond to $\mathrm{Bo}_a^2\tilde{t} = 0.1$ and $\mathrm{Bo}_a^2\tilde{t} = 10$, respectively. (d) Dotted lines in the lower left and upper right correspond to $\mathfrak{N}_f^2\tilde{t} = 0.1$ and $\mathfrak{N}_f^2\tilde{t} = 10$, respectively.

Appendix E

Additional Details on Normal Surface Evaporation

This appendix extends the work presented in Ch. 4 and provides further details of the solution of the total velocity potentials for the elliptic and Cartesian coordinate systems. The front velocity of the fan-shaped domain agree asymptotically with the one-dimensional solution of constant cross-section and with a given reduced two-dimensional solution defined by a semicircular inlet shape. The general numerical methodology is described. Additionally, the shape of the expanding front and the asymptotic behavior of the front velocity are discussed in greater depth.

E.1 Velocity Potential for the Capillary Flow with Evaporation in Expanding 2D Media

E.1.1 Evaporation Potential for 2D Expanding Porous Media in Elliptic Coordinates

Restating the system for the 2D flow in the elliptic coordinate system with evaporation given in Eqs. (4.3.14) and (4.3.15);

$$\frac{1}{a^2 \left[\cosh^2(\eta) - \cos^2(\psi)\right]} \left(\frac{\partial^2 \varphi}{\partial \eta^2} + \frac{\partial^2 \varphi}{\partial \psi^2}\right) = -Q, \tag{E.1.1}$$

and boundary conditions,

$$\left.\frac{\partial \varphi}{\partial \psi}\right|_{\psi=0} = 0, \tag{E.1.2a}$$

$$\left.\frac{\partial \varphi}{\partial \psi}\right|_{\psi=\pi} = 0, \tag{E.1.2b}$$

$$\left.\varphi\right|_{\eta=0} = \varphi_0 = -\frac{k}{\mu} P_c, \tag{E.1.2c}$$

$$\left.\varphi\right|_{\eta=\eta_f} = 0. \tag{E.1.2d}$$

The system may be solved using superposition to separate the influence of the capillary forces, ξ, and the evaporation effects on the potential, ζ;

$$\varphi(\eta, \psi) = \xi(\eta) + \zeta(\eta, \psi). \tag{E.1.3}$$

The solution of the capillary potential, ξ, is readily determined from the homogeneous differential equation, $\mathrm{d}^2\xi/\mathrm{d}\eta^2 = 0$, and the boundary conditions given by Eqs. (E.1.2c) and (E.1.2d);[*]

$$\xi(\eta) = \frac{kP_c}{\mu}\left(-\frac{\eta_f - \eta}{\eta_f}\right). \tag{E.1.4}$$

---

[*] See Eq. (2.3.5).

Appendix E. Additional Details on Normal Surface Evaporation

The evaporation potential, ζ, is solved from the non-homogenous Eq. (E.1.1) with purely homogenous boundary conditions in the form of Eqs. (E.1.2). Using trigonometric identities, the right-hand side of Eq. (E.1.1) is rearranged into a truncated Fourier series;

$$\frac{\partial^2 \zeta}{\partial \eta^2} + \frac{\partial^2 \zeta}{\partial \psi^2} = \left[-\frac{1}{2}Qa^2 \cosh(2\eta) \right] + \left(\frac{1}{2}Qa^2 \right) \cos(2\psi), \tag{E.1.5}$$

The first term of the right-hand side corresponds to the zero-order term of a Fourier-cosine series, while the second term is second-order. Thus, we define ζ as a cosine series in ψ;

$$\zeta(\eta, \psi) = \sum_{n=0}^{\infty} H_n(\eta) \cos(n\psi). \tag{E.1.6}$$

This also satisfies the homogeneous Neumann boundary conditions in ψ, Eqs. (E.1.2a) and (E.1.2b).

Substitution of Eq. (E.1.6) into Eq. (E.1.5) allows the solution to be reduced to an infinite series of ordinary differential equations (ODEs), where each differential equation comes from a different cosine term. However, the individual ODEs are non-homogeneous only for $n = 0$ and 2, so the differential equations are homogeneous with purely homogeneous boundary conditions for all other values of n. Thus, zero is the only admissible solution for each of these other cases, or

$$H_n(\eta) \equiv 0, \qquad \text{for } n = 1, 3, 4, \ldots \tag{E.1.7}$$

The non-homogeneous ordinary differential equation for $n = 0$ is

$$\frac{d^2 H_0(\eta)}{d\eta^2} = -\frac{1}{2}Qa^2 \cosh(2\eta), \tag{E.1.8a}$$

with homogeneous boundary conditions at $\eta = 0$ and $\eta = \eta_f$. Integrating the ODE and substituting for the boundary conditions, we find the solution

$$H_0(\eta) = -\frac{Qa^2}{8} \left[\frac{\eta - \eta_f + \eta_f \cosh(2\eta) - \eta \cosh(2\eta_f)}{\eta_f} \right]. \tag{E.1.8b}$$

Appendix E. Additional Details on Normal Surface Evaporation

This corresponds to the behavior of the evaporation potential without accounting for angular dependence. The ordinary differential equation for $n = 2$ is

$$\frac{d^2 H_2(\eta)}{d\eta^2} - 4H_2(\eta) = \frac{1}{2}Qa^2. \tag{E.1.9a}$$

When homogeneous boundary conditions are applied, this yields the solution

$$H_2(\eta) = -\frac{1}{8}Qa^2 \left\{ \frac{\sinh(2\eta_f) - \sinh(2\eta) - \sinh[2(\eta_f - \eta)]}{\sinh(2\eta_f)} \right\}. \tag{E.1.9b}$$

By Eq. (E.1.6), the evaporation potential, ζ, is the combination of the partial potential solutions;

$$\zeta(\eta, \psi) = H_0(\eta) + H_2(\eta)\cos(2\psi), \tag{E.1.10a}$$

$$= -\frac{Qa^2}{8} \left\{ \frac{\eta - \eta_f + \eta_f \cosh(2\eta) - \eta \cosh(2\eta_f)}{\eta_f} \right.$$
$$\left. + \frac{\sinh(2\eta_f) - \sinh(2\eta) - \sinh[2(\eta_f - \eta)]}{\sinh(2\eta_f)}\cos(2\psi) \right\}. \tag{E.1.10b}$$

This gives the solution for the evaporation potential in elliptic coordinates and satisfies Eqs. (E.1.5) and (E.1.2) in homogenous form.

Therefore, the total velocity potential in the elliptic coordinate system is expressed by the sum of the capillary and evaporation potentials as shown in Eq. (E.1.3). Simplifying the evaporation potential by trigonometric identities, the dimensionless form of the combined potentials is

$$\tilde{\varphi} = -\frac{\eta_f - \eta}{\eta_f}$$
$$- \frac{1}{8}\left(\frac{\mu a^2 Q}{kP_c}\right) \left\{ \frac{\eta - \eta_f + \eta_f \cosh(2\eta) - \eta \cosh(2\eta_f)}{\eta_f} \right.$$
$$\left. + \frac{\sinh(\eta_f - \eta)\sinh(\eta)}{\cosh(\eta_f)}\cos(2\psi) \right\}. \tag{E.1.11}$$

This is the solution given in Eq. (4.3.16).

E.1.2 Detailed Derivation of Capillary Flow with Evaporation in a Cartesian Geometry

We develop the frontal position and bulk velocity equations for the Cartesian geometry using potential flow theory with evaporation. This is a reworking of the method given in previous work[24] which is similar to the solution by Fries *et al.*[80] when gravity is ignored. The Cartesian coordinate system naturally expresses the wicking in thin strips of constant cross section, which is similar to the elliptic system when the front shape is only slightly deformed around the edges. In the Cartesian geometry, the differential equation for the velocity potential, Eq. (4.2.4), immediately reduces to

$$\frac{\mathrm{d}^2\varphi}{\mathrm{d}x^2} = -Q, \tag{E.1.12}$$

with relevant boundary conditions in the x-direction,

$$\varphi|_{x=0} = -\frac{k}{\mu}P_\mathrm{c}, \tag{E.1.13a}$$

$$\varphi|_{x=L} = 0. \tag{E.1.13b}$$

The liquid saturated domain extends from the inlet, $x = 0$, to the front position, $x = L$. The domain spans the y-direction from $-a$ to a with no flux through the boundaries, and similarly, the z-direction spans from 0 to δ, where $\delta \ll 2a$. The capillary potential is easily found by integrating for the case of $Q = 0$ and applying the boundary conditions, Eq. (E.1.13). Additionally, the evaporation potential is also determined by direct integration of Eq. (E.1.12) with homogeneous boundary conditions. The resulting total velocity potential in dimensionless form is

$$\tilde{\varphi} = -\left(\frac{\tilde{L} - \tilde{x}}{\tilde{L}}\right) - \frac{1}{2}\mathfrak{N}_\mathrm{n}\left(\tilde{x}^2 - \tilde{L}\tilde{x}\right). \tag{E.1.14}$$

This shows that the power law behavior of the capillary potential is linear in space, while the evaporation potential is quadratic. Differentiating the potential with respect

to x gives the velocity in the x-direction,

$$\tilde{v}_x = \frac{1}{\tilde{L}} - \frac{1}{2}\mathfrak{N}_\mathrm{n}\left(2\tilde{x} - \tilde{L}\right). \tag{E.1.15}$$

Then substituting for $\tilde{x} = \tilde{L}$ gives the velocity of the front for 1D capillary flows;

$$\tilde{v}_f = \frac{1}{\tilde{L}} - \frac{1}{2}\mathfrak{N}_\mathrm{n}\tilde{L}. \tag{E.1.16}$$

This shows that the magnitude of the frontal velocity without evaporation is inversely proportional to the saturation length, while the velocity is proportional to the distance of the front in the evaporation term. This is physically important because the capillary potential decreases due to hydrodynamic drag, but contributes to the forward motion of the front.

However, as the liquid propagates, the strength of the evaporation effect grows due to increased surface area, and reduces the speed of the frontal motion because of the negative sign in front of the term. The frontal velocity is integrated according to Eq. (4.2.5), $\int_0^L (1/v_f)\,\mathrm{d}x = \int_0^t \mathrm{d}t$, and the result may be expressed as an implicit solution for the front position, $L(t)$;

$$\ln\left(1 - \frac{1}{2}\mathfrak{N}_\mathrm{n}\tilde{L}^2\right) = -\mathfrak{N}_\mathrm{n}\tilde{t}. \tag{E.1.17a}$$

When the implicit equation is rearranged, we find the front position as an explicit function of the time in dimensionless units,

$$\tilde{L}(\tilde{t}) = \sqrt{\frac{2}{\mathfrak{N}_\mathrm{n}}\left[1 - \exp\left(-\mathfrak{N}_\mathrm{n}\tilde{t}\right)\right]}. \tag{E.1.17b}$$

We note in[24] that this solution is in strong agreement with the solution by Fries *et al.*[80] for the case of evaporation only. The volumetric flow is determined from the expression,

$$U = \int_0^\delta \int_{-a}^a [v_x|_{x=0}]\,\mathrm{d}y\,\mathrm{d}z. \tag{E.1.18}$$

Substituting the velocity in the x-direction and simplifying,

$$\tilde{U} = \frac{2}{\tilde{L}} + \mathfrak{N}_\mathrm{n}\tilde{L}. \tag{E.1.19}$$

E.1.3 Velocity at Asymptotically Small and Large Front Advancement

The solution derived of the front velocity for the elliptic case in section 4.3.2 may be verified by asymptotic comparison with the solutions the Cartesian and polar geometries given in sections E.1.2 and 4.3.1, respectively. The front position itself cannot be analytically compared between these solutions; similarly, the bulk velocities will not be directly contrasted due to the integral expression in the elliptic case. The velocity potential is implicitly verified because the frontal velocity is a direct result of the potential.

Comparison to Cartesian geometry solution at small front advancement

The solution of the frontal velocity for a strip of constant cross section oriented in the y-direction is given in Eq. (E.1.16),

$$\tilde{v}_{f,\,\mathrm{cart}} = \frac{1}{\tilde{y}_f} - \frac{1}{2}\mathfrak{N}_{\mathrm{n}}\tilde{y}_f. \tag{E.1.20}$$

This simpler solution also approximates the solution for the 2D fan at early times and high evaporation numbers. Considering the behavior along the y-axis ($\psi = \pi/2$) of the velocity derived in elliptic geometry, the form of Eq. (4.3.20a) may be simplified;

$$\begin{aligned}
\tilde{v}_{f,\,\mathrm{ell}} = {} & \frac{1}{\eta_f \cosh(\eta_f)} \\
& - \frac{1}{4}\mathfrak{N}_{\mathrm{n}}\left[\frac{2\eta_f \sinh(2\eta_f) - \cosh(2\eta_f) + 1}{2\eta_f \cosh(\eta_f)} + \frac{\sinh(\eta_f)}{[\cosh(\eta_f)]^2}\right].
\end{aligned} \tag{E.1.21a}$$

Substituting $\cosh(\eta_f) \approx 1$ and $\sinh(\eta_f) \approx \eta_f$, then recognizing $\eta_f \approx \tilde{y}_f$ for $\eta_f < 1$, the first order expression for the velocity simplifies,

$$\tilde{v}_{f,\,\mathrm{ell}} \approx \frac{1}{\tilde{y}_f} - \frac{1}{2}\mathfrak{N}_{\mathrm{n}}\tilde{y}_f = \tilde{v}_{f,\,\mathrm{cart}}. \tag{E.1.21b}$$

Thus, we see that the front motion will behave similarly for early times and short advancement of the liquid because these two solutions are in asymptotic agreement.

Comparison to polar geometry for low evaporation rates and large front advancement

At large front advancement, the solution of the front velocity in the elliptic geometry is similar to solution in the polar geometry. The front velocity in polar coordinates is

$$\tilde{v}_{f,\text{pol}} = \frac{1}{\tilde{r}_f \ln(\tilde{r}_f)} - \frac{1}{4}\mathfrak{N}_\text{n}\left[2\tilde{r}_f - \frac{\tilde{r}_f}{\ln(\tilde{r}_f)} + \frac{1}{\tilde{r}_f \ln(\tilde{r}_f)}\right]. \tag{E.1.22a}$$

as given by rearrangement of Eq. (4.3.6). Simplified for large $\tilde{r}_f$, the dominant terms reduce on the right hand side,

$$\tilde{v}_{f,\text{pol}} \approx \frac{1}{\tilde{r}_f \ln(\tilde{r}_f)} - \frac{1}{2}\mathfrak{N}_\text{n}\tilde{r}_f. \tag{E.1.22b}$$

This equation describes the effective front velocity for large time expansions with low evaporation rates. Therefore, the velocity of the front for the elliptic coordinate system, Eq. (4.3.20a), may be compared to verify the solution for small evaporation number. Evaluating the elliptic solution along the x-axis ($\psi = 0$) and simplifying with trigonometric identities, we find

$$\begin{aligned}
\tilde{v}_{f,\text{ell}} &= \frac{1}{\eta_f \sinh(\eta_f)} \\
&\quad - \frac{1}{4}\mathfrak{N}_\text{n}\left[2\cosh(\eta_f) - \frac{\sinh(\eta_f)}{\eta_f} - \frac{1}{\cosh(\eta_f)}\right].
\end{aligned} \tag{E.1.23a}$$

We observe $\tilde{r}_f^2 = \sinh^2(\eta_f)\sin^2(\psi) + \cosh^2(\eta_f)\cos^2(\psi) = \cosh^2(\eta_f)$ for $\psi = 0$, which gives $\tilde{r}_f = \cosh(\eta_f)$. For large values of η_f, we may approximate the functions $\sinh(\eta_f) = \sqrt{\tilde{r}_f^2 - 1} \approx \tilde{r}_f$ and $\eta_f = \cosh^{-1}(\tilde{r}_f) \approx \ln(\tilde{r}_f)$. When we keep only the highest order term of the evaporation portion and apply these simplified relationships, the asymptotic expression reduces to

$$\tilde{v}_{f,\text{ell}} \approx \frac{1}{\tilde{r}_f \ln(\tilde{r}_f)} - \frac{1}{2}\mathfrak{N}_\text{n}\tilde{r}_f \approx \tilde{v}_{f,\text{pol}}. \tag{E.1.23b}$$

Thus, both approximations of the front velocity at large expansion, Eqs. (E.1.22b) and (E.1.23b), match in the limit of large $\tilde{r}_f$ and small $\mathfrak{N}_\text{n}$, and so in this limit the front position will behave similarly (see Figure E.4).

E.1.4 Numerical Solution of the Position and Bulk Velocity Equations

To produce data for analysis, the differential equation of the front position for the elliptic system, Eq. (4.3.20b), and the integral equation for the bulk velocity, Eq. (4.3.22), require numerical time integration. We apply a fourth order Runge–Kutta solver[32] to the nonlinear ordinary differential equation, Eq. (4.3.20b), to determine the front position with an initial condition of $\eta_f = 0$ at a non-zero early time, $0 < \tilde{t} \ll 1$, for numerical stability. The equation is then integrated in a specific time-sequence, along values of constant ψ out to sufficiently large time—usually $\tilde{t} = 10^6$. The data is naturally computed in elliptic variables and is converted back into Cartesian coordinates by applying the elliptic coordinate transformation given in Eq. (4.3.13). To determine the value of the bulk velocity from Eq. (4.3.22), we integrate over the angular variable, ψ, with cubic splines at every time step, which noticeably increases computational cost. The data for the polar and linear cases of the implicit solutions of the front position, Eqs. (4.3.7) and (4.3.24), respectively, are used directly, and the result may be put into Eqs. (4.3.12) and (4.3.27) to compute the bulk velocity.

The simplifications inherent in the models of 2D capillary flow with evaporation discussed in this paper may be relaxed. Using computational methods, the geometry of the porous medium can be modified to fit a wide variety of prospective systems for capillary driven motion, including medical diagnostic devices or microfluidic fuel cells.[17,21,50,61] The evaporation rate is assumed to be constant with respect to space and time which may not be the case due to various nonlinear effects of change in temperature, convection, surface chemistry, and other physical phenomena on the evaporation rate from the thin porous medium. The differential equations for the motion of the front in 2D expanding flows, Eqs. (4.3.6) and (4.3.20b), may be applied without any loss of generality for evaporation as a well behaved function of time, $Q(t)$, because $y_f(t)$ is determined numerically. To account for a spatially non-homogeneous

evaporation rate, a Greens function technique may be applied to the solution of the potential for some $Q(x, y; t)$. Both of these additions must be made with caution as significant discontinuities in functions of time and space lead to unphysical results; a sudden increase in evaporation rate causes rapid drying of the medium near the wet front, in which case the Green–Ampt model breaks down.

E.2   Front Shape Evolution

We detail in this section further results of the 2D expanding flow in capillary media with evaporation. First, we illustrate the time evolution of the shape of the liquid front for the 2D elliptic fan and compare to the empirical observations with good agreement. Other details on advancement of the front and the steady state front shape are given. Then we consider the behavior of the front velocity itself and show that both the front velocity and bulk velocities also demonstrate the three flow regimes noted in the text with Fig. 4.6.

E.2.1   Shape of the Liquid Front

Liquid infiltration into a porous medium is most naturally understood by observing the liquid frontal position progressing through the entire porous domain, which we do by considering a single system with evaporation. In Fig. E.1a, we observe the developing front shape versus time for a physical system with a noticeable but small evaporation number, $\mathfrak{N}_n = 0.1$, which is a common order of magnitude for experiment. The figure illustrates the shape of the front transitioning from flat center with slight curvature around the inlet sides for $\tilde{t} < 0.1$ into a nearly semi-circular shape by $\tilde{t} > 10$. Naturally, the flow should deform from the Lucas–Washburn rectangular plug into the polar system of equal radius, hence the observation makes sense both physically

(a) Cartesian coordinates.
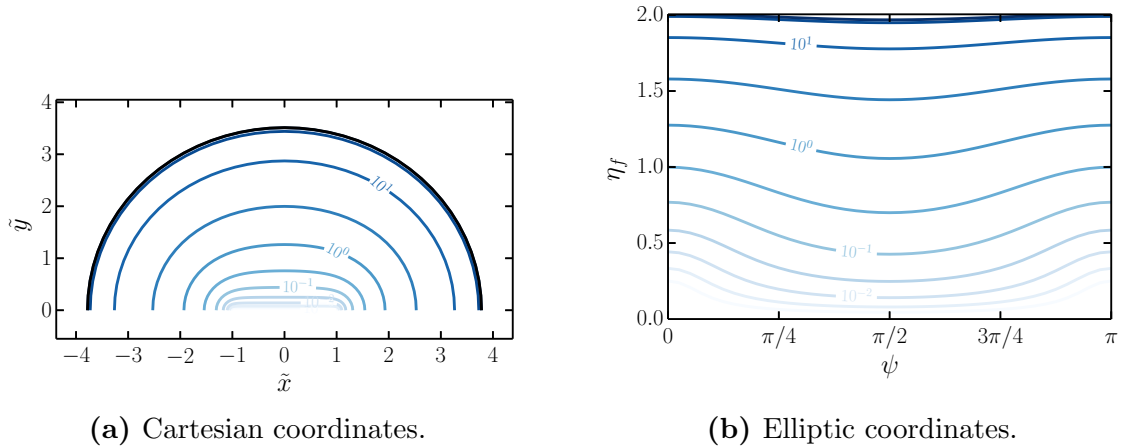
(b) Elliptic coordinates.

Figure E.1. Development of the liquid front shape over time of an imbibing liquid with evaporation, $\mathfrak{N}_n = 0.1$, via flow through an linear inlet. Figure b is the data computed in elliptic coordinates, and figure a is the same computed data transformed into Cartesian coordinates via Eq. (4.3.13).

and in connection to the asymptotic cases.[57] Finally, it is clear that by $\tilde{t} = 100$ the liquid front is no longer advancing, and the system has reached steady state where the flow at the entrance equals the evaporation flux. In Figure E.1b we see the value of the front position in elliptic coordinates, η_f, is not in fact constant with the angular variable, ψ, as is assumed for the derivation of the potential. This discrepancy occurs because the metric coefficients—which factor into the derivation of the front position equation, Eq. (4.3.20b)—are dependent on ψ.

The shape of the liquid front predicted by the theory agrees with experimental observations presented in Fig. E.2. Both images in the figure were taken at times where the wicking liquid is still advancing and not visibly slowed by evaporation. Figure E.2a shows the front shape at an early time is mostly flat around the middle while displaying some curvature near the edges of the flow. The second image, Fig. E.2b, shows the water significantly advanced such that the middle of the front is curved as well, but the shape does not yet appear to be a circle. Thus, the empirical
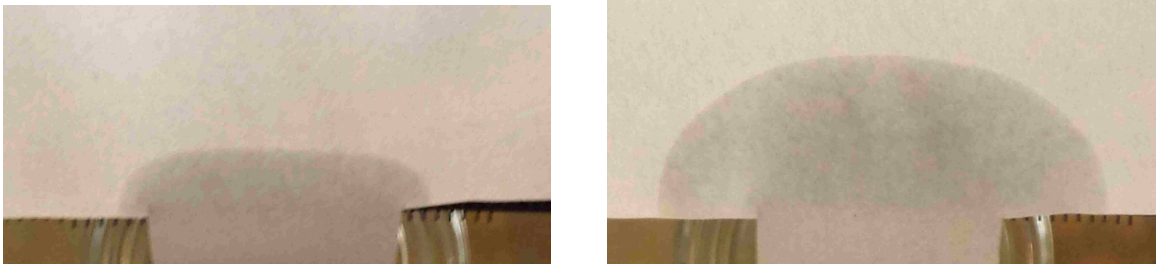
(a) Early front shape ($\tilde{t} \approx 0.1$).

(b) Progressing front shape ($\tilde{t} \approx 1$).

Figure E.2. Experimentally observed front shape at early infiltration. Water fully wets the paper, so the front of the liquid is well defined. The front shape transforms from a plug shape (a) to nearly an ellipse (b).

observations support the front shape predicted by the solution of Eq. (4.3.20b) for a half plane with a straight inlet line. This is quite remarkable as we assumed in choosing the coordinate system that the potential would be bound by expanding ellipses. However, the front motion deviates as prescribed by the metric coefficients from the actual shape of an ellipse and so the solution naturally deforms the front shape from a line source into a circle, which in fact shows that the choice of elliptic coordinates is reasonable. So unlike in the 1D and 2D polar cases, the shape of the isopotential lines in the wetted domain of the 2D elliptic case is not the same as the velocity.

The experiments were conducted specifically to observe the qualitative shape of the front of the liquid as it advanced into the medium. Whatman 1001-185 grade 1 qualitative filter paper was used for the experimental porous medium. The paper was laid on a horizontal mesh in a small enclosure to minimize airflow and disturbances at 296 K, 32% humidity, and elevation 1 mile. The inlet strip was cut to 1 inch width and 1.5 inches long and was almost fully immersed in a 50 mL jar filled with deionized water. The fanning portion of the medium was cut into a semicircle of radius 3 inches. The images in Figures E.2a and E.2b were taken at 0.65 and 4.25 minutes after the liquid reached the fan entrance, respectively.[*]

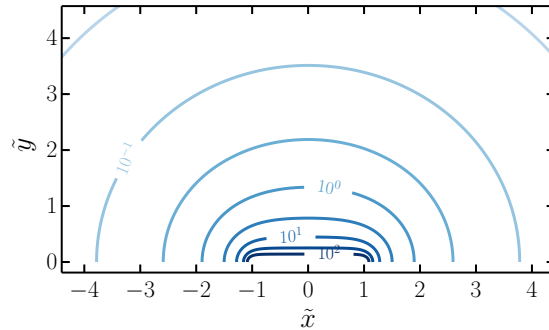[*] Quantitative evaporation experiments are discussed in § G.

Figure E.3. Steady state front shape at given evaporation rates.

Thus, instead of applying elliptic coordinates to fully describe the system and expecting to observe confocal ellipses which grow with time, we have found a different shape which is arguably more physical than perfect ellipses as we have considered qualitatively in Figure E.1a and demonstrated experimentally Figure E.2. The time dependent behavior of the frontal motion deviates from the exact elliptic shape assumed in solving the potential, but the deformation of the front shape from a line source into a circle is correct for this physical system. Therefore, these results bare sufficient relation to the spacial relationships of the flow shape to realistically investigate the effects of evaporation on an imbibing liquid.

Figure E.3 illustrates the shape of the liquid front when the infiltration has reached a steady state at various evaporation numbers. This figure may be useful in design of the size of a porous domain in an environment with a given evaporation number. Comparing to Figure E.1a, which shows the time dependent nature of the infiltration into the domain, we see that the essential shape of the front is extremely similar where the steady state fronts are not an explicitly elliptical in shape, but deform from nearly rectangles into circles. The front shape for evaporation numbers greater than ten is almost perfectly flat near the y-axis, while edges of the liquid flow appear very nearly elliptical.
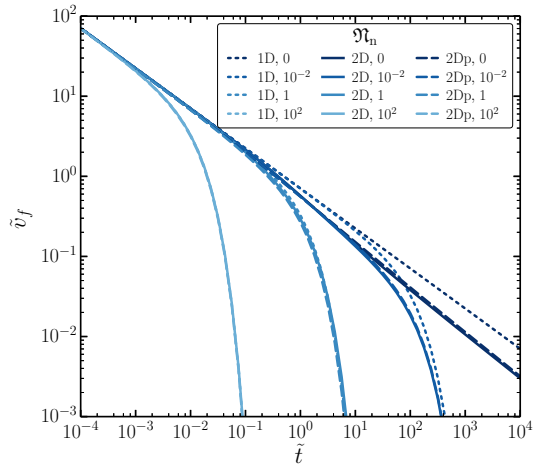
Figure E.4. Comparison of front velocity, $\tilde{v}_f$, versus time, $\tilde{t}$, with asymptotic solutions.

E.2.2 Flow Behavior of the Front Velocity and Bulk Velocity

Figure E.4 shows the front velocity of the elliptic case, Eq. (4.3.20a), plotted against the Cartesian and polar solutions, Eqs. (E.1.16) and (4.3.6), respectively. This figure shows quantitatively how close the asymptotic comparisons discussed in section E.1.3 are to each other. Note that in the velocity space the only really significant deviations are where the Cartesian solution deviates from the other two in the limit of low evaporation, *e.g.* $\mathfrak{N}_n < 10^{-1}$ and $\tilde{t} > 10^2$. Otherwise, all three solutions of the front velocity are nearly identical when plotted logarithmically. The values for the front velocity without evaporation agree with the data given in Figure 4b of our previous paper[23].

The front velocity gives the clearest picture of the distinct regimes given by the product $\mathfrak{N}_n\tilde{t}$. In Figure E.5, we see that the contours are almost vertical lines, constants with evaporation rate, for all values $\mathfrak{N}_n\tilde{t} < 0.1$. For $\mathfrak{N}_n\tilde{t} > 10$ there is no data plotted—the figure is devoid of contour lines in the upper right portion—because the front velocity has dropped so significantly relative to the capillary driven velocity

Figure E.5. Contour plot of front velocity over evaporation number and time for the elliptic solution. Dashed black lines represent $\mathfrak{N}_n \tilde{t} = 0.1$ and $\mathfrak{N}_n \tilde{t} = 10$ in the lower left and upper right, respectively. The upper right corner is blank because the numerical value of the flow velocity is too insignificant to plot; the lowest contours plotted are $\tilde{v}_f = 10^{-5}$.

rates that we can consider the system to have reached steady state. In between these two values, the contours drop off very rapidly. So we see from this figure that the bounding lines of $\mathfrak{N}_n \tilde{t} = 0.1$ and 10 parameterize the three flow regimes very well. In essence this shows that the evaporation can have an effect on the flow at times only 1% of the time to reach steady state.

Figure E.6 produces a detailed contour plot of the bulk velocity versus time and evaporation number. This was generated by the assumed constant front shape equation of the bulk velocity, Eq. (4.3.23), instead of the integral equation, Eq (4.3.22), which was used in Figure 4.7. It shows essentially the same phase behavior observed in Figures 4.6 and E.5. However, one notable difference from those figures is the wider spacing of contour lines in the lower right corner. This is the effect of the higher finite bulk flow rate for the 2D case which is visible in the right side of Figure 4.7a. We also observe that the steady state bulk velocity is fully horizontal by $\mathfrak{N}_n \tilde{t} = 10$. Both
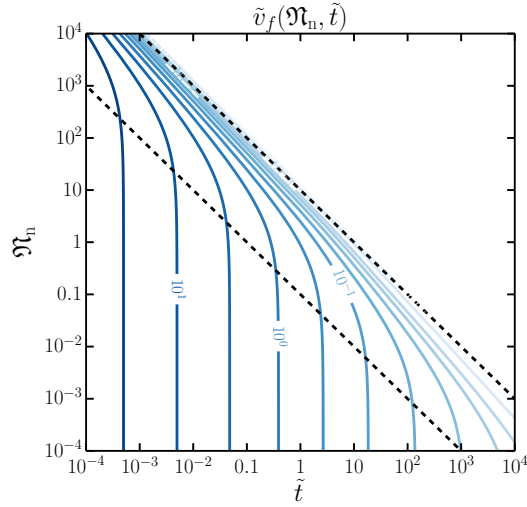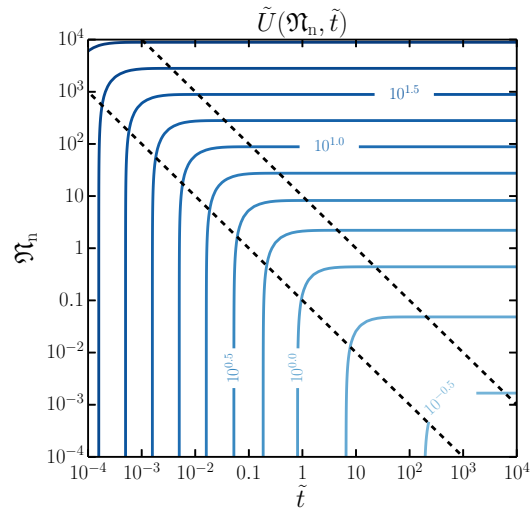
Figure E.6. Contour plot of bulk velocity over evaporation number and time for the elliptic solution. Dashed black lines represent $\mathfrak{N}_n \tilde{t} = 0.1$ and $\mathfrak{N}_n \tilde{t} = 10$ in the lower left and upper right, respectively.

Figs. E.5 and E.6 confirm the time dependent regimes of flow observed in Figure 4.6.

Appendix F

Additional Details on Restraint by Gravity and Side Evaporation

F.1   Supplemental Derivations

In this section, we outline the derivations of the side evaporation and gravity potentials given in Secs. 5.3 and 5.4. We use separation of variables to solve the two-dimensional partial differential equations for each case.

F.1.1   Polar Restraining Gravity Potential

The velocity potential for the restraining gravity effect is given by the differential equation,

$$\frac{\partial^2 \gamma}{\partial r^2} + \frac{1}{r}\frac{\partial \gamma}{\partial r} + \frac{1}{r^2}\frac{\partial^2 \gamma}{\partial \theta^2} = 0, \tag{F.1.1}$$

Appendix F. Additional Details on Restraint by Gravity and Side Evaporation

were the boundary conditions are

$$\left[-\frac{1}{r}\frac{\partial\gamma}{\partial\theta}\right]\Big|_{\theta=0} = 0, \tag{F.1.2a}$$

$$\left[\frac{1}{r}\frac{\partial\gamma}{\partial\theta}\right]\Big|_{\theta=\pi} = 0, \tag{F.1.2b}$$

$$[\gamma|_{r=r_0} = -s_{\mathrm{g}}\frac{k\rho g}{\mu}r_f\sin(\theta), \tag{F.1.2c}$$

$$[\gamma|_{r=r_f} = 0. \tag{F.1.2d}$$

Using separation of variables, $\gamma(r,\theta) = R(r)\Theta(\theta)$, the equation in the angular direction is

$$\frac{\mathrm{d}^2\Theta}{\mathrm{d}\theta^2} + \lambda\Theta = 0. \tag{F.1.3}$$

This is solved by the simple harmonic series,

$$\Theta = C_1\cos\left(\sqrt{\lambda}\,\theta\right) + C_2\sin\left(\sqrt{\lambda}\,\theta\right). \tag{F.1.4}$$

Taking the derivative, we see at $\theta = 0$ that $C_2 = 0$. Furthermore, applying the other boundary condition, we constrain the eigenvalues to be $\sqrt{\lambda} = n$. So the solution of angular potential is given by the series,

$$\Theta = \sum_{n=0}^{\infty} C_{1n}\cos(n\theta). \tag{F.1.5}$$

The differential equation in the radial direction is

$$r^2\frac{\mathrm{d}^2 R}{\mathrm{d}r^2} + r\frac{\mathrm{d}R}{\mathrm{d}r} - \lambda R = 0. \tag{F.1.6}$$

This is an Euler–Cauchy equation which is clearly solved by

$$R(r) = D_1 r^{-n} + D_2 r^n. \tag{F.1.7}$$

Then applying the condition at the wet front, $[R|_{r=r_f} = 0$, we find $D_1 = -D_2 r_f^{2n}$, and the solution is,

$$R(r) = -D_2\left(r_f^{2n} - r^{2n}\right)r^{-n}. \tag{F.1.8}$$

Appendix F. Additional Details on Restraint by Gravity and Side Evaporation

Combining $R(r)$ and $\Theta(\theta)$, the potential is of the form,

$$\gamma = \sum_{n=1}^{\infty} c_n \left(r_f^{2n} - r^{2n} \right) r^{-n} \cos(n\theta). \tag{F.1.9}$$

Substituting the final boundary condition and applying orthogonality, the series coefficients are determined,

$$c_n = \frac{2}{\pi} \frac{k\rho g}{\mu} r_f \frac{1 + (-1)^n}{1 - n^2} \frac{r_0^n}{r_f^{2n} - r_0^{2n}} \tag{F.1.10}$$

Substituting this form and changing the index of the summation to $n = 2j$ because only even values of n are non-zero, we get the gravity potential in polar coordinates;

$$\tilde{\gamma} = -\frac{4}{\pi} \mathrm{Bo}_a \tilde{r}_f \sum_{j=1}^{\infty} \frac{1}{(2j)^2 - 1} \frac{\tilde{r}_f^{4j} - \tilde{r}^{4j}}{\tilde{r}_f^{4j} - 1} \frac{1}{\tilde{r}^{2j}} \cos(2j\theta). \tag{F.1.11}$$

F.1.2 Polar Side Evaporation Potential

The side evaporation potential is expressed by the same differential equation,

$$\frac{\partial^2 \omega}{\partial r^2} + \frac{1}{r} \frac{\partial \omega}{\partial r} + \frac{1}{r^2} \frac{\partial^2 \omega}{\partial \theta^2} = 0, \tag{F.1.12}$$

but with the different boundary conditions,

$$\left[-\frac{1}{r} \frac{\partial \omega}{\partial \theta} \right]_{\theta=0} = -q_s, \tag{F.1.13a}$$

$$\left[\frac{1}{r} \frac{\partial \omega}{\partial \theta} \right]_{\theta=\pi/2} = 0, \tag{F.1.13b}$$

$$\left[\omega \right]_{r=r_0} = 0, \tag{F.1.13c}$$

$$\left[\omega \right]_{r=r_f} = 0. \tag{F.1.13d}$$

Observe that the non-homogenous BC is in the θ-direction instead of the radial direction as it was with the gravity potential. The variables are separable, so we define $\omega(r, \theta) = R(r)\Theta(\theta)$ to find the equation in the radial direction

$$r^2 \frac{\mathrm{d}^2 R}{\mathrm{d} r^2} + r \frac{\mathrm{d} R}{\mathrm{d} r} = -\lambda R. \tag{F.1.14}$$

Appendix F. Additional Details on Restraint by Gravity and Side Evaporation

As an Euler–Cauchy equation, we apply the form $R(r) = Cr^k$ and find from the indicial equation, $k = \pm i\sqrt{\lambda} = 0 \pm i\beta$. This gives the harmonic series,

$$R(r) = C_1 \cos(\beta \ln(r)) + C_2 \sin(\beta \ln(r)). \tag{F.1.15}$$

From the boundary condition at the inlet, $C_1 = 0$, and from the second boundary condition we find the eigenvalues are

$$\beta_n = \frac{n\pi}{\ln(r_f/r_0)}. \tag{F.1.16}$$

This gives the series equations

$$\tilde{R}(\tilde{r}) = \sum_{n=1}^{\infty} C'_{2n} \sin\left(n\pi \frac{\ln(\tilde{r})}{\ln(\tilde{r}_f)}\right). \tag{F.1.17}$$

The differential equation in the θ-direction is

$$\frac{\mathrm{d}^2\Theta}{\mathrm{d}\theta^2} - \lambda\Theta = 0, \tag{F.1.18}$$

which is evidently solved by hyperbolic sine and cosine series,

$$\Theta(\theta) = D_1 \cosh\left(\sqrt{\lambda}\,\theta\right) + D_2 \sinh\left(\sqrt{\lambda}\,\theta\right). \tag{F.1.19}$$

The homogenous BC gives the relation between the coefficients $D_1 = -D_2 \coth\left(\sqrt{\lambda}\frac{\pi}{2}\right)$, and the solution form becomes,

$$\Theta(\theta) = -D_2 \left[\coth\left(\sqrt{\lambda}\frac{\pi}{2}\right)\cosh\left(\sqrt{\lambda}\,\theta\right) - \sinh\left(\sqrt{\lambda}\,\theta\right)\right]. \tag{F.1.20}$$

Combining the separated variables, we get the solution

$$\tilde{\omega} = \sum_{n=1}^{\infty} C_n \sin\left(n\pi \frac{\ln(\tilde{r})}{\ln(\tilde{r}_f)}\right) \left[\coth\left(n\pi \frac{\pi/2}{\ln(\tilde{r}_f)}\right)\cosh\left(n\pi \frac{\theta}{\ln(\tilde{r}_f)}\right) - \sinh\left(n\pi \frac{\theta}{\ln(\tilde{r}_f)}\right)\right]. \tag{F.1.21}$$

The coefficients were determined from the final boundary condition,

$$C_n = -2\mathfrak{N}_{\mathrm{s}} \frac{[1 - (-1)^n \tilde{r}_f] \ln(\tilde{r}_f)}{n^2\pi^2 + (\ln(\tilde{r}_f))^2}. \tag{F.1.22}$$

Thus the full side evaporation potential for polar coordinates is,

$$\tilde{\omega} = -2\mathfrak{N}_{s} \sum_{n=1}^{\infty} \frac{[1 - (-1)^{n}\tilde{r}_{f}]\ln(\tilde{r}_{f})}{n^{2}\pi^{2} + (\ln(\tilde{r}_{f}))^{2}} \sin\left(n\pi\frac{\ln(\tilde{r})}{\ln(\tilde{r}_{f})}\right)$$
$$\times \left[\coth\left(n\pi\frac{\pi/2}{\ln(\tilde{r}_{f})}\right)\cosh\left(n\pi\frac{\theta}{\ln(\tilde{r}_{f})}\right) - \sinh\left(n\pi\frac{\theta}{\ln(\tilde{r}_{f})}\right)\right]. \tag{F.1.23}$$

F.1.3   Spherical Restraining Gravity Potential

The partial differential equation for the gravitational velocity potential is

$$\frac{\partial^{2}\gamma}{\partial r^{2}} + \frac{2}{r}\frac{\partial\gamma}{\partial r} + \frac{1}{r^{2}}\frac{\partial^{2}\gamma}{\partial\theta^{2}} + \frac{\cot(\theta)}{r^{2}}\frac{\partial\gamma}{\partial\theta} = 0, \tag{F.1.24}$$

with boundary conditions,

$$\left[-\frac{1}{r}\frac{\partial\gamma}{\partial\theta}\right]_{\theta=0} = 0, \tag{F.1.25a}$$

$$\left[\frac{1}{r}\frac{\partial\gamma}{\partial\theta}\right]_{\theta=\frac{\pi}{2}} = 0, \tag{F.1.25b}$$

$$[\gamma]_{r=r_{0}} = -s_{g}\frac{k\rho g}{\mu}r_{f}\cos(\theta), \tag{F.1.25c}$$

$$[\gamma]_{r=r_{f}} = 0. \tag{F.1.25d}$$

We separate along the variables with $\gamma(r,\theta) = R(r)\Theta(\theta)$. In the angular direction the separate potential is,

$$\frac{d^{2}\Theta}{d\theta^{2}} + \cot(\theta)\frac{d\Theta}{d\theta} + \lambda\Theta = 0. \tag{F.1.26}$$

This equation is solved by Legendre functions where the eigenvalues are $\lambda = p(p+1)$,

$$\Theta(\theta) = C_{1}\,P_{p}(\cos(\theta)) + C_{2}\,Q_{p}(\cos(\theta)). \tag{F.1.27}$$

Appendix F. Additional Details on Restraint by Gravity and Side Evaporation

From the boundary condition along the z-axis, $C_2 = 0$, and the other boundary condition quickly constrains the eigenvalues to

$$0 = C_1 \left[\frac{\mathrm{d}\,\mathrm{P}_p(\cos(\theta))}{\mathrm{d}\theta} \right]_{\theta=\frac{\pi}{2}}, \qquad \text{(F.1.28a)}$$

$$p = 2n. \qquad \text{(F.1.28b)}$$

Thus, the potential in the angular dimension is the series,

$$\Theta = \sum_{n=0}^{\infty} C_n \, \mathrm{P}_{2n}(\cos(\theta)). \qquad \text{(F.1.29)}$$

Now the separated solution in the radial direction is

$$r^2 \frac{\mathrm{d}^2 R}{\mathrm{d}r^2} + 2r \frac{\mathrm{d}R}{\mathrm{d}r} - \lambda R = 0, \qquad \text{(F.1.30)}$$

where $\lambda = 2n(2n+1)$. This Euler–Cauchy equation is solved by in the form $R(r) = D_1 r^{2n} + D_2 r^{-(2n+1)}$. From the boundary condition at the front, the solution simplifies to;

$$R(r) = D_2 \frac{\left(\frac{r_f}{r}\right)^{2n+1} - \left(\frac{r}{r_f}\right)^{2n}}{r_f^{2n+1}}. \qquad \text{(F.1.31)}$$

Combining the separated equations,

$$\tilde{\gamma} = \sum_{n=0}^{\infty} c_n \frac{\left(\frac{\tilde{r}_f}{\tilde{r}}\right)^{2n+1} - \left(\frac{\tilde{r}}{\tilde{r}_f}\right)^{2n}}{\tilde{r}_f^{2n+1}} \, \mathrm{P}_{2n}(\cos(\theta)). \qquad \text{(F.1.32)}$$

The boundary condition,

$$c_m = \mathrm{Bo}_a \frac{(-1)^{m+1} \tilde{r}_f}{1 - \tilde{r}_f^{-(4m+1)}} \frac{4m+1}{(2m-1)(2m+2)} \frac{(2m)!}{2^{2m}(m!)^2} \qquad \text{(F.1.33)}$$

Finally, the gravitational velocity potential is produced;

$$\tilde{\gamma} = -\mathrm{Bo}_a \tilde{r}_f \sum_{n=0}^{\infty} \frac{(-1)^n (4n+1)}{(2n-1)(2n+2)} \frac{(2n)!}{2^{2n}(n!)^2} \frac{\left(\frac{\tilde{r}_f}{\tilde{r}}\right)^{2n+1} - \left(\frac{\tilde{r}}{\tilde{r}_f}\right)^{2n}}{\tilde{r}_f^{2n+1} - \tilde{r}_f^{-2n}} \, \mathrm{P}_{2n}(\cos(\theta)). \qquad \text{(F.1.34)}$$

F.1.4   Spherical Side Evaporation Potential

The differential equation for the side evaporation potential in spherical coordinates is,

$$\frac{\partial^2 \omega}{\partial r^2} + \frac{2}{r}\frac{\partial \omega}{\partial r} + \frac{1}{r^2}\frac{\partial^2 \omega}{\partial \theta^2} + \frac{\cot(\theta)}{r^2}\frac{\partial \omega}{\partial \theta} = 0, \tag{F.1.35}$$

along with the boundary conditions,

$$\left[\frac{1}{r}\frac{\partial \omega}{\partial \theta}\right]_{\theta=0} = 0, \tag{F.1.36a}$$

$$\left[\frac{1}{r}\frac{\partial \omega}{\partial \theta}\right]_{\theta=\frac{\pi}{2}} = q_s, \tag{F.1.36b}$$

$$\left[\omega\right]_{r=r_0} = 0, \tag{F.1.36c}$$

$$\left[\omega\right]_{r=r_f} = 0. \tag{F.1.36d}$$

Separating the differential equation with $\omega(r,\theta) = R(r)\Theta(\theta)$, the equation in the radial direction is

$$r^2\frac{\mathrm{d}^2 R}{\mathrm{d}r^2} + 2r\frac{\mathrm{d}R}{\mathrm{d}r} + \lambda R = 0. \tag{F.1.37}$$

The roots of the indicial equation are $-\frac{1}{2} \pm \frac{1}{2}\sqrt{1-4\lambda}$, which gives the solution in the form,

$$\tilde{R}(\tilde{r}) = \frac{1}{\sqrt{\tilde{r}}}\left[C_1'\cos\left(-\frac{1}{2}\sqrt{4\lambda-1}\ln(r)\right) + C_2'\sin\left(-\frac{1}{2}\sqrt{4\lambda-1}\ln(\tilde{r})\right)\right]. \tag{F.1.38}$$

From the boundary condition at $r = r_0$, the cosine series must be zero or $C_1' = 0$. The boundary condition at $r = r_f$ constrains the eigenvalues to the form

$$\lambda_n = \frac{1}{4} + \frac{(n\pi)^2}{[\ln(\tilde{r}_f)]^2}. \tag{F.1.39}$$

Thus, the solution in the radial direction is given by the series,

$$\tilde{R}(\tilde{r}) = \frac{1}{\sqrt{\tilde{r}}}\sum_{n=1}^{\infty} C_n'\sin\left(n\pi\frac{\ln(\tilde{r})}{\ln(\tilde{r}_f)}\right). \tag{F.1.40}$$

The separated differential equation in the θ-direction is

$$\frac{d^2\Theta}{d\theta^2} + \cot(\theta)\frac{d\Theta}{d\theta} - \lambda\Theta = 0. \tag{F.1.41}$$

This equation is solved by Legendre functions in the form,

$$\Theta_n = D_1\,\mathrm{P}_{n\pi/\ln(\tilde{r}_f)-1/2}(\cos(\theta)) + D_2\,\mathrm{Q}_{n\pi/\ln(\tilde{r}_f)-1/2}(\cos(\theta)) \tag{F.1.42}$$

The homogeneous Neumann boundary condition at $\theta = 0$ reduces the solution to

$$\Theta_n = D_{1,n}\,\mathrm{P}_{n\pi/\ln(\tilde{r}_f)-1/2}(\cos(\theta)) \tag{F.1.43}$$

due to the derivative of the second Legendre function being undefined. The solution form is now,

$$\tilde{\omega} = \frac{1}{\sqrt{\tilde{r}}}\sum_{n=1}^{\infty} C_n\,\mathrm{P}_{n\pi/\ln(\tilde{r}_f)-1/2}(\cos(\theta))\sin\left(\frac{n\pi}{\ln(\tilde{r}_f)}\ln(\tilde{r})\right). \tag{F.1.44}$$

Applying the final boundary condition, we get the coefficient is

$$C_n = -\mathfrak{N}_\mathrm{s}\frac{m\pi\left[(-1)^m\tilde{r}_f^{3/2} - 1\right]}{(m\pi)^2 + \left[\ln\left(\tilde{r}_f^{3/2}\right)\right]^2}\frac{2}{[m\pi/\ln(\tilde{r}_f) + 1/2]\,\mathrm{P}_{m\pi/\ln(\tilde{r}_f)+1/2}(0)} \tag{F.1.45}$$

Combining, the 3D side evaporation potential is

$$\tilde{\omega} = -2\mathfrak{N}_\mathrm{s}\sum_{n=1}^{\infty}\frac{n\pi\left[(-1)^n\tilde{r}_f^{3/2} - 1\right]}{(n\pi)^2 + \left[\ln\left(\tilde{r}_f^{3/2}\right)\right]^2}\frac{\mathrm{P}_{n\pi/\ln(\tilde{r}_f)-1/2}(\cos(\theta))}{[n\pi/\ln(\tilde{r}_f) + 1/2]\,\mathrm{P}_{n\pi/\ln(\tilde{r}_f)+1/2}(0)}\frac{\sin\left(n\pi\frac{\ln(\tilde{r})}{\ln(\tilde{r}_f)}\right)}{\sqrt{\tilde{r}}}. \tag{F.1.46}$$

Appendix G

Experiments on Capillary–Driven Flow in Thin Expanding Porous Media with Evaporation

G.1 Background

Recent work on microfluidic devices and medical diagnostics have motivated a deeper understanding of the dynamics of wetting porous media. Shaped porous paper has found use in advancing multiple simultaneous medical tests using single fluid samples.[48–50] Furthermore, some sugar based micro fuel cells use wicking in paper to continue driving the reactant solution by the passive and non-energy intensive process of capillary action and evaporation.[17,21,22,73] Some other applications of wicking include wet soils, building materials, and underground contaminant transport.[4,7,63] Thus, the rate of fluid uptake into the porous medium must be understood quantitatively for accurate design of these devices.

Lucas and Washburn[54,55] determined the position of the front advances as the

square root of the contact time in wetting capillary flows. This is also applicable to porous media when the front is assumed to be discontinuous between wetted and dry regions.[71] Xiao *et al.*[60] observed some discrepancies from this behavior that may be due to the effects of both gravity and evaporation. Fries *et al.*[80] showed the decrease in front motion caused by evaporation with partial agreement with experiments. Ref.[24] discusses the 1D evaporation in further depth and show that interfaces through which the evaporation occurs affect the behavior of the front.* It is also observed that a dimensionless quantity, called the evaporation capillary number, governs the rate at which the evaporation effects the flow in the porous medium. This has been extended into the case of 2D flows with circular inlets[95] and flat inlets.[82] However, these most recent studies have not been validated with physical experiments as is necessary before they may be acceptable for use in device design.[22]

In this appendix, we discuss experiments on 1D and 2D capillary wicking with evaporation losses from thin media and their relation to proposed theories. Initially dry paper strips and fans are partially immersed in a beaker of water and the front position is measured at regular time intervals. We hypothesize that the observed wetting fronts will match the predictions of the theoretical models.

In the following section we review key analytical relations from the recent theoretical models of 1D and 2D wicking with evaporation. Sec. G.3 details the experimental methods. Sec. G.4 compares the experiments to the theory, and the conclusions are given in Sec. G.5.

---

* The theories investigated in this chapter are given in Chs. 3 and 4.

G.2 Theory

In this section, we lay out the essential equations which describe wicking in thin porous media. These are principally the equations of front position and fluid uptake rate.

G.2.1 Flow in Thin Strips of Constant Cross Section

Lucas[54] and Washburn[55] demonstrated the central relationship for capillary imbibition, also called the Lucas–Washburn Equation (LWE)

$$\frac{1}{2}\left(\frac{L}{a}\right)^2 = \frac{\varphi_0 t}{a^2}. \tag{G.2.1}$$

where L is the wetted length, a is half the size of the inlet, $\varphi_0 = kP_c/\mu$ is the maximum capillary potential, and t is the wetted time. Here we have presented the LWE in the form wherein it is applicable to flow in porous media of constant cross section with a discontinuous wetting interface.[53,71] This is referred to as a 1D capillary wicking. The characteristic parameters of the wetting porous media are the permeability, k, the capillary pressure P_c, and the viscosity, μ. The total uptake of fluid, U, from the reservoir and into the porous medium is related to the inverse square root of the imbibition time, $U \sim 1/\sqrt{t}$.

Capillary Flow with Evaporation

The wicking of liquids is significantly effected by evaporation.* The evaporation capillary number, $\mathfrak{N}_n$, describes the relative effects of the evaporation rate, Q, to the

---

* Here we are primarily revisiting the work in Ch. 3. In particular, the evaporation capillary number is detailed in Sec. 3.4.1 and Eq. (3.4.2a). The following equations are originally given as Eqs. (3.3.29), (3.4.3), (3.3.35), and (4.3.28), respectively. This theory is alternatively derived in Sec. E.1.2 and compared to the literature in Sec. 3.A.

Appendix G. Experiments on Expanding Media with Evaporation

capillary diffusivity;

$$\mathfrak{N}_n = \frac{\mu a^2 Q}{k P_c} = \frac{\text{characteristic mass flux of evaporation}}{\text{characteristic mass flux of wicking}}. \qquad \text{(G.2.2)}$$

This number indicates the strength of the evaporation rate on the flow and its inverse approximates the time at which evaporation becomes important in the behavior of the system.

The position of the front with time is described

$$\frac{1}{2}\mathfrak{N}_n \tilde{L}^2 = 1 - \exp(-\mathfrak{N}_n \tilde{t}), \qquad \text{(G.2.3)}$$

where $\tilde{L} = L/a$ is the front position in dimensionless form, and $\tilde{t} = k P_c t / (\mu a^2)$. This agrees with the solution given by Fries *et al.*[80]. At large times the equation reduces to the steady-state front position as a relation to the evaporation number

$$\tilde{L}_{ss} = \sqrt{\frac{2}{\mathfrak{N}_n}}. \qquad \text{(G.2.4)}$$

The bulk flow rate into the porous medium is increased by the evaporation

$$\tilde{U} = \frac{2}{\tilde{L}} + \mathfrak{N}_n \tilde{L}, \qquad \text{(G.2.5)}$$

where $\tilde{U} = (\mu / k P_c \delta) U$, and δ is the small thickness of the porous medium in the z-direction such that $\delta \ll 2a$. For the 1D-like flow, we also find an explicit expression for the steady state the bulk velocity versus evaporation number

$$\tilde{U}_{ss} = \sqrt{8 \mathfrak{N}_n}. \qquad \text{(G.2.6)}$$

G.2.2   Flow in Thin Fanning Porous Media

The theoretical model for wicking in a two-dimenaionally expanding domain through a flat inlet is described by elliptic coordinates;*

$$x = a \cosh(\eta) \cos(\psi), \tag{G.2.7a}$$

$$y = a \sinh(\eta) \sin(\psi). \tag{G.2.7b}$$

Therefore when a point in elliptic coordinates is known, (η, ψ), the values in Cartesian coordinates may be readily determined. The front position equation for the 2D elliptic expansion is found via

$$\frac{\mathrm{d}\eta_f}{\mathrm{d}\tilde{t}} = \frac{1}{\cosh^2(\eta_f) - \cos^2(\psi)} \left\{ \frac{1}{\eta_f} - \frac{1}{4} \mathfrak{N}_{\mathrm{n}} \left[\frac{2\eta_f \sinh(2\eta_f) - \cosh(2\eta_f) + 1}{2\eta_f} - \tanh(\eta_f) \cos(2\psi) \right] \right\}. \tag{G.2.8}$$

This first order nonlinear differential equation does not have an analytical solution and so it requires a numerical method to evaluate the front position with time. Note that this elliptic solution may be approximated at large expansions by a domain with a semi-circular inlet similar to the work done by Hyväluoma *et al.*[61] and Liu *et al.*.[95].

In general, the bulk velocity must be computed from an integral expression because the front position weakly depends on ψ.

$$\tilde{U} = \int_0^\pi \frac{1}{\eta_f} + \frac{1}{4} \mathfrak{N}_{\mathrm{n}} \left[\frac{\cosh(2\eta_f) - 1}{2\eta_f} + \tanh(\eta_f) \cos(2\psi) \right] \mathrm{d}\psi. \tag{G.2.9}$$

By assuming an elliptic front shape, this approximately simplifies to

$$\tilde{U} = \frac{\pi}{\eta_f} + \frac{\pi}{8} \mathfrak{N}_{\mathrm{n}} \left[\frac{\cosh(2\eta_f) - 1}{\eta_f} \right]. \tag{G.2.10}$$

---

* In the following summary of theory, we outline the key work presented in Ch. 4. The following equations are first given as Eqs. (4.3.13), (4.3.20b), (4.3.22), and (4.3.23), respectively.

G.2.3 Power Law Approximations

The solutions given above may be approximated by simple power laws to describe the earliest time evaporation effects.* Setting the axis of the flow along the y-direction, as is the case for the centerline of the 2D case, we consider the position of the front by $\tilde{y}_f$. For 1D capillary flow with evaporation, the first order effect of the evaporation is given by

$$\frac{1}{2}\left(\tilde{y}_f^2 + \frac{1}{4}\mathfrak{N}_\mathrm{n}\tilde{y}_f^4\right) \approx \tilde{t}. \tag{G.2.11}$$

This is only accurate only for the early time effects of the evaporation, approximately up to $\mathfrak{N}_\mathrm{n}\tilde{t} < 1$. For 2D radial flow (derived from the polar coordinate approximation which is applicable at large advancements) the power series is similar, but of a higher order

$$\frac{1}{2}\left\{\tilde{y}_f^2 \ln(\tilde{y}_f) + \frac{1}{4}\mathfrak{N}_\mathrm{n}\tilde{y}_f^4[\ln(\tilde{y}_f)]^2\right\} \approx \tilde{t}. \tag{G.2.12}$$

Along with the steady-state relationships, these two relations are useful for estimation of the time behaviors of the systems.

G.3 Methods

In this section, we discuss the experimental methods and configurations used for data acquisition of wicking in porous media. Additionally, the numerical optimization procedure for the fitting and comparison of the theory to the empirical results is outlined.

---

* This discussion is given in its full form in Sec. 4.4.4, where the following two equations are Eqs. (4.4.4) and (4.4.5).

Appendix G. Experiments on Expanding Media with Evaporation

G.3.1   Experimental

The experiments were designed to reproduce the results for the Lucas–Washburn relation with evaporation and the 2D elliptic expansion with evaporation.[*] The experiments measured the wet front position and in some cases the movement of the fluid into the porous medium via the mass lost from the reservoir. The evaporation rate was controlled by keeping the wetting porous media in a closed box to minimize airflow and disturbances with a volume of approximately 2 m^3, a constant temperature around 23 °C, and maintaining the humidity to within $\pm 2\%$ of a given set point. The humidity was controlled manually via the operation of a humidifier (located at the rear of the box) when indicated by a digital humidity meter (seen on the right side of the experimental configurations shown in Figs. G.1 and G.2). The local elevation is approximately one mile above sea level.

Data was taken at regular intervals up to four hours by which time a steady state was reached. The porous media were dipped into 50 mL jars (the reservoir of liquid) filled with deionized water. The front position was measured using an elementary ruler and all the jars were weighed on a digital scale accurate to 0.0001 grams to determine the volumetric absorption rate (except in the third set of experiments, where this was not analyzed). The porous medium in all experiments was Whatman 1001-185 grade 1 qualitative filter paper.

Experiment 1: Vertical Fans

This experiment was carried out to reproduce unpublished work carried out by other groups and determine the variation of the evaporation rate with the humidity. In the first set of experiments three fans were clipped vertically as shown in Fig. G.1. The

---

[*] The first two series of experiments were conducted by Madelaine S. Chavez in the summer of 2014; the third set was done by Daniel M. Gilliam the following summer.
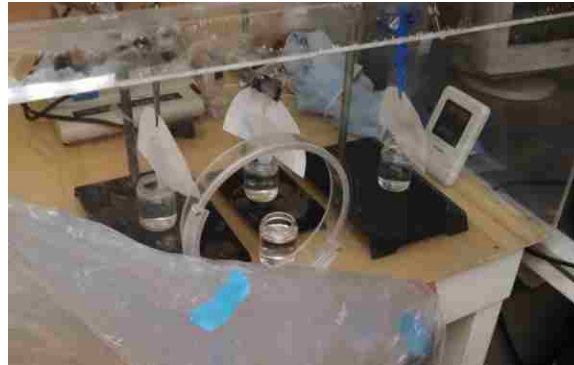
Figure G.1. Laboratory configuration for vertical fan wetting experiments.

Figure G.2. Laboratory configuration for horizontal wetting experiments.

fourth jar without a fan, nearer the front of the box, is the control for evaporation loss of liquid from the jars. Data was taken in prescribed intervals from five minutes to an hour and a half.Both the height of the wetted liquid (the front position) and the mass of each of the jars was measured at each time, where the timing began when the porous media were first put into the jars. The fan radii were 3.5 inches, with tails of 3 and 11/16 inches long. The humidity was held at 30%, 40%, and 50% for each of the three data series.

Experiment 2: Horizontal Fans and Strips

In the second experiment, data was collected on three strips of constant cross section and three fanning domains to facilitate direct comparison between the LWE with

Appendix G. Experiments on Expanding Media with Evaporation

evaporation and the 2D elliptic solution. Although no influence due to gravity was observed in the first experiment, the experimental apparatus was redesigned with a horizontal mesh to lay the media on to eliminate any direct effects of gravity, as illustrated in Fig. G.2. The three initially dry rectangular strips were placed on the wire mesh nearest to the back of the box. The three fans were set on the front of the mesh. On both sides in between the initially dry strips and the fans sat the two fully wetted rectangular strips intended for evaporation rate measurements. The jar for control of evaporation from the reservoir was placed near the right behind the mesh.*

The tail length was reduced to have less effect on the flow (the exposed tail surface area increases over the experiment so the effect of the evaporation on this part of the porous domain is not known precisely). The width of all strips and tails were one inch, and the tails of the strips and fans were 2.25 inches in length (the portion which extends below the mesh and immerses in the reservoir). The initially dry strips were 8.5 total inches long, while the fully wetted strips were only 5.25 inches. The fan was cut with a radius of 3.5 inches.

The experiment time was set to zero when the liquid reached the inlet to the fans and data was taken up to three hours.Wetted length was measured both along the x- and y-directions to account for the variable effects of the flat geometry on the front shape. The effect of the varying evaporation rate was tested for six different humidities from 20% to 70% in increments of 10%. Higher humidities caused capillary condensation in the media and did not produce a reliable wetting front position measurement; this even began to occur after two hours for 70% humidity.

---

* The data may be analyzed so the parameters of φ_0 and Q are found independently, although this particular analytical procedure has not been conducted. The fully-wetted strips would determine the value of the evaporation rate, Q, while the initially dry strips, obeying the LWE at early times, would determine the capillary potential, φ_0. Ideally, with the known parameter values the behavior of the flow in the wetting fans would be fully predictable, and the experimental data for the fans should match the theoretical prediction without any optimization procedure.

Experiment 3: Horizontal Fans

In the third set of experiments, we desired to analyze the effects of inlet size on the motion of the front.* The inlets strips to the porous fans ranged from 0.25, 0.5, and 0.75 inches wide and the experiments were conducted separately at 30%, 40%, and 50% humidity. The tail of each fan was 1.5 in long, and the radius of the fans was 3 inches. Horizontal wetting strips and evaporation control strips were not used, because these were sufficiently explored in the second experiment, and they have a much less significant inlet size effect. Otherwise the configuration was similar to the second experiment, shown in Fig. G.2. In this experiment the rate of absorption into the porous media was not measured via the mass lost from the reservoir jars. The data was taken at prescribed intervals from one minute to about four hours.Because the jars were not weighed, the front position could be measured at closer intervals and so the data was earlier and more often, which was beneficial in accurately determining the capillary potential.

G.3.2   Numerical

Data Analysis and Optimization

The experimental data sets were tabulated for all measurements, items, and times.The length was measured in either in mm or inches. The mass loss from the control jar was subtracted from that of the other jars and divided by the time interval to give the mass loss rate per jar, and through the density of water converted to volume per time in units of mL/min. Then the data for the three texts was averaged and the

---

* The pictures in Fig. E.2 were taken as part of this experiment to show the qualitative evolution of the fan shape as compared to the theoretical prediction given in Fig. E.1, and discussed in Sec. E.2.

standard deviation taken as an estimate of error. Thus, the experimental data was prepared for analysis.

The theoretical values of the front position is calculated directly by Eq. (G.2.3) in the 1D strips, while a Runge–Kutta numerical method is used to solve Eq. (G.2.8)[*] The bulk velocity for the 1D case is also calculated directly from Eq. (G.2.5). The bulk velocity for 2D flow given in Eq. (G.2.9) requires numerically integration over the instantaneous front length using cubic splines.[†]

Once the theoretical data was computed and empirical data had been processed into dimensionless form, an interpolating function is made from the theoretical data, and the theoretical values at the desired experimental times are calculated. These two data sets were then used to compute the correlation residual,

$$R^2 = \sum_{i=1}^{N} \left[\tilde{y}_{f,\,\text{theo}}(t_i) - \tilde{y}_{f,\,\text{expr}}(t_i) \right]^2 . \qquad \text{(G.3.1)}$$

The residual was minimized using an implementation of the BFGS optimization method in python™, with the theoretical data recomputed at each iteration as the value of the evaporation needed to change. This requires initial estimates of the physical parameters φ_0 and Q as well as the time deviation, Δt_0 as we will discuss below. All of these equations were implemented and computed in python™ 2.7.

Initialization of parameters

In determining the closeness of fit of the predicted flow model, we need to know the physical parameters of the system to give initial values for the optimization. When we are analyzing the flow in 1D strips, we use the LWE and it's modification with

---

[*] Other descriptions of the numerical methods are given in Secs. 3.3.5 and E.1.4.   [†] In future these bulk velocities could then be directly compared to the experimental volumetric flow data using the parameters found from analysis of the front length.

evaporation to find the parameters. The known parameter is a, while φ_0 and Q are undetermined, but vary by less than an order of magnitude. The initial guess of the evaporation number, $\mathfrak{N}_n^*$, is easily found by rearranging Eq. (G.2.4)

$$\mathfrak{N}_n^* = \frac{2a^2}{L_{\text{ss}}^2}.\tag{G.3.2}$$

So we take the final front position as the steady state and determine the evaporation number. However, this assumes that the front has completely come to rest by the last point in the data. The capillary potential is related to the slope of the plotted line of the capillary flow. Rearranging the LWE, Eq. (G.2.1), we may choose a data point of a given time and position and estimate the capillary potential,

$$\varphi_0^* = \frac{1}{2}\left(\frac{L}{a}\right)^2\frac{a^2}{t}.\tag{G.3.3}$$

To find the value of the evaporation rate, Q^*, we use the evaporation number and capillary potential determined above, and substitute into the reordered form of Eq. (G.2.1),

$$Q^* = \frac{\varphi_0^*}{a^2}\mathfrak{N}_n^*.\tag{G.3.4}$$

To account for measurement error of the initial time, a time correction, Δt_0, is incorporated into the model. We redefine the dimensionless time for all data in the form,

$$\tilde{t}^* = \varphi_0^*\frac{t - \Delta t_0}{a^2}.\tag{G.3.5}$$

Rearranging the equation, we find

$$\Delta t_0^* = t - \frac{a^2\tilde{t}^*}{\varphi_0^*}.\tag{G.3.6}$$

From which we may determine the initial time correction. All of these parameters are now initialized in a physically motivated manner which should bring convergence to the is a stiff nonlinear optimization problem described previously.

For the radial expansion in fanning media the parameters φ_0^* and Δt_0^* are determined as given above in Eqs. (G.3.3) and (G.3.6) because they are determined through early time data, wherein the behaviors are nearly the same for 1D and 2D. However, the evaporation number should be determined using the correct 2D behavior as is necessitated for larger expansions in a fanning domain. Setting the velocity to zero in Eq. (G.2.8) and steady-state front position

$$\mathfrak{N}_{\mathrm{n}}^* = \frac{8}{2\eta_f \sinh(2\eta_f) - \cosh(2\eta_f) + 1 - 2\eta_f \tanh(\eta_f)\cos(2\psi)}. \tag{G.3.7}$$

G.4   Results

In this section, we compare the theoretical models to the experimental data using the data from the three sets of front position measurements described above.We find the values both unknown physical parameters the capillary potential, φ_0 and the evaporation rate, Q (via measurement of the evaporation capillary number, $\mathfrak{N}_{\mathrm{n}}$), and analyze the accuracy of the method. These optimized parameters also are useful in making the experimental data dimensionless or conversely bringing the theoretical fit into dimensional variables. The residual is calculated to quantify error between the predicted and empirical plots.

G.4.1   First Experiment: Vertical Fans

The averages of the experimental data for the vertically clipped long-tailed fans are shown in Figure G.3. Figure G.3a shows three key qualitative similarities to the theoretical results for the behavior of the front position (infiltration length) with time. First, at early times the slope is significantly greater than for later times, indicating that the flow goes progressively from capillary dominated flow to evaporation dominated. Second, as the humidity increases by increments of 10% the evaporation rate
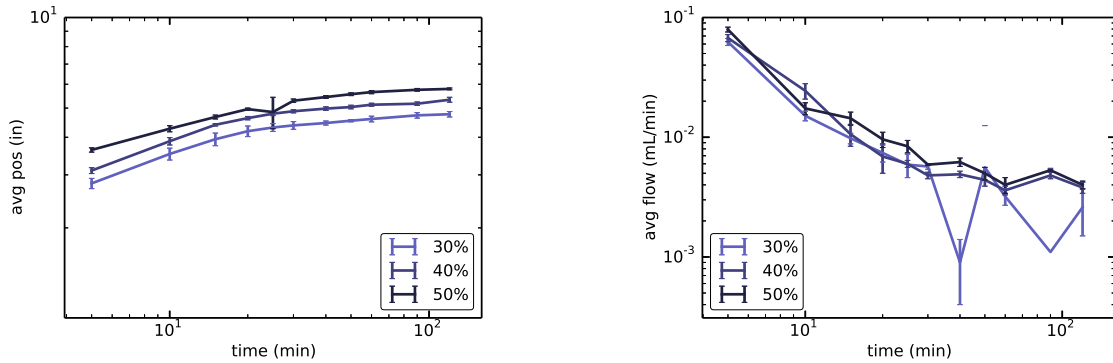
(a) Position of the front with time. **(b)** Volumetric flow rate with time.

Figure G.3. Changing infiltration behavior with respect to humidity.

decreases, and the front movement is not slowed down as quickly. Finally, the front position does not progress at long times—on the order of greater than two hours—which indicates steady state has been reached as expected. One difference between the theoretical predictions and the empirical data is that the magnitude of the front position is noticeably greater for lower evaporation rates at early times. According to the theory, at early enough time the evaporation should have no effect and the three lines above should sit atop each other; this does not appear to be the case.* This separation of the lines indicates that the evaporation effect is significant only five minutes into the experiment as we discuss later through understanding the quantitative description of the system.

In Figure G.3b, the calculated mass flow rate into the medium is shown as it varies over time. The data is noisy because the mass flow is the difference between a previous and current weight, and this kind of discrete derivative is highly sensitive to variations in the measured values. Thus, the mass flow into the porous media is not quantitatively analyzed in this chapter because of the magnitude of these errors. The relation between the different humidities is not as strong as for the positions;

---

* For example see Figure 4.4, where the early time plots perfectly line up for different evaporation numbers in both the 1D and 2D cases.

(a) Imbibition in y-direction.

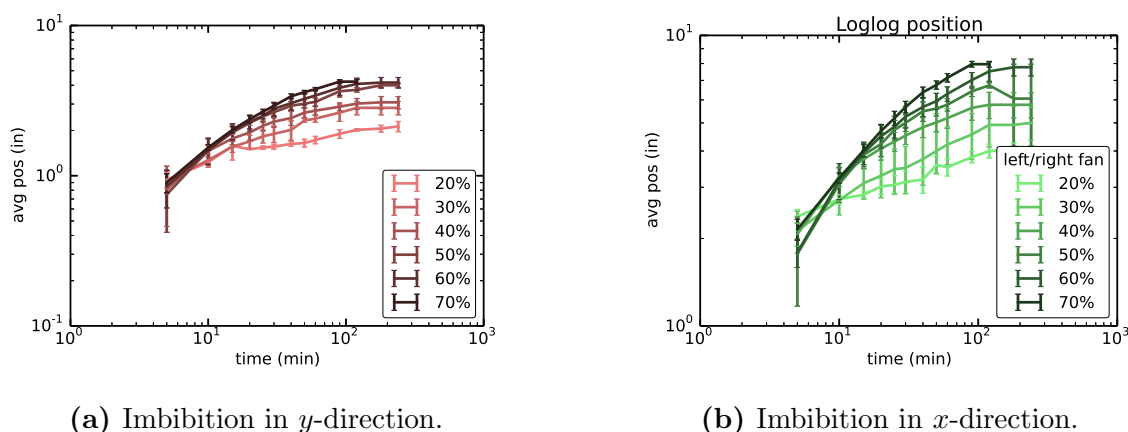**(b)** Imbibition in x-direction.

Figure G.4. Changing infiltration behavior with respect to humidity for horizontal fans.

the 50% trend is almost always greater than the 40%, but the 30% fluctuates heavily. However, the flow rate clearly decreases at the beginning of the experiment, while it hovers near a steady state value on the order of 0.004 mL/min near the end. This matches the qualitative predictions of the theoretical models as these strips are able to drive a finite quantity of fluid at an approximately constant rate over long periods of time.

G.4.2 Second Experiment: Fans and Strips

In this experiment, we desired to compare the 1D and 2D systems from first-principles. Fig. G.4a shows the front position along the central y-axis of the flow. We see a progressive decrease in the steady state front as the humidity decreases because the evaporation rate is increasing. In contrast Fig. G.4b gives the wetted distance across the x-axis along the sides of the fan domain. This quantifies the variation in the wetted front length. Fig. G.5 shows the front position for the wetted strips. The front position advances further for this 1D-like flow than for the 2D expanding flow shown in Fig. G.4a. It was observed that some of the times the front shape in the strips
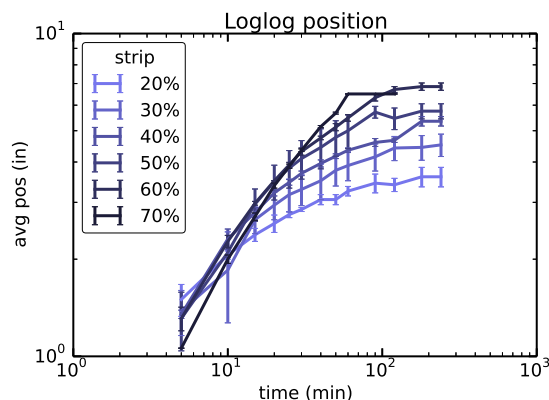
Figure G.5. Changing front position for horizontal strips with varying humidity.

was slightly parabolic, likely due to a small evaporation from the side boundaries.*

Though data was taken on the rate of fluid uptake into the porous medium, we do not discuss any related results here. Similar to the first experiment, this data was noisy and difficult to analyze; qualitatively showing the drop in flow rate and steady state flow.

This set of experiments showed some challenges to testing the theoretical results experimentally. Ambient humidity is not directly convertible into evaporation rate; ideally this must be controlled for and measured by the wetted strips. However, the wetted strips did not necessarily reach steady state evaporation rate until at least an hour into the experiment. The variation of humidity can be used to change the evaporation rate only within a fairly narrow range. For the given temperature, holding a stable 20% humidity was not easy to do at the location. Experiments beyond 70% humidity failed because capillary condensation into the medium was strong and the front position quickly became too diffuse to measure. This is why the humidities are limited from 20–70% as shown in the figures.

---

* See Fig. 3.4 for theory.

(a) 30% humidity.
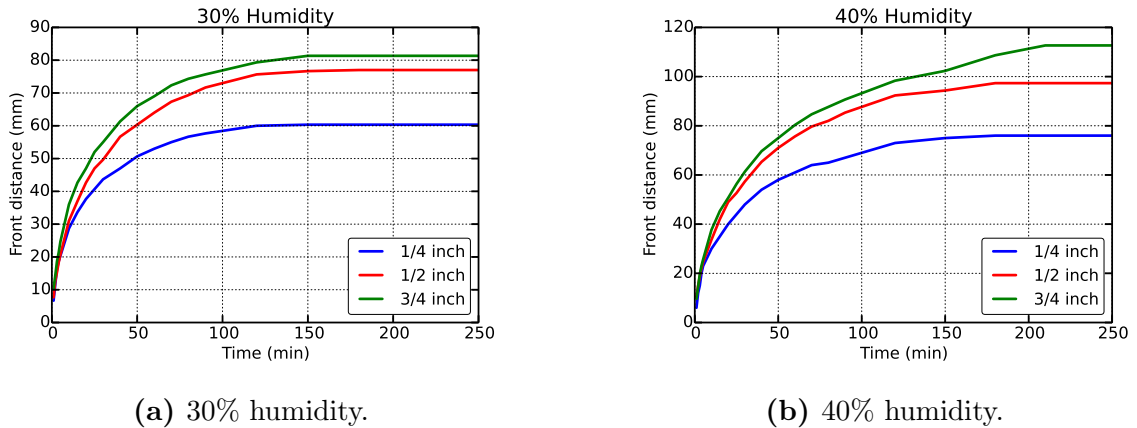

(b) 40% humidity.

Figure G.6. Changing front position for 2D fans of varying inlet size at 30% and 40% humidity.

G.4.3 Third Experiment: Effect of Fan Inlet Size

The third experiment showed variations in the front position behavior with inlet size, a, and humidity, effectively Q, as expected. The front position over time with varying inlet size is illustrated for humidities of 30, 40, and 50% in Figs. G.6a, G.6b, and G.7, respectively. As in all cases above the capillary potential, φ_0, should be a constant throughout the experiments. In all three figures, we observe that the front
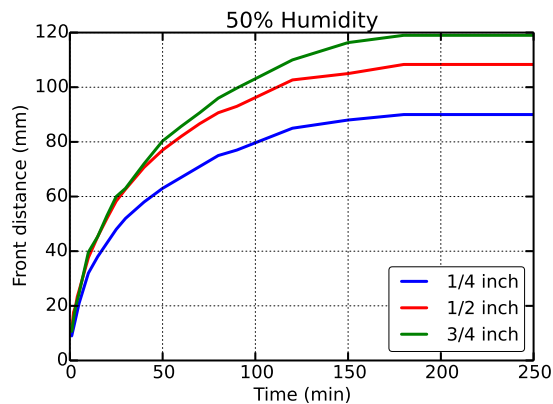

Figure G.7. Changing front position for 2D fans of varying inlet size at 50% humidity.

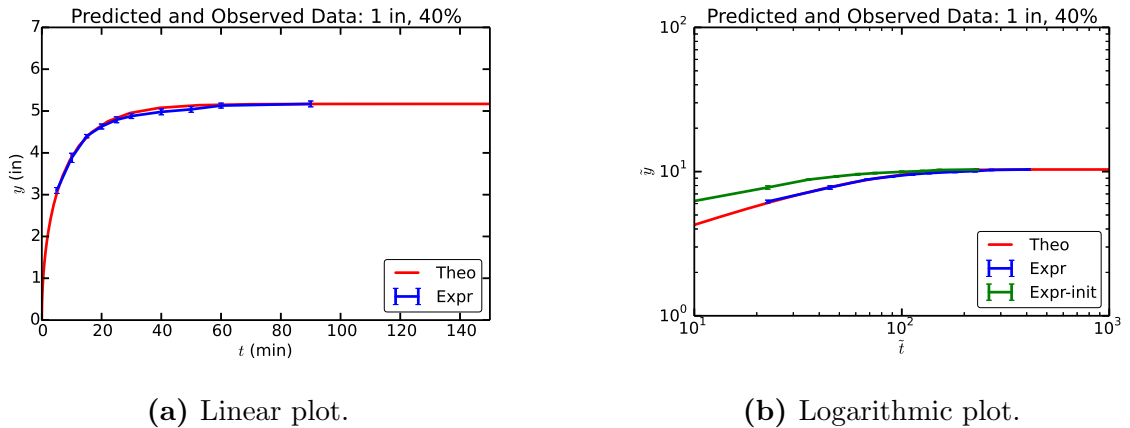**(a)** Linear plot.   **(b)** Logarithmic plot.

Figure G.8. Example closeness of fit to theoretical prediction to 1D strip data. The initial and converged theoretical predictions are shown for comparison. The humidity is 40%.

position advances more quickly going from quarter inch to half than from half inch to three quarters. This stems from the definition of dimensionless time, $\tilde{t} = \varphi_0 t / a^2$, where the effect of the inlet size reduces the dimensionless time quadratically. In other words, had the largest inlet size been a full inch instead of 3/4, then we would have expected a nearly equal linear increase in advancement for each of the intervals of advancement for the three porous domains. As the humidity is varied, we also observe that the steady state front position advances; *e.g.* for the smallest inlet size, we have steady state positions of 60, 76, and 91 mm.

G.4.4 Analysis and Discussion

Closeness of Fit

Figure G.8 shows an example of a strong fitting of the theoretical prediction to the experimental data. This shows that the 1D model can fit the 1D flow data with close accuracy. Fig. G.8a shows a linear plot of the data, which gives a clearer picture of the match at later times, while Fig. G.8b gives the same data plotted logarithmically. We

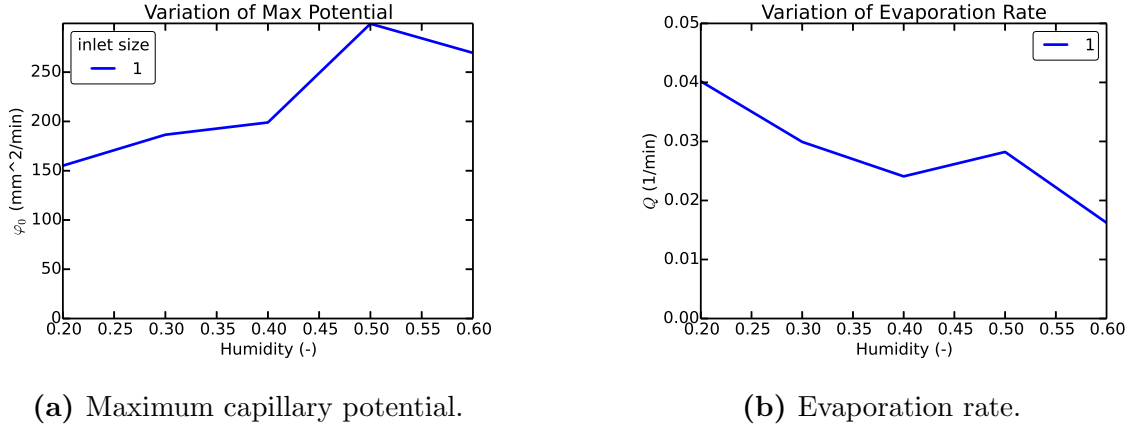**(a)** Maximum capillary potential.　　　　**(b)** Evaporation rate.

Figure G.9. Optimized parameter variation for strips from second set of experiments.

also see that the first theoretical prediction based on the initialized parameter values is close, but significantly improved by the further optimization. In this case, both the linear and logarithmic plots match the data very strongly; in some other data sets one or the other does not fit as well because of early or middle time deviations.

Some errors were observed in the process of the analysis. The $L^2 \ln(L)$ effect in the 2D expansion, seen in Eq. (G.2.12), versus L^2 behavior in the LWE with evaporation means that applying the 1D or 2D theory to the same medium will result in a logarithmic deviation in the measurement of φ_0 depending on which theory is appropriate for the given medium. For the first set of experiments, the experimental data was only taken shortly after dimensionless time $\tilde{t} > 1$. This means that the varying front shape of the fans was already affecting the flow and so the LWE-like behavior had been deviated from. In a few of the cases of lower evaporation rate, it is also likely that the evaporative steady state had not yet been reached, which inhibited the optimized theoretical data from fitting with the experimental.

Experimental Parameter Determination

In Figure G.9, we plot the values of the parameters, φ_0 and Q, as optimized from the experimental data as described in Sec. G.3.2, for the 1D strips in the second experiment. Ideally, the maximum capillary potential, φ_0, should be a constant, while the evaporation rate, Q, should be a monotonically decreasing function with respect the the humidity and should be consistent for various domains. However, in the figure, the max potential varies from 150 to 300 mm^2/min; this is likely due to insufficient early time data to better constrain the potential. The evaporation number and capillary potential, being related, means that the variation in φ_0 causes spurious variation in the computed evaporation rate. So, while we observe a reasonable downward trend of the evaporation rate—going from 0.04/min to 0.02/min over the span of 20% to 60% humidity—we notice that at 50% humidity the evaporation rate increases slightly. In part, these errors in the measure parameters stem from the difficulty in optimizing the data correctly. The shape of the data is numerically very stiff as seen in Fig. G.8a, and this makes the process very difficult to do accurately.

In this section, we do not investigate the ramifications of the theory on predicted values of the bulk velocity.Also, the data for the 70% humidity was not analyzed because the data was not able to be taken as far into the steady-state regime and would therefor not be as accurate.

Figure G.10 shows the parameters extracted from the 2D fan using the 2D flow model. The parameters should be comparable between the 1D strips and the 2D fans at given humidities. However, in most cases, the optimized values of the capillary potential and the evaporation rate are lower from the 2D data. The match seems to be closest at higher percent humidities, *e.g.* 50% and 60%, while 30% is especially different between the two data sets. The capillary potential has a high variation—on the order of a factor of three from 20% to 60% humidity. Now, we may notice in both

(a) Maximum capillary potential.
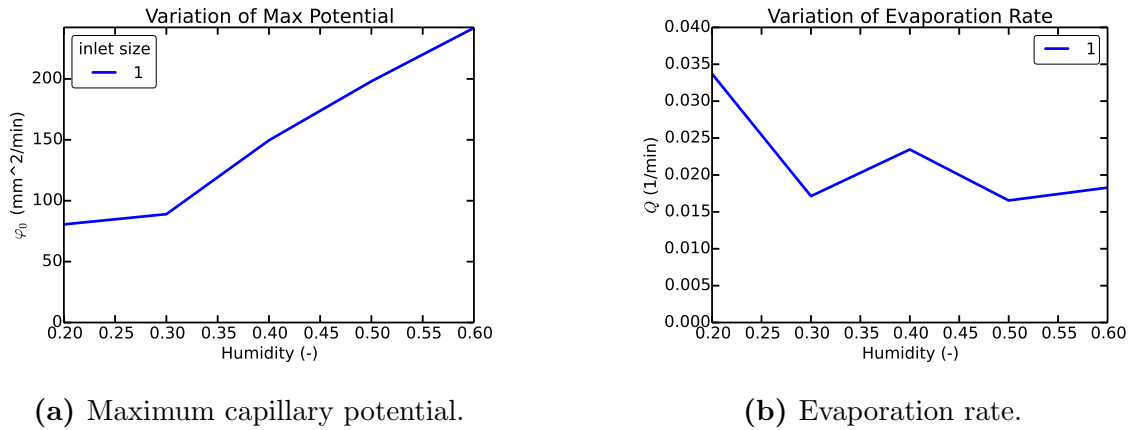
(b) Evaporation rate.

Figure G.10. Optimized parameter variation for fans from second set of experiments.

Figs. G.9b and G.10b that the evaporation rate varies only by about a factor of two over the span of a forty percentage point change. This indicates that small changes in ambient humidity do not have very strong effects on the over-all rate of evaporation from the surface of the porous medium.

Figure G.11 shows the optimized parameters from the data for the third experiment. The trend lines are for different size of the domain inlet, however they generally trend reasonably near to each other as would be expected from the theory (they should
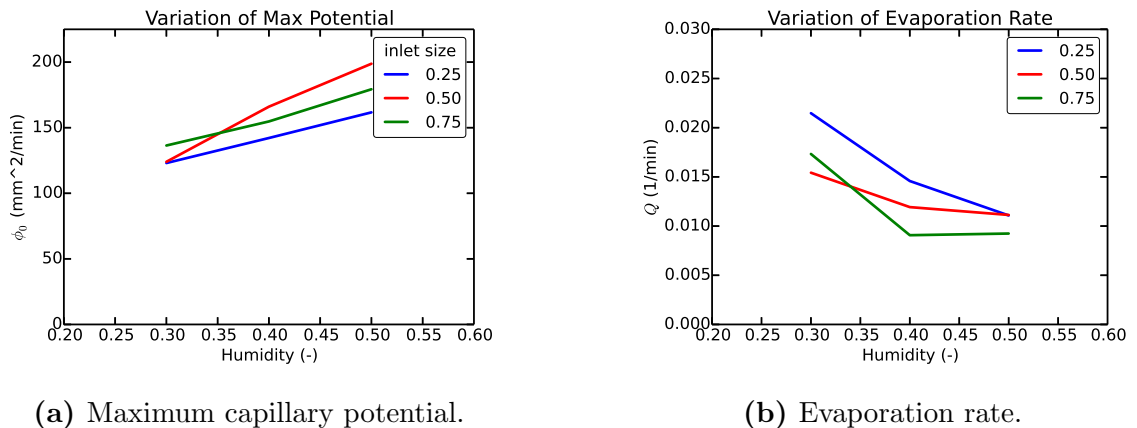

(a) Maximum capillary potential.

(b) Evaporation rate.

Figure G.11. Optimized parameter variation from third set of experiments.

be identical). The observed variation in the maximum capillary potential is not as large as with the second experiment. This is likely due to the several additional data points early and late in the experiment (*e.g.* starting at one minute instead of five). At given humidities, the evaporation rate measured in this experiment is lower than in the previous experiment It is possible that the temperature was not identical in the two experiments. The closeness of the evaporation rates also indicates that the evaporation number is being very useful in extracting the dynamic behavior of the front.

G.5 Conclusions

The experiments could benefit from several improvements in future work. Firstly, the error in the experiments would be reduced by automating the measurement of the front position and mass of the fluid reservoirs. This would be accomplished with a camera suspended above the wetting media taking images at regular intervals while the liquid beakers are permanently positioned on accurate scales. Data acquisition software would then generate the dataset. The automated system would improve the control for the internal temperature and humidity and as a result should give a more consistent evaporation rate. Acquiring more data at the very early times of the experiment, where $\tilde{t} \ll \mathfrak{N}_n$, would make the predicted values of the capillary potential and start time more accurate. The porous fans should have shorter tails to accurately observe the early spreading of the fluid into the 2D domain. The automated system could also go further into the steady state behavior, because there should be fewer errors accumulated in the longer time data. Ideally the work in the vertical wicking experiment should account for the effect of the restraint on the flow by gravity.[75] To check the self-consistency of the theory, the parameters determined using the front position may be used to independently predict the mass absorption rate by

the porous paper. This may resolve the discrepancies observed in Fries *et al.*[80] and further explored in Barry *et al.*.[81] A wider variety of experiments with various liquids, types of media, *etc.* would change the capillary potential and span a more significant portion of the range of theoretical predictions; this could give further insights into the limitations of the proposed theory. The theory may be extended by developing a semi-analytical expression for flow in a fan with a tail to accurately predict the flow in the physical media which have been tested, and we may analyze the accuracy of the predicted theoretical power law and steady state approximations of the given systems. Additionally, experimental comparisons may be done on the reaction rate effects of a sucrose reaction as a function of the flow in the fanning porous medium.[21,22]

In this chapter we applied the mathematical techniques developed for solving capillary flow problems to relevant experimental data. In this work, we developed numerical methods to analyze experimental data and compare to the theoretical models. Results correlate well with recently developed theoretical models, and produce the physical values of the evaporation rate and capillary potential. We observed empirically that the dimension of the flow domain decreases length of penetration of the liquid at a given time but increases imbibition rate into the medium. The evaporation supports continuous flow of liquid into the porous media. The evaporation-capillary number correlates to the steady state and gives the evaporation rate in the porous medium. We found that the evaporation rate is more stable with respect to humidity variations than expected.

Appendix H

Transport in Stress Corroding Aluminum Pores

H.1 Introduction

Stress corrosion cracking (SCC) is the most common final state preceding failure of manufactured aluminum parts. This process occurs as an interplay between chemical corrosion and mechanical stress coupled to degrade the strength of the material through crack propagation. SCC commonly grows from corroded pits on the surface. At the tip of the crack, hydrogen reaches the interstitial sites within the aluminum alloy matrix to degrade the local strength of the metal; this is referred to as hydrogen embrittlement. In some cases, microbes can accelerate the corrosion rate. Within the crack, the fluid flow is effected by the surface chemistry, the multi-ion interactions, diffusiophoresis, electrolytic reactions, and other effects.

From the solid mechanics perspective, molecular dynamics has been used to model the crack propagation atomistically.[138] Lattice Boltzmann methods, as a model of gas-like interactions, has not naturally incorporated solid mechanics into the methodology,

but it may be coupled to other methods such as finite difference or discrete element solid mechanics models of the solid domain deformations if desired.[139] The extended finite element method (XFEM) is specially designed for modeling of crack propagation in solids and would be useful in understanding larger time scale crack failure.[140] A significant literature on SCC in alloys exists for comparison of model results with experiments, for example see work by Macdonald.

In this appendix, we build on the work in Ch. 6 and apply our methods to the SCC problem.* In this appendix, we first outline the methods used in Sec. H.2, then illustrate our preliminary results in Sec. H.3, and finally summarize the results and future work in Sec. H.4. The goal of this work is to improve our understanding of this the corrosion fatigue process in aluminum.

H.2   Methods

This appendix uses the multiphase and multi-species models utilized in Ch. 6 and further detailed in Apx. C. The Shan–Chen multiphase model provides a computationally simple model of fluids in the spinodal thermodynamic state, as we discuss in further detail in Sec. C.2.4.[111] In all models, the solid domains were sketched manually in a digital image editing software. For the two-phase model, periodic boundary conditions were used in both directions. Additionally, the fluids by solids have attractive forces which manifest as a capillary pressure at the two-phase interface.

We detailed the multi-component method in Sec. C.3.1. We apply the passive solute component model with one explicit species and one implicit solvent species ac-

---

* In fact, the work of this chapter was conducted first because the failure of the part is of highest interest. However, the pitting corrosion became the primary focus because it is the more fundamental fluid process from which we could build up models of stress cracking, and SCC is also a much larger scale problem.

counting for full advection in the low concentration limit of the explicit species.[111]For LBGK models the diffusivity is not fully independent of the viscosity of the fluids, but has the computational advantage of a simple first order equilibrium collision approximation.

Fully physical models of stress corrosion cracking requires an accurate model of the solid mechanics of crack propagation. Ideally, the mechanical behaviors would be derived from *ab initio* constitutive relationships via molecular dynamics simulations. A first means of constraining the fluid behavior is using the immersed boundary methods (IBM) to describe a moving solid boundary, fluctuating with the oscillatory mechanical strain that the part undergoes during usage. The IBM gives a versatile formulation of Lagrangian solid points and is often used for flexible solids. The IBM would need to be specially extended to account for fracture tip advancement in the full crack failure model. The discrete element method couples with the lattice Boltzmann method as a Lagrangian method with rigid solids and can be used for the boundary oscillations due to metal flexing. Alternatively, finite elements may be used to model solid mechanics and couple to the fluid mechanics. The extended finite element method models the behavior of crack tip propagation through material failure.

H.3   Results

H.3.1   Capillary Condensation

In Fig. H.1 we observe the coalescence process into a single crack. The density of the fluid is initialized with random initial density variations of order 5% with a density in the super-saturated regime and no prescribed velocity or gravitational force. The pseudo-potential is described by the exponential equation of state with a density-

(a) Initial density.

(b) Density at time 128.

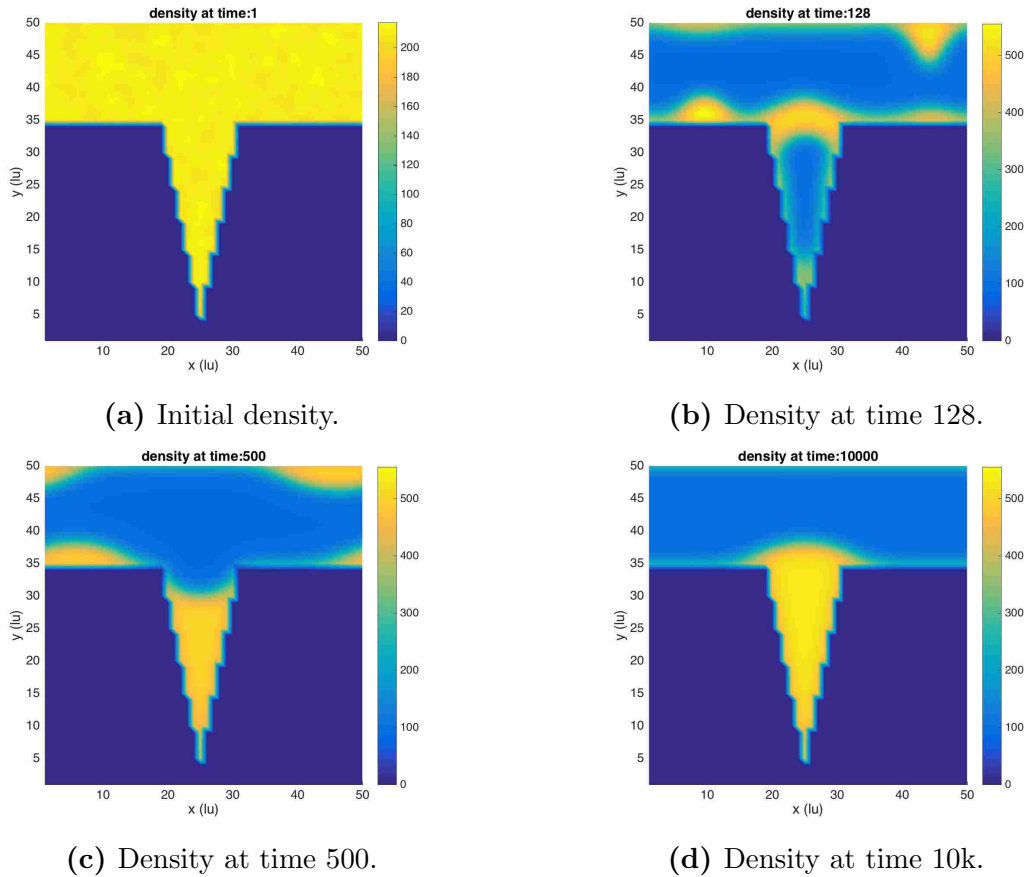**(c)** Density at time 500.

(d) Density at time 10k.

Figure H.1. Capillary condensation in a single crack.

based attractive surface potential. As the simulation progresses the fluid separates into liquid and gas and condenses into several droplets on the surface, some of which fill the crack. The crack continues to attract the fluid to condense preferentially in the crack until all fluid in the bulk have condensed over the crack by acquiring the fluids from the other droplets. Thus, the simulation gives the expected crack condensation behavior.

The simulation was then enlarged for a domain with two larger cracks, one wider than the other. In Figure H.2 we see the condensation process into the two cracks. First, we observe the condensation process initially occurring around the mouths of

(a) Initial density.

(b) Incompletely condensed.

(c) Early fluid levels in cracks.
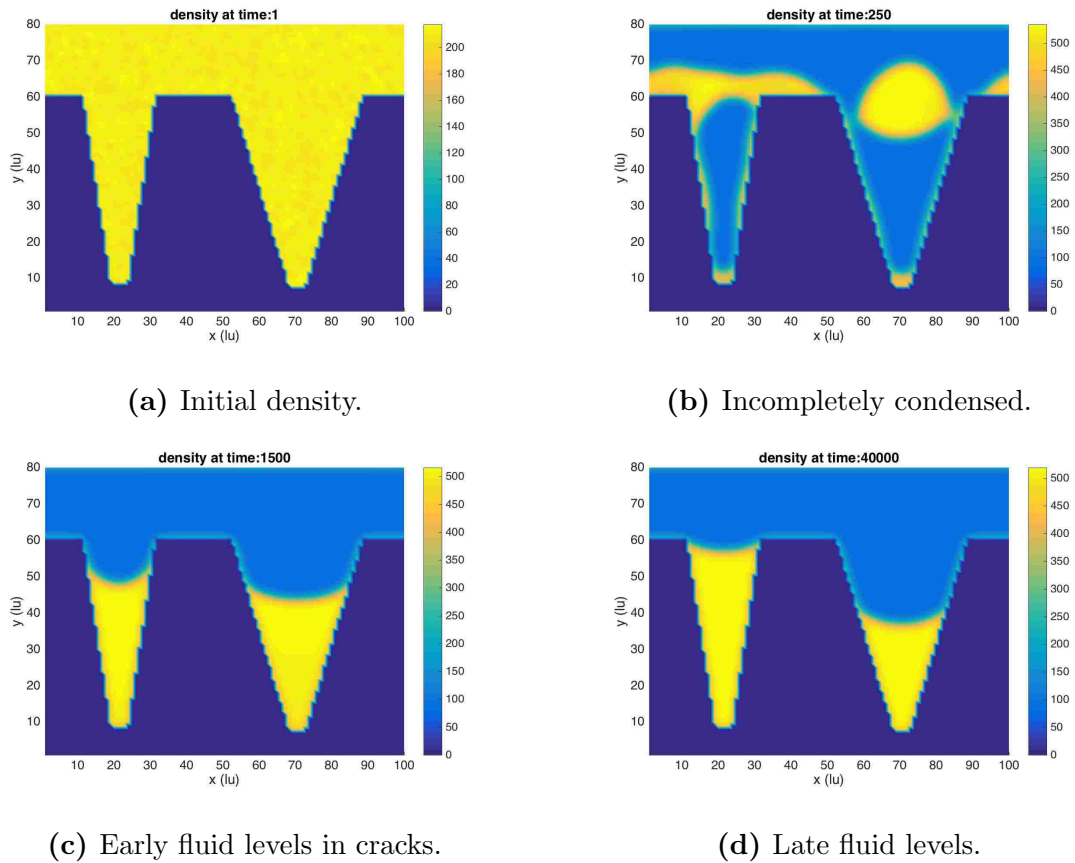
(d) Late fluid levels.

Figure H.2. Capillary condensation in two cracks.

the cracks. Both cracks then fill partially with liquid, however we see that the smaller crack has a much higher curvature than the larger because of the capillary pressure with the narrower walls. So evaporation from the surface of the larger pore liquid then condenses in the narrower crack to minimize the free energy of the system. We can see that the radius of curvature at a much later time is nearly identical in the two cracks. It should be noted that this is a slow process on the order of thirty times longer to reach this equilibrium state than to initially fill the cracks. The equilibrium is dependent on the geometry; specifically liquids condense preferentially in narrow cracks. This is similar to the bubble migration in a subsurface pit observed in Fig. 6.3.
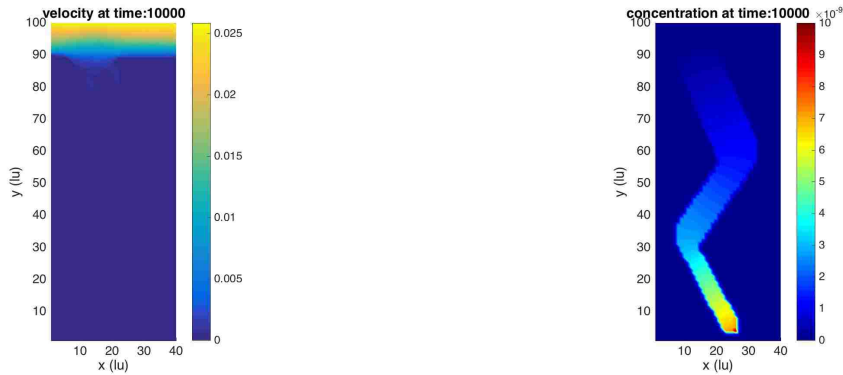
(a) Velocity over crack.

(b) Steady diffusion profile.

Figure H.3. Diffusion through a jagged crack.

H.3.2 Multispecies Transport

In Fig. H.3 we see the results of a simulation of species advection-diffusion from the tip of a deep jagged crack due to a dissolution process. The diffusion does not include electrochemical effects such as surface potential and electroosmosis. Bulk fluid flows from left to right over the crack via the lattice Boltzmann BGK equation, but we see that the velocity within the crack is not significant. A constant concentration source term is placed at the crack tip to add the ionic species into the fluid. Near the crack tip the transport is nearly pure diffusion because the flow is less than three orders of magnitude that of the velocity outside the crack.Thus, we do not need to consider advection as a primary transport mode in future simulations of species transport in static cracks.

H.4 Conclusions

Numerous improvements in methods may be made to advance the models for this project. First, the transport of solutes within the channel due to motion of the

solid crack walls may be implemented with the immersed boundary method.[141] The moving boundaries would be initially implemented with a naive solid grid, but in future, rely on the immersed boundary method for better resolution of the solid.[142] The mechanical strain may be computed using discrete elements or finite elements. For corroborating the fluid results with finite elements, we may use COMSOL® to prototype the simulations and GOMA to probe further depth in the physics. To understand the propagation of the crack tip, the extended finite element method may be used. Other physical effects on the fluid transport may be included such as electrochemistry, surface reactions, with particular interest in the hydrogen absorption at the crack tip. As the current models are not fully computationally optimized, they can be rewritten in a compiled language such as C++ or Fortran, and a one-dimensional parallel domain decomposition may be used along the length of the crack to accelerate the method because of the aspect ratio of the pore length is significantly greater than the width.

In this preliminary study, we showed that species transport within static cracks is dominated by diffusion and not by net flow or advection of the fluid. This indicates a longer timescale is needed for the simulation process, especially with cracks of common physical aspect ratios. Also, we have demonstrated the effect of parasitic capillary effects of small pores. Thus, water will preferential condense in narrower pores, and also not diffuse from them as easily. This is a mechanism for the degradation of small cracks. However, these models require a significantly more computational power than pitting corrosion due to the larger length and time scales and wider range of multi-physics phenomena.

Appendix I

Discrete Pore Models of Flow in Monoporous Particles

I.1 Background

In this appendix, we explore finite element methods of discrete pore modeling as a complimentary approach to the work given in Ch. 7. There we showed the application of the lattice Boltzmann method (LBM) to the simulation fluid motion in discrete porous materials, with an emphasis on biporous media, and we discussed elementary methods of parallel implementation of the LBM. However, to understand the macroscopic permeability from a pore scale, we should determine at least empirically, if not theoretically, a relation between the flow around a particle, its porosity, and the resulting net flow through the particle. In this chapter, we also set out to determine the applicability of a 2D model of porous transport in a particle to real 3D particles. Now, we review some of the relevant background to these problem.

In analogy with heat transport, the permeability of a porous medium, which is related to the porosity, is the hydraulic 'conductivity'.[4,8] This is shown through the

Appendix I. Discrete Pore Models of Flow in Monoporous Particles

Darcy equation[5], which facilitates the solution of systems with small pressure gradients and large system size with respect to the pore radius of the medium. In 1901, Philipp Forshheimer proposed a modification to the Darcy law that behaved more realistically at the early times of imbibition by adding in an inertial term to the equation. Furthermore, another common extension to Darcy's law was proposed by Brinkman to allow the model to function at very high permeabilities by adding in the locally-averaged viscous term contained in the Navier–Stokes equations.[20,129,130] Finally, these three models are often combined into the Darcy–Brinkman–Forchheimer equation which is often used, coupled with the energy equations, for heat transfer problems.[143] This equation allows for a wide range of capabilities although it approaches the coupled Navier–Stokes equations in computational difficulty.[144]

The finite element method is an extremely flexible and useful tool in modern computational modeling. Using variational principles, FEM allows the user to solve the system of interest by breaking the domain of the system into smaller spaces, or elements, and solving approximations to the desired solution across the elements. The finite element method approximates the solution of differential equations by converting the solution form into a series of basis functions, then the basis functions are applied to the weak form of the differential equation. This gives a matrix system which may be inverted directly to give the approximate solution of linear differential equations, or may be iterated for nonlinear systems. The convergence rate of the method is commonly second order in space, while in time it may be first order or greater depending on the need of the problem.

Finite elements is increasingly used in solving the fluid dynamics of porous systems. It's flexibility makes it especially practical in simultaneously solving multiple, interacting physical phenomena. FEM is sometimes used for discrete porous models in fractured media but is not often used for three dimensional bundles of tubes due to the computational complexity of the simulation domain. This will limit our use of

Appendix I. Discrete Pore Models of Flow in Monoporous Particles

finite element codes to smaller problems. For continuous porous models, the Poisson equation may be solved for Darcy models of the porous medium.[36] More complex continuum models of effective behaviors of porous media may also be solved. In our work these features allow the finite element method to be a framework for solutions which complement what is primarily found using lattice Boltzmann. It is desired that the capabilities of the two methods intersect to a degree which allows them to have comparable results.

The recent literature shows several examples of research into the geometries of interest. Transition Reynolds numbers, Re, for cylinders and spheres as referred to below will be on the order of $1 < \text{Re} < 100$. It is worthwhile noting that many of the discrete grids used in the simulations are circular/spherical and not cartesian.

In bimodal porous materials, recent computational work on modeling heat transport in approximately 2D bidisperse porous media domains have shown a growing interest in continuum models of complex fluid domains.[145,146] Fractal models have also utilized effective fractal dimensionality of a medium to approximate the internal fluid transport properties.[26,147]

The current literature also contains several examples of research into the flow around porous materials. It is worthwhile to note that many of the discrete grids used in the simulations are circular/spherical and not cartesian. The sources discussed below did not use discrete pores, but instead utilized the continuum equations for the porous medium. Yu, *et al.* numerically studied permeable cylinders and spheres to investigate the effects on the wake of small Reynolds number flows with the variation of the Darcy number.[131,148] They utilized the finite volume method in 2D and 3D axisymmetric coordinates to solve the Darcy–Brinkman–Forchheimer model within the object. Using the Darcy–Brinkman equation, Vainshtien, *et al.* analytically give streamlines through and around spheroids (oblate disks) in Stokes flow and high Darcy numbers.[149] Kim and Phillips discuss the use of the less-common dissipative

particle dynamics method for fluid flow in an array of cylinders.[150] For packed beds in general, Maier, *et al.* discuss the dispersion of fluids through cylinders of packed spheres and the simulation of fluid motion by the Monte Carlo method.[151] They observe peak flow effects in the average fluid motion near the walls. Overall, the literature provides a variety of prior works that are potentially useful comparisons for our fluid system.[152–156]

In the following section we discuss some of the underlying theory of discrete and continuum porous models. Sec. I.3 outlines the simulations and methods. Sec. I.4 presents the results for 2D-like and 3D particles, and Sec. I.5 gives the future work and conclusions.

I.2   Theory

Darcy spurred the physical analysis of porous media with the development of his now eponymous equation,

$$\mathbf{v} = -\frac{k}{\mu}\boldsymbol{\nabla}P \tag{I.2.1}$$

where $\mathbf{v}$ is the volumetric flux (or velocity) of fluid through the porous medium, k is the porosity, μ is the viscosity of the fluid, and P is the pressure, where each variable averages over a size much greater than the individual pores.[5] In essence, equation (I.2.1) defines the macroscopic parameter of porosity so that the flux through the medium may be directly related to the pressure applied to the system.

A key relationship implicit in the continuum modeling of a porous medium is the connection between permeability with the pore radius, porosity, and other material factors. This is unfortunately, a complex system-dependent interaction; however, some experimental algebraic models do exist.[8] A particular theoretical model is the

Kozeny–Carman equation,

$$k = \frac{1}{2} \frac{\phi^3}{(2\pi r/A)^2}, \tag{I.2.2}$$

which relates the the permeability with the void volume and other parameters of the medium.[30,56]

The Reynolds number and the Darcy Number are dimensionless numbers relevant to the analysis of porous particles and may be defined

$$\mathrm{Re} = \frac{\rho U_\infty D}{\mu}, \tag{I.2.3a}$$

$$\mathrm{Da} = \frac{k}{D^2}, \tag{I.2.3b}$$

where ρ is the fluid density, μ is the fluid viscosity, U_∞ is the characteristic velocity, D is the particle diameter, and k is the permeability.[131] This is an elementary approximation to fluid models around spheres and packed beds and focusses on the Stokes flow regime, or $\mathrm{Re} \ll 1$. For solid cylinders and spheres, Van Dyke[157] outlines the basic discussion on the singular perturbation issues of higher-order solutions of symmetric fluid flows around the particles.

I.3 Methods

Simulations were run on discrete porous particles using COMSOL® to understand the permeability of porous media from the porescale, with a goal of extending this to biporous media.[158] The software and method was chosen due to its flexibility for fluid applications, adaptable user interface, and easy access to the software. COMSOL® is a commercial multiphysics code which includes several fluid and porous media models as well as capabilities for 2D, 2D axisymmetric, and 3D simulations. The finite element method was used to investigate the effects on the ratio of fluid through versus around a porous spherical particle by changing various system parameters.

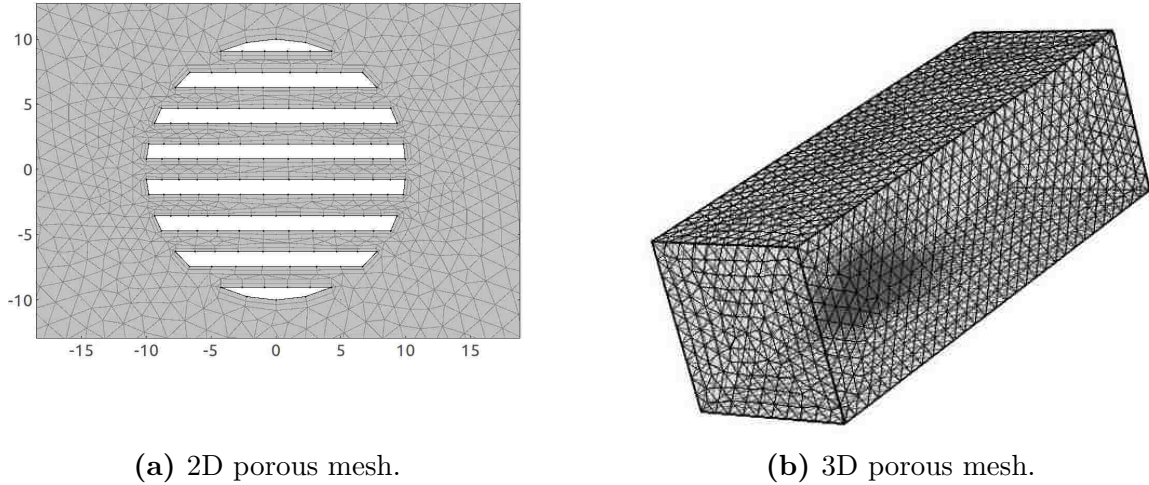*Appendix I. Discrete Pore Models of Flow in Monoporous Particles*

(a) 2D porous mesh.

(b) 3D porous mesh.

Figure I.1. 2D and 3D FEM meshes.

The focus of this preliminary work was placed on the 2D simulations so that the computational runs would be tractable. Some 3D models were explored, however meshing difficulties reduced the variety of media tested; hence 3D is lightly explored in the appendix. In two dimensions the model is effectively a cylinder, while in three dimensions the model particle is a sphere. Figure I.1a shows the 2D mesh for a particle with seven 0.8 μm pores. In Fig. I.1b the mesh for a 3D quarter-space with quarter sphere on an edge—effectively a sphere when using symmetric boundary

(a) 1 Pore.

(b) 3 Pores.

(c) 5 Pores.

(d) 7 Pores.
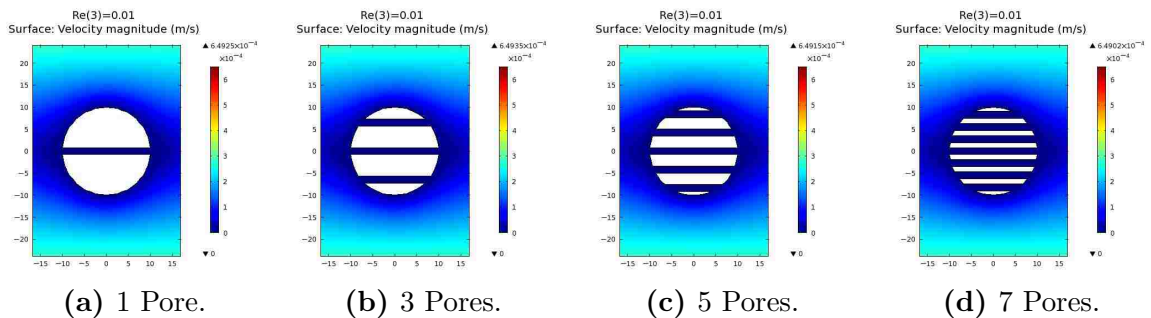
Figure I.2. Increasing numbers of discrete internal pores.

conditions—shows the large number of elements that are needed around the particle, while the majority of the fluid domain may be solved with larger element sizes. The continuum equations of porous media [*e.g.* Eqn. (I.2.1)] may be used as a model for the internal fluid motion in the particle; instead rectangles (2D) and tubes (3D) layed parallel penetrate through the objects as a model for discrete pores. The particle radius in all the models explored is 10 µm, while in 2D models the pore radii ranged from 0.8–1.1 µm and the number of pores varied from 1–7. Figure I.2 shows four different examples of 2D particles with different numbers of internal pores. Across different simulation runs, the Reynolds number of the system was also made to vary from 0.001–20 with a default value of 0.01. These ranges keep the simulation in the laminar (usually Stokes) region of the behavior of the Navier–Stokes equations for cylindrical and spherical objects. The model fluid was water at 20°C, with a density of 998.2 kg/m^3 and viscosity of 1.002×10^{-3} Pa-s.

I.4 Results

I.4.1 Two–Dimensional Models

The data on the flow field through the cross-section of the fluid motion showed the distinct effects of the porous medium on the fluid motion. As shown in Fig. I.3a, the fluid is largely detoured around the particles. However, motion through the pores increase significantly with the velocity of the fluid (Fig. I.3b). The higher velocity also brings the maximum of the fluid speed closer to the surface of the particle. The cross-sections were also integrated over space to find both the total fluid that had transversed the whole fluid domain as well as just the particles.

This entire matrix of simulations (184 simulations) took 26 minutes to run and usually each simulation was about 40,000 triangular elements. The results are plotted

(a) Full cross-section.
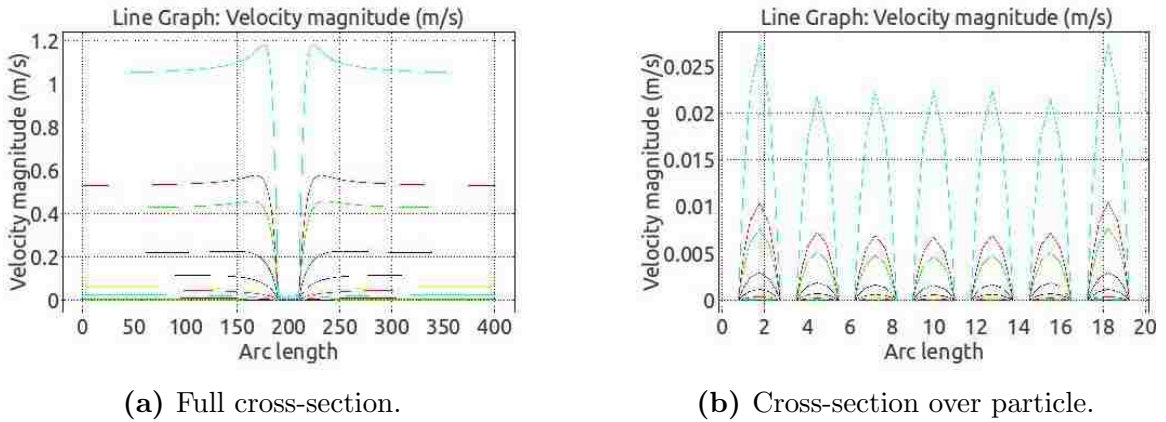

(b) Cross-section over particle.

Figure I.3. Cross-section velocity for seven pore 2D cylinder with varying Reynolds number.

in Fig. I.4 with the colored data. The fraction of fluid flowing through the particle increases drastically with increasing Reynolds number. Similarly, increasing Darcy number also increases the flow through the particle, however the slope is not as great. The gray colored plane represents a plane of best fit through this data. In the direction of the Darcy number the slope is approximately 0.5, while in the direction of the Reynolds number the slope is around one. This leads to the following hypothesis; for a cylindrical porous object in an infinite fluid medium

$$\frac{\iint_{A_{\mathrm{xsec}}} v_x \, \mathrm{d}A_{\mathrm{xsec}}}{v_\infty A_{\mathrm{xsec}}} \sim \mathrm{Re}^1 \mathrm{Da}^{1/2} \tag{I.4.1}$$

for small Re and Da. In words, the flux of liquid through a particle relative to the flux it displaces increases linearly with the Reynolds number of the system and with the square root of the Darcy number of the particle for Reynolds and Darcy numbers approaching zero. The exact reasons for this result have not yet been explored in depth. It is hoped that from the inverse of this relationship, the permeability of complex particles may be measured. This would be of practical benefit in understanding biporous particles.

The matrix of two-dimensional simulations gave a wealth of data concerning the

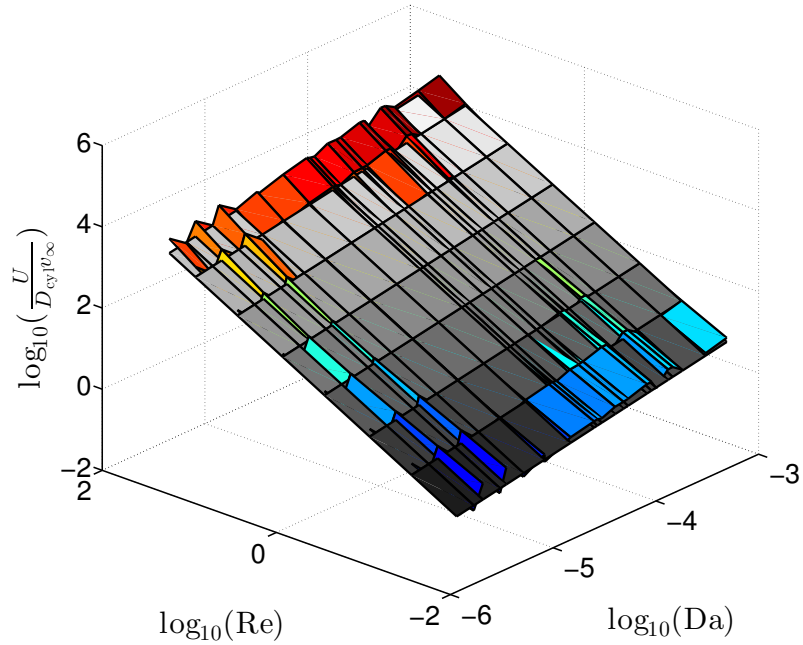*Appendix I. Discrete Pore Models of Flow in Monoporous Particles*

Figure I.4. Flow behavior with varying Reynolds and Darcy numbers in 2D.

low Reynolds number behaviors of the discrete particles. First, as shown in Fig. I.5, the shape of the fluid motion is significantly affected by the velocity of the fluid.
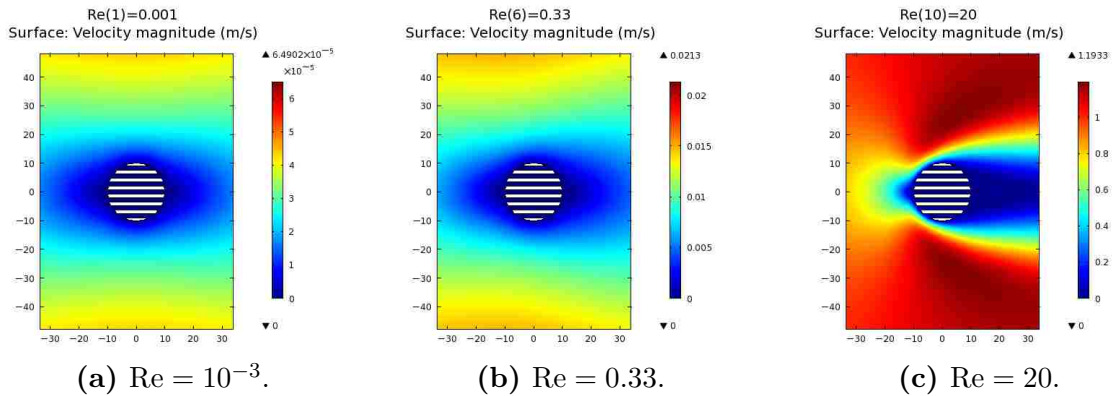

(a) $\mathrm{Re} = 10^{-3}$.   **(b)** $\mathrm{Re} = 0.33$.   **(c)** $\mathrm{Re} = 20$.

Figure I.5. Asymmetry of velocity with varying Reynolds number.

Appendix I. Discrete Pore Models of Flow in Monoporous Particles

At very low (Stokes) Reynolds number the flow is symmetric as shown in Fig. I.5a. However, the flow field begins to deform as the Reynolds number reaches 1 (Fig. I.5b) and has acquired a tail which is not yet oscillating at Re = 20 as illustrated in Fig. I.5c. This phenomenon is a validation to the discrete pore model because it is consistent with well known effects for solid cylinders.

I.4.2   Three–Dimensional Models

The three-dimensional simulations had mixed success in running. The solid sphere was able to be run with only minor refinements to the default physics. With 90,000 tetrahedral (tet) elements the simulation ran in about 15 minutes. The single pore simulation required 115,000 tet elements and took close to a half hour to run. This required adjusting the boundary layers and the adaptivity of the mesh for the simulation to run well. The solid sphere and single-pore sphere showed very similar flow profiles as compared qualitatively in Figs. I.6a and I.6b. It is especially important to note that the total volume fraction going through the sphere is quite insignificant to what goes around it.

Simulations with additional pores were attempted, however they did not successfully run. In Fig. I.7 meshes for a seven pore sphere (a) and thirty-four pore sphere (b) are shown. In both instances the simulations failed due to the multi-grid solver being unable to coarsen the mesh sufficiently to begin simulating the domain; in other words the system failed to initialize. It is surprising that this was not also the case for the single pore, although the symmetry boundary conditions next to the pore may have influenced the successful run.

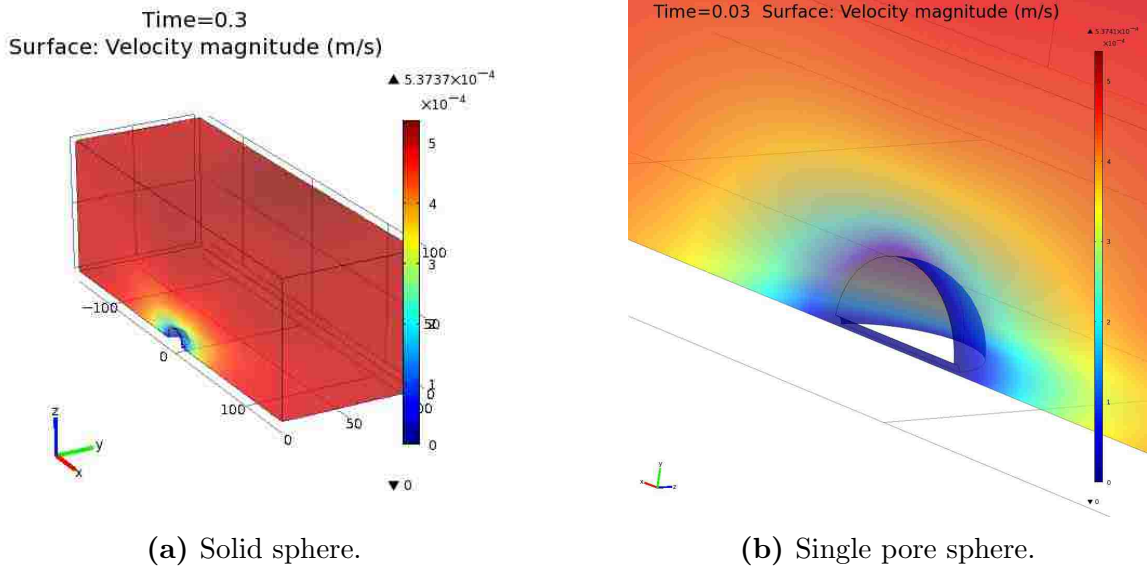**(a)** Solid sphere. **(b)** Single pore sphere.

Figure I.6. Simulation of 3D solid particle and particle with a single pore.

Comparison of Behavior Between 2D and 3D Discrete Pore Models

The simulations of the particle with a 1 µm radius pore in the center and a Reynolds number of 0.01 in two and three dimensions were compared (Fig. I.8). It was found
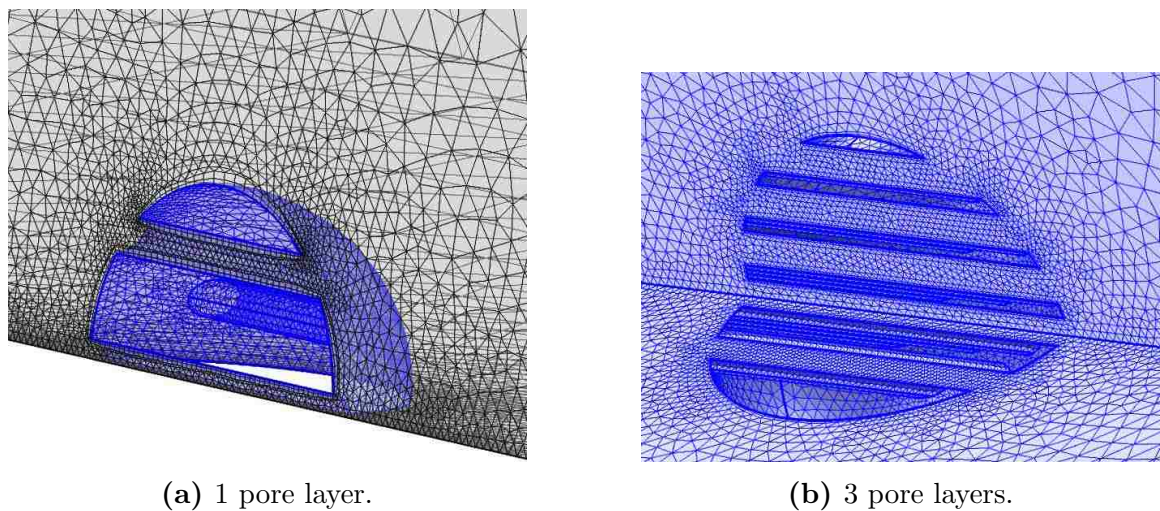

(a) 1 pore layer. **(b)** 3 pore layers.

Figure I.7. Various numbers of internal pores.

Appendix I. Discrete Pore Models of Flow in Monoporous Particles

(a) Half cross-section.

(b) Half cross-section of particle.
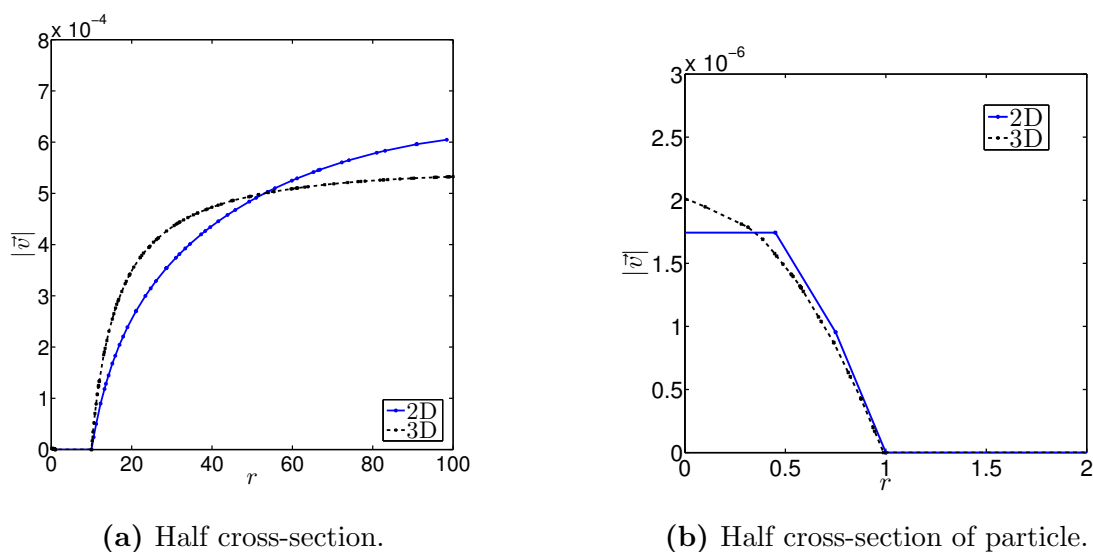
Figure I.8. Cross-section velocity (m/s) versus radius (µm) for single pore models in 2D and 3D.

that the linear cross-sectional flow profile outside the particles were significantly different. In Fig. I.8a the 3D model increases in flow and then levels off much more quickly than the 2D simulation. This is reasonable since in three dimensions the flow would be effected less by a sphere than by a full cylinder of equal radius as there is more volume and surface area to the cylinder to affect fluid motion. However, in Fig. I.8b the flow profiles within the pore appear very similar. The integral of the linear cross-section for 2D is 1.31×10^{-6} m²/s and for the 3D pore the integral is 1.37×10^{-6} m²/s. This is a limited result as the profile of the 2D simulation is not completely resolved as shown by the blue curve in Fig. I.8b. The similar values of the flow is important as it shows that the flow profile within the pore may be comparable in behavior between two and three dimensional systems. Ultimately, three dimensional systems were difficult computationally to resolve, however may still bring some helpful insights. The linear cross-section of a cylinder and sphere of the same specifications gave very similar flow profiles.

I.5   Summary

The three-dimensional meshes should be modified until they are able to work for a greater number of pores, and then run over a variety of Reynolds numbers and with varying pore sizes. This will probably be done on a more limited scale than the 2D simulations due to the computational time involved. It would be beneficial to compare the geometric effects of 2D and fully 3D particle models and how that impacts the interpretation of flow behavior. Finite elements are capable of discretizing is continuum models (such as the Darcy or the Darcy–Brinkman equations) of the internal porous nature of the particles; this would be a useful extension to be quantitatively compared to these discrete porous models. Other FEA software may be used, such as GOMA—an open source code from Sandia National Laboratories—which has built in continuum approximations of approximate pore distributions.[159] We may modify the size of the fluid domains and shift to periodic boundary conditions, so that the system would be treated either a slurry or packed bed of spheres in cubic or body-centered cubic lattices. Finally, a 2D finite element model of biporous media would bring full extension of the FEA to connect with the LBM results.

We have discussed some discrete pore models of fluid flow through particles using COMSOL®. We found for 2D particles that the flow through the inside of the particle varies proportional to the Reynolds number around the particle and the square root of the Darcy number of the particle itself. This indicated a possible means of computationally determining permeability from the flow cross-section of the particle. Furthermore, we showed that the flow around the exterior of 2D and 3D particles is distinctly different, while the flows through the particles is parabolic. Thus, we believe for low pressure differential pressures across a particle, that 2D is a reasonable approximation for 3D flow and permeability affects.

Appendix I. Discrete Pore Models of Flow in Monoporous Particles

This glossary lists the symbols and abbreviations used in this dissertation.

Glossary

Acronyms

BC   Boundary Condition

BGK   Bhatnagar–Gross–Krook

ECN   Evaporation–Capillary Number

FEM   Finite Element Method

GAT   Green–Ampt Theory

LBE   Lattice Boltzmann Equation

LBM   Lattice Boltzmann Method

LGCA Lattice Gas Cellular Automata

LHS   Left Hand Side

LPBM Lattice Poisson–Boltzmann Method

MPI   Message Passing Interface

RHS   Right Hand Side

SCC   Stress Corrosion Cracking

UNM   University of New Mexico

Symbols

0   Prescribed boundary value

0   Through inlet

Appendix I. Discrete Pore Models of Flow in Monoporous Particles

a Half width of inlet

α Discrete distribution function index

α Liquid/solid contact angle

Bo   Bond number

Bo_a Modified Bond number

C Concentration

c_s Lattice sound speed

D_σ Diffusion of species

Da   Darcy number

δ z-direction thickness of thin porous media

δ_t Lattice time step

$\mathbf{E}$ Electric field

e Energy per mass

e Fundamental electric charge

$\mathbf{e}_\alpha$ Discrete unit velocity

ε_r Relative permittivity

ε_0 Vacuum permittivity

eq   Equilibrium

η Elliptic spatial variable

$\mathbf{F}$ Force term

f Distribution function

f Front position

f   Through front interface

G Multiphase fluid-fluid interaction strength

g Species distribution function

Appendix I. Discrete Pore Models of Flow in Monoporous Particles

G_{ads}	Multiphase fluid-solid interaction strength
γ	Gravity velocity potential
γ	Interfacial tension
h	Electric potential distribution function
i	Lattice coordinate in x-direction
i	Through inlet
$\mathbf{j}$	Fluid momentum density
j	Integer index
j	Lattice coordinate in y-direction
k	Permeability
k	Reaction rate
k_b	Boltzmann constant
k_f	Reaction rate in the fluid
k_w	Reaction rate of the wall
L	Wetted length
ℓ_x	lattice size in the x-direction
ℓ_y	lattice size in the y-direction
$\mathbf{M}$	LBM MRT moment inversion matrix
m	Integer index
$\mathfrak{N}$	Evaporation-capillary number
n	Capillary diffusion order
n	Integer index
n_c	Integral weight of corner/diagonal velocities
$\mathfrak{N}_{\mathrm{f}}$	Front interface evaporation-capillary number
n_∞	Bulk ionic number density

Appendix I. Discrete Pore Models of Flow in Monoporous Particles

$\mathfrak{N}_n$	Normal surface evaporation-capillary number
$\mathfrak{N}_s$	Side boundary evaporation-capillary number
n_s	Integral weight of side velocities
n_s	Solid occupancy of lattice
ν	Dynamic viscosity
ν	Lattice viscosity
Ω	Collision opperator
ω	Distribution function weights
ω	Side evaporation velocity potential
$\bar{\omega}$	Electric potential distribution function weights
ω_c	Integral weight of corner/diagonal velocities
ω_s	Integral weight of side velocities
$\mathbf{p}$	Momentum
P	Pressure
P_c	Capillary pressure
φ	Total velocity potential
Ψ	Electric potential
ψ	Asimuthal variable
ψ	Inter-particle potential
Q	Normal surface evaporation rate
q_f	Front interface evaporation rate
q_s	Side boundary evaporation rate
R_1	First principle radius of curvature
R_2	Second principle radius of curvature
R	Gas constant

Appendix I. Discrete Pore Models of Flow in Monoporous Particles

r	Radius
Re	Reynolds number
ρ	Fluid density
ρ_e	Electron density
$\mathbf{S}$	LBM scattering matrix
$\hat{\mathbf{S}}$	Orthogonalized LBM MRT scattering matrix
σ	Species index
s	Through side boundary
SS	Steady state
T	Temperature
t	Time
τ	Relaxation time
τ_{D_σ}	Species relaxation time
θ	Primary angular variable
$\mathbf{u}$	Velocity
U	Bulk velocity
u	Velocity in the x-direction
$\mathbf{v}$	Velocity
v	Velocity in the y-direction
$\mathbf{x}$	Position
x	Position in the $\hat{\mathbf{i}}$ direction
ξ	Capillary velocity potential
y	Position in the $\hat{\mathbf{j}}$ direction
z	Ionic electric charge
z	Position in the $\hat{\mathbf{k}}$ direction

References

[1] Carroll NJ, Pylypenko S, Atanassov PB, Petsev DN. Microparticles with bimodal nanoporosity derived by microemulsion templating. *Langmuir*. 2009; 25(23):13540–13544.

[2] Qian KK, Bogner RH. Application of mesoporous silicon dioxide and silicate in oral amorphous drug delivery systems. *Journal of pharmaceutical sciences*. 2012;.

[3] Föll H, Christophersen M, Carstensen J, Hasse G. Formation and application of porous silicon. *Materials Science and Engineering: R: Reports*. 2002;39(4):93–141.

[4] Bear J. *Dynamics of Fluids in Porous Media*. Dover Books on Physics & Chemistry. Dover Publications. 1972.

[5] Darcy HPG. *Dètermination des lois d'ècoulement de l'eau à travers le sable*. Victor Dalmont. 1856.

[6] Yuan Z, Garcia AL, Lopez GP, Petsev DN. Electrokinetic transport and separations in fluidic nanochannels. *Electrophoresis*. 2007;28(4):595–610.

[7] Keating EH, Vesselinov VV, Kwicklis E, Lu Z. Coupling Basin-and Site-Scale Inverse Models of the Española Aquifer. *Ground water*. 2003;41(2):200–211.

[8] Dullien FAL, et al. *Porous Media: Fluid Transport and Pore Structure*: vol. 2. Academic Press San Diego. 1992.

[9] Harris S. *An introduction to the theory of the Boltzmann equation*. Courier Corporation. 2004.

[10] Landau LD, Lifshitz EM. *Statistical Physics (Part 1)*. No. 5 in Course of Theoretical Physics. Elsevier Science. 1996.

REFERENCES

[11] Landau LD, Lifshitz EM. *Fluid Mechanics.* No. 6 in Course of Theoretical Physics. Butterworth–Heinemann. 1987.

[12] Lifshitz EM, Pitaevskiĭ LP. *Physical Kinetics.* No. 10 in Course of Theoretical Physics. Butterworth–Heinemann. 1981.

[13] Succi S. *Lattice Boltzmann Equation for Fluid Dynamics and Beyond.* Oxford University Press. 2001.

[14] McGee H. Corks, Cork Taints & Corked Wine. `http://www.herbmuseum.ca/content/corks-cork-taints-corked-wine`. Accessed: 2016-10-24.

[15] Babadagli T. Current Research Projects: Fractured and Heterogeneous Systems. `https://sites.ualberta.ca/~tayfun/research.htm`. Accessed: 2016-10-24.

[16] Defects in brickwork. `http://www.designingbuildings.co.uk/wiki/Defects_in_brickwork`. Accessed: 2016-10-24.

[17] Villarrubia CWN, Lau C, Ciniciato GP, Garcia SO, Sibbett SS, Petsev DN, Babanova S, Gupta G, Atanassov P. Practical electricity generation from a paper based biofuel cell powered by glucose in ubiquitous liquids. *Electrochemistry Communications.* 2014;45:44–47.

[18] Ashley CE, Carnes EC, Phillips GK, Padilla D, Durfee PN, Brown PA, Hanna TN, Liu J, Phillips B, Carter MB, et al. The targeted delivery of multicomponent cargos to cancer cells by nanoporous particle-supported lipid bilayers. *Nature materials.* 2011;10(5):389–397.

[19] Burleigh DT. Interesting Failures. `http://www.corrosionhelp.com/failures.htm`. Accessed: 2016-09-31.

[20] Whitaker S. The Forchheimer equation: a theoretical development. *Transport in Porous media.* 1996;25(1):27–61.

[21] Ge J, Schirhagl R, Zare RN. Glucose-Driven Fuel Cell Constructed from Enzymes and Filter Paper. *J Chem Educ.* 2011;88:1283–1286.

[22] Villarrubia CWN, Soavi F, Santoro C, Arbizzani C, Serov A, Rojas-Carbonell S, Gupta G, Atanassov P. Self-feeding paper based biofuel cell/self-powered hybrid μ-supercapacitor integrated system. *Biosensors and Bioelectronics.* 2016; 86:459–465.

REFERENCES

[23] Benner EM, Petsev DN. Potential flow in the presence of a sudden expansion: Application to capillary driven transport in porous media. *Phys Rev E.* 2013; 87:033008.

[24] Benner EM, Petsev DN. Evaporation Influences on Wicking in Thin Porous Strips. In: Wolfe D. *Porous Media: Theory, Properties and Applications.* Nova Science Publishers. 2016: chap. 3, 87–124.

[25] Zaid B, Saidi D, Benzaid A, Hadji S. Effects of pH and chloride concentration on pitting corrosion of AA6061 aluminum alloy. *Corrosion Science.* 2008; 50(7):1841–1847.

[26] Yu B, Cheng P. A fractal permeability model for bi-dispersed porous media. *International journal of heat and mass transfer.* 2002;45(14):2983–2993.

[27] Pylypenko S, Olson TS, Carroll NJ, Petsev DN, Atanassov P. Templated platinum/carbon oxygen reduction fuel cell electrocatalysts. *The Journal of Physical Chemistry C.* 2010;114(9):4200–4207.

[28] Zill DG, Wright WS. *Advanced Engineering Mathematics.* Jones & Bartlett Learning. 2009.

[29] McQuarrie DA. *Mathematical methods for scientists and engineers.* University Science Books. 2003.

[30] Bird RB, Stewart WE, Lightfoot EN. *Transport Phenomena.* Wiley International edition. Wiley. 2007.

[31] Moon PH, Spencer DE. *Field Theory Handbook: Including Coordinate Systems, Differential Equations and Their Solutions.* Springer–Verlag. 1988.

[32] Sauer T. *Numerical Analysis.* Pearson Addison Wesley. 2006.

[33] Gautschi W. *Numerical analysis.* Birkhäuser Boston. 2011.

[34] Hughes TJR. *The Finite Element Method: Linear Static and Dynamic Finite Element Analysis.* Dover Publ. 2000.

[35] Reddy JN. *An Introduction to the Finite Element Method.* McGraw-Hill Series in Mechanical Engineering. McGraw-Hill Education. 2006.

[36] Wang HF, Anderson MP. *Introduction to Groundwater Modeling: Finite Difference and Finite Element Methods.* Elsevier Science. 1995.

REFERENCES

[37] Anderson JD. *Computational fluid dynamics: the basics with applications*. McGraw–Hill series in aeronautical and aerospace engineering. McGraw–Hill. 1995.

[38] Ferziger JH, Perić M. *Computational methods for fluid dynamics*: vol. 2. Springer Berlin etc. 1999.

[39] Brebbia CA, Walker S. *Boundary element techniques in engineering*. Elsevier. 2013.

[40] Monaghan JJ. Smoothed particle hydrodynamics. *Annual review of astronomy and astrophysics*. 1992;30:543–574.

[41] Wu J, Li Z. Density-functional theory for complex fluids. *Annu Rev Phys Chem*. 2007;58:85–112.

[42] Karniadakis G, Beskok A, Aluru N. *Microflows and nanoflows: fundamentals and simulation*: vol. 29. Springer. 2005.

[43] Frenkel D, Smit B. Understanding molecular simulation: from algorithms to applications. *Computational sciences series*. 2002;1:1–638.

[44] Ezuber H, El-Houd A, El-Shawesh F. A study on the corrosion behavior of aluminum alloys in seawater. *Materials & Design*. 2008;29(4):801–805.

[45] McCafferty E. Sequence of steps in the pitting of aluminum by chloride ions. *Corrosion Science*. 2003;45(7):1421–1438.

[46] DuQuesnay DL, Underhill PR, Britt HJ. Fatigue crack growth from corrosion damage in 7075-T6511 Aluminium alloy under aircraft loading. *International Journal of Fatigue*. 2003;25(5):371–377.

[47] Wheeler TD, Stroock AD. The transpiration of water at negative pressures in a synthetic tree. *Nature*. 2008;455:208–212.

[48] Fenton EM, Mascarenas MR, López GP, Sibbett SS. Multiplex Lateral-Flow Test Strips Fabricated by Two-Dimensional Shaping. *ACS Applied Materials & Interfaces*. 2009;1(1):124–129. PMID: 20355763.

[49] Martinez AW, Phillips ST, Whitesides GM. Diagnostics for the Developing World: Microfluidic Paper-Based Analytical Devices. *Anal Chem*. 2010;82:3–10.

[50] Mendez S, Fenton EM, Gallegos GR, Petsev DN, Sibbett SS, Stone HA, Zhang Y, Lopez GP. Imbibition in Porous Membranes of Complex Shape: Quasi-stationary Flow in Thin Rectangular Segments. *Langmuir*. 2010;26:1380–1385.

REFERENCES

[51] Churaev NV. *Liquid and Vapour Flows in Porous Bodies: Surface Phenomena*: vol. 13 of *Topics in Chemical Engineering*. New York: Gordon and Breach. 2000.

[52] Julio SSD, Shallenberger WH. Bioslurping – Horizontal Radial Flow – Theory and Experimental Validation. *J Hazardous Substance Res*. 2002;3:6–1 – 6–19.

[53] Bell JM, Cameron FK. The flow of liquids through capillary spaces. *The Journal of Physical Chemistry*. 1906;10(8):658–674.

[54] Lucas R. Ueber das Zeitgesetz des Kapillaren Aufstiegs von Flussigkeiten. *Kolloid Z*. 1918;23:15.

[55] Washburn EW. The Dynamics of Capillary Flow. *Phys Rev*. 1921;17:273–283.

[56] Happel JR, Brenner H. *Low Reynolds Number Hydrodynamics*. Mechanics of Fluids and Transport Processes Series. Kluwer. 1983.

[57] Hall C. Water Movement in Porous Building Materials IV. The Initial Surface Absorption and the Sorptivity. *Build Environ*. 1981;16:201–207.

[58] Wilson MA, Hoff WD, Hall C. Water Movement in Porous Building Materials XI. Capillary Absorption from a Hemispherical Cavity. *Build Environ*. 1994; 29:99–104.

[59] Philip JR. In: *Water in the Unsaturated Zone, Proceedings of the Wageningen Symposium*. Absorption and infiltration in two-and three-dimensional systems: vol. 1. 1966; 503–516.

[60] Xiao J, Stone HA, Attinger D. Source-like Solution for Radial Imbibition into a Homogeneous Semiinfinite Porous Medium. *Langmuir*. 2012;28:4208–4212.

[61] Hyväluoma J, Raiskinmäki P, Jäsberg A, Koponen A, Kataja M, Timonen J. Simulation of liquid penetration in paper. *Phys Rev E*. 2006;73:036705.

[62] Philip JR. *Theory of Infiltration*. Advances in Hydroscience. New York: Academic Press. 1969.

[63] Gummerson RJ, Hall C, Heft WD, Hawkes R, Holland GN, Moore WS. Unsaturated water flow within porous materials observed by NMR imaging. *Nature*. 1979;281:56–57.

[64] Lavi B, Marmur A, Bachmann J. Porous Media Characterization by the Two-Liquid Method: Effect of Dynamic Contact Angle and Inertia. *Langmuir*. 2008; 24:1918–1923.

REFERENCES

[65] Wilkes JO. *Fluid Mechanics for Chemical Engineers with Microfluidics and CFD*. New York: Prentice Hall. 2006.

[66] Rowlinson JS, Widom B. *Molecular Theory of Capillarity*. Dover books on chemistry. Dover Publications. 2002.

[67] Achour NS, Hamdaoui M, Nasrallah SB. Wicking and Evaporation of Liquids in Knitted Fabrics: Analytic Solution of Capillary Rise Restrained by Gravity and Evaporation. *Int J Innov Res Sci Eng Technol*. 2015;9(7):1371–1376.

[68] Hornberger GM. *Elements of physical hydrology*. JHU Press. 1998.

[69] Bear J. *Hydraulics of groundwater*. Courier Corporation. 2012.

[70] Richards LA. Capillary conduction of liquids through porous mediums. *Journal of Applied Physics*. 1931;1(5):318–333.

[71] Green WH, Ampt GA. Studies on soil physics: I. Flow of air and water through soils. *J Agric Sci*. 1911;4:1–24.

[72] Swartzendruber D. Derivation of a two-term infiltration equation from the Green–Ampt model. *Journal of Hydrology*. 2000;236(3):247–251.

[73] Elizalde E, Urteaga R, Berli CL. Rational design of capillary-driven flows for paper-based microfluidics. *Lab on a Chip*. 2015;15(10):2173–2180.

[74] Barry DA, Parlange JY, Sander GC, Sivaplan M. A class of exact solutions for Richards' equation. *Journal of Hydrology*. 1993;142(1):29–46.

[75] Fries N, Dreyer M. An analytic solution of capillary rise restrained by gravity. *Journal of colloid and interface science*. 2008;320(1):259–263.

[76] Barry DA, Wissmeier L, Parlange JY, Sander GC, Lockington DA. Comment on "An analytic solution of capillary rise restrained by gravity" by N. Fries and M. Dreyer. *Journal of colloid and interface science*. 2009;338(1):293–295.

[77] Philip JR. Falling-head ponded infiltration with evaporation. *Journal of Hydrology*. 1992;138(3):591–598.

[78] Hohenbichler G, Köppl A, Schneider W. Evaporation of a liquid flowing through a slender porous cylinder. *Acta mechanica*. 1994;107(1-4):21–32.

[79] Lockington D, Parlange JY, Lenkopane M. Capillary absorption in porous sheets and surfaces subject to evaporation. *Transport in porous media*. 2007; 68(1):29–36.

[80] Fries N, Odic K, Conrath M, Dreyer M. The effect of evaporation on the wicking of liquids into a metallic weave. *Journal of colloid and interface science.* 2008; 321(1):118–129.

[81] Barry DA, Parlange JY, Lockington DA, Wissmeier L. Comment on The effect of evaporation on the wicking of liquids into a metallic weave by N. Fries, K. Odic, M. Conrath and M. Dreyer. *Journal of colloid and interface science.* 2009; 336(1):374–375.

[82] Benner EM, Petsev DN. Evaporation Effect on Two-Dimensional Wicking in Porous Media. 2016;p. unpublished manuscript.

[83] Prat M. Recent advances in pore-scale models for drying of porous media. *Chemical engineering journal.* 2002;86(1):153–164.

[84] Lehmann P, Assouline S, Or D. Characteristic lengths affecting evaporative drying of porous media. *Physical Review E.* 2008;77(5):056309.

[85] Sadeghi M, Shokri N, Jones SB. A novel analytical solution to steady-state evaporation from porous media. *Water Resources Research.* 2012;48(9).

[86] Faghri A, Zhang Y. *Transport Phenomena in Multiphase Systems.* Elsevier Science. 2006.

[87] Civan F. *Porous Media Transport Phenomena.* Wiley. 2011.

[88] Fries N, Dreyer M. The transition from inertial to viscous flow in capillary rise. *Journal of colloid and interface science.* 2008;327(1):125–128.

[89] Masoodi R, Languri E, Ostadhossein A. Dynamics of liquid rise in a vertical capillary tube. *Journal of colloid and interface science.* 2013;389(1):268–272.

[90] Murad MA, Cushman JH. Multiscale flow and deformation in hydrophilic swelling porous media. *International Journal of Engineering Science.* 1996; 34(3):313–338.

[91] Homsy GM. Viscous fingering in porous media. *Annual review of fluid mechanics.* 1987;19(1):271–311.

[92] Chen Z, Huan G, Ma Y. *Computational Methods for Multiphase Flows in Porous Media.* Computational Science and Engineering. Society for Industrial and Applied Mathematics. 2006.

[93] Philip JR. Flow in porous media. *Annual Review of Fluid Mechanics.* 1970; 2(1):177–204.

REFERENCES

[94] Brooks RH, Corey AT. Hydraulic properties of porous media and their relation to drainage design. *Transactions of the ASAE*. 1964;7(1):26–0028.

[95] Liu M, Wu J, Gan Y, Hanaor DAH, Chen CQ. Evaporation limited radial capillary penetration in porous media. *Langmuir*. 2016;32(38):9899–9904.

[96] Shahraeeni E, Or D. Pore-Scale Analysis of Evaporation and Condensation Dynamics in Porous Media. *Langmuir*. 2010;26(17):13924–13936.

[97] Lewis RW, Roberts PJ, Schrefler BA. Finite element modeling of two-phase heat and fluid flow in deforming porous media. *Transport in Porous Media*. 1989;4(4):319–334.

[98] Cairncross RA, Madasu S, Schunk PR. A finite element formulation for modeling dynamic wetting on flexible substrates and in deformable porous media. *Tech. rep.*: Sandia National Laboratories. 2004.

[99] Szekely J, Neumann A, Chuang Y. The rate of capillary penetration and the applicability of the Washburn equation. *Journal of Colloid and Interface Science*. 1971;35(2):273–278.

[100] Benner EM, Petsev DN. see Supplementary Material: Evaporation Effect on Two-Dimensional Wicking in Porous Media. 2016;p. Supplementary Material.

[101] Philip JR. Steady infiltration from buried point sources and spherical cavities. *Water Resources Research*. 1968;4(5):1039–1047.

[102] Milczarek JJ, Fijal-Kirejczyk I, Zoladek J, Chojnowski M, Kowalczyk G. Effect of gravitation on water migration in granular media. *Acta Physica Polonica A*. 2008;113:1245.

[103] Zhang J, Klasky M, Letellier BC. The aluminum chemistry and corrosion in alkaline solutions. *Journal of Nuclear Materials*. 2009;384(2):175–189.

[104] Cottis RA. Guides to Good Practice in Corrosion Control—Stress Corrosion Cracking. *National Physical Laboratory, Teddington*. 2000;.

[105] Kamoutsi H, Haidemenopoulos GN, Bontozoglou V, Pantelakis S. Corrosion-induced hydrogen embrittlement in aluminum alloy 2024. *Corrosion Science*. 2006;48(5):1209–1224.

[106] Bhatnagar PL, Gross EP, Krook M. A Model for Collision Processes in Gases. I. Small Amplitude Processes in Charged and Neutral One-Component Systems. *Physical Review*. 1954;94:511–525.

[107] Chen H, Chen S, Matthaeus WH. Recovery of the Navier–Stokes equations using a lattice-gas Boltzmann method. *Physical Review A*. 1992;45(8):R5339.

[108] McNamara GR, Zanetti G. Use of the Boltzmann equation to simulate lattice-gas automata. *Physical Review Letters*. 1988;61(20):2332–2335.

[109] Wolf-Gladrow DA. *Lattice-gas cellular automata and lattice Boltzmann models: an introduction*. Springer. 2004.

[110] He X, Luo LS. Theory of the lattice Boltzmann method: From the Boltzmann equation to the lattice Boltzmann equation. *Physical Review E*. 1997;56(6):6811.

[111] Sukop MC, Thorne Jr DT. *Lattice Boltzmann Modeling, an Introduction for Geoscientists and Engineers*. Springer. 2006.

[112] Zou Q, He X. On pressure and velocity boundary conditions for the lattice Boltzmann BGK model. *Physics of Fluids*. 1997;9(6):1591–1598.

[113] Inamuro T, Yoshino M, Ogino F. A non-slip boundary condition for lattice Boltzmann simulations. *Physics of Fluids*. 1995;7(12):2928–2930.

[114] Shan X, Chen H. Lattice Boltzmann model for simulating flows with multiple phases and components. *Physical Review E*. 1993;47:1815–1819.

[115] Martys NS, Chen H. Simulation of multicomponent fluids in complex three-dimensional geometries by the lattice Boltzmann method. *Physical review E*. 1996;53(1):743.

[116] Chen S, Doolen GD. Lattice Boltzmann method for fluid flows. *Annual review of fluid mechanics*. 1998;30(1):329–364.

[117] Ebihara KI, Kaburaki H. Lattice Boltzmann simulation of solution chemistry for crevice corrosion. *Mathematics and Computers in Simulation*. 2006;72(2):117–123.

[118] Succi S, Smith G, Kaxiras E. Lattice Boltzmann simulation of reactive microflows over catalytic surfaces. *Journal of statistical physics*. 2002;107(1-2):343–366.

[119] Kang Q, Zhang D, Chen S, He X. Lattice Boltzmann simulation of chemical dissolution in porous media. *Physical Review E*. 2002;65(3):036318.

[120] Kang Q, Zhang D, Chen S. Simulation of dissolution and precipitation in porous media. *Journal of Geophysical Research: Solid Earth*. 2003;108(B10).

[121] Fleharty ME, van Swol F, Petsev DN. Manipulating Semiconductor Colloidal Stability Through Doping. *Physical review letters*. 2014;113(15):158302.

[122] Wang J, Wang M, Li Z. Lattice Poisson–Boltzmann simulations of electro-osmotic flows in microchannels. *Journal of Colloid and Interface Science*. 2006; 296(2):729–736.

[123] Wang M, Kang Q. Modeling electrokinetic flows in microchannels using coupled lattice Boltzmann methods. *Journal of Computational Physics*. 2010; 229(3):728–744.

[124] He X, Li N. Lattice Boltzmann simulation of electrochemical systems. *Computer Physics Communications*. 2000;129(1):158–166.

[125] Fleharty ME, van Swol F, Petsev DN. Charge Regulation at Semiconductor-Electrolyte Interfaces. *Journal of colloid and interface science*. 2014;.

[126] Rathod SB, Ward TL. Hierarchical porous and composite particle architectures based on self assembly and phase separation in droplets. *Journal of Materials Chemistry*. 2007;17(22):2329–2335.

[127] Sano T, Yanagishita H, Kiyozumi Y, Mizukami F, Haraya K. Separation of ethanol/water mixture by silicalite membrane on pervaporation. *Journal of membrane science*. 1994;95(3):221–228.

[128] Carroll NJ, Rathod SB, Derbins E, Mendez S, Weitz DA, Petsev DN. Droplet-based microfluidics for emulsion and solvent evaporation synthesis of monodisperse mesoporous silica microspheres. *Langmuir*. 2008;24(3):658–661.

[129] Forchheimer P. Wasserbewegung durch boden. *Z Ver Deutsch Ing*. 1901; 45(1782):1788.

[130] Brinkman HC. A calculation of the viscous force exerted by a flowing fluid on a dense swarm of particles. *Applied Scientific Research*. 1949;1(1):27–34.

[131] Yu P, Zeng Y, Lee TS, Chen XB, Low HT. Steady flow around and through a permeable circular cylinder. *Computers & Fluids*. 2011;42(1):1–12.

[132] Pacheco PS. *An Introduction to Parallel Programming*. An Introduction to Parallel Programming. Elsevier Science. 2011.

[133] Gustafson JL, Montry GR, Benner RE. Development of parallel methods for a 1024-processor hypercube. *SIAM journal on Scientific and Statistical Computing*. 1988;9(4):609–638.

REFERENCES

[134] Pan C, Luo LS, Miller CT. An evaluation of lattice Boltzmann schemes for porous medium flow simulation. *Computers & fluids*. 2006;35(8):898–909.

[135] Boltzmann L. *Lectures on Gas Theory*. Dover Books on Physics. Dover Publications. 2012.

[136] Du R, Shi B, Chen X. Multi-relaxation-time lattice Boltzmann model for incompressible flow. *Physics Letters A*. 2006;359(6):564–572.

[137] Huang H, Sukop M, Lu X. *Multiphase lattice Boltzmann methods: Theory and application*. John Wiley & Sons. 2015.

[138] Zhou SJ, Lomdahl PS, Thomson R, Holian BL. Dynamic crack processes via molecular dynamics. *Physical review letters*. 1996;76(13):2318.

[139] Boutt DF, Cook BK, McPherson BJOL, Williams JR. Direct simulation of fluid-solid mechanics in porous media using the discrete element and lattice-Boltzmann methods. *Journal of Geophysical Research: Solid Earth*. 2007; 112(B10).

[140] Moës N, Belytschko T. Extended finite element method for cohesive crack growth. *Engineering fracture mechanics*. 2002;69(7):813–833.

[141] Chiu WKS, Joshi AS, Grew KN. Lattice Boltzmann model for multi-component mass transfer in a solid oxide fuel cell anode with heterogeneous internal reformation and electrochemistry. *The European Physical Journal-Special Topics*. 2009;171(1):159–165.

[142] Favier J, Revell A, Pinelli A. A Lattice Boltzmann–Immersed Boundary method to simulate the fluid interaction with moving and slender flexible objects. *Journal of Computational Physics*. 2014;261:145–161.

[143] Amhalhel G, Furmański P. Problems of modeling flow and heat transfer in porous media. *Journal of Power Technologies*. 1997;85:55–88.

[144] Yang DX, Li GW, Zhang DL. A CE/SE Scheme for Flows in Porous Media and Its Applications. *Aerosol and Air Quality Resarch*. 2009;9(2):266–276.

[145] Revnic C, Grosan T, Pop I, Ingham DB. Free convection in a square cavity filled with a bidisperse porous medium. *International Journal of Thermal Sciences*. 2009;48(10):1876–1883.

[146] Kumari M, Pop I. Mixed convection boundary layer flow past a horizontal circular cylinder embedded in a bidisperse porous medium. *Transport in porous media*. 2009;77(2):287–303.

REFERENCES

[147] Malek K, Coppens MO. Effects of surface roughness on self-and transport diffusion in porous media in the Knudsen regime. *Physical review letters.* 2001; 87(12):125505.

[148] Yu P, Zeng Y, Lee TS, Chen XB, Low HT. Numerical simulation on steady flow around and through a porous sphere. *International Journal of Heat and Fluid Flow.* 2012;36(0):142–152.

[149] Vainshtein P, Shapiro M, Gutfinger C. Creeping flow past and within a permeable spheroid. *International journal of multiphase flow.* 2002;28(12):1945–1963.

[150] Kim JM, Phillips RJ. Dissipative particle dynamics simulation of flow around spheres and cylinders at finite Reynolds numbers. *Chemical engineering science.* 2004;59(20):4155–4168.

[151] Maier RS, Kroll DM, Bernard RS, Howington SE, Peters JF, Davis HT. Hydrodynamic dispersion in confined packed beds. *Physics of Fluids.* 2003;15:3795.

[152] Bhattacharyya S, Dhinakaran S, Khalili A. Fluid motion around and through a porous cylinder. *Chemical engineering science.* 2006;61(13):4451–4461.

[153] Jones IP. Low Reynolds number flow past a porous spherical shell. *Mathematical Proceedings of the Cambridge Philosophical Society.* 1973;73:231–238.

[154] Wu RM, Lee DJ. Highly porous sphere moving through centerline of circular tube filled with Newtonian fluid. *Chemical engineering science.* 1999; 54(23):5717–5722.

[155] Naito H, Fukagata K. Numerical simulation of flow around a circular cylinder having porous surface. *Physics of Fluids.* 2012;24(11):117102–117102.

[156] Gushchin VA, Kostomarov AV, Matyushin PV, Pavlyukova ER. Direct numerical simulation of the transitional separated fluid flows around a sphere and a circular cylinder. *Journal of Wind Engineering and Industrial Aerodynamics.* 2002;90(4):341–358.

[157] van Dyke M. *Perturbation methods in fluid mechanics*: vol. 9. Parabolic Press Stanford, California. 1975.

[158] Comsol. *Multiphysics Reference Guide for COMSOL 4.0.* 2010.

[159] Schunk PR, Rao RR, Chen KS, Labreche DA, Sun ACT, Hopkins MM, Moffat HK, Roach RA, Hopkins PL, Notz PK, Roberts SA, Sackinger PA, Subia SR, Wilkes ED, Baer TA, Noble DR, Secor RB. *GOMA 6.0: A full-Newton finite element program for free and moving boundary problems with coupled fluid/solid momentum, energy, mass, and chemical species transport: User's guide.* 2013.

Index

Index